University of Alberta

ULTRAFAST PHOTONIC APPLICATIONS FOR TERAHERTZ WAVEFORM GENERATION

by

Jonathan F. Holzman

A thesis submitted to the Faculty of Graduate Studies and Research in partial fulfillment

of the requirement for the degree of Doctor of Philosophy

Department of Electrical and Computer Engineering

Edmonton, Alberta

Fall 2003

National Library
of Canada

Acquisitions and
Bibliographic Services

395 Wellington Street
Ottawa ON K1A 0N4
Canada

Bibliothèque nationale
du Canada

Acquisisitons et
services bibliographiques

395, rue Wellington
Ottawa ON K1A 0N4
Canada

Your file Votre référence
ISBN: 0-612-87990-9
Our file Notre référence
ISBN: 0-612-87990-9

Canada

University of Alberta

Library Release Form

Name of Author: Jonathan F. Holzman

Title of Thesis: Ultrafast Photonic Applications for Terahertz Waveform Generation

Degree: Doctor of Philosophy

Year this Degree Granted: 2003

September 23, 2003

University of Alberta

Faculty of Graduate Studies

The undersigned certify that they have read, and recommended to the Faculty of Graduate Studies and Research for acceptance, a thesis entitled ULTRAFAST PHOTONIC APPLICATIONS FOR TERAHERTZ WAVEFORM GENERATION submitted by Jonathan F. Holzman in partial fulfillment of the requirement for the degree of Doctor of Philosophy.

Dr. J. F. Whitaker

September 18, 2003

Dedication

This thesis is dedicated to my family…
for all of their love and support.

Abstract

This thesis presents theoretical and experimental work on the generation of both terahertz (THz) electrical waveforms and free-space THz radiation. Transmission-line-coupled THz electrical waveform generation is introduced first, through the concepts of photoconductive (PC) self-switching and PC frozen wave generation. The PC self-switching technique is demonstrated in both microstrip and coplanar experimental geometries. Here, it is found that electrical pulses as short as 1.2 ps can be generated with a microstrip ultrathin silicon (Si) PC switch, and electrical pulses as short as 2 ps can be generated with a coplanar gallium arsenide (GaAs) PC switch. These results demonstrate a significant increase in the PC switching speed of conventional Si and GaAs devices. In addition to this work, the concept of PC frozen wave generation is introduced as an attractive source for THz electrical waveforms. This technique makes use of a direct-current (DC) to radio-frequency (RF) conversion process that maps the spatial extent of the bias electrode structure onto the temporal shape of the electrical transient. By employing sufficiently short electrode spacings, it is shown that the operation of the device can be extended into the THz frequency-domain.

The concept of PC switching is applied next to the generation of free-space THz radiation. To start, the operational capabilities of a conventional GaAs PC THz emitter are analyzed. It is determined that the operation of the GaAs emitter is limited by both space-charge and near-field THz screening under high optical pump fluences. To overcome these limitations, the ZnSe PC THz emitter is introduced next. The ZnSe PC device offers a substantially higher dielectric breakdown strength (compared to semi-

insulating GaAs) and can, therefore, be scaled to extremely large THz powers by increasing the external bias field. Finally, crystalline and polycrystalline ZnSe samples are applied to the detection of free-space THz radiation. It is found that both the crystalline and polycrystalline samples are effective detectors of free-space THz waveforms.

Acknowledgements

I wish to thank my supervisor, Dr. Abdulhakem Elezzabi, for his support, encouragement, and guidance over the past few years. Your helpful criticisms and numerous suggestions have made all of the work contained in this thesis possible. Thank you to Dr. Fred Vermeulen, as well, for your thought-provoking discussions and imaginative insight into the fascinating world of electromagnetics.

Thank you to Dr. Ken Westra and Keith Franklin from the University of Alberta's Nanofabrication Facility for providing the facilities necessary to fabricate and test each of the devices presented here. Also, a special thank you to Blair Harwood, Ben Bathgate, Herbert Dexel, Barry Arnold, Martin Reidner, and Mike Boissonneault for their expert technical advice and endless patience over the past few years.

Finally, I would like to thank my peers Michael Cummings, Scott Irvine, Anthony Dechant, and Ken Chau for all of their assistance, insight...and camaraderie.

Table of Contents

1.0 INTRODUCTION

2.0 GENERATION AND DETECTION OF TERAHERTZ ELECTRICAL WAVEFORMS

3.0 GENERATION AND DETECTION OF FREE-SPACE TERAHERTZ WAVEFORMS

4.0 CONCLUSIONS

APPENDICES

List of Figures

List of Abbreviations

CVD	chemical vapour deposition
DC	direct-current
EO	electro-optic
FWG	frozen wave generator
FWHM	full-width-at-half-maximum
LO	longitudinal-optic
LT	low-temperature
MBE	molecular-beam-epitaxy
PC	photoconductive
PVD	physical vapour deposition
RC	resistance-capacitance
RD	radiation-damaged
RF	radio-frequency
RMS	root-mean-square
SOS	Si-on-sapphire
TEM	transverse electromagnetic
THz	terahertz
TO	transverse-optic

CHAPTER 1.0

INTRODUCTION

1.1 Terahertz Generation

In 1888, Heinrich Hertz successfully demonstrated the generation and transmission of broadband electromagnetic pulses. With this discovery, he pioneered the contemporary field of radio science [1]. By generating and transmitting subnanosecond electromagnetic pulses, he proved, for the first time, that electromagnetic energy can be made to propagate in the form of "electric waves" [2]. Since that time, research into the formation of electromagnetic waveforms has continued, spurred by a desire to produce exceedingly short pulse durations and increasingly broad bandwidths. The thesis which follows seeks to continue in these footsteps, by extending the generation capabilities of electromagnetic sources into the terahertz (THz) regime and by developing new THz detection schemes.

THz waveforms can be loosely defined as electromagnetic transients with frequency components that extend from 100 GHz to 30 THz. The ability to generate and transmit these ultrafast electromagnetic signals is the goal of numerous areas of contemporary research. Crystal oscillators and transmission lines, for instance, have dominated the field of electronics over the past few decades, providing broadband electrical signal generation and transmission for frequencies up to 100 GHz. While these electronic sources are successful in producing stable *low-frequency* signals, they are severely lacking in their ability to generate signals beyond the gigahertz regime. The field of laser research, on the other hand, has been very successful over the past few decades at generating *high-frequency* electromagnetic radiation. These coherent laser sources are capable of generating and transmitting radiation at frequencies beyond 30 THz. Unfortunately, numerous technical obstacles associated with the far-infrared have prevented the practical application of these sources at much lower frequencies.

The region that lies between the generation capabilities of electronic sources and laser sources is often described as the THz regime. The THz portion of the electromagnetic spectrum has become a topic of growing interest as electronics researchers seek the broadband benefits of THz electrical sources and laser researchers seek the far-infrared penetrating properties of THz radiation sources. THz electrical pulses have, for example, been recently employed in a variety of applied research fields. The ultrawide bandwidths, short pulse durations, and temporal coherence of these electronic signals make them ideal for time-resolved applications such as the broadband characterization of electronic devices [3]-[5] and high-speed intra-chip signal transmission [6]. Likewise, the development of free-space THz radiation sources has given rise to a variety of enterprising applications, including THz impulse ranging [7], [8], THz-ray imaging [9], [10], ultrafast charge carrier dynamical studies [11], [12], and THz time-domain spectroscopy [13]-[16]. Indeed, the short pulse durations and ultrawide bandwidths associated with these THz electrical pulses and free-space THz waveforms make them ideal for a number of contemporary applications.

1.2 Scope of this Thesis

The generation of both transmission line-coupled THz electrical transients and free-space THz radiation is based largely upon the technique of photoconductive (PC) switching. A simplified schematic of this PC generation process is shown in figure 1.2.1. The key elements to the operation of this device are the optically active semiconductor substrate, the biased transmission line structure on the surface, and the small PC gap in the transmission line. Here, the continuity of this transmission line is interrupted by a small PC gap. The presence of this gap and the large dark resistivity of the semiconductor substrate, together, ensure that the nominal potential on the grounded cathode remains well below the biased potential on the anode. Upon illuminating the PC gap with a near-instantaneous above-bandgap optical pulse, however, electrons are liberated from the valence band to the conduction band in the semiconductor, and the resistance across the switch is dramatically decreased. As a result, the potential on the cathode is increased, and an electrical pulse is formed on the transmission line. The duration of this electrical transient is governed largely by the charge carrier dynamics in the semiconductor plasma.

It is interesting to note that, in addition to the formation of this electrical pulse on the transmission line, free-space THz waveforms can result from the optical activation of this device. Photo-excitation of the switch, and the subsequent acceleration of the semiconductor charge carriers in the biased PC gap, will create a time-varying photo-current. The time derivative of this current maps itself onto the electric field in the far-field regime of the emitter. If the photo-generation mechanism is fast enough (on a subpicosecond timescale for instance), the frequency content of the radiated waveform can span into the THz spectrum.

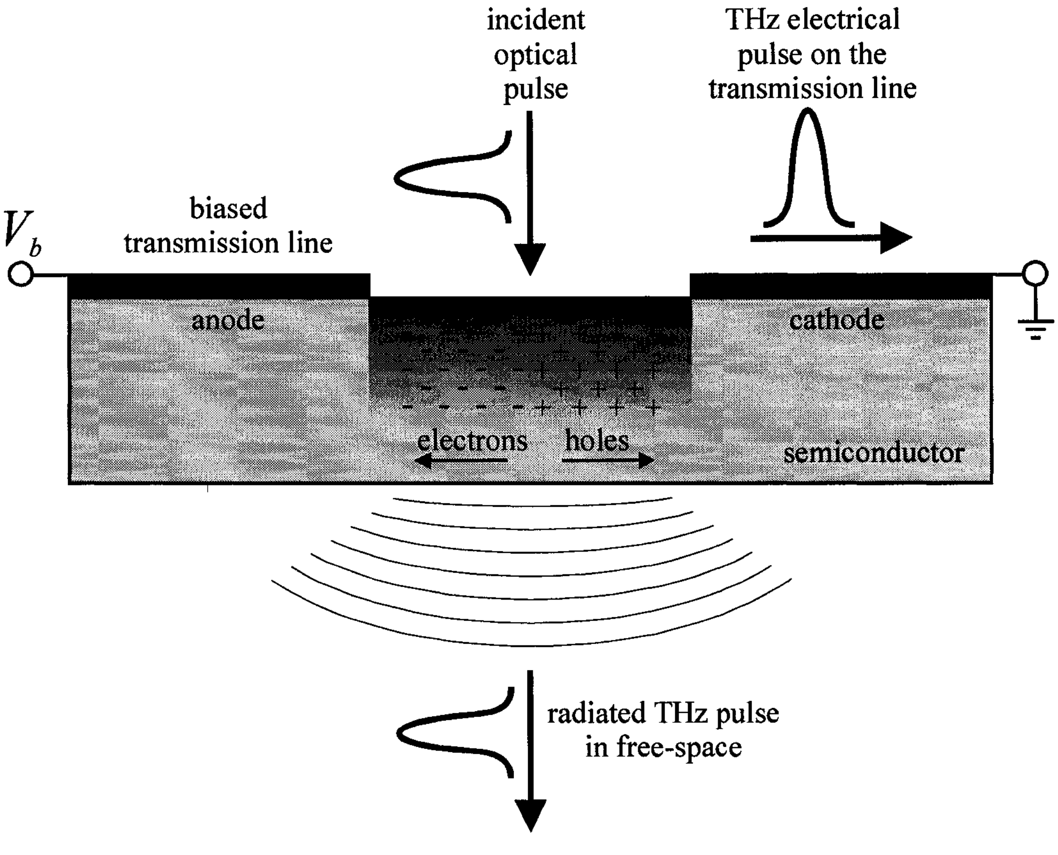

Figure 1.2.1 A depiction of the optical generation of both THz electrical transients and free-space THz radiation. An ultrashort optical pulse illuminates the PC gap, generating an electron-hole plasma. The subsequent bias field-induced acceleration of these charge carriers produces a photo-current on the transmission line and a radiated electric field in the far-field regime of the emitter.

The thesis which follows presents theoretical and experimental work on development of novel THz generation and detection schemes. Here, the PC THz generation processes are applied to the formation of both transmission line-coupled THz electrical waveforms and free-space THz radiation. The work is divided into these two major areas of research. Chapter 2.0 describes first the generation of transmission line-coupled THz electrical waveforms. After a brief explanation of the experimental setup employed (section 2.2), the concept of PC self-switching is introduced through theoretical and experimental work on ultrathin silicon (Si) PC self-switching (section 2.3) and coplanar gallium arsenide (GaAs) PC self-switching (section 2.4). Here, it is shown that ultrashort THz electrical pulses can be formed on transmission lines through a time-delayed multi-switching process. Next, the idea of using a time-delayed generation mechanism for the formation of THz electrical waveforms is applied to the concept of PC frozen wave generation (section 2.5). Unlike self-switching–where the temporal profile of the electrical pulse is controlled by the optical time-delay between competing turn-on and turn-off processes–frozen wave generation utilizes a delay in the propagation of the electrical transient to form multi-cycle THz electrical waveforms. Lumped-element circuit models for the ultrathin Si PC switch, the coplanar PC switch, and the PC frozen wave generator (FWG) are presented to explain the operation of each device.

Chapter 3.0 moves beyond the generation of transmission line-coupled THz electrical waveforms to the domain of free-space THz radiation. Here, it is found that freely propagating electromagnetic waveforms can be generated and detected in the far-field regime of a PC switch. After describing the generation and detection system for the free-space THz pulses (section 3.2), the principal of PC THz generation is presented through a study of a conventional GaAs PC emitter. It is found in section 3.3 that the operation of GaAs devices is limited largely by near-field THz screening and space-charge screening effects at high optical pump powers. In an effort to overcome these saturation effects, section 3.4 introduces the ZnSe PC dipole THz emitter. ZnSe has an order of magnitude larger breakdown field strength than semi-insulating GaAs and can, therefore, be operated at significantly higher bias voltages (eliminating the need for large pump powers and the corresponding THz saturation). Finally, section 3.5 studies the application of ZnSe towards the detection of free-space THz electromagnetic transients–a topic which is becoming increasingly important as the bandwidth of the generated THz signals continues to increase.

Chapter 1.0 References:

[1] H. Hertz, "Über die Ausbreitungsgeschwindigkeit der electrodynamischen Wirkungen," *Ann. Phys.* **34**, pp. 551-569, 1888.

[2] H. Hertz, *Electric Waves: Being Researches on the Propagation of Electric Action with Finite Velocity through Space*, translated by D. E. Jones (Dover, New York, 1962), pp. 107-123.

[3] M. Y. Frankel, J. F. Whitaker, G. A. Mourou, "Optoelectronic transient characterization of ultrafast devices," *IEEE J. Quantum Electron.* **28**, pp. 2313-2324, 1992.

[4] M. Frankel, "500-GHz characterization of an optoelectronic s-parameter test structure," *IEEE Microwave Guided Wave Lett.* **4**, pp. 118-120, 1994.

[5] M. Y. Frankel, S. Gupta, J. A. Valdmanis, G. A. Mourou, "Terahertz attenuation and dispersion characteristics of coplanar transmission lines," *IEEE Trans. Microwave Theory Tech.* **39**, pp. 910-916, 1991.

[6] R. W. McGowan and D. Grischkowsky, "Experimental time-domain study of THz signals from impulse excitation of a horizontal surface dipole," *Appl. Phys. Lett.* **74**, pp. 1764-1766, 1999.

[7] R. A. Cheville and D. Grischkowsky, "Time domain terahertz impulse ranging studies," *Appl. Phys. Lett.* **67**, pp. 1960-1962, 1995.

[8] R. W. McGowan, R. A. Cheville, and D. Grischkowsky, "Direct observation of the Gouy phase shift in THz impulse ranging," *Appl. Phys. Lett.* **76**, pp. 670-672, 2000.

[9] Z. Jiang and X.-C. Zhang, "Terahertz imaging via electrooptic effect," *IEEE Trans. Microwave Theory Tech.* **47**, pp. 2644-2650, 1999.

[10] D. M. Mittleman, R. H. Jacobsen, and M. C. Nuss, "T-ray imaging," *IEEE J. Select. Topics Quantum Electron.* **2**, pp. 679-692, 1996.

[11] M. Schall, M. Walther, C. Winnewisser, H. Helm, and P. Uhd Jepsen, "Subpicosecond time-resolved terahertz time-domain spectroscopy of transient carrier dynamics in semiconductors," *Proc. SPIE* **3828**, pp. 220-227, 1999.

[12] K. P. Lui and F. A. Hegmann, "Ultrafast carrier relaxation in radiation-damaged silicon on sapphire studied by optical-pump-terahertz-probe experiments," *Appl. Phys. Lett.* **78**, pp. 3478-3480, 2001.

[13] M. van Exter and D. Grischkowsky, "Optical and electronic properties of doped silicon from 0.1 to 2 THz," *Appl. Phys. Lett.* **56**, pp. 1694-1696, 1990.

[14] M. Brucherseifer, P. Haring Bolivar, and H. Kurz, "Combined optical and spatial modulation THz-spectroscopy for the analysis of thin-layered systems," *Appl. Phys. Lett.* **81**, pp. 1791-1793, 2002.

[15] M. van Exter. Ch. Fattinger, and D. Grischkowsky, "Terahertz time-domain spectroscopy of water vapour," *Opt. Lett.* **14**, pp. 1128-1130, 1989.

[16] P. Y. Han, M. Tani, M. Usami, S. Kono, R. Kersting, and X.-C. Zhang, "A direct comparison between terahertz time-domain spectroscopy and far-infrared Fourier transform spectroscopy," *J. Appl. Phys.* **89**, pp. 2357-2359, 2001.

CHAPTER 2.0

GENERATION AND DETECTION OF TERAHERTZ ELECTRICAL WAVEFORMS

2.1 Background

The single largest advancement in the generation of THz electrical pulses was the development of the PC switch in 1975 [1]. Here, Auston showed that picosecond electrical pulses could be formed by optical excitation of a biased semiconductor gap on a microstrip transmission line. The availability of picosecond pulsed laser sources, along with the subpicosecond response time of the electron-hole plasma generation process, meant that ultrashort electrical pulses with extremely short durations and exceedingly broad bandwidths could be formed from these devices. Since this pioneering experiment, research has continued toward the generation of shorter electrical pulses, with the main thrust of this effort being to enhance the recovery time of the PC switch. While the turn-on process of the electrical pulse generation process can be extremely fast (limited mainly by the free-carrier generation rate and the optical pulse duration), the turn-off process of the electrical transient is constrained by the long carrier lifetime of the electron-hole plasma (limited mainly by recombination processes in the semiconductor). As such, conventional PC switching with semiconductors such as GaAs and Si can produce, at best, electrical pulses with durations of 1.2 ns [2] and 20 ns [3], respectively.

To overcome the recovery time limitations associated with standard PC switching, devices have been fabricated using a variety of unconventional semiconductor materials– some of which include amorphous Si [4], low-temperature (LT) molecular-beam-epitaxy-(MBE-) grown GaAs [5], [6], and radiation-damaged (RD) Si-on-sapphire (SOS) [7]. The fabrication processes for the amorphous Si devices (thermal decomposition of silane through chemical vapour deposition (CVD)) [4], the LT-GaAs devices (MBE growth at 200^0C on semi-insulating GaAs) [8], and the RD SOS devices (ion implantation with 200 keV O^+ ions at 1 x 10^{15} cm^{-2} and 100 keV O^+ ions at 1 x 10^{15} cm^{-2}) [9] serve to introduce carrier traps and recombination centres within the lattice to inhibit the continuation of charge carrier transport. The carrier lifetime within the device is reduced, therefore, and the generated electrical transient is terminated (here the convention has been adopted that the term lifetime refers to both carrier trapping and carrier recombination, whereas the recombination time refers solely to carrier recombination). Unfortunately, PC switching with RD substrates and LT-grown substrates is limited somewhat by issues of practicality. The processing of these substrates is not always compatible with complicated device architectures, and the introduction of lattice defects can severely limit the carrier mobility. Furthermore, LT-grown substrates, such as LT-GaAs, require MBE processing, which is both cost- and time-intensive.

For the reasons mentioned above, methods that do not rely upon carrier trapping for the termination of the electrical transient are of great use in the formation of transmission line-coupled THz electrical pulses. With this in mind, Krökel et al. introduced the process of edge-illuminated PC switching [10]. Their innovative approach relies on the high degree of electric field asymmetry that exists between the electrodes of a biased PC switch (with a majority of the field being concentrated in a small region next to the positive anode) [11]. Edge-illumination occurs when this (and only this) high-field region is illuminated by an above-bandgap optical pulse, and the charge carriers within the resulting local electron-hole plasma screen the external field. As the potential across the gap cannot change on this femtosecond timescale [12], [13], the electric field within the gap redistributes itself, such that the field within the illuminated region is decreased and the field in the unilluminated region is increased. Maxwell's equations dictate that this time-varying field will produce a displacement current and an electric field transient. In this way, an ultrashort current pulse is formed on the transmission line (even though the actual photo-excitation of charge carriers follows a step-like response). Like PC switching with ultrashort-lifetime semiconductors, edge-illuminated PC switching is hindered by some practical limitations. The excitation process is extremely sensitive to the beam alignment, as it requires tight focusing onto the micron-scale high-field anode region of the PC gap. Reproducibility for the signal generation process is therefore an issue. Furthermore, the electrical pulse generation process is driven solely by the displacement current across the gap (rather than the conduction current) and is, consequently, limited in amplitude.

To overcome the difficulties associated with both recombination-limited and edge-illuminated semiconductor switching, chapter 2.0 introduces the concept of PC self-switching. Self-switching is a novel PC excitation technique that does not rely upon the carrier lifetime in the substrate. Instead, the incident optical pulse is used to both turn-on and turn-off the electrical pulse on the transmission line. The concept is presented first in a microstrip version in section 2.3, using a high-resistivity ultrathin Si substrate. The work that is presented here is based largely on a list of our recent publications on the theoretical [14] and experimental [15], [16] aspects of this device. The same self-switching process is demonstrated next for a coplanar PC switch in section 2.4. Here, it is shown that ultrashort electrical pulses can be formed on coplanar transmission lines using a GaAs substrate. Both the theoretical and experimental [17] attributes of this novel device are presented. Finally, the last section (section 2.5), looks at the technique of PC frozen wave generation. Like self-switching, frozen wave generation employs a time-delayed switching process. Unlike self-switching, however, the gating process responsible for generation of the THz transient is prescribed by the spatial extent of the transmission line structure. Our analysis of this technique [18] shows that–with proper device design–THz electrical waveforms can be formed on transmission lines through a photo-induced direct-current (DC) to radio-frequency (RF) conversion process.

2.2 The Generation and Detection System

The first step in designing and building an efficient source for transmission-line-coupled THz electrical transients will be to develop a sensitive measurement technique for subpicosecond sampling of the electrical waveforms. Conventional electrical waveform measurement systems–such as sampling oscilloscopes and spectrum analyzers–fail in this application as their frequency responses remain well below 100 GHz. To reach this objective, therefore, a *time-resolved* excitation and detection system is employed. Time-resolved measurements rely upon a finite and controllable time-delay between the generation mechanism and the sampling mechanism. This relative delay is continually varied during the time-resolved sampling process to map the temporal features of the ultrafast event.

Generation and detection of subpicosecond electrical transients requires that the PC pulse formation process and the electrical pulse detection process occur on a femtosecond timescale. The high-power optical pump pulse (responsible for generating the transient) and the low-power optical probe pulse (responsible for detecting the transient) must, therefore, be exceedingly short in duration. To meet this condition, the Ti:sapphire laser system shown in figure 2.2.1 is employed. This oscillator (Femtosource Pro, Femtolasers Produktions GmbH) is a Kerr-lens mode-locked pulsed laser source that operates at a central frequency of 800 nm with an 80 MHz repetition rate. The unit provides optical pulses with 10 fs durations and is, therefore, ideally suited to this investigation. As shown in the figure, the output of this laser is split by an 80/20 beamsplitter into the pump and probe beams, and each of these beams is directed independently to the THz electrical waveform system. Given that the arrival time for the

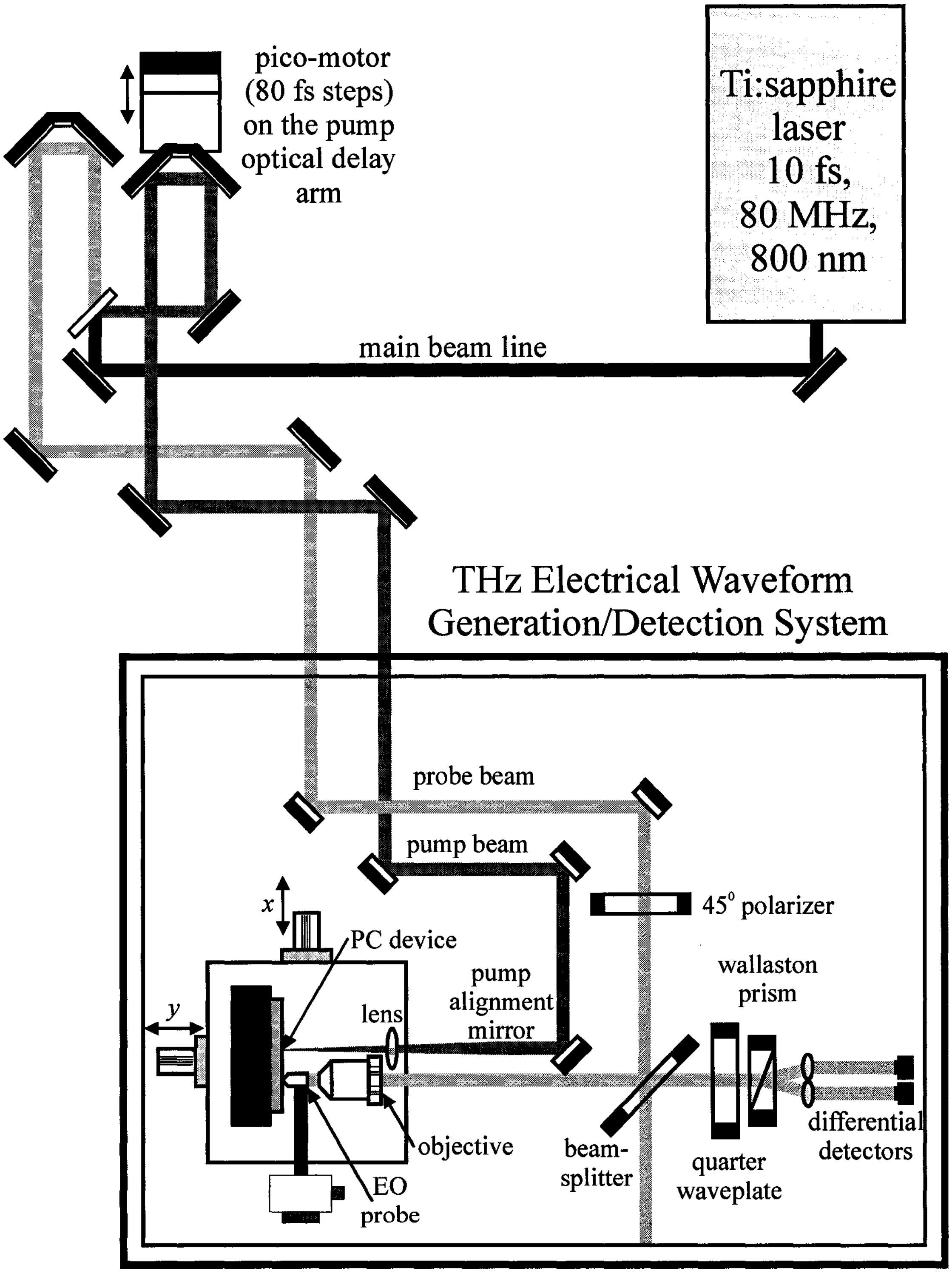

Figure 2.2.1 The complete setup for the generation and detection of THz electrical waveforms. The main beam is split by the first beamsplitter into pump and probe beams. These beams are then directed to the THz electrical generation and detection system.

pump and probe pulses is set by the optical path length of each of these two branches, the relative time-delay between the pump excitation process and the probe detection process can be scanned by varying the relative path length between these lines. For the setup shown in figure 2.2.1, the pump beam arrival time is varied by way of a motorized translation stage on the pump optical delay arm. The stage is stepped forward in 12 μm increments, allowing the probe to sample the electrical transient with 80 fs time steps (for time-resolved experiments requiring even shorter temporal resolutions, an alternative scanner with a 0.463 fs time step is employed).

To make effective use of the exceedingly short pump and probe pulse durations, it is important to incorporate an electric field sampling process that is equally fast. With this in mind, the technique of electro-optic (EO) sampling is found to be well-suited to this application [19], [20], [21]. EO sampling is fundamentally based upon the nonlinear polarization response of non-centrosymmetric media. The EO process is, therefore, able to sample (in both time and space) the electric field lines of various transmission line structures with a femtosecond resolution. Indeed, the key design issue for the detection system will focus on the engineering issues involved in mapping the time-varying electrical transient on the transmission line onto the polarization state of the co-propagating probe beam. To do this, the technique known as external EO sampling is employed. By carefully positioning an EO crystal above either a microstrip (figure 2.2.2(a)) or coplanar transmission line (figure 2.2.2(b)), the transverse component of the fringing field from the electrical transient can be made to induce a field-dependent birefringence in the crystal. This birefringence can then be mapped onto the polarization state of a co-propagating probe beam (by way of the THz field-induced phase

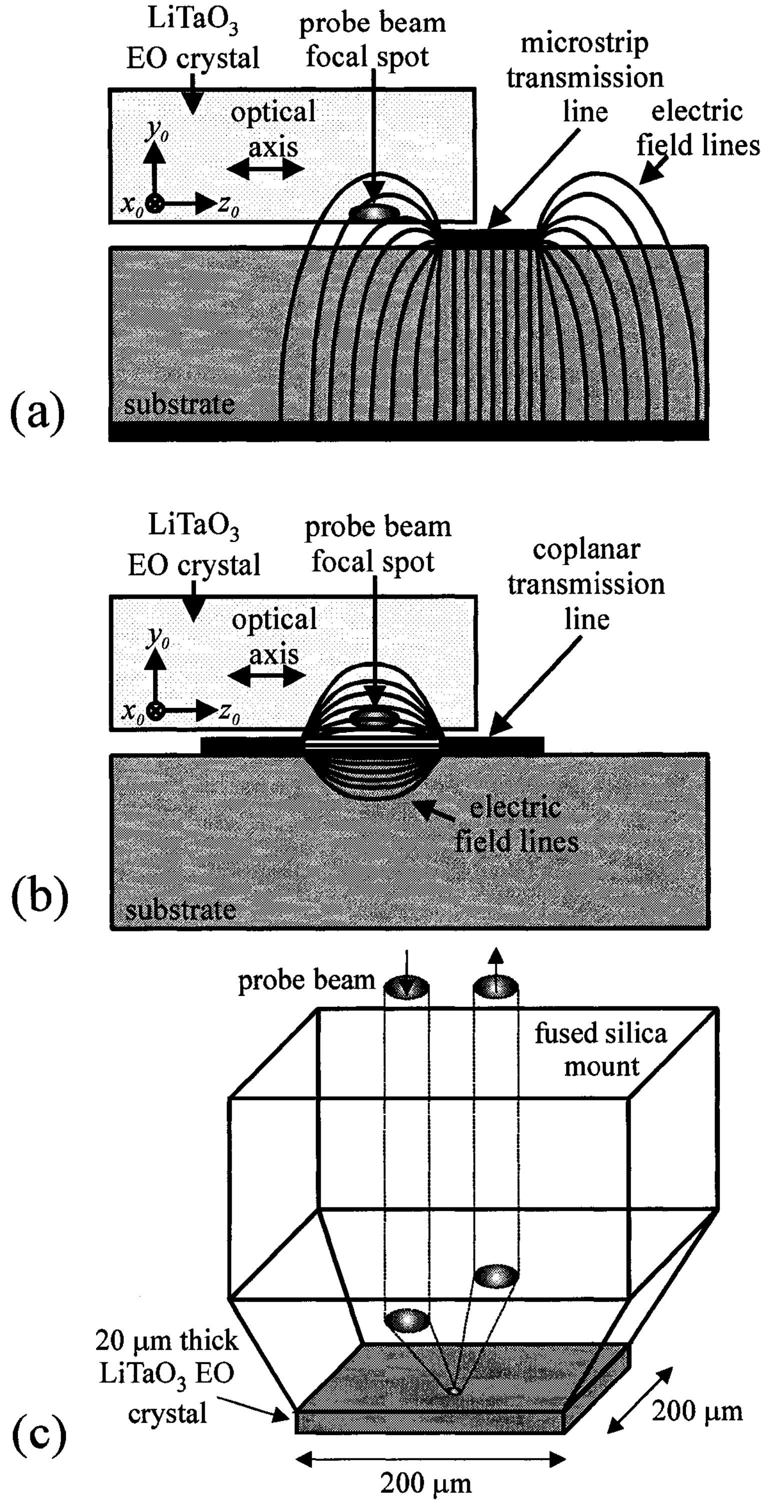

Figure 2.2.2 A close-up view of the EO sampling process is shown for a (a) microstrip transmission line and a (b) coplanar transmission line. The entire EO probe is shown in (c).

retardation). The magnitude of the phase retardation is measured finally by passing the probe beam through a quarter waveplate and wallaston prism and onto a pair of differential photodetectors. In this way, the magnitude of the THz field is linearly proportional to the differential probe power between the beams exiting the wallaston prism.

To fully realize the detection capabilities of this EO sampling system, it is important to understand the nonlinear characteristics of the sampling crystal. For the investigations described in the following sections, a $LiTaO_3$ EO crystal is employed. $LiTaO_3$ is a positive uniaxial crystal, with extraordinary and ordinary refractive indices of 2.180 and 2.176, respectively [22]. The small difference between these indices provides for a small static birefringence between the orthogonal polarizations of the probe beam–minimizing both the phase offset and the lateral beam displacement at dielectric interfaces. In contrast to this, EO materials such as $LiNbO_3$ (which is commonly used for high-speed EO modulators), suffer from a large static birefringence and are, therefore, less advantageous. A detailed theoretical analysis of the EO response of the $LiTaO_3$ probe is presented in Appendix A.

The experimental schematic for the THz electrical waveform generation and detection system is shown in detail in the lower portion of figure 2.2.1. The pump and probe beams enter the system and are directed independently toward the PC device through a 15 cm focal length lens and 0.18 NA, 10× microscope objective, respectively. To maximize the amplitude of the photo-generated signal, the location and size of the pump focal spot are optimized by way of the pump beam alignment mirror. The photo-excitation conditions are monitored during this process by observing the PC gap through an inclined stereoscope (mounted above the system) (not shown) and by monitoring the DC resistance across the gap (through the bias voltage connector). When the pump focal spot completely illuminates the PC gap and the resistance measured across the gap is minimized, the photo-excitation conditions are optimal (the photo-injection of charge carriers, in this case, drastically lowers the resistivity of the gap, decreasing the measured resistance). Next, the probe beam is aligned to sample the electric field on the transmission line. To do this, the beam is passed through the 45^0 polarizer and focused into the $LiTaO_3$ EO probe shown in figure 2.2.2(c) [23]. The reflected spots on the beamsplitter are monitored as the EO probe is translated. The sampling system is aligned when the reflected beams indicate that the probe beam passes through the crystal in the direction of propagation of the electrical transient with little lateral beam deflection. By allowing the probe beam and the electrical waveform to co-propagate in this way, the interaction length and measured signal strength are greatly improved. The EO signal is extracted, finally, by passing the probe beam through the quarter waveplate and wallaston prism pair and focusing the resulting orthogonally-polarized beams onto the differential detectors.

While the time-resolved system described above seeks to provide an ultrashort temporal resolution for the scan, it is of equal importance to obtain a high degree of sensitivity for the THz signal. To accomplish this, phase-sensitive lock-in detection is incorporated into the detection system. By modulating the experimental conditions at a high frequency–either by chopping the optical beam or modulating the bias voltage–and locking the detection system into this frequency, it is possible to overcome the large laser and acoustic-frequency noise levels associated with DC and low-frequency measurements (see, for example, the noise reduction chopper system described in Appendix B). For the THz electrical waveform system employed in this case, the bias voltage is modulated at a frequency of 3.05 MHz, and the differential current signal from the photodetectors is electronically mixed with a 3.00 MHz reference signal to produce a phase-sensitive output at the 50 kHz difference frequency; in-depth details on this mixing system are described in Appendix C [24]. The 50 kHz output from the electronic mixer is sent finally to a lock-in amplifier (Stanford Research Systems SR830 DSP lock-in amplifier) and recorded by data acquisition software (LabView) as a function of the pump-probe time-delay to produce a time-resolved image of the ultrafast transient on the transmission line.

2.3 Ultrathin Si Photoconductive Self-Switching

2.3.1 Theoretical Framework

Ultrafast optically activated semiconductor switches play a major role in the generation of ultra-broadband THz electrical waveforms. Significant progress has been made in the generation of these ultrashort electrical transients using semiconductor switches operating in the PC linear mode [25], [26], the nonlinear mode, or the avalanche mode [27], [28]. Similarly, numerous innovative techniques have been developed for the characterization [29], [30] and detection [21], [31]-[41] of these ultrafast electrical pulses. In comparison with conventional electronic switches, PC switches are easy to fabricate and offer significant improvements in both the switching speed and power handling capabilities.

As mentioned in section 2.1, a great amount of research has been devoted to the development of PC devices with decreased switch recovery times. As an alternative approach, the current section introduces the efficient generation of femtosecond and picosecond electrical pulses using a novel carrier lifetime-independent PC self-switching process. Here, the switching mechanism takes advantage of the fast rising edge of the optical pulse to turn-on and later turn-off the ultrafast electrical transient. The key feature behind this self-switching process is the use of an ultrathin semiconductor substrate (in this case Si) as the PC medium. The device, which is shown in figure 2.3.1.1(a), is comprised of a metallic microstrip transmission line (with an optically activated PC gap) on the surface of the substrate and a metal ground plane on the underside of the substrate. Of prime importance to the operation of this self-switching technique is the fact that the semiconductor substrate is kept extremely thin (less than or equal to the penetration depth of the excitation pulse). By using a 10 μm thick Si substrate (the penetration depth for

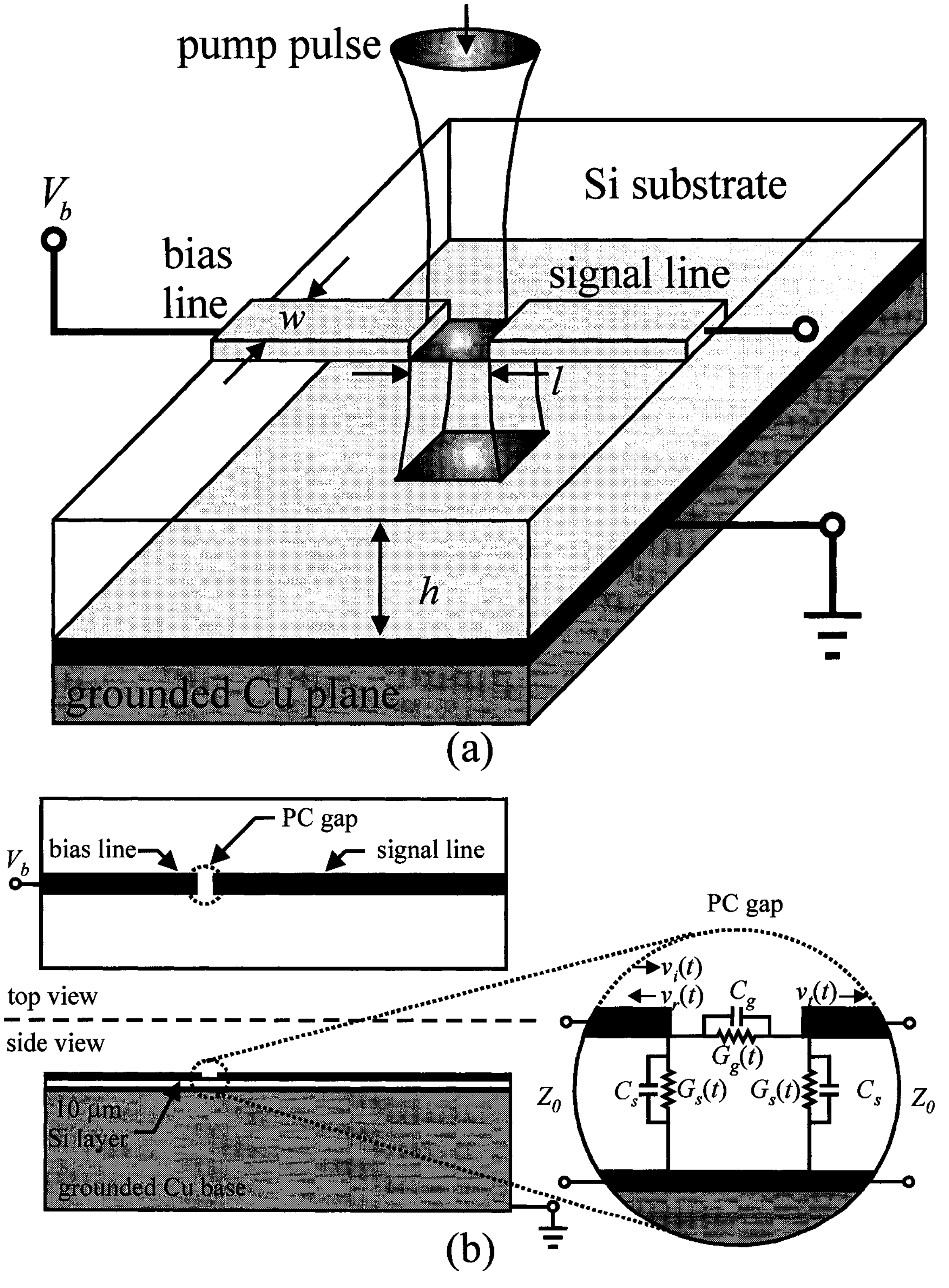

Figure 2.3.1.1 The (a) layout for the ultrathin Si PC switch, and the (b) corresponding lumped-element circuit model. Biasing is applied to the bias line on the left of the gap, the electrical signal is measured on the signal line on the right of the gap, and grounding is applied to the grounded Cu base.

800 nm radiation), the optical excitation pulse can be made to both turn-on the voltage pulse at the output of the PC gap (by shorting the terminals on the Si surface) and turn-off the voltage pulse at the output of the PC gap (by shorting the output back down towards ground). The time-delay between these turn-on and turn-off processes, as well as the resistance-capacitance (RC) response times of the PC gap terminals, will dictate the shape and duration of the resulting voltage pulse.

A variant of this self-switching technique has proven successful in the past with multi-wavelength optical excitation of a PC switch on a thick substrate [1]. In that scheme, nanosecond electrical pulses were generated using *two* optical pulses of different wavelengths: one with a small penetration depth to short the transmission line on the surface, the other with a large penetration depth to create a short to the ground plane. However, the added complexities of the multi-wavelength excitation processes and the long pulse durations made this scheme somewhat impractical.

To optimize the ultrathin Si PC device design and allow for the efficient generation of ultrashort electrical pulses, it is necessary to understand the relationship that exists between the optical excitation conditions and the time-evolution of the voltage waveforms on the transmission line. To accomplish this, the lumped-element circuit model shown in the inset of figure 2.3.1.1(b) is employed [14]. The model includes a time-varying gap conductor, $G_g(t)$, describing the conduction current across the gap, and a constant gap capacitance, C_g, describing the displacement current across the gap. Unlike conventional PC gap models [35], the model also includes two time-varying shunt conductors, $G_s(t)$, and two shunt capacitors, C_s, to incorporate the finite shunt conduction and displacement currents that are formed between the microstrip transmission line on the surface and the underlying ground plane.

During photo-excitation, the conductance associated with $G_g(t)$ increases from the dark conductance of the Si substrate to the intensity-dependent illuminated conductance (as the photo-injected charge carriers reduce the resistivity of the PC gap). For near-instantaneous optical illumination, this shorting action occurs on a very fast time scale, creating a voltage waveform at the switch output that resembles a step function. The shunt conductance elements, $G_s(t)$, on the other hand, are not excited instantaneously. Instead, these conductors remain at their dark conductance values until the excitation pulse has propagated through the Si substrate–a process that will take approximately 110 fs, given a substrate thickness of h = 10 μm and a refractive index of $n_{Si} = 3.42$. At the input of the PC gap, the impedance mismatch and reflection coefficient are altered, and the voltage at the switch input falls. Similarly, at the output of the PC gap, the impedance will be greatly diminished, driving the output waveform back down towards ground. This multi-switching process produces an ultrashort electrical pulse whose duration is largely independent of the carrier dynamics in the PC substrate.

The first step in analyzing the PC switch is to obtain an understanding of the relationship that exists between the charge carrier generation process and the formation of the electrical waveforms on the transmission line. The charge carrier generation process in the Si layer is initiated by the optical pump pulse, whose intensity,

$$I(z,t) = \frac{(1-R)E_p}{\tau_p}\exp\left[-\alpha z - 4\ln 2\left(t - t_o - z n_{Si}/c\right)^2 \big/ \tau_p^2\right], \qquad (2.3.1.1)$$

decays exponentially as it travels into the substrate (in the $+z$ direction). Here, E_p is the pump energy fluence, τ_p = 10 fs is the full-width-at-half-maximum (FWHM) of the optical pulse, $R = 0.30$ is the reflectivity of the Si surface, $\alpha = 10^3\ \mathrm{cm}^{-1}$ is the absorption coefficient for 800 nm radiation in Si, c is the speed of light, and t_o is the pump-probe zero-time for the time-resolved process. The resulting charge carrier dynamics in the PC gap are dominated largely by motion of the electrons, whose density distribution, $n(z,t)$, is described in space and time by the equation

$$\frac{\partial n(z,t)}{\partial t} = -\frac{n(z,t)}{\tau_r} + \frac{\alpha}{h\nu} I(z,t), \tag{2.3.1.2}$$

where $\tau_r = 20$ ns is the charge carrier lifetime, h is Planck's constant, and $\nu = 375$ THz is the central frequency of the incident optical beam. The first and second terms on the right-hand-side of equation 2.3.1.2 describe the carrier recombination and generation processes, respectively (dynamical effects such as carrier drift and ambipolar carrier diffusion are ignored, in this case, as they occur on longer timescales). Equation 2.3.1.2 can be further simplified by the fact that the charge carrier lifetime for the PC switch of interest is much longer than the picosecond timescale of the electrical pulse generation process. As such, the first term is eliminated, and the remaining term is integrated analytically to give the electron density function,

$$n(z,t) = \frac{(1-R)\alpha E_p \sqrt{\pi}}{4\sqrt{\ln 2}\, h\nu}\left\{1 + erf\left[2\sqrt{\ln 2}\left(t - t_o - z n_{Si}/c\right)/\tau_p\right]\right\}\exp(-\alpha z), \tag{2.3.1.3}$$

as a function of space and time.

To arrive at an appropriate expression for the time-varying conductance terms, the optically generated electron-hole plasma is linked to the conductance terms through the photo-induced conductivity,

$$\sigma(z,t) = \mu_{eff}\, e n(z,t), \tag{2.3.1.4}$$

in the Si layer. With this, the gap conductance term, $G_g(t)$, and the shunt conductance terms, $G_s(t)$, are approximated as

$$G_g(t) = \frac{w}{l}\int_0^h \sigma(z,t)dz \tag{2.3.1.5}$$

and

$$G_s(t) = \frac{wl}{\int_0^h \frac{dz}{\sigma(z,t)}}, \tag{2.3.1.6}$$

given a gap width of w = 20 μm , a gap length of l = 20 μm, an electronic charge e, and an effective mobility for the Si substrate of μ_{eff}= 1780 cm^2/V·s.

The relationship between the incident, $v_i(t)$, reflected, $v_r(t)$, and transmitted, $v_t(t)$, waveforms on the microstrip transmission line are linked, next, to the time-varying conductance response of the PC gap through straightforward application of circuit laws. Specifically, by equating the current entering the PC gap,

$$\begin{aligned} \frac{v_i(t)-v_r(t)}{Z_0} &= G_g(t)[v_i(t)+v_r(t)-v_t(t)]+G_s(t)[v_i(t)+v_r(t)] \\ &\quad +C_g\left[\frac{dv_i(t)}{dt}+\frac{dv_r(t)}{dt}-\frac{dv_t(t)}{dt}\right]+C_s\left[\frac{dv_i(t)}{dt}+\frac{dv_r(t)}{dt}\right], \end{aligned} \tag{2.3.1.7}$$

and the current leaving the PC gap,

$$\begin{aligned} \frac{v_t(t)}{Z_0} &= G_g(t)[v_i(t)+v_r(t)-v_t(t)]-G_s(t)[v_t(t)] \\ &\quad +C_g\left[\frac{dv_i(t)}{dt}+\frac{dv_r(t)}{dt}-\frac{dv_t(t)}{dt}\right]-C_s\left[\frac{dv_t(t)}{dt}\right], \end{aligned} \tag{2.3.1.8}$$

the differential equations

$$\begin{aligned}\frac{dv_r(t)}{dt} = {} & \left[\frac{-G_g(t)}{C_g}\right]v_i(t) + \left[\frac{-G_g(t)}{C_g}\right]v_r(t) + \left[\frac{G_g(t)}{C_g} + \frac{G_s(t)}{C_s} + \frac{1}{Z_0 C_g}\right]v_t(t) \\ & - \frac{dv_i(t)}{dt} + \left[1 + \frac{C_s}{C_g}\right]\frac{dv_t(t)}{dt},\end{aligned} \tag{2.3.1.9}$$

and

$$\begin{aligned}\frac{dv_t(t)}{dt} = {} & \left[\frac{G_s(t)}{C_g} + \frac{G_g(t)}{C_g} - \frac{1}{Z_0 C_g}\right]v_i(t) + \left[\frac{G_s(t)}{C_g} + \frac{G_g(t)}{C_g} + \frac{1}{Z_0 C_g}\right]v_r(t) + \\ & + \left[\frac{-G_g(t)}{C_g}\right]v_t(t) + \left[1 + \frac{C_s}{C_g}\right]\frac{dv_i(t)}{dt} + \left[1 + \frac{C_s}{C_g}\right]\frac{dv_r(t)}{dt},\end{aligned} \tag{2.3.1.10}$$

are arrived at. Here, Z_0 refers to the impedance of the transmission line. Using equations 2.3.1.9 and 2.3.1.10, along with the fact that the incident waveform remains constant at one-half the bias voltage ($v_i(t) = V_b/2$), the simultaneous differential equations for the incident, reflected, and transmitted waveforms are found to be

$$\frac{dv_i(t)}{dt} = 0, \tag{2.3.1.11}$$

$$\begin{aligned}\frac{dv_r(t)}{dt} = {} & \left[\frac{-C_s Z_0 G_s(t) - C_s Z_0 G_g(t) - C_g Z_0 G_s(t) + C_s + C_g}{2C_s C_g Z_0 + C_s^2 Z_0}\right]v_i(t) \\ & + \left[\frac{-C_s Z_0 G_s(t) - C_g Z_0 G_s(t) - C_s Z_0 G_g(t) - C_s - C_g}{2C_s C_g Z_0 + C_s^2 Z_0}\right]v_r(t) \\ & + \left[\frac{C_s Z_0 G_g(t) - C_g Z_0 G_s(t) - C_g}{2C_s C_g Z_0 + C_s^2 Z_0}\right]v_t(t),\end{aligned} \tag{2.3.1.12}$$

and

$$\begin{aligned}\frac{dv_t(t)}{dt} &= \left[\frac{-C_g Z_0 G_s(t) + C_s Z_0 G_g(t) + C_g}{2C_s C_g Z_0 + C_s^2 Z_0}\right] v_i(t) \\ &+ \left[\frac{-C_g Z_0 G_s(t) + C_s Z_0 G_g(t) - C_g}{2C_s C_g Z_0 + C_s^2 Z_0}\right] v_r(t) \\ &+ \left[\frac{-C_g Z_0 G_s(t) - C_s Z_0 G_g(t) - C_s Z_0 G_s(t) - C_g - C_s}{2C_s C_g Z_0 + C_s^2 Z_0}\right] v_t(t),\end{aligned} \tag{2.3.1.13}$$

respectively. Simultaneously solving equations 2.3.1.11-2.3.1.13 for a particular bias voltage will give a description of the performance of this ultrathin Si PC switch. Care must be taken, however, to understand the limitations of the lumped-element model presented. By using discrete circuit elements to describe the operation of this switch, it is assumed that the transit times within the device are insignificant relative to the smallest timescale of interest. If this is not true, a distributed element model would be required. On the other hand, details of the photo-generated carrier dynamics, such as ohmic contact effects and relaxation kinetics, are assumed to be encompassed within the circuit elements described.

The first step in solving for the transmitted voltage waveform, $v_t(t)$, at the output of the PC switch, is to obtain the time-varying responses for the gap and shunt conductance elements. This is accomplished by numerically integrating the electron density function, $n(z,t)$, in equations 2.3.1.4, 2.3.1.5, and 2.3.1.6. The results for a pump spot diameter of 20 μm and pump beam average powers of 30, 50, and 70 mW (corresponding to pump energy fluences of 119, 200, and 279 μJ/cm^2) are shown in figures 2.3.1.2(a), 2.3.1.2(b), and 2.3.1.2(c), respectively. The response of the gap conductance element, $G_g(t)$, to each of the three photo-excitation levels shows a relatively slow transition (over a period of 110 fs) from the initial dark conductance level to the

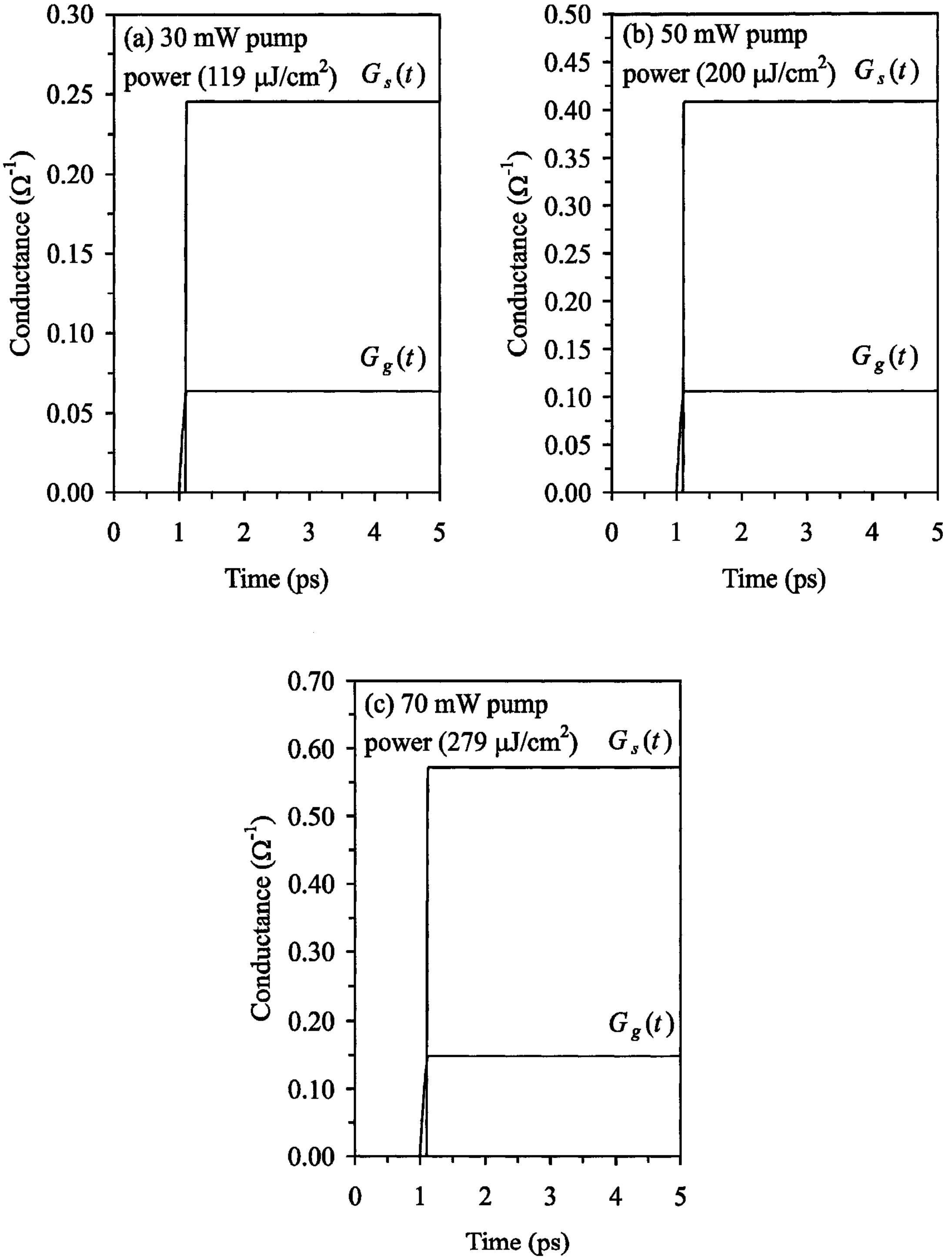

Figure 2.3.1.2 Theoretical gap and shunt conductance terms for the ultrathin Si PC switch, given average pump powers of (a) 30, (b) 50, and (c) 70 mW (corresponding to pump energy densities of 119, 200, and 279 μJ/cm², respectively).

illuminated level, while the response of the shunt conductance elements, $G_s(t)$, rises from the background level to the illuminated level in a step-like manner at a time of 110 fs. The main reason for this difference is the 110 fs time-delay of the optical pulse as it propagates through the 10 μm thick Si layer. Indeed, while the gap conductance element is able to rise during the initial stages of excitation, the shunt conductance elements must remain at a low level until an appreciable amount of the illuminating radiation reaches the ground plane.

Having successfully determined the time-varying expressions for the gap and shunt conductance terms, the transmitted voltage waveform is found by numerically solving equations 2.3.1.11, 2.3.1.12, and 2.3.1.13. The details, describing the fifth-order Runge-Kutta numerical method employed, are presented in Appendix D. Given a bias voltage of V_b = 10 V, and estimates of the circuit model parameters of C_g = 10 fF, C_s = 200 fF, and Z_0 = 120 Ω, the transmitted voltage waveform is calculated for average pump powers of 30, 50, and 70 mW (corresponding to pump energy densities of 119, 200, and 279 μJ/cm^2, respectively). The results are shown in figure 2.3.1.3. It is evident from the unipolar shape of the voltage waveforms, that the ultrathin Si PC device responds in a manner that is very different from the step-like response of conventional Si PC switches (where carrier recombination is needed to terminate the voltage waveform). By employing this self-switching technique, the speed of the device is brought from a nanosecond regime to a subpicosecond regime. It is also apparent from figure 2.3.1.3, that the speed of the self-switching PC response is a strong function of the incident pump intensity. The 30, 50, and 70 mW pump powers used in the simulation produce voltage pulses with rise-times of 0.38, 0.23, and 0.17 ps, respectively, and FWHM values of 1.8,

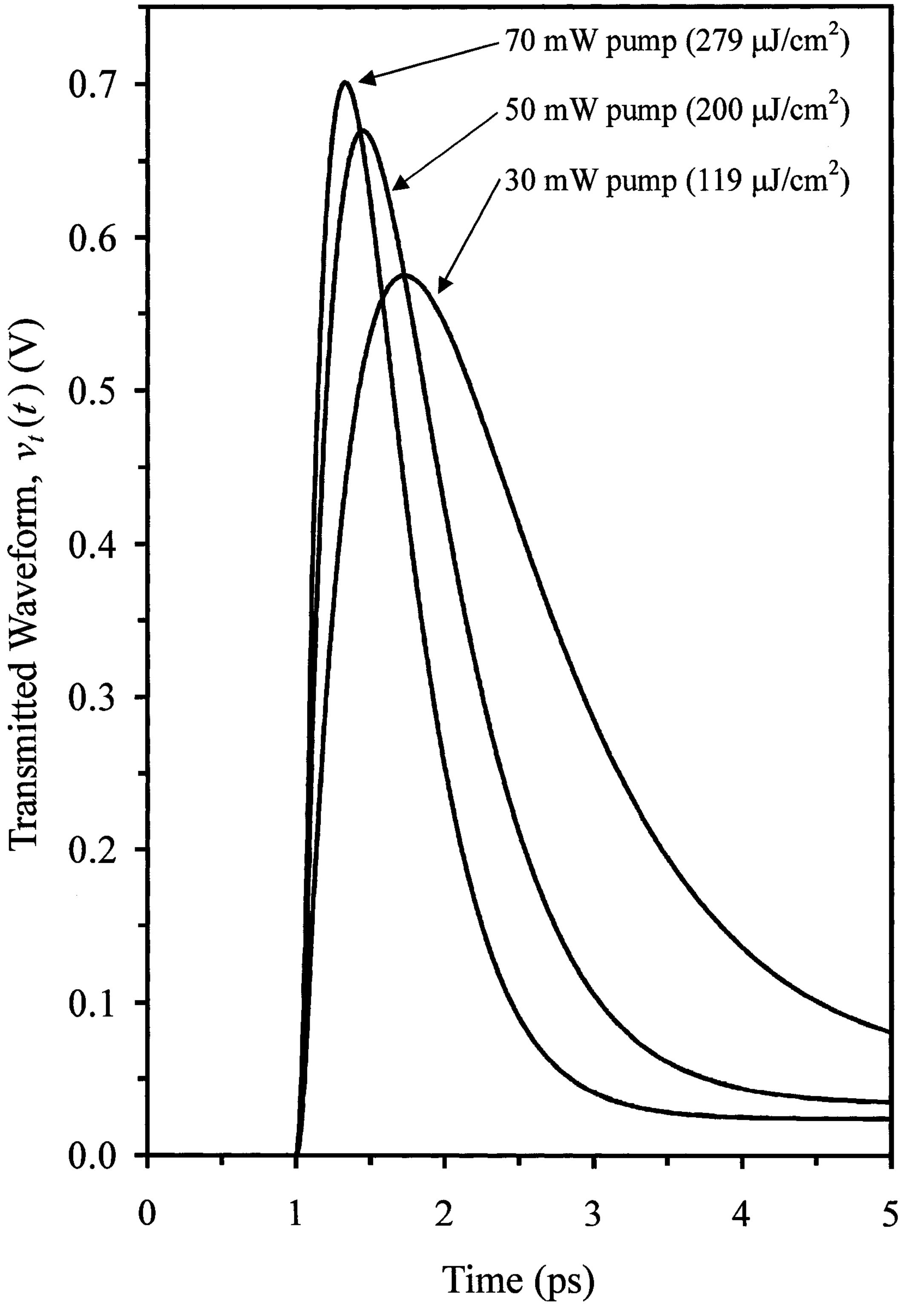

Figure 2.3.1.3 Transmitted voltage waveforms, $v_t(t)$, predicted by the ultrathin Si PC switch lumped-element model for average pump powers of 30, 50, and 70 mW (corresponding to pump energy fluences of 119, 200, and 279 μJ/cm², respectively).

1.0, and 0.74 ps, respectively, suggesting that the operation of the device can be improved by using increasingly large excitation intensities. The reason for this relationship between the level of photo-excitation and the duration of the voltage pulse can be understood in terms of the RC time constants of the PC gap. By pumping the semiconductor with increasingly large intensities, the gap and shunt conductance terms are driven to exceedingly large values. The resulting decrease in the gap and shunt resistance values reduces the RC time constant constraints of the device, allowing the initially-charged capacitive elements to be rapidly discharged. In the high-excitation limiting case–where the RC time constants are essentially eliminated–the voltage waveform is expected to follow the ultrafast PC response of the time-varying conductance terms, producing a 110 fs voltage pulse whose duration is limited solely by the optical propagation time through the Si substrate.

2.3.2 Experimental Framework

To test the operation of the ultrathin Si PC switch, the experimental setup shown in figure 2.3.2.1(a) is designed and built [15], [16]. The PC device is prepared from a high-resistivity float-zone-Si wafer (3.5 kΩ·cm) that is mechanically ground to a thickness of 12 μm and then optically polished to a final thickness of 10 μm [42]. A 50/150 nm Ti/Au metallization is performed on both sides of the 10 μm thick ultrathin wafer, and the underside of the substrate is electrically contacted to a Cu base with a thin layer of In metal. In this way, the Cu base acts as a ground plane and a mechanical support structure. Photolithographic processing is then used to pattern a 1 cm long, 20 μm wide microstrip transmission line on the surface, with a 20 × 20 μm^2 PC gap.

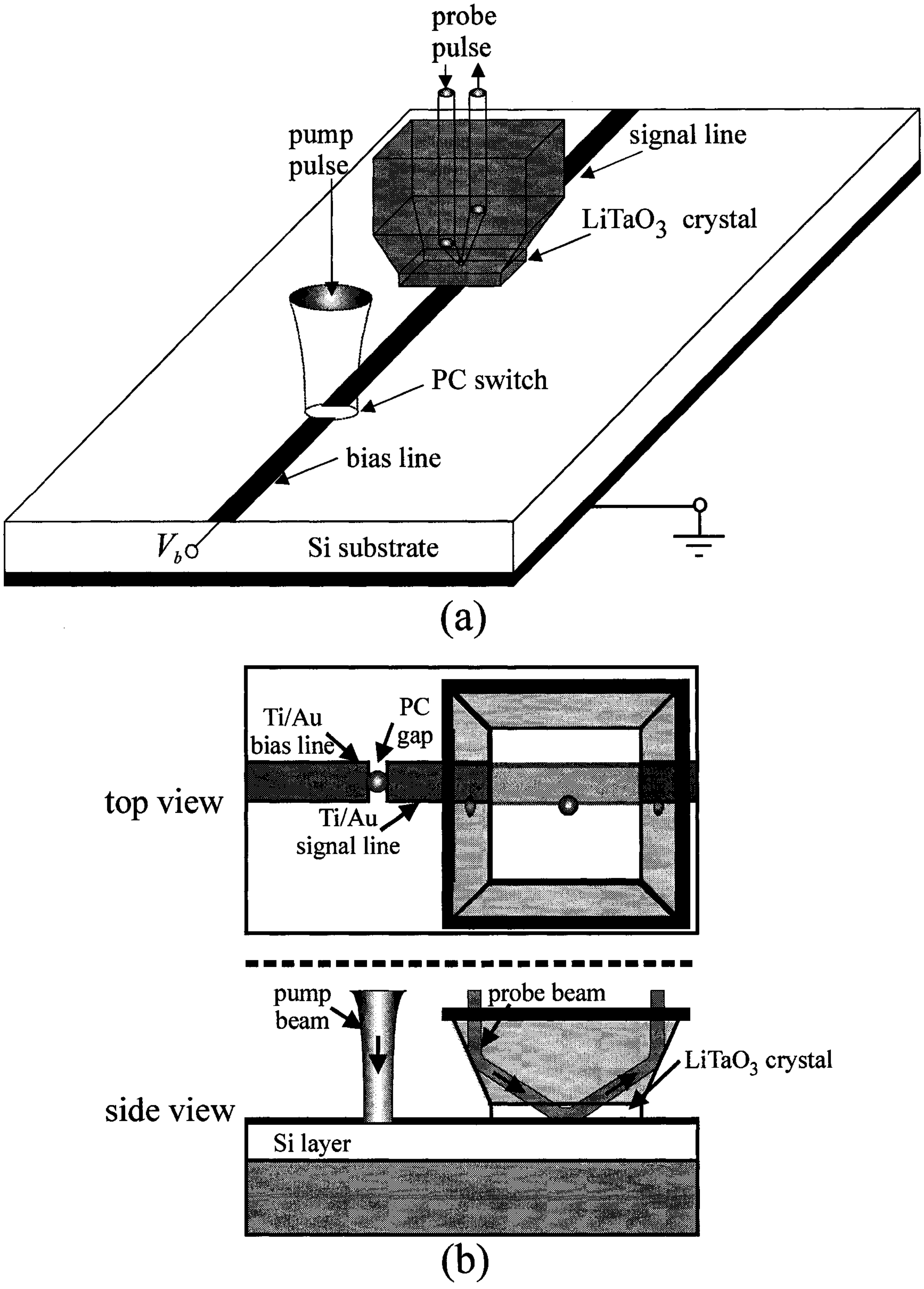

Figure 2.3.2.1 A (a) diagram of the generation and detection system for the ultrathin Si PC switch, and the (b) experimental schematic for PC excitation (by the pump) and EO sampling (by the probe).

Photo-excitation and biasing of the ultrathin Si PC switch are accomplished by the Ti:sapphire laser and bias voltage mixing unit described in section 2.2. Sampling of the generated electrical pulse is carried out by the total-internal-reflection $LiTaO_3$ EO probe shown in the figure. The EO crystal mount is positioned (approximately 10 μm) above the microstrip transmission line–such that the probe beam samples the fringing field on the edge of the transmission line. A plan-view and profile-view of the resulting generation and detection system are shown in figure 2.3.2.1(b).

Typical EO measurement results for sampling on the transmission line, given an average pump power of 70 mW and a bias voltage of $V_b = 20\ V_{p\text{-}p}$, are shown in figure 2.3.2.2. The pump beam is focused to a spot size of 20 μm (yielding a pump energy fluence of 279 $\mu J/cm^2$), and EO sampling is carried out on the transmission line at a distance of 400 μm from the PC gap. The unipolar shape of the waveform does, indeed, show a voltage pulse rather than a voltage step, suggesting that the $8 \times 10^{17}\ cm^{-3}$ photo-injected carrier density employed is sufficient to initiate current conduction through the entire PC gap volume. The asymmetric shape of the observed voltage pulse is a result of the different RC times of the two competing PC processes. The 0.6 ps rise-time of the voltage pulse seen in the figure is dominated by the current conduction process across the PC gap, whereas the 1.4 ps exponential-like fall-time is due largely to the conduction through the substrate. The combination of these competing electrical processes produces a voltage pulse whose FWHM is 1.2 ps. This ultrashort pulse duration is significantly shorter than the 20 ns charge carrier lifetime inherent to Si PC devices [3] and is, to our knowledge, is the shortest conduction-current-driven electrical pulse generated using intrinsic Si.

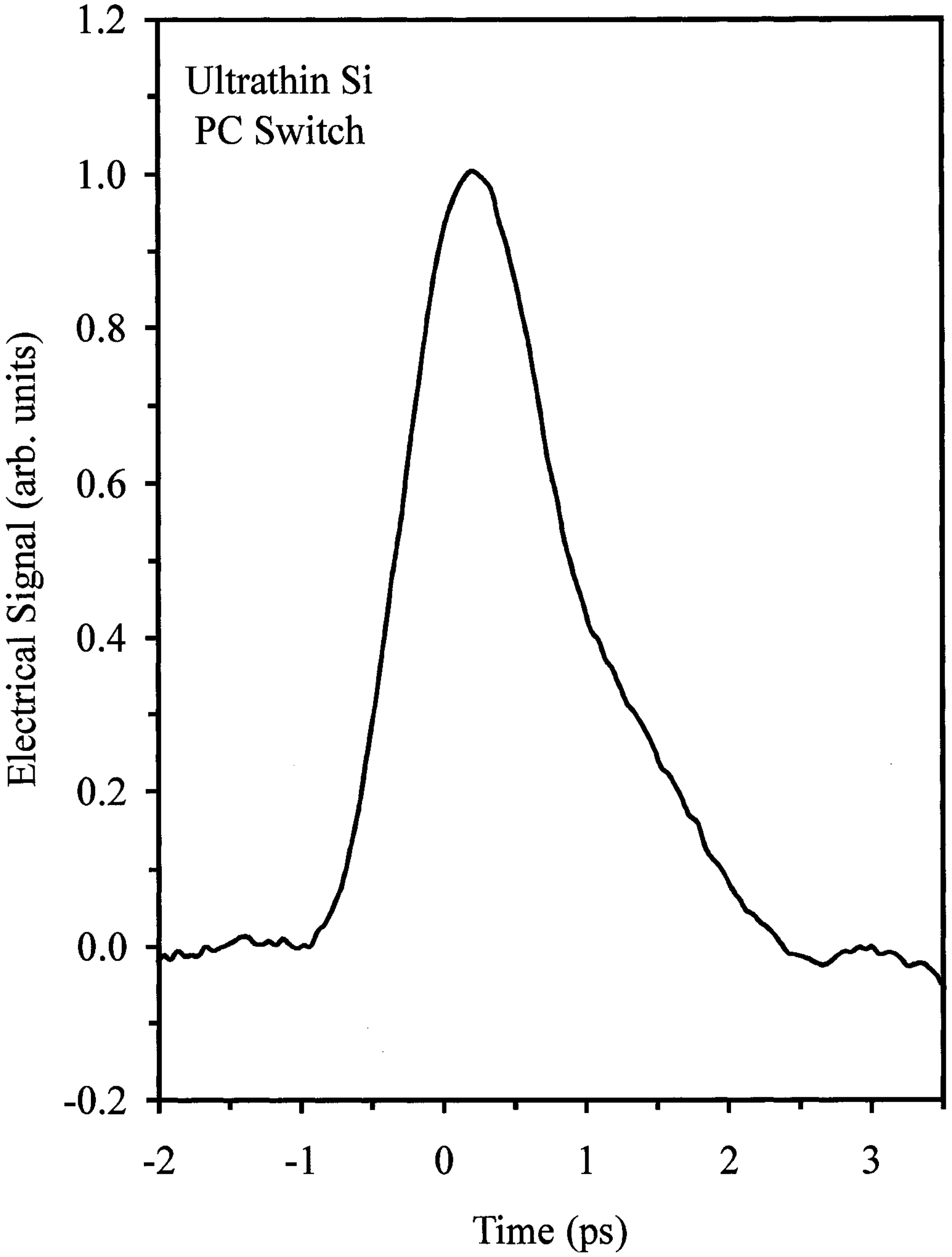

Figure 2.3.2.2 A typical ultrashort electrical pulse produced by the ultrathin Si PC switch. The THz electrical pulse is generated using a pump power of 70 mW and a 20 μm spot size (corresponding to a pump energy fluence of 279 μJ/cm^2).

The measured 1.2 ps electrical pulse can be compared to the theoretical results calculated in section 2.3.1. In the model, it was found that a 0.74 ps electrical pulse could be formed with photo-excitation by a 70 mW pump beam. The slight discrepancy between the measured and calculated pulse durations can be explained through a variety of mechanisms. Firstly, the values for the capacitance elements are only order-of-magnitude estimates for the capacitive terms [44], and it is the relative difference between these values that plays a large role in determining the final shape of the pulse. Secondly, EO sampling is carried out on the transmission line at a distance of 400 μm from the PC gap. The THz waveform will, therefore, undergo pulse broadening from material and transmission line dispersive effects [45], [46], [47]. Thirdly, the $LiTaO_3$ EO probe has a finite temporal resolution defined by the optical pulse dispersion in the fused silica mount and the velocity mismatch between the probe beam in the $LiTaO_3$ crystal and the voltage pulse on the transmission line. While it is difficult to estimate the effects of optical pulse broadening in the fused silica mount, it is possible to estimate the temporal resolution due to the velocity mismatch between the voltage pulse and the probe beam. Using microstrip transmission line analysis software [48], the velocity of the voltage pulse is estimated to 1×10^8 m/s. Likewise, the velocity of the optical probe pulse in the plane of the semiconductor surface is calculated to be 6.88×10^7 m/s, given a refractive index of 2.18 and a probe spot angle of incidence of 30°. Taking the 20 μm probe spot size in the experiment to be the interaction length for the EO sampling process, the temporal broadening is calculated to be approximately 100 fs. Finally, it is likely that the estimates for the time-varying conductance terms in the model are over-estimated. The values that are calculated are arrived at by assuming a parallel plate configuration for the gap and shunt values. In reality, the conduction processes occur through the metal-semiconductor interfaces at the input and output terminals of the PC gap [49]. This constriction will serve to lower the overall current flow for the gap and shunt terms and raise the resistance associated with these elements. The resulting increase in the RC time constants associated with the device will, in turn, broaden the electrical pulse duration.

2.4 Coplanar Photoconductive Self-Switching

2.4.1 Theoretical Framework

While the ultrathin Si PC switch is successful in producing ultrashort electrical pulses, its application to ultrafast PC switching in general is somewhat limited as the self-switching process is invariably linked to the large penetration depth of the Si substrate (10 μm) [50]. The penetrations depths associated with semiconductors such as GaAs (0.74 μm) [50] and InAs (0.14 μm) [50], in comparison, are too small to allow for the implementation of a free-standing and practical device design. Alternative device architectures are, therefore, necessary to realize a successful PC self-switching device with these semiconductors.

In this section, a novel PC self-switching design is presented [17]. The device employs a coplanar transmission line layout on a GaAs substrate, where–unlike the ultrathin Si PC switch–the turn-on and turn-off processes are decoupled from the transit time-delay in the semiconductor substrate. The optical delay between the pulse formation and termination processes is provided, instead, by an SiO_2 optical delay layer located on top of the GaAs surface. This coplanar PC self-switching device is shown in figures 2.4.1.1(a) and 2.4.1.1(b). Here, the incident pump pulse illuminates the PC gap between the bias line and the signal line (the bias-to-signal gap) and the PC gap between the signal line and the ground line (the signal-to-ground gap). The finite optical delay-time between these two photo-excitation processes generates an ultrashort electrical pulse on the coplanar transmission line, whose duration is determined by the SiO_2 optical delay-time and the RC time constants constraints of the PC gaps, rather than the charge carrier lifetime in the GaAs substrate.

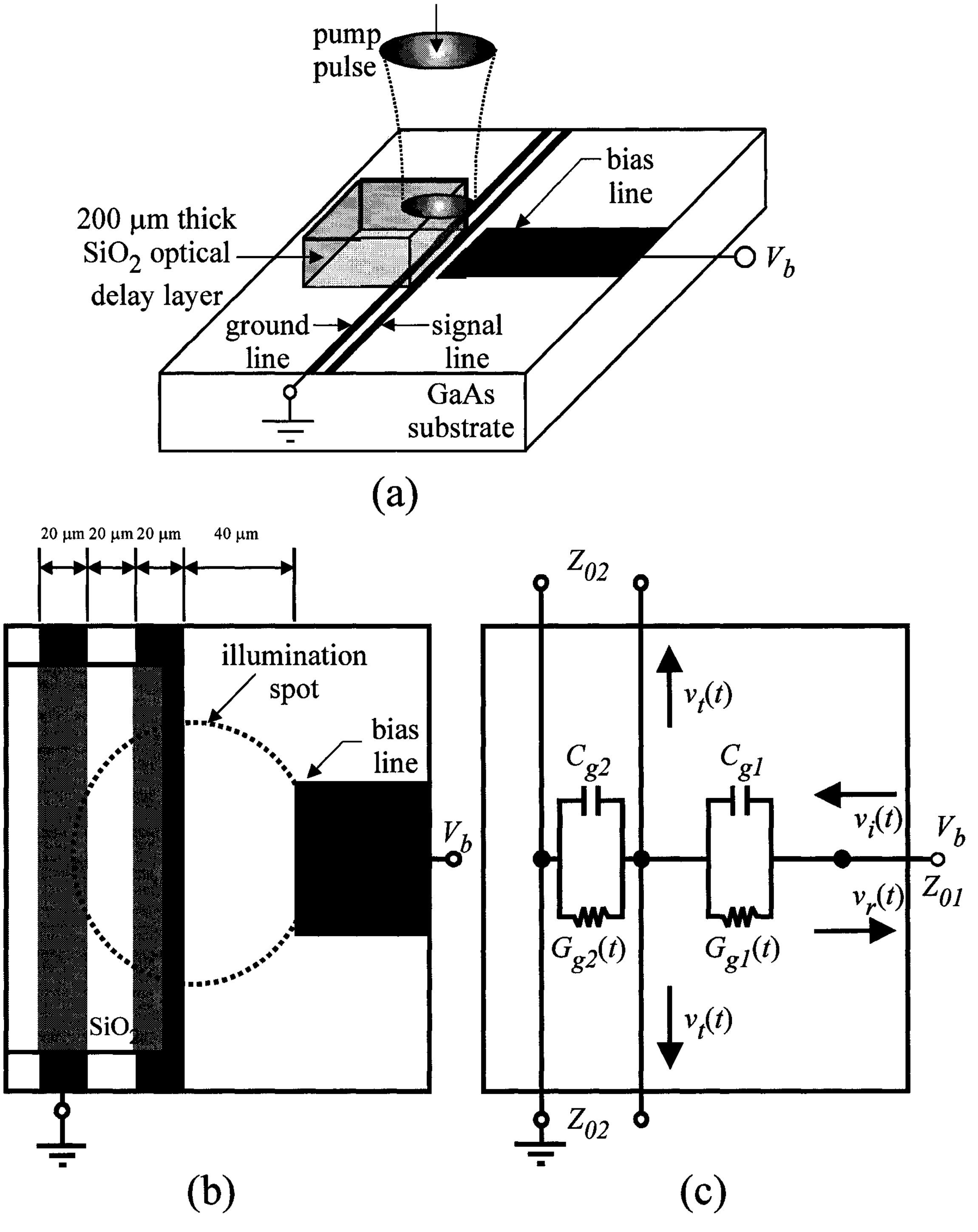

Figure 2.4.1.1 The (a) layout, (b) overhead schematic, and (c) lumped-element model for the coplanar PC switch. In the model, C_{g1} and $G_{g1}(t)$ describe the capacitance and conductance of the bias-to-signal gap, and C_{g2} and $G_{g2}(t)$ describe the capacitance and conductance of the signal-to-ground gap.

To allow for efficient generation of the ultrashort electrical pulses, it is important to fully understand the relationship that exists between the device design and the resulting electrical pulse duration. To do this, the lumped-element model shown in figure 2.4.1.1(c) is employed. Much like the ultrathin Si PC switch model, the conduction and displacement currents within the PC gaps are represented by parallel connections of conductors and capacitors. The gap conductance and gap capacitance associated with the turn-on process of the bias-to-signal gap are modeled by the elements $G_{g1}(t)$ and C_{g1}, respectively, while the gap conductance and gap capacitance associated with the turn-off process of the signal-to-ground gap are modeled by the elements $G_{g2}(t)$ and C_{g2}, respectively. Optical activation of the switch drives the two conductance terms from their initial dark conductance values to their fully-illuminated values (though the turn-off process is delayed for a period of 333 fs by the 200 μm thick SiO_2 optical delay layer). Using the photo-injected charge carrier density function in equation 2.3.1.3 and the expression for the conductivity in equation 2.3.1.4, the time-varying gap conductance functions are calculated through the relations,

$$G_{g1}(t) = \frac{w}{l_1}\int_0^{\delta}\sigma(z,t)dz\,, \tag{2.4.1.1}$$

and

$$G_{g2}(t) = \frac{w}{l_2}\int_0^{\delta}\sigma(z,t)dz\,. \tag{2.4.1.2}$$

Here, $w = 100$ μm is the width of the PC region (equal to the pump spot diameter), $l_1 = 40$ μm is the length of the bias-to-signal gap, $l_2 = 20$ μm is the length of the signal-to-ground gap, and $\delta = 0.74$ μm is the penetration depth of the GaAs substrate [50]. The voltage on the transmission line is calculated next by summing the current through each node [35],

$$\begin{aligned}\frac{v_i(t)-v_r(t)}{Z_{01}} &= C_{g1}\frac{d}{dt}\left[v_i(t)+v_r(t)-v_t(t)\right]+G_{g1}(t)\left[v_i(t)+v_r(t)-v_t(t)\right]\\ &= C_{g2}\frac{dv_t(t)}{dt}+\left[G_{g2}(t)+\frac{2}{Z_{02}}\right]v_t(t),\end{aligned} \tag{2.4.1.3}$$

and applying the boundary conditions

$$v_i(t)=\frac{V_b}{2} \tag{2.4.1.4}$$

and

$$\frac{dv_i(t)}{dt}=0 \tag{2.4.1.5}$$

on the incident waveform. Here, Z_{01} is the impedance of the bias transmission line, and Z_{02} is the impedance of the coplanar signal transmission line. Equations 2.4.1.3-2.4.1.5 together produce the second-order differential equation

$$\begin{aligned}&C_{g1}C_{g2}Z_{01}\frac{d^2v_t(t)}{dt^2}\\ &+\left[C_{g1}+C_{g2}+\frac{2C_{g1}Z_{01}}{Z_{02}}+C_{g2}Z_{01}G_{g1}(t)+C_{g1}Z_{01}G_{g2}(t)\right]\frac{dv_t(t)}{dt}\\ &+\left[\frac{2}{Z_{02}}+G_{g1}(t)+G_{g2}(t)+\frac{2Z_{01}}{Z_{02}}G_{g1}(t)+Z_{01}G_{g1}(t)G_{g2}(t)\right]v_t(t)\\ &+\left[C_{g1}Z_{01}\frac{dG_{g2}(t)}{dt}\right]v_t(t)-G_{g1}(t)V_b=0,\end{aligned} \tag{2.4.1.6}$$

for the transmitted voltage waveform.

Calculated time-varying results for the conductance terms $G_{g1}(t)$ and $G_{g2}(t)$ are shown in figure 2.4.1.2(a). Details on the numerical solution of this equation are shown in Appendix E. Here, the incident pump beam has an average power of P_{pump} = 135 mW, a pulse duration of τ_p = 100 fs, and a spot size of 100 μm (corresponding to a pump energy

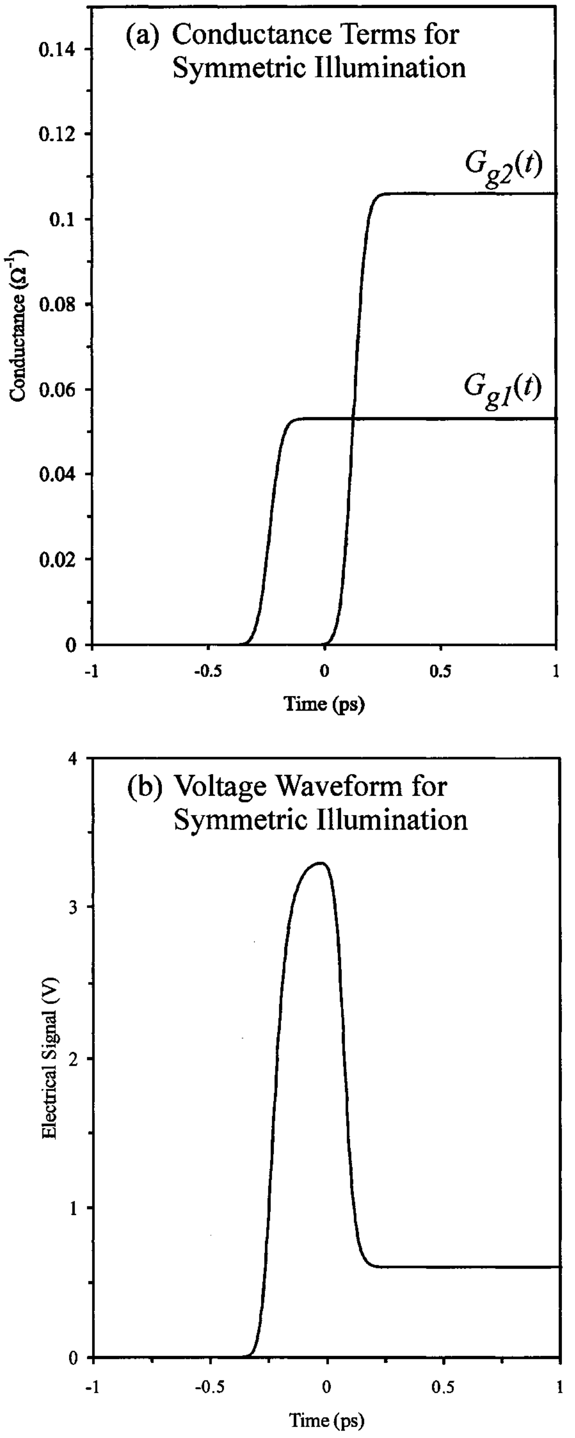

Figure 2.4.1.2 The (a) theoretical conductance terms, $G_{g1}(t)$ and $G_{g2}(t)$, and the (b) resulting voltage waveform, $v_t(t)$, for symmetric illumination of the coplanar PC switch by a 135 mW pump beam. A bias voltage of $V_b = 22.5$ V is applied to the device.

fluence of 21.5 μJ/cm^2). The coplanar PC device is modeled by a bias-to-signal capacitance of C_{g1} = 0.5 fF, a signal-to-ground capacitance of C_{g2} = 1 fF, a bias line impedance of Z_{01} = 270 Ω [48], and a coplanar transmission line impedance of Z_{02} = 100 Ω [51]. It is readily apparent from figure 2.4.1.2(a) that the conductance terms rise from their dark conductance values on an extremely short timescale, though the gap conductance term, $G_{g2}(t)$, is delayed by the propagation of the pump pulse through the 200 μm thick SiO_2 optical delay layer. The factor of two difference in the steady-state values of the conductance elements can be attributed to the fact that the length of the bias-to-signal gap is twice that of the signal-to-ground gap. The use of a uniform illumination spot across both of the gaps (and the resulting uniform conductivity within the gaps), in this case, keeps the conductance across the bias-to-signal gap at half the value of the signal-to-ground gap for all levels of photo-carrier injection.

The transmitted voltage waveform generated by the coplanar PC switch for symmetric illumination of the device above is shown in figure 2.4.1.2(b) for a bias voltage of V_b = 22.5 V. A voltage pulse is readily apparent in the figure. The processes of shorting the signal-to-ground gap and reflecting the bias voltage on the input bias line, together, produce a unipolar electrical waveform on the coplanar transmission line–the duration of which is independent of the 250 ps lifetime in GaAs. It is also apparent from the figure that a steady-state voltage background is formed from the excitation of the PC switch. This steady-state value is due to the fact that the reflected waveform does not fully compensate for the incident waveform (which remains at half the bias voltage).

To decrease the steady-state voltage background, the photo-excitation conditions of the device can be tuned. Unlike the ultrathin Si PC switch, where the gap and shunt conductance levels are indelibly linked, the coplanar PC switch geometry offers the possibility of independently controlling the level of photo-excitation in the bias-to-signal gap and the signal-to-ground gap. By directing more of the incident pump beam onto the signal-to-ground gap, for example, the steady-state potential on the signal line can be driven down further towards ground and the background level can be reduced. To prove this point, figures 2.4.1.3(a) and 2.4.1.3(b) show the gap conductance terms and the transmitted voltage waveform for the case where the incident intensity on the bias-to-signal gap is ten times greater than the intensity on the signal-to-ground gap. The steady-state voltage background, in this case, shows a marked decrease in amplitude. Indeed, by carefully controlling the photo-excitation conditions, ultrashort electrical pulses can be formed by the coplanar PC switch with little or no background voltage.

2.4.2 Experimental Framework

To test the operation of the coplanar PC switch, the experimental setup shown in figure 2.4.2.1 is employed [17]. The device is fabricated from the metallization and photolithographic patterning of a 50/150 nm Ti/Au film on a 600 μm thick semi-insulating GaAs substrate (10^7 Ω·cm). The coplanar PC switch is arranged in an interdigitated metal-semiconductor-metal layout with the bias voltage (V_b = 45 $V_{p\text{-}p}$) applied to the bias line on the right and grounding applied to the ground line on the left. Two 20 μm wide metal lines with a separation of 20 μm form the coplanar transmission line responsible for propagating the photo-generated THz electrical waveform. A 200 μm thick SiO_2 optical delay layer is positioned above the coplanar transmission line to cover the semiconductor region between the signal line and the ground line.

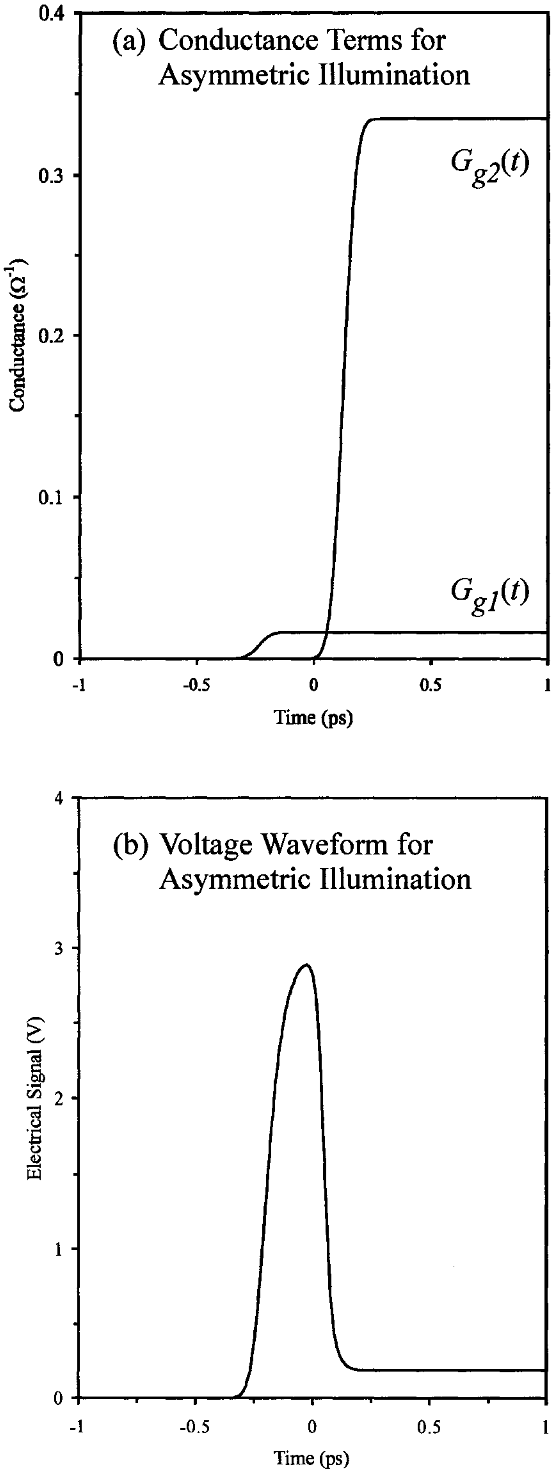

Figure 2.4.1.3 The (a) theoretical conductance terms, $G_{g1}(t)$ and $G_{g2}(t)$, and the (b) resulting voltage waveform, $v_t(t)$, for asymmetric illumination of the coplanar PC switch by a 135 mW pump beam. A bias voltage of $V_b = 22.5$ V is applied to the device.

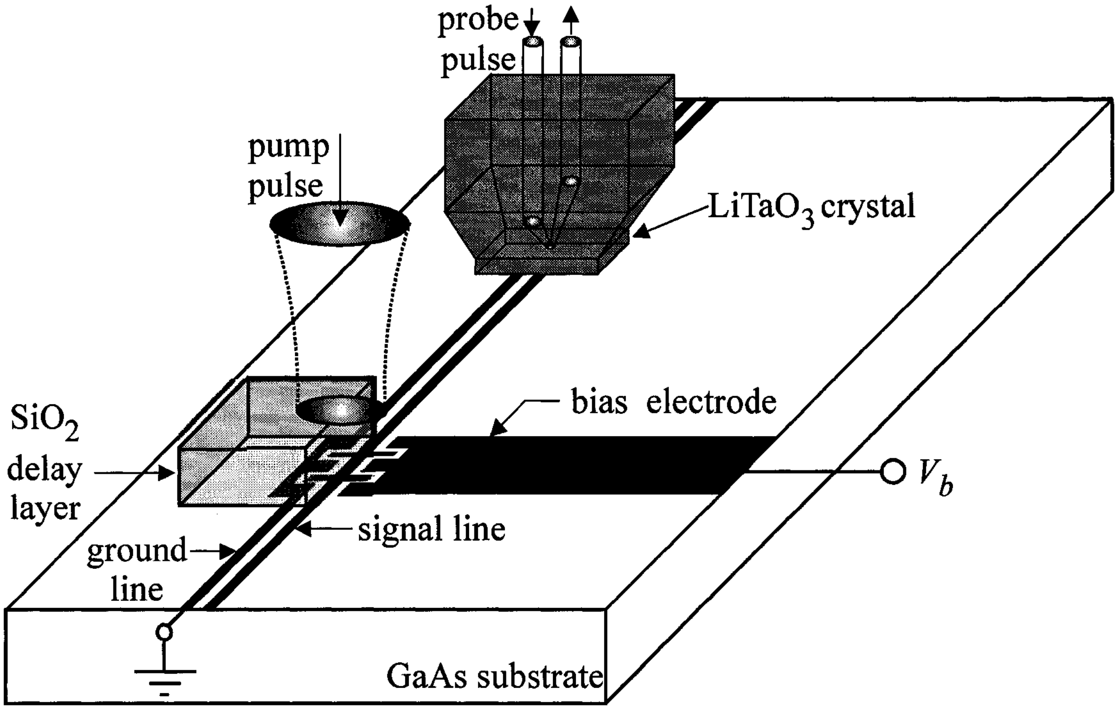

Figure 2.4.2.1 Layout for the generation and detection of THz electrical transients using the coplanar PC switch. The pump pulse excites both the bias-to-signal gap and the signal-to-ground gap. The probe beams samples the electric field on the coplanar transmission line.

In order to test the device, a 10 fs, 800 nm mode-locked Ti:sapphire laser is employed. The laser produces the 135 mW pump beam and the 20 mW probe beam necessary for the time-resolved generation and detection processes described in section 2.2. The alignment conditions of the pump beam are optimized by observing the coplanar PC switch through an inclined stereoscope mounted above the system and by monitoring the DC resistance across the bias-to-signal gap and the signal-to-ground gap. The probe beam inside the $LiTaO_3$ EO probe samples the fringing electric field above the coplanar transmission line at a distance of 500 μm from the PC switch.

To establish a baseline for the photo-generated electrical pulse durations, the coplanar PC switch is operated initially under the partial illumination conditions shown in figure 2.4.2.2(a). Here, the interdigitated metal-semiconductor-metal PC switch is biased on the signal line, and the pump illumination spot is aligned such that charge carrier generation occurs *only* within the signal-to-ground gap. With this partial illumination setup, the PC gap discharging process necessary for terminating the voltage pulse is not present. A typical electrical waveform generated by this arrangement is shown in figure 2.4.2.2(b). It is readily apparent from this figure that the delayed turn-off process for the electrical transient is indeed absent, and the response is step-like in nature. The resulting EO signal demonstrates an electrical rise-time of 2.5 ps–limited by the discharge time of the PC switch–and a fall-time of approximately 250 ps–limited by the charge carrier lifetime of the GaAs substrate (not shown).

For the next step, the system is tested under conditions of full illumination. The pump beam is aligned such that the spot covers both the bias-to-signal gap and the signal-to-ground gap, and the bias voltage is applied to the bias line. The experimental layout

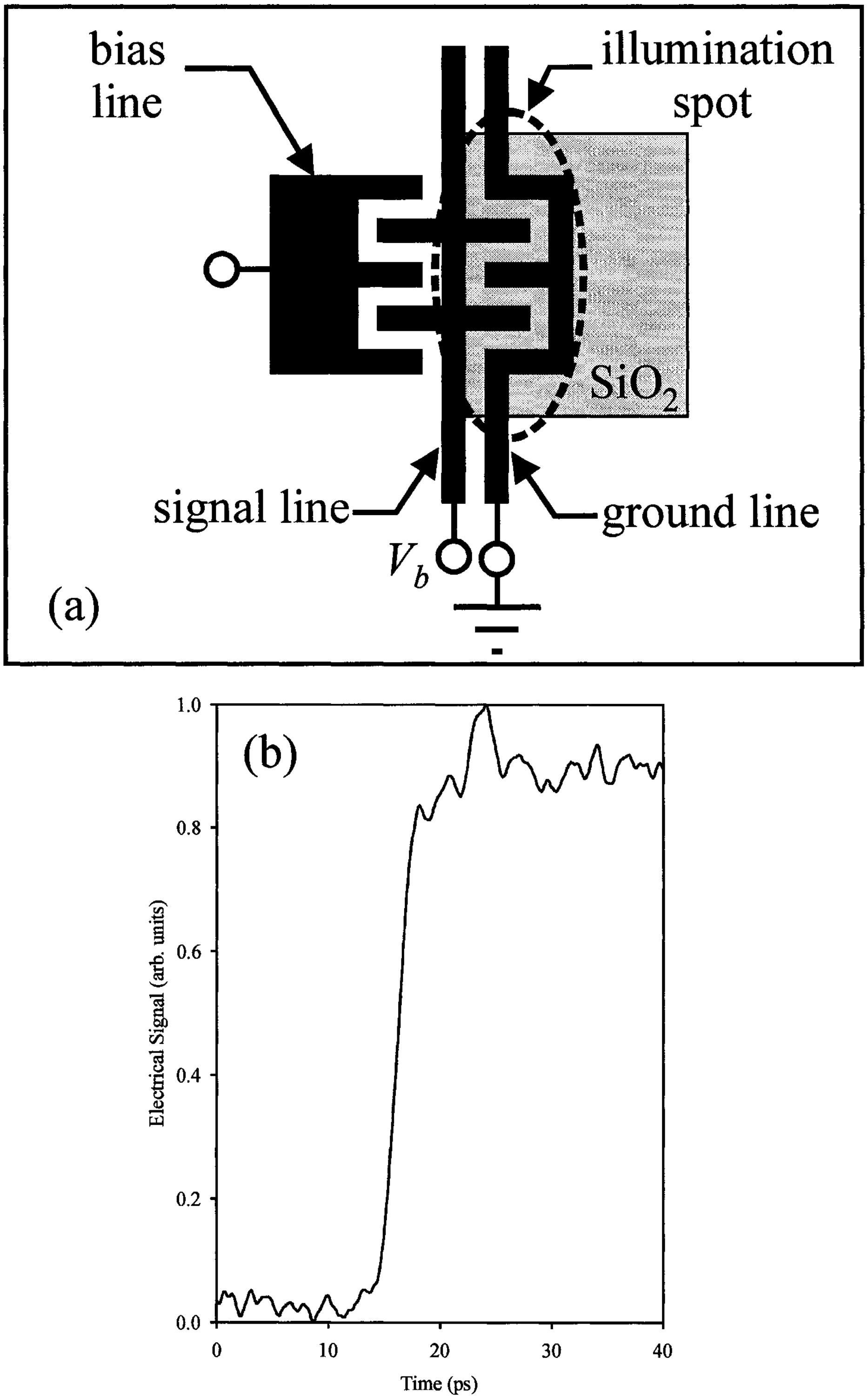

Figure 2.4.2.2 The (a) schematic for incomplete illumination of the interdigitated coplanar PC switch and a (b) typical generated waveform. Biasing is applied to the signal line and illumination covers only the signal-to-ground gap.

and a typical electrical pulse produced by the device are shown in figures 2.4.2.3(a) and 2.4.2.3(b), respectively. It is readily apparent from the time-domain waveform that the device is able to produce electrical pulses with rise-times (2.5 ps) and durations (7 ps) on a picosecond timescale. These values demonstrate a reduction in the pulse width of figure 2.4.2.2(b) by a factor of 36. It should be noted, however, that the tail of the pulse shown in figure 2.4.2.3(b) reaches a steady-state value of approximately 20% of the peak amplitude. As described in section 2.4.1, this background level is due to an incomplete reflection of the incident waveform on the bias line and a low conductance level in the signal-to-ground gap.

To further improve the PC switching response, the steady-state background must be eliminated, and the response time of the device must be decreased. To accomplish these goals, the conductance of the bias-to-signal gap is decreased below that of the signal-to-ground gap by both increasing the length of the bias-to-signal gap and preferentially directing the beam toward the signal-to-ground gap. In addition, the interdigitated metal-semiconductor-metal layout is removed to decrease the electrical response times associated with the charging and discharging processes. With these modifications, the experimental setup (shown in figure 2.4.2.4(a)) now resembles the PC geometry modeled in section 2.4.1, with a bias-to-signal gap length of l_1 = 40 μm and a signal-to-ground gap length of l_2 = 20 μm. Typical EO sampling results for a pump power of 135 mW and a 100 μm spot size are shown in figure 2.4.2.4(b). It is readily apparent from the time-domain waveform that the steady-state saturation tail is essentially eliminated. Furthermore, the response time of the device is greatly reduced, and the duration of the electrical pulse is decreased to 2 ps. This ultrashort pulse duration

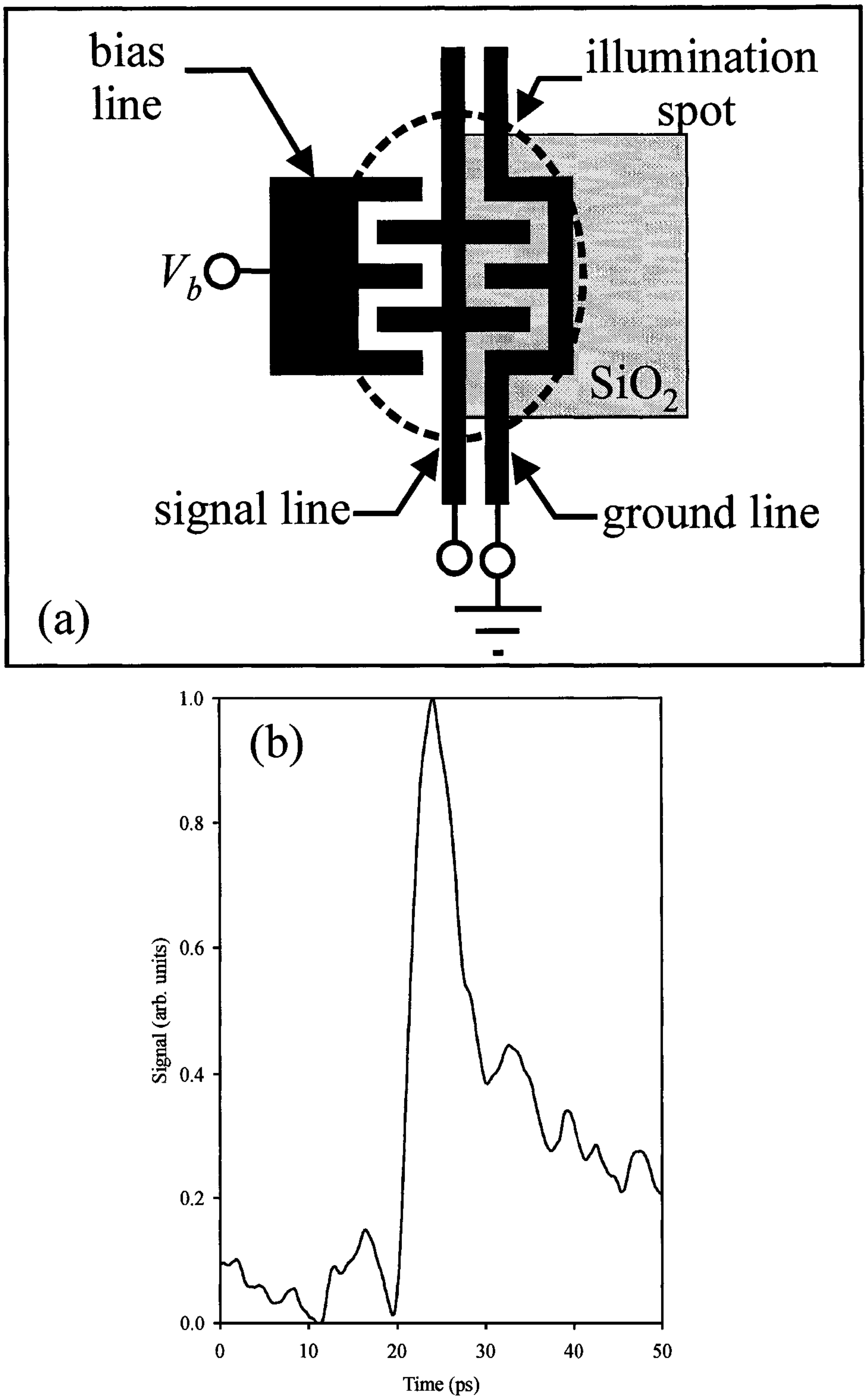

Figure 2.4.2.3 The (a) schematic for complete illumination of the interdigitated coplanar PC switch and a (b) typical generated waveform. Biasing is applied to the bias line and illumination covers both the bias-to-signal gap and the signal-to-ground gap.

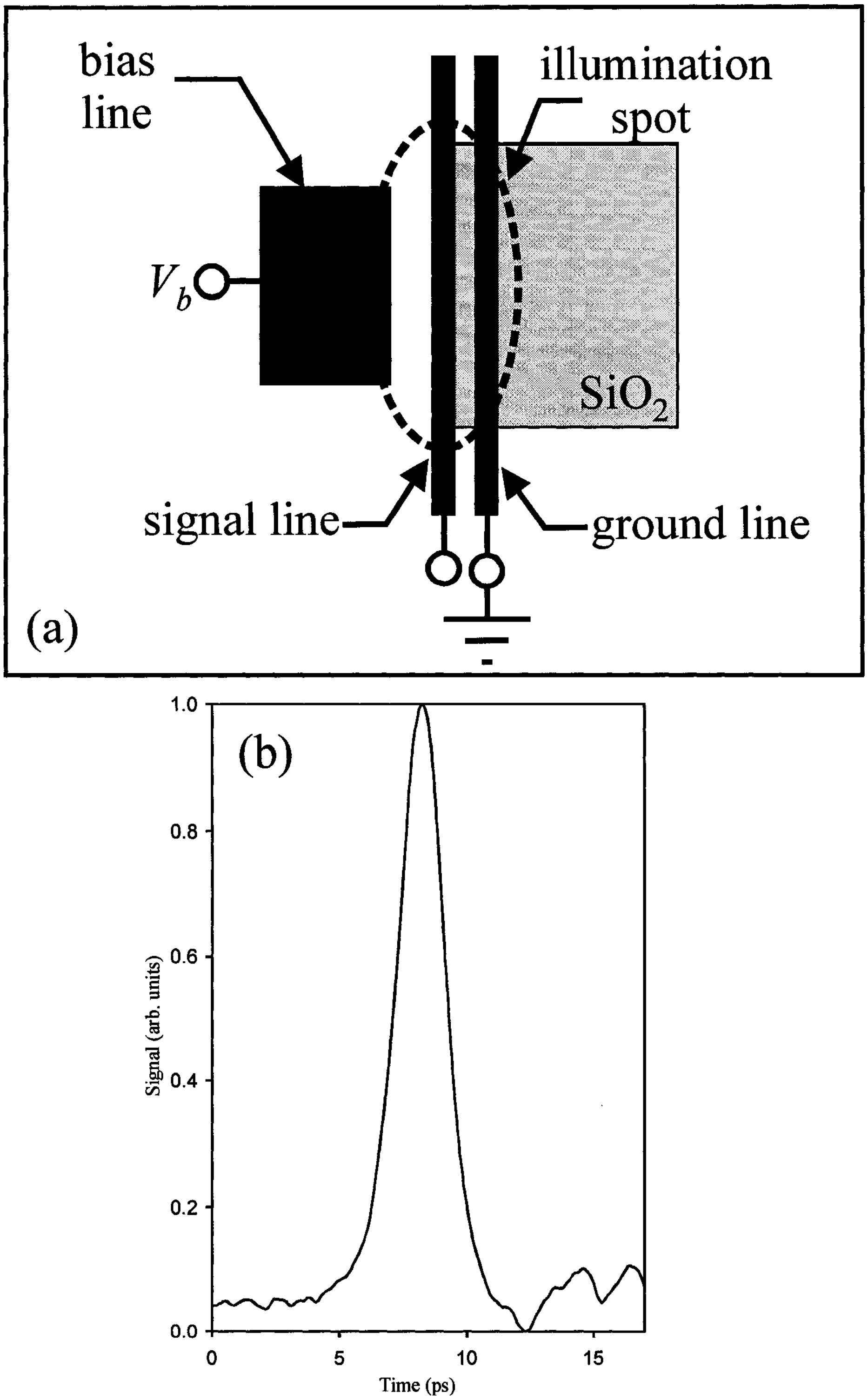

Figure 2.4.2.4 The (a) schematic for complete illumination of the non-interdigitated coplanar PC switch and a (b) typical generated waveform. Biasing is applied to the bias line and illumination covers both the bias-to-signal gap and the signal-to-ground gap.

is 125 times shorter than the carrier lifetime inherent to the GaAs substrate. In comparing the experimental results of figure 2.4.2.4(b) with the theoretical results presented in section 2.4.1, it is interesting to note the significant difference between the theoretical pulse duration (0.25 ps) and the experimental pulse duration (2 ps). This discrepancy can be understood through several mechanisms inherent to the pulse generation and detection processes. Firstly, as was the case for the ultrathin Si PC switch, the measurement bandwidth of the detection system is not instantaneous. The finite EO sampling bandwidth of the system can attribute for some (though not all) of the exceedingly long measured electrical pulse duration. Secondly, the response times associated with the competing electrical switching processes are likely to have been underestimated in the model. Indeed, the dielectric loading of the SiO_2 optical delay layer as well as metal-semiconductor junction effects (such as the lack of Ohmic contacts) significantly increase the RC response times for the device. Thirdly, and most importantly, dispersion due to propagation on the coplanar transmission line is expected to play a major role in broadening the electrical pulse. Previous research into THz electrical pulse propagation on coplanar transmission lines [52], [53] suggests that high-frequency signals, such as the pulses generated by the coplanar PC switch, are highly susceptible to the formation of substrate modes during propagation. In contrast to coplanar transmission lines on infinitely thick substrates (where radiation losses dominate), coplanar transmission lines on finite thickness substrates lose energy to the formation of substrate modes. The onset of this modal dispersion is often estimated through the semiempirical relation [52]

$$\sqrt{\varepsilon_{eff}(f)} = \sqrt{\varepsilon_{eff}(0)} + \frac{\sqrt{\varepsilon_{eff}(\infty)} - \sqrt{\varepsilon_{eff}(0)}}{1 + a\left(f/f_{TE}\right)^{-b}}, \tag{2.4.2.1}$$

where a and b are semiempirical fitting constants, $\varepsilon_{eff}(f)$ is the frequency-dependent dielectric function for propagation on the transmission line, $\varepsilon_{eff}(0)$ = is the quasi-static dielectric constant, $\varepsilon_{eff}(\infty)$ is the high-frequency dielectric constant, and

$$f_{TE} = \frac{c}{4h\sqrt{\varepsilon_r - 1}} \qquad (2.4.2.2)$$

is the cutoff frequency above which non-transverse electromagnetic (non-TEM) substrate modes are formed. Here, h is the substrate thickness and ε_r = 13.1 is the dielectric constant of the GaAs substrate. If electrical pulses with frequency components above f_{TE} propagate on the transmission line, they become severely distorted from modal dispersion. For the h = 600 μm thickness of the GaAs substrate used in this investigation, this onset will occur at 36 GHz–which is well within the bandwidth of the 0.25 ps theoretical electrical pulse formed by the coplanar PC switch. Modal dispersion (as well as the other dispersive effects) are, therefore, expected to play a major role in broadening the ultrashort electrical pulse. Interestingly, a comparison of the coplanar PC switch design and the ultrathin Si PC switch design suggests that the electrical pulses produced by the Si switch will witness significantly less broadening, as the exceedingly small thickness of the Si substrate (10 μm) produces a non-TEM cutoff frequency (f_{TE} = 2.4 THz) that is well above the bandwidth of the photo-generated electrical pulse. This likely contributes to the reduced pulse duration measured for the ultrathin Si PC switch. The coplanar PC switch, on the other hand, uses a thick GaAs substrate, making it highly susceptible to modal dispersion and electrical pulse broadening. For this reason, thin substrates are currently being studied for application to the propagation of ultrahigh-frequency (THz) electrical transients [33], [47], [54].

2.5 Photoconductive Frozen Wave Generation

2.5.1 Theoretical Framework

Ultrafast optically activated semiconductor switching plays a major role in the ongoing development of ultrahigh-frequency THz electrical sources. This light activated electronic switching process was introduced in sections 2.3 and 2.4 through the technique of PC self-switching. Here it was found that ultrashort THz electrical pulses could be formed through the application of a time-delayed self-switching scheme. The current section seeks to expand on this recombination-independent PC switching process by introducing the technique of PC frozen wave generation. In contrast to PC self-switching–where the turn-on and turn-off processes of the device are controlled by a time-delay in the optical pump pulse–frozen wave generation makes use of an electrical transit time-delay in the propagation of the transmitted and reflected voltage waveforms on the transmission line. Like microstrip and coplanar PC self-switching, frozen wave generation does not rely upon ultrafast carrier recombination for the formation of the THz electrical transients; unlike PC self-switching, frozen wave generation offers the possibility of producing multi-cycle voltage transients with a variety of waveform shapes.

The idealized layout for a FWG is shown in figure 2.5.1.1. The upper portion of this figure shows the initial standing wave voltage that exists on the transmission line. In this initial state, the FWG is comprised of four alternately biased ($\pm V_b$) transmission line segments (of length $L_{\lambda/2}$) that are separated by an array of open switches. Upon closing these switches, the initial standing wave pattern is transformed into the two counter-propagating traveling waves shown in the lower portion of the figure. There are several key features to take note of from this FWG output. Firstly, the traveling

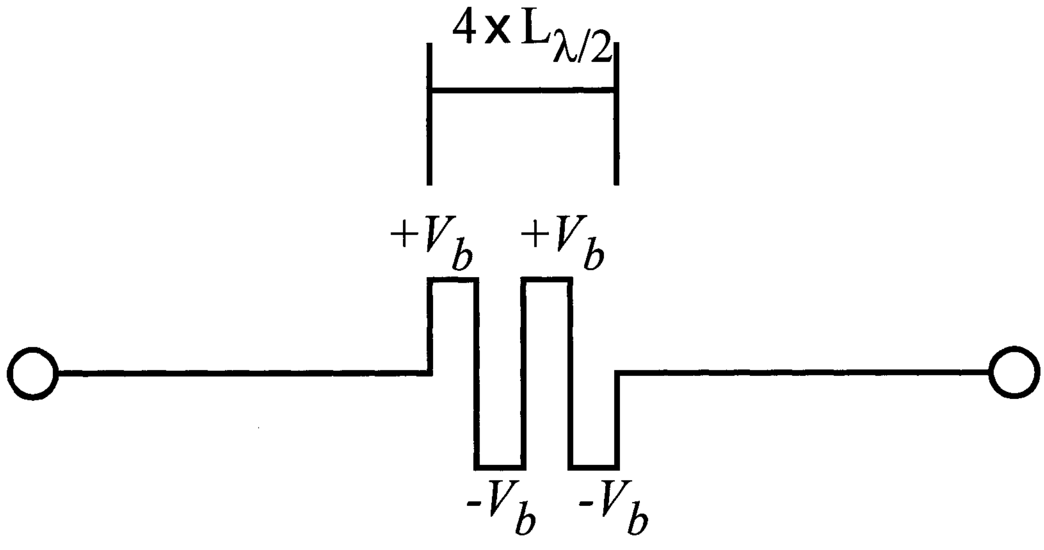

Initial Standing Wave

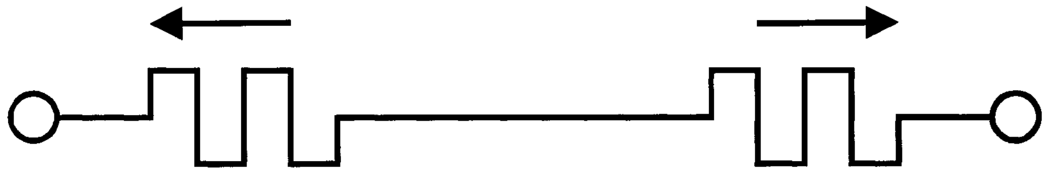

Counter-Propagating Traveling Waves

Figure 2.5.1.1 The idealized arrangement for frozen wave generation. Upon activating the device, the initial DC standing-wave is transformed into two counter-propagating RF waveforms.

waveforms exhibit maximum amplitudes of one-half the initial bias voltage ($\pm V_b/2$). By increasing the DC voltage applied to each bias segment, therefore, the signal on the transmission can be scaled to large amplitudes. Secondly, the spatial structure of the initial standing wave is seen to map itself onto the temporal structure of the voltage waveform propagating on the transmission line. This DC to RF conversion process implies that FWG structures with small half-wavelength transmission line segment lengths ($L_{\lambda/2}$) can be used to produce photo-generated electrical transients with small temporal periods and high central frequencies. Moreover, the bandwidth of the resulting THz waveform can be tailored by simply controlling the number of bias segments incorporated into the structure. Introducing more bias segments into the device will, for example, increase the number of oscillations in the voltage waveform and narrow the bandwidth of the signal.

The initial attempt at frozen wave generation was performed by Weibel in 1964 [55]. In his pioneering experiment, a series array of charged capacitors was simultaneously discharged through a chain of spark gaps. The result was a high power (5 kA) transient with a 1.5 MHz frequency response. While the signal amplitudes produced by his device were extremely large, the temporal response was severely limited–as his use of large charged capacitors greatly increased the response time of his discharging circuit. To improve upon the temporal response of this technique and generate higher frequency signals, frozen wave generation was further developed through the introduction of PC switching. Proud and Norman [56] applied the fast switching times associated with Si PC switching to the excitation process and were able to generate significantly faster transients. Using half-wavelength coaxial transmission line segments of length $L_{\lambda/2} = 1.5$ m, they produced multi-cycle waveforms with frequencies up to 50 MHz–being limited mainly by the optical pulse duration of their laser system (10 ns, 1 mJ nitrogen laser). With the advent of short-pulse laser systems, the technique of frozen wave generation was further developed by Lee et al. In his experiment [57], a picosecond laser system with short optical pulse durations was used, in conjunction with short half-wavelength coaxial transmission line segments ($L_{\lambda/2} = 0.5$ m), to produce 250 MHz multi-cycle electrical waveforms. The technique of frozen wave generation was brought into the gigahertz regime, finally, by Thaxter et al. These researchers were able to produce 6 GHz electrical waveforms with a FWG that incorporated exceedingly small ($L_{\lambda/2} = 1$ cm) half-wavelength microstrip transmission line segments [58].

While previous efforts at employing frozen wave generation have been successful at generating electrical transients at or below the gigahertz level, it is important to realize that the concept of frozen wave generation can also be applied to the generation of THz electrical waveforms. If half-wavelength transmission line segments with sufficiently small lengths are employed, the waveform period can be brought down to a picosecond timescale, and the frequency content can be extended into the THz regime. In contrast to the idealized FWG response shown in figure 2.5.1.1, however, the actual response of the device will be limited by a variety of practical constraints. Signal degradation due to effects such as electrical reflections and material losses will affect the overall amplitude, while pulse broadening mechanisms such as transmission line dispersion and material dispersion will affect the overall frequency response. The most important practical issue is, however, the RC response time for each PC gap. The electrical response time associated with each switch must be made sufficiently small to allow the transient response of the structure to fully form the counter-propagating THz waveforms.

To design and build a successful FWG, it will be necessary to fully understand the relationship that exists between the PC excitation process and the formation of the voltage transient. To gain this understanding, the model shown in figure 2.5.1.2 is employed. Here, the structure is rendered as a series-connection of PC gaps and transmission line segments–each of which is alternately biased at $\pm V_b$. The conduction current and displacement current through each gap (shown in detail in the figure inset) are represented by the time-varying gap conductor, $G_g(t)$, and the gap capacitor, C_g, respectively [35]. Operation of the device relies upon the time-evolution of the gap conductance elements which, under optical illumination, modify the reflected, $v_r(t)$, and the transmitted, $v_t(t)$, waveforms. Given an incident waveform, $v_i(t)$, for each PC gap and a transmission line impedance of Z_0, the current continuity equation,

$$\frac{v_i(t)-v_r(t)}{Z_0}=C_g\frac{dv_r(t)}{dt}-C_g\frac{dv_t(t)}{dt}+G_g(t)[v_i(t)+v_r(t)-v_t(t)]=\frac{v_t(t)}{Z_0}, \qquad (2.5.1.1)$$

is found. From this, the simultaneous differential equations,

$$\frac{dv_i(t)}{dt}=0, \qquad (2.5.1.2)$$

$$\frac{dv_r(t)}{dt}+\left[\frac{1}{2Z_0C_g}+\frac{G_g(t)}{C_g}\right]v_r(t)=\frac{v_i(t)}{2Z_0C_g}, \qquad (2.5.1.3)$$

and

$$\frac{dv_t(t)}{dt}+\left[\frac{1}{2Z_0C_g}+\frac{G_g(t)}{C_g}\right]v_t(t)=\frac{G_g(t)v_i(t)}{C_g}, \qquad (2.5.1.4)$$

are determined for the incident, reflected, and transmitted waveforms, respectively. Finally, by approximating the time-varying conductance across each gap as the step-

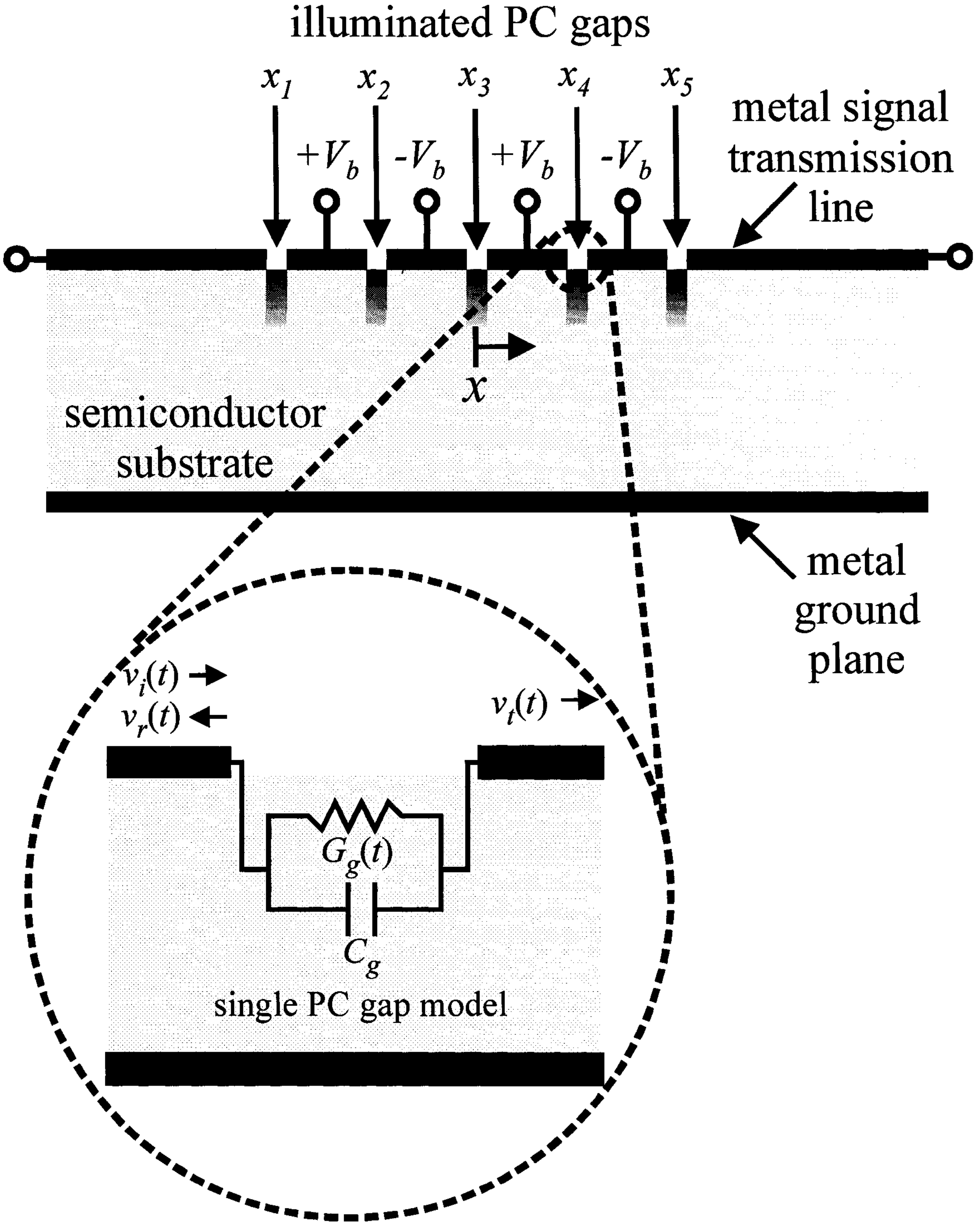

Figure 2.5.1.2 The experimental layout for the FWG. The model is shown for one of the PC gaps in the inset. Each PC gap responds to the optical excitation with incident, $v_i(t)$, reflected, $v_r(t)$, and transmitted, $v_t(t)$, waveforms.

response,

$$G_g(t) = \begin{cases} 0, & t < 0 \\ G_g, & t \geq 0 \end{cases}, \tag{2.5.1.5}$$

the incident, reflected, and transmitted waveforms for each gap are found to be [35]

$$v_i(t) = \frac{V_{diff,i}}{2}, \tag{2.5.1.6}$$

$$v_r(t) = \frac{V_{diff,i}}{2} \frac{1 + 2Z_0 G_g \exp(-t/\tau)}{1 + 2Z_0 G_g}, \tag{2.5.1.7}$$

and

$$v_t(t) = \frac{V_{diff,i}}{2} \frac{2Z_0 G_g}{1 + 2Z_0 G_g} \left[1 - \exp(-t/\tau)\right], \tag{2.5.1.8}$$

where $V_{diff,i}$ is the difference between the initial voltage to the left of the i^{th} gap and the initial voltage to the right of the i^{th} gap. Here, the RC time constant for the switching process is defined as

$$\tau = \left(\frac{1}{2Z_0 C_g} + \frac{G_g}{C_g} \right)^{-1}. \tag{2.5.1.9}$$

To simplify the analysis, the complete voltage response is expressed as the superposition of the initial stationary wave on the transmission line,

$$v_{stationary}(x,t) = \begin{cases} 0, & x < -2L_{\lambda/2} \\ +V_b, & -2L_{\lambda/2} \leq x < -L_{\lambda/2} \\ -V_b, & -L_{\lambda/2} \leq x < 0 \\ +V_b, & 0 \leq x < L_{\lambda/2} \\ -V_b, & L_{\lambda/2} \leq x < 2L_{\lambda/2} \\ 0, & x > 2L_{\lambda/2} \end{cases}, \tag{2.5.1.10}$$

and the forward and reverse waves produced by each individual PC gap. Here, the first, second, third, fourth, and fifth PC gaps (located at $x_1 = -2L_{\lambda/2}$, $x_2 = -L_{\lambda/2}$, $x_3 = 0$, $x_4 = L_{\lambda/2}$, and $x_5 = 2L_{\lambda/2}$) are characterized by initial voltage differences of $V_{diff,1} = -V_b$, $V_{diff,2} = +2V_b$, $V_{diff,3} = -2V_b$, $V_{diff,4} = +2V_b$, and $V_{diff,5} = -V_b$, respectively. Using these terms, the forward and reverse traveling waves produced by the i^{th} PC gap can be expressed as

$$v_{for,i}(x,t) = V_{diff,i} \times \left(\frac{Z_0 G_g}{1 + 2Z_0 G_g} \right) \times \begin{cases} 0, & \left[t - (x - x_i)\sqrt{\varepsilon_{eff}}/c\right] < 0 \\ \left\{1 - \exp\left\{-\left[t - (x - x_i)\sqrt{\varepsilon_{eff}}/c\right]/\tau\right\}\right\}, & \left[t - (x - x_i)\sqrt{\varepsilon_{eff}}/c\right] \geq 0 \end{cases} \tag{2.5.1.11}$$

and

$$v_{rev,i}(x,t) = V_{diff,i} \times \left(\frac{-Z_0 G_g}{1 + 2Z_0 G_g} \right) \times \begin{cases} 0, & \left[t + (x - x_i)\sqrt{\varepsilon_{eff}}/c\right] < 0 \\ \left\{1 - \exp\left\{-\left[t + (x - x_i)\sqrt{\varepsilon_{eff}}/c\right]/\tau\right\}\right\}, & \left[t + (x - x_i)\sqrt{\varepsilon_{eff}}/c\right] \geq 0 \end{cases} \tag{2.5.1.12}$$

respectively, for an effective dielectric constant on the transmission line of ε_{eff}. The overall voltage waveform on the transmission line is found, finally, by linear superposition to be

$$v(x,t) = v_{stationary}(x,t) + \sum_{i=1}^{5} v_{for,i}(x,t) + \sum_{i=1}^{5} v_{rev,i}(x,t). \tag{2.5.1.13}$$

Results for this FWG theoretical model are shown in figure 2.5.1.3; details on the numerical solution of equation 2.5.1.13 are shown in Appendix F. The voltage is shown as a function of the spatial dimension, x, at various points in time, and PC gap parameters of $Z_0 = 100\ \Omega$, $G_g = 10\ \Omega^{-1}$, $C_g = 0.1$ pF, and $n_{eff} = 3$ are incorporated into the model. The transformation of the initial DC standing wave into two counter-propagating RF traveling waves is readily apparent in the figure. For the $L_{\lambda/2}$ = 50 μm half-wavelength transmission line segment length used in the simulation, the period of oscillation for the

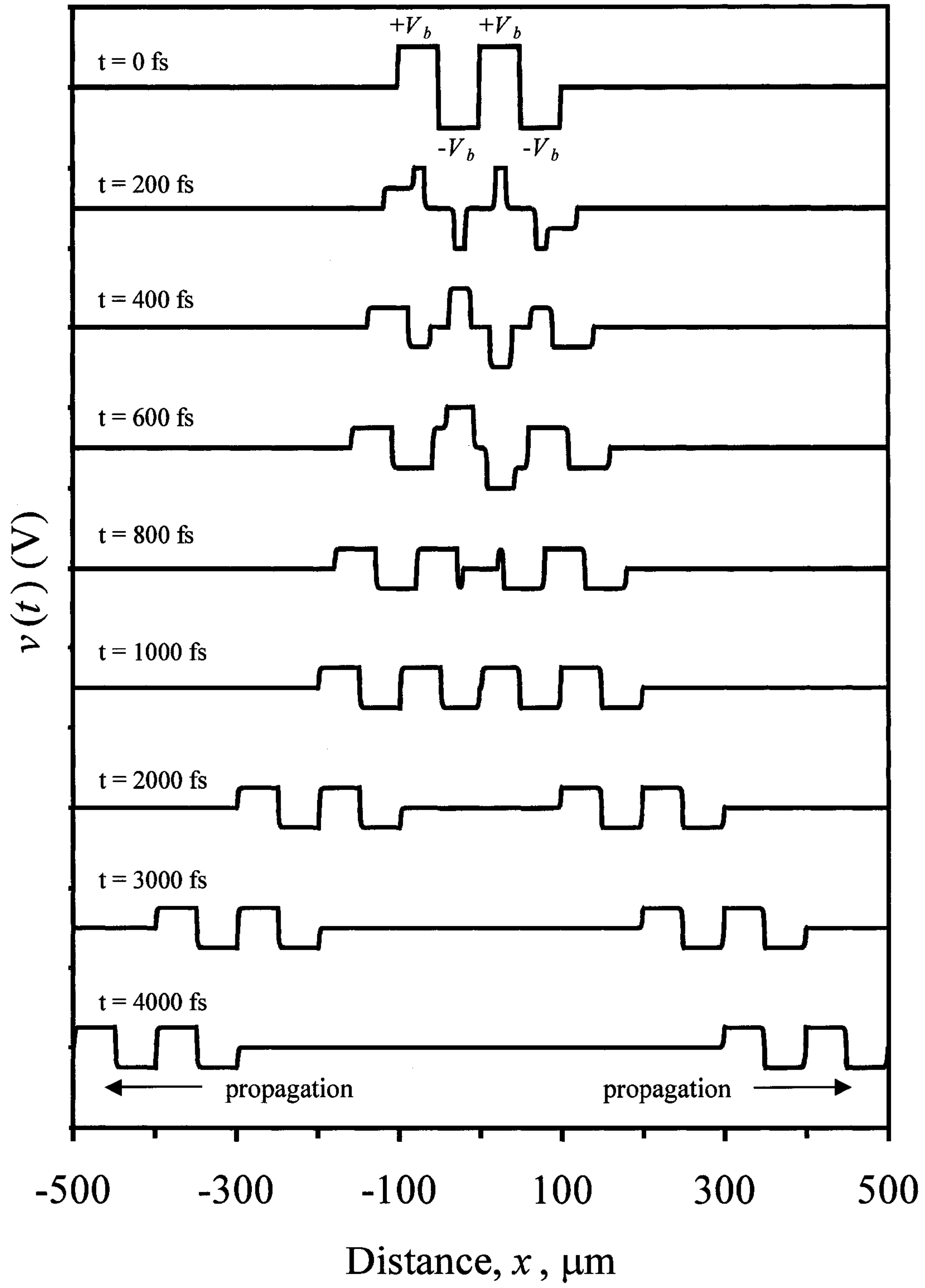

Figure 2.5.1.3 The FWG waveforms predicted by the model for PC gaps defined by $C_g = 0.1$ pF, $G_g = 10\,\Omega^{-1}$, and $Z_0 = 100\,\Omega$.

waveform is found to be 1 ps (corresponding to a central frequency response of 1 THz). In addition, the large gap conductance and small gap capacitance together allow the two traveling waves associated with this simulation to be accurate replicas of the initial standing wave on the transmission line (simply scaled by one-half). As a comparison, simulation results are presented in figure 2.5.1.4 for the case where the gap capacitance has been increased to $C_g = 10$ pF. It is readily apparent from this new figure that the two counter-propagating RF waves no longer resemble the original DC function. The increased response time for each gap has smeared the rising and falling edges across the waveforms and decreased the amplitude of the transient to a value that is substantially less than one-half the bias voltage. Clearly, to design and build a FWG with both a high frequency response and a large voltage amplitude, it will be necessary to generate the voltage transients on a sufficiently short timescale.

2.5.2 Experimental Framework

The principal objective of this section is to extend the operation of the FWG to the THz regime. The schematic for such a device is shown in figure 2.5.2.1(a) [18]. The FWG microcircuit is fabricated using standard photolithographic techniques with 50/150 nm Ti/Au metallization on a 600 μm thick semi-insulating (10^7 Ω·cm) GaAs substrate. Four 20 μm wide bias electrodes and five 30 μm wide PC gaps bridge the 230 μm long gap in the coplanar transmission line–which is, itself, composed of two 20 μm wide metal lines separated by 20 μm. To activate the device, the FWG electrodes are alternately biased at $\pm V_b$, and the optical pump beam is simultaneously focused onto each of the five PC gaps. The resulting experimental setup is shown in figure 2.5.2.1(b).

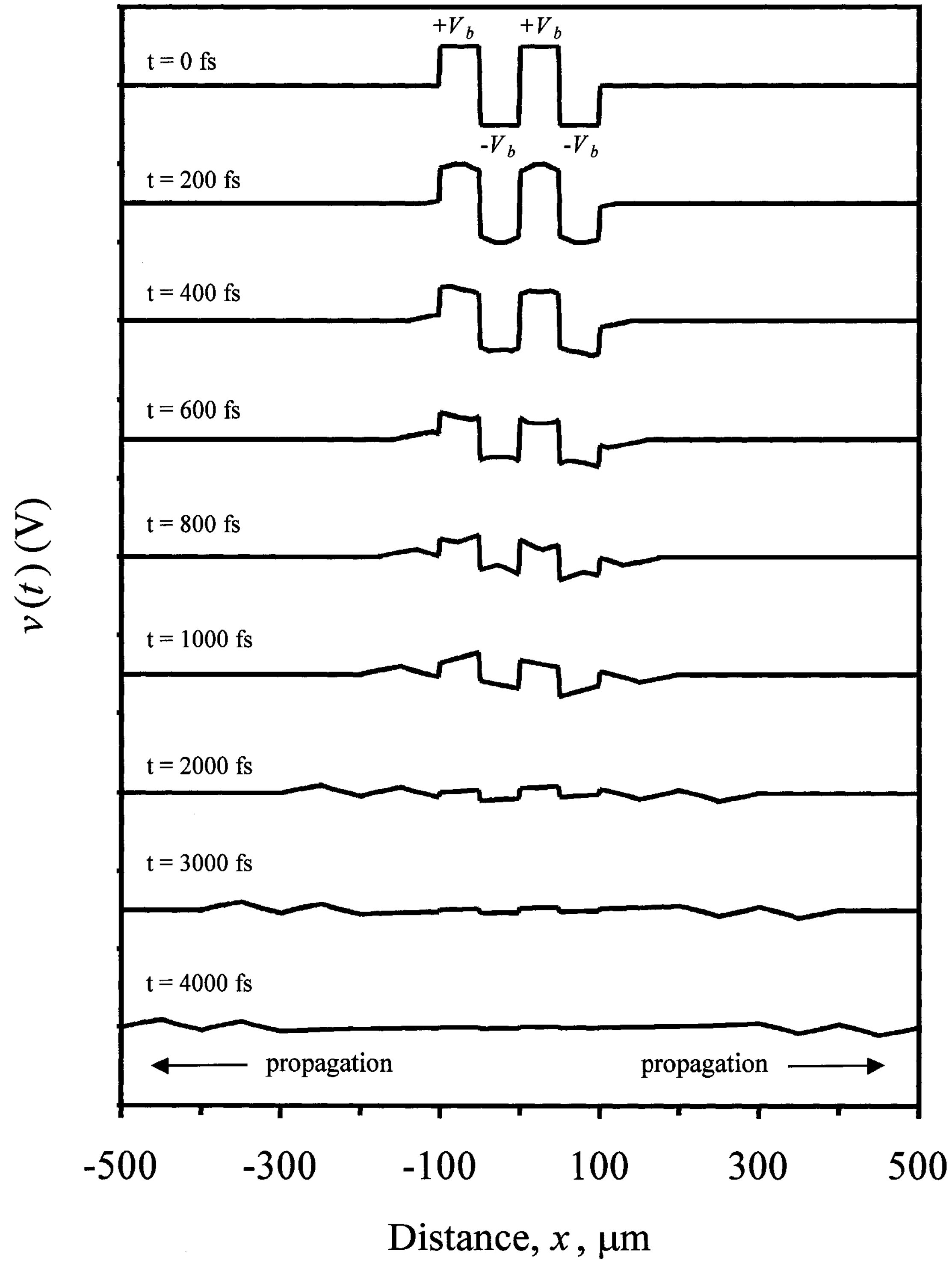

Figure 2.5.1.4 The FWG waveforms predicted by the model for PC gaps defined by $C_g = 10$ pF, $G_g = 10\,\Omega^{-1}$, and $Z_0 = 100\,\Omega$.

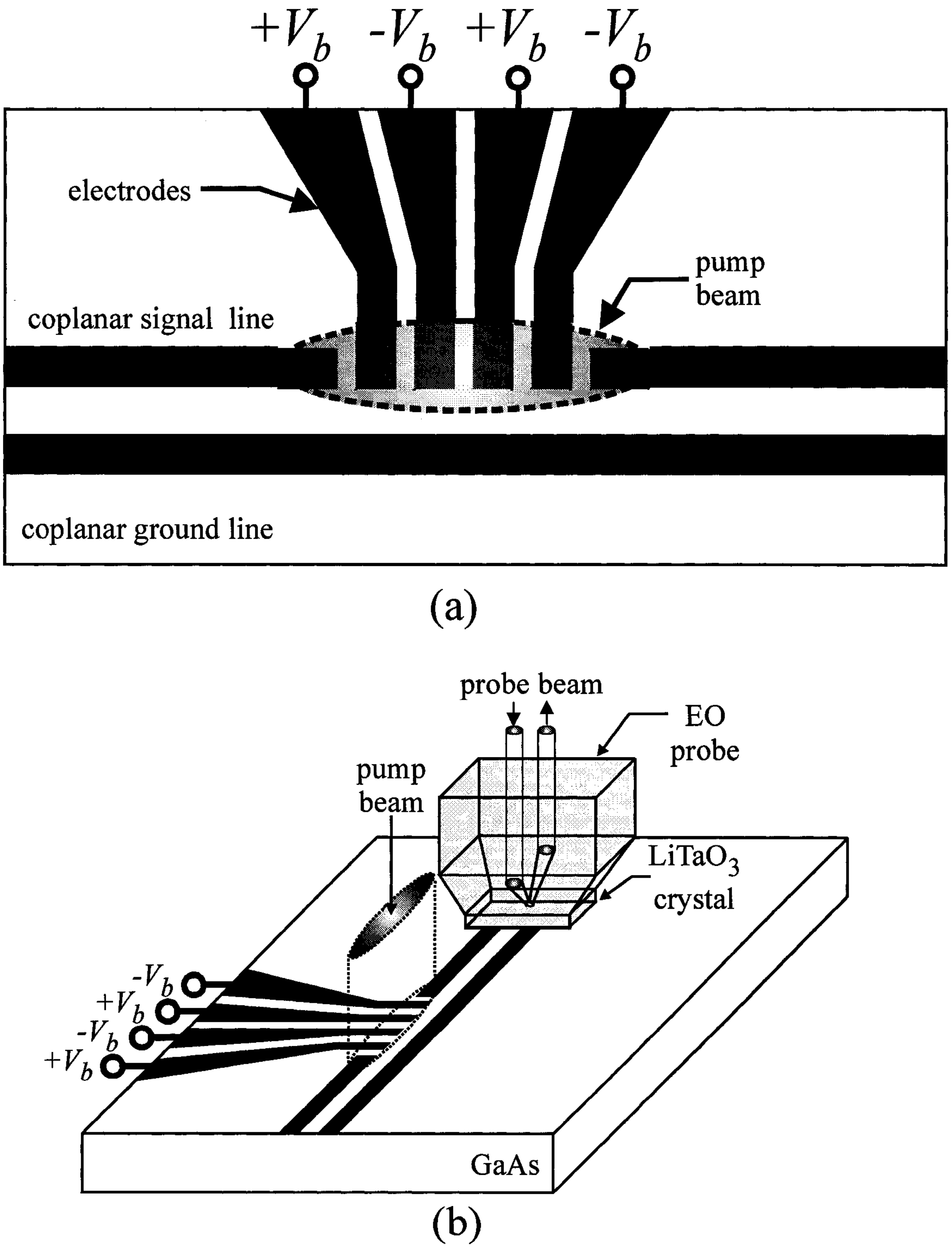

(a)

(b)

Figure 2.5.2.1 The (a) schematic for the PC FWG and the (b) overall experimental layout for the generation and detection system. Optical excitation is carried out across all of the PC gaps, and sampling occurs on the coplanar transmission line (with the $LiTaO_3$ EO probe).

To measure the temporal features of the ultrafast transient on the transmission line, the time-resolved pump-probe scanning system described in section 2.2 is employed. Here, a 100 mW pump beam is focused onto all of the PC gaps in the FWG to generate the voltage waveform, and a 20 mW probe beam is directed into the $LiTaO_3$ EO probe to sample the voltage waveform. By scanning through the temporal delay between the pump and probe pulses and monitoring the polarization phase retardation of the probe beam, a time-domain representation of the electrical signal on the coplanar transmission line is constructed. To lower the noise levels in the system and enhance the experimental sensitivity, the high-frequency (3 MHz) electronic mixing and differential lock-in detection techniques described in Appendix C are employed. The high-frequency biasing arrangement is modified slightly, however, to accommodate the fact that the alternating electrodes require opposite polarities. In this case, the positive electrodes in the FWG are biased directly from the signal source (giving an effective bias voltage of +10 $V_{p\text{-}p}$), while the negative electrodes in the FWG are biased through a 1:1 transformer (giving a 180° phase shift and an effective bias voltage of -10 $V_{p\text{-}p}$).

Typical time-domain results for EO sampling at a distance of 400 μm from the FWG are shown in figure 2.5.2.2(a). The figure shows four prominent voltage peaks of alternating polarity spanning a time interval of 6.4 ps. The amplitude of these voltage peaks decreases steadily with time such that the second positive peak amplitude is one-third of the first positive peak amplitude. This decaying amplitude is due to multiple electrical reflections from the impedance mismatch between the transmission line segments and the photo-excited gaps as the pulse train propagates through the FWG segments. Portions of the voltage waveform that are generated furthest from the point of

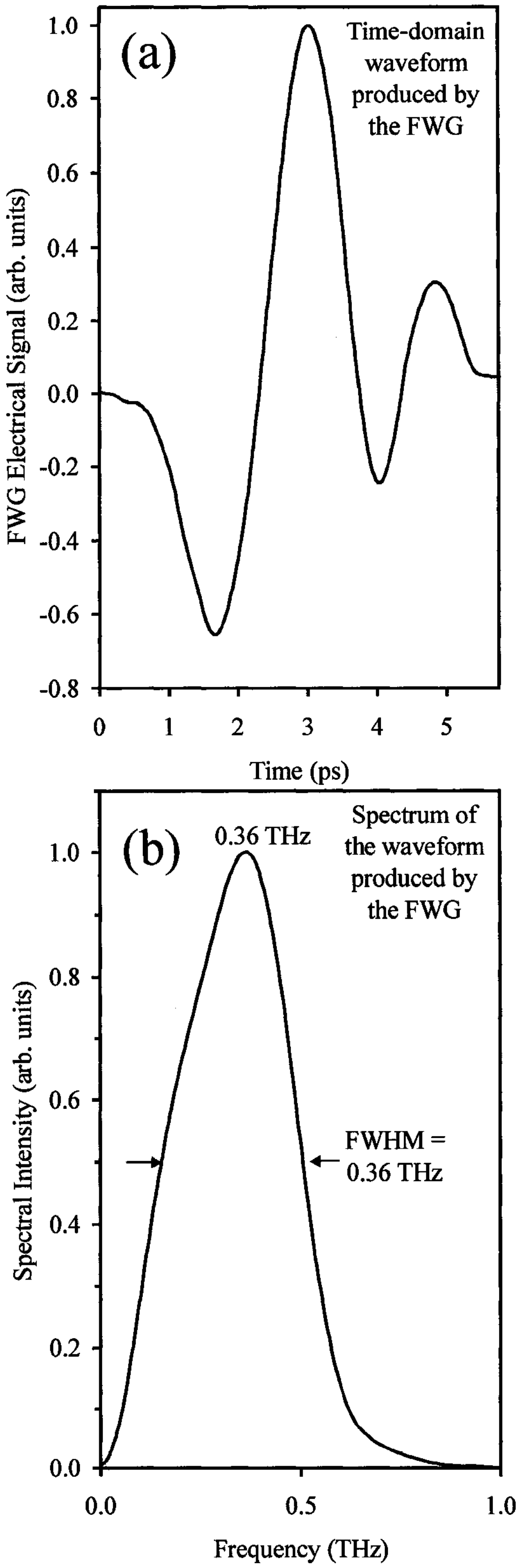

Figure 2.5.2.2 The (a) time-domain THz electrical waveform and (b) spectral intensity produced by the PC FWG. Sampling occurs 400 μm from the FWG.

sampling will undergo the largest number of reflections and suffer the greatest attenuation. Similar reflection effects are witnessed in low-frequency FWG experiments with two or more froze wave cycles [59], [60].

The signal in figure 2.5.2.2(a) shows two 2.5 ps voltage cycles. The 0.4 THz central frequency associated with this period agrees approximately with the central frequency of the spectral intensity curve shown in figure 2.5.2.2(b). Since the waveform is generated in a spatially periodic structure, of which a significant length consists of an optically generated plasma, the corresponding wavelength is expected to differ significantly from that of a standard dielectric-loaded transmission line. Using an effective dielectric constant of 12 and a wavelength of 100 μm, standard dielectric-loaded transmission line analysis [58] would suggest that the full-wave period is approximately 1 ps, corresponding to a central frequency of 1 THz. The large difference between this predicted central frequency and the measured central-frequency of figure 2.5.2.2(b) makes clear that this array of PC switches acts very differently from a standard transmission line of similar dimensions. Moreover, the presence of material dispersion in the substrate and modal dispersion on the transmission line are expected to broaden the temporal characteristics of the waveform (in the same way that these processes affected the waveforms on the coplanar transmission line of section 2.4).

The EO sampling results presented thus far have focused on transmission line-coupled voltage waveforms. Numerous obstacles to the transmission of these high frequency signals do exist, however. As mentioned above, dispersive effects, such as modal dispersion [45], [46], [52], are known to broaden the duration of the waveform, while radiative and material losses [53] decrease the overall amplitude. To minimize these pulse dispersion and signal attenuation effects, time-resolved sampling experiments are often conducted within close proximity to the point of PC generation. This constraint does, however, pose numerous practical limitations to high-frequency applications (where THz signal propagation beyond a few millimetres is often required). To overcome the adverse effects of high-frequency THz signal propagation on transmission lines, therefore, the current FWG design is incorporated into an intra-chip broadcasting setup. This alternative transmission technique transmits the FWG waveforms by coupling them to the pair of resonantly-excited dipole transmitter-receiver antennas shown in figure 2.5.2.3(a). The 160 μm long dipole transmitter is coupled to the coplanar transmission line at the output of the FWG, while the 160 μm long dipole receiver is positioned at a distance of 400 μm from the transmitter. To measure the received electrical transient, the $LiTaO_3$ probe is positioned over the dipole receiver for EO sampling. The overall test structure is shown in figure 2.5.2.3(b).

Typical EO sampling results for the FWG broadcasting setup are shown in figure 2.5.2.4(a). The timescale for this figure is adjusted so that the zero-time correlates with the time at which the electrical signal arrives at the transmitting dipole. Though several features are evident in the figure, the most prominent characteristic is the two-cycle bipolar THz oscillation commencing at 15 ps (shown in detail in figure 2.5.2.4(b)). This 15 ps time interval corresponds to the time it takes the THz radiation pattern to reflect off the back-side of the GaAs substrate and be picked up by the receiver [61]. For a 600 μm thick substrate and a transmitter-receiver separation of 400 μm, this propagation distance is in the near-field regime–a point that is supported by the fact that the received signal in figure 2.5.2.4(b) is a scaled replica of the transmitted signal in figure 2.5.2.2(a) [62].

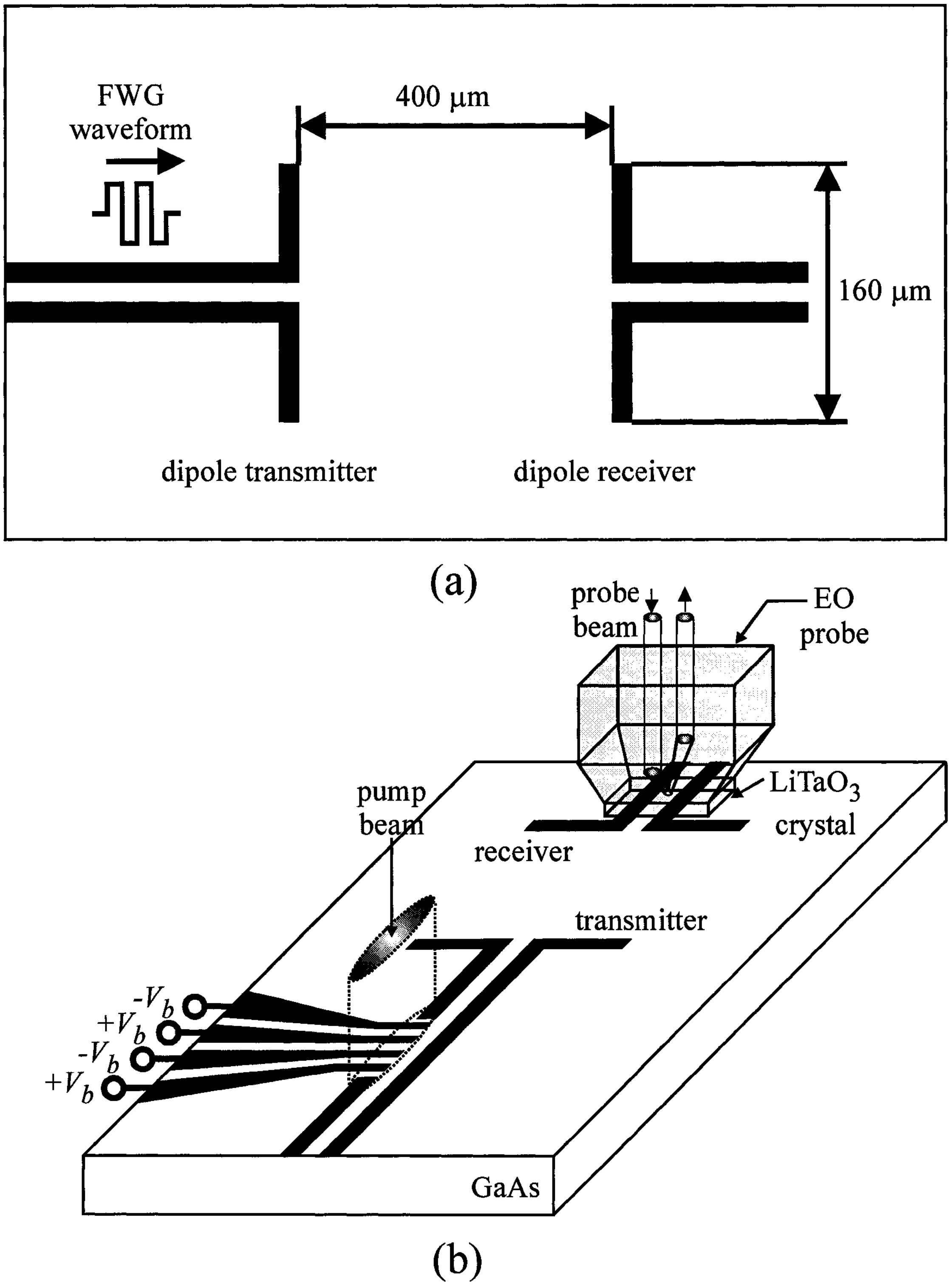

Figure 2.5.2.3 The (a) integrated dipole transmitter-receiver pair and the (b) overall experimental FWG generation and detection system.

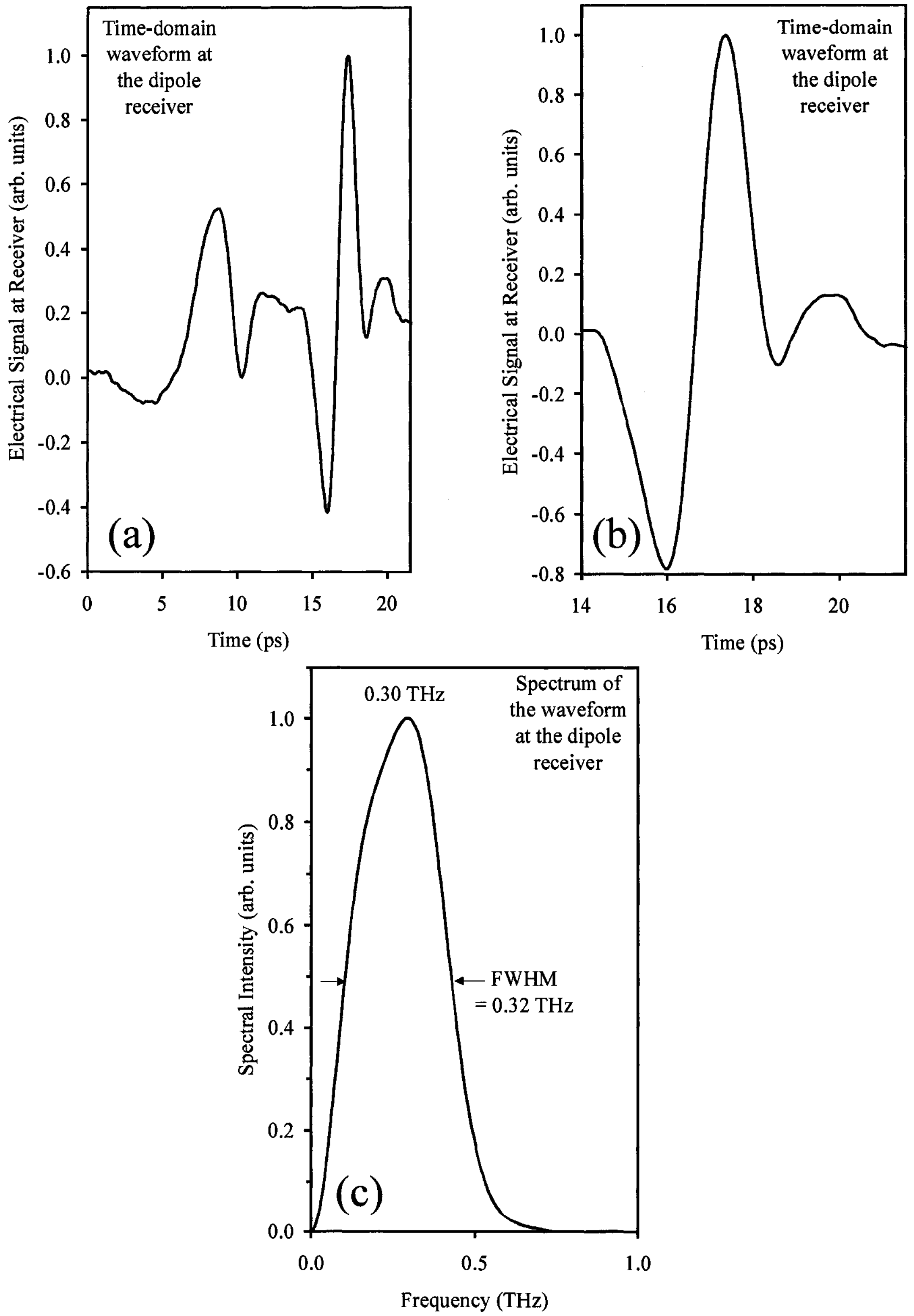

Figure 2.5.2.4 The (a) full time-domain electrical waveform measured at the dipole receiver, a (b) close-up of the THz waveform at the receiver, and the (c) spectral intensity of theTHz waveform at the dipole receiver.

An important point related to the broadcasting characteristics of dipole antennas on dielectric half-spaces is that they cannot be made to radiate far-field electric field components along the plane of the dielectric [63]. In comparison, though, near-field waves can be made to transmit along the surface [61]. These near-field surface patterns propagate as two independent waveforms: one that travels through the air and one that travels through the substrate. The difference in refractive index between these two media will introduce a time-delay between the arrival of the surface wave in the air and the arrival of the surface wave in the dielectric. A closer inspection of figure 2.5.2.4(a) does, indeed, show the presence of time-varying waveforms before the arrival of the waveform at 15 ps. Given a propagation distance of 400 μm between the transmitter and the receiver, the near-field surface waves in the air and the GaAs substrate are seen to arrive at times of 1.3 ps and 4.8 ps, respectively. The overall time-domain waveform is the superposition of these two near-field patterns and the reflected THz pattern.

The ability of the dipole transmitter and receiver to broadcast and detect the FWG signals is based largely on the resonance response of the antenna design. By using a dipole transmitter-receiver pair with a half-wave resonance peak at the central frequency of the FWG signal, for example, it is possible to optimize the signal transmission characteristics of the system. The 160 μm long dipole antennas shown in figure 2.5.2.3(a) are characterized by a free-space half-wave resonant frequency of f_r = 0.92 THz. This resonant frequency is modified, however, by the presence of the GaAs half-space below the antenna. To estimate this modified value, the effective resonant frequency,

$$f_{eff} = \frac{f_r}{\sqrt{\varepsilon_{eff}}}, \tag{2.5.2.1}$$

is calculated for the system, using a weighted average for the effective dielectric constant,

$$\varepsilon_{eff} = \frac{(\varepsilon_r + 1)}{2}. \qquad (2.5.2.2)$$

Given a dielectric constant of $\varepsilon_r = 13.1$ for the GaAs substrate, the effective resonant frequency for the dipoles is predicted to be $f_{eff} = 0.35$ THz [64]. The similarity between this resonant frequency and the 0.36 THz peak frequency of figure 2.5.2.2(b) suggests that the 160 μm dipole length is well suited for the FWG transmission system. To verify this, the spectral intensity of the received FWG waveform (shown in figure 2.5.2.4(c)) is calculated and compared to the frequency response of the generated FWG waveform. Though the spectrum of the received waveform is similar in form to the spectrum of the transmitted waveform, the peak value is shifted downward by 50 GHz, indicating that the dipole resonance occurs at a slightly lower value than predicted. This downward shift in the resonant frequency has been observed in other *centre-fed* dipole investigations, however, and is attributed to bias line termination effects in the antenna (as opposed to *end-fed* dipole antennas where little downward resonant frequency shifting is observed) [64].

Chapter 2.0 References:

[1] D. H. Auston, "Picosecond optoelectronic switching and gating in silicon," *Appl. Phys. Lett.* **26**, pp. 101-103, 1975.

[2] J. S. Weiner and P. Y. Yu, "Free carrier lifetime in semi-insulating GaAs from time-resolved band-to-band photoluminescence," *J. Appl. Phys.* **55**, pp. 3889-3891, 1984.

[3] J. Meyer, A. Y. Elezzabi, and M. K. Y. Hughes, "Infrared absorption and momentum relaxation of free carriers in silicon generated by subpicosecond above band gap radiation," *IEEE J. Quantum Electron.* **31**, pp. 729-734, 1995.

[4] D. H. Auston, P. Lavallard, N. Sol, and D. Kaplan, "An amorphous silicon photodetector for picosecond pulses," *Appl. Phys. Lett.* **36**, pp. 66-68, 1980.

[5] X. Zheng, Y. Xu, R. Sobolewski, R. Adam, M. Mikulics, M. Siegel, and P. Kordo, "Femtosecond response of a free-standing LT-GaAs photoconductive switch," *Appl. Opt.* **42**, pp. 1726-1731, 2003.

[6] A. Y. Elezzabi, J. Meyer, M. K. Y. Hughes, and S. R. Johnson, "Generation of 1-ps Infrared Pulses at 10.6 μm by Use of Low-Temperature-Grown GaAs as an Optical Semiconductor Switch," *Opt. Lett.* **19**, pp. 898-900, 1994.

[7] F. E. Doany, D. Grischkowsky, and C. C. Chi, "Carrier lifetime versus ion-implanted dose in silicon on sapphire," *Appl. Phys. Lett.* **50**, pp. 460-462, 1987.

[8] F. W. Smith, H. Q. Le, V. Diadiuk, M. A. Hollis, A. R. Calawa, S. Gupta, M. Frankel, D. R. Dykaar, G. A. Mourou, and T. Y. Hsiang, "Picosecond GaAs-based photoconductive optoelectronic detectors," *Appl. Phys. Lett.* **54**, pp. 890-892, 1989.

[9] M. B. Ketchen, D. Grischkowsky, T. C. Chen, C-C. Chi, I. N. Duling III, N. J. Halas, J-M. Halbout, J. A. Kash, and G. P. Li, "Generation of subpicosecond electrical pulses on

coplanar transmission lines," *Appl. Phys. Lett.* **48**, pp. 751-753, 1986.

[10] D. Krökel, D. Grischkowsky, and M. B. Ketchen, "Subpicosecond electrical pulse generation using photoconductive switches with long carrier lifetimes," *Appl. Phys. Lett.* **54**, pp. 1046-1047, 1989.

[11] U. D. Keil, D. R. Dykaar, R. F. Kopf, and S. B. Darack, "Reflectivity measurements of femtosecond carrier and field dynamics in semiconductors," *Appl. Phys. Lett.* **64**, pp. 3267-3269, 1994.

[12] E. Sano and T. Shibata, "Mechanism of subpicosecond electrical pulse generation by asymmetric excitation," *Appl. Phys. Lett.* **55**, pp. 2748-2750, 1989.

[13] S. Alexandrou, C.-C. Wang, R. Sobolewski, and T. Y. Hsiang, "Generation of subpicosecond electrical pulses by nonuniform illumination of GaAs transmission-line gaps," *IEEE J. Quantum Electron.* **30**, pp. 1332-1338, 1994.

[14] J. F. Holzman, A. Y. Elezzabi, and F. E. Vermeulen, "Ultrafast photoconductive self-switching of subpicosecond electrical pulses," *IEEE J. Quantum Electron.* **36**, pp. 130-136, 2000.

[15] J. F. Holzman, F. E. Vermeulen, B. W. Arnold, and A. Y. Elezzabi, "Photoconductive gating of picosecond electrical pulses on thinned-silicon substrates," *Electron. Lett.* **36**, pp. 1225-1226, 2000.

[16] J. F. Holzman, F. E. Vermeulen, and A. Y. Elezzabi, "Generation of 1.2 ps electrical pulses through parallel-gating in ultra-thin silicon photoconductive switches," *Appl. Phys. Lett.* **79**, pp. 4249-4251, 2001.

[17] J. F. Holzman, F. E. Vermeulen, and A. Y. Elezzabi, "Recombination-independent photogeneration of ultrashort electrical pulses," *Appl. Phys. Lett.* **76**, pp. 134-136, 2000.

[18] J. F. Holzman, F. E. Vermeulen, and A. Y. Elezzabi, "Frozen wave generation of bandwidth tunable two-cycle THz radiation," *J. Opt. Soc. Am. B* **17**, pp. 1457-1463, 2000.

[19] J. A. Valdmanis, G. Mourou, and C. W. Gabel, "Picosecond electro-optic sampling system," *Appl. Phys. Lett.* **41**, pp. 211-212, 1982.

[20] J. Nees and G. A. Mourou, "Noncontact electro-optic sampling with a GaAs injection laser," *Electron. Lett.* **22**, pp. 918-919, 1986.

[21] U. D. Keil and D. R. Dykaar, "Electro-optic sampling and carrier dynamics at zero propagation distance," *Appl. Phys. Lett.* **61**, pp. 1504-1506, 1992.

[22] B. E. A. Saleh and M. C. Teich, *Fundamentals of Photonics*, (John Wiley & Sons, New York, 1991), pp. 696-736.

[23] M. Y. Frankel, R. H. Voelker, and J. N. Hilfiker, "Coplanar transmission lines on thin substrates for high-speed low-loss propagation," *IEEE Trans. Microwave Theory Tech.* **42**, 396-402, 1994.

[24] J. M. Chwalek and D. R. Dykaar, "A mixer based electro-optic sampling system for submillivolt detection," *Rev. Sci. Instrum.* **61**, pp. 1273-1276, 1990.

[25] U. D. Keil and D. R. Dykaar, "Ultrafast pulse generation in photoconductive switches," *IEEE J. Quantum Electron.* **32**, pp. 1664-1671, 1996.

[26] D. H. Auston, "Picosecond photoconductors: Physical properties and applications," in *Picosecond Optoelectronic Devices*, C. H. Lee Ed., (Academic, Orlando, FL, 1984), pp. 73-117.

[27] A. Rosen, P. Stabile, and P. Herczfeld, "Innovative switching technology," in *High-Power Optically Activated Solid-State Switches*, A. Rosen and F. Zutavern Eds., (Artech

House, Boston, MA, 1994), pp. 139-186.

[28] P. S. Cho, P. T. Ho, J. Goldhar, and C. H. Lee, “Photoconductivity in ZnSe under high electric fields,” *IEEE J. Quantum Electron.* **30**, pp. 1489-1497, 1994.

[29] T. Pfeifer, H. M. Heiliger, T. Loffler, C. Ohlhoff, C. Meyer, G. Lupke, H. G. Roskos, and H. Kurz, “Optoelectronic on-chip characterization of ultrafast electric devices: Measurement techniques and applications,” *IEEE J. Selec. Topics on Quantum Electron.* **2**, pp. 586-603, 1996.

[30] M. Y. Frankel, J. F. Whitaker, and G. Mourou, “Optoelectronic transient characterization of ultrafast devices,” *IEEE J. Quantum Electron.* **28**, pp. 2313-2324, 1992.

[31] A. Y. Elezzabi and M. R. Freeman, “Ultrafast magneto-optic sampling of picosecond current pulses,” *Appl. Phys. Lett.* **68**, pp. 3546-3548, 1996.

[32] A. Nahata, T. F. Heinz, and J. A. Misewich, “High-speed electrical sampling using optical second-harmonic generation,” *Appl. Phys. Lett.* **69**, pp. 746-748, 1996.

[33] M. Nagel, C. Meyer, H. M. Heiliger, T. Dekorsy, H. Kurz, R. Hey, and K. Ploog, “Optical second-harmonic probe for ultra-high frequency on-chip interconnects with benzocyclobutene,” *Appl. Phys. Lett.* **72**, pp. 1018-1020, 1998.

[34] A. C. Davidson and F. W. Wise, “Picosecond photoconductive sampling with nanosecond carrier lifetimes using an integrated inductive loop,” *Appl. Phys. Lett.* **66**, pp. 2259-2261, 1995.

[35] D. H. Auston, “Impulse response of photoconductors in transmission lines,” *IEEE J. Quantum Electron.* **19**, pp. 639-648, 1983.

[36] D. H. Auston, “Ultrafast optoelectronics,” in *Ultrashort Laser Pulses and*

Applications, W. Kaiser, Ed., (Springer, Berlin, 1988), pp. 183-233.

[37] R. H. Jacobsen, P. Uhd Jepsen, S. R. Keiding, B. H. Larsen, and T. Holst, "Photoconductive sampling of subpicosecond pulses using mutual inductive coupling in coplanar transmission lines," *J. Appl. Phys.* **80**, pp. 4214-4216, 1996.

[38] R. K. Lai, J. R. Hwang, J. Ness, T. B. Norris, and J. F. Whitaker, "A fiber-mounted, micromachined photoconductive probe with 15 nV/Hz$^{1/2}$ sensitivity," *Appl. Phys. Lett.* **69**, pp. 1843-1845, 1996.

[39] J. A. Valdmanis and G. Mourou, "Subpicosecond electrooptic sampling: principles and applications," *IEEE J. Quantum Electron.* **22**, pp. 69-78, 1986.

[40] B. H. Kolner and D. M. Bloom, "Electro-optic sampling in GaAs integrated circuits," *IEEE J. Quantum Electron.* **22**, pp. 79-93, 1986.

[41] K. J. Weingarten, M. J. W. Rodwell, and D. M. Bloom, "Picosecond optical sampling of GaAs integrated circuits," *IEEE J. Quantum Electron.* **24**, pp. 198-220, 1988.

[42] Subsequent attempts have employed a back-etching process to thin the wafer. This alternative technique eliminates the need for wafer grinding and polishing.

[44] M. Maeda, "An analysis of gap in microstrip transmission lines," *IEEE Trans. Microwave Theory Tech.* **20**, pp. 390-396, 1972.

[45] J. F. Whitaker, T. B. Norris, G. Mourou, and T. Y. Hsiang, "Pulse dispersion and shaping in microstrip lines," *IEEE Trans. Microwave Theory Tech.* **35**, pp. 41-47, 1987.

[46] Y. Qian and E. Yamashita, "Phase compensation and waveform reshaping of picosecond electrical pulses using dispersive microwave transmission lines," *IEEE Trans. Microwave Theory Tech.* **39**, pp. 924-929, 1991.

[47] H. Roskos, M. C. Nuss, K. W. Goossen, D. W. Kisker, A. E. White, K. T. Short, D. C. Jacobson, and J. M. Poate, “Propagation of picosecond electrical pulses on a silicon-based microstrip line with buried cobalt silicide ground plane,” *Appl. Phys. Lett.* **58**, pp. 2604-2606, 1991.

[48] The program employed is Agilent Technologies’ AppCAD Version 3.0.2.

[49] S. S. Gevorgian, “Microwave conductivity of optically-excited gap in a semiconductor microstrip,” *Electron. Lett.* **26** , pp. 1921-1922, 1990.

[50] D. E. Aspnes and A. A. Studna, “Dielectric functions and optical parameters of Si, Ge, GaP, GaAs, GaSb, InP, InAs, and InSb from 1.5 to 6.0 eV,” *Phys. Rev. B* **27**, pp. 985-1009, 1983.

[51] R. K. Hoffmann, *Handbook of Microwave Integrated Circuits*, (Artech House, Norwood, MA, 1987), pp. 362-366.

[52] D. S. Phatak and A. P. Defonzo, “Dispersion characteristics of optically excited coplanar striplines: Pulse propagation,” *IEEE Trans. Microwave Theory Tech.* **38**, pp. 654-661, 1990.

[53] J.-H. Son, H.-H. Wang, J. F. Whitaker, and G. A. Mourou, “Picosecond pulse propagation on coplanar striplines on lossy semiconductor substrates: Modeling and experiments,” *IEEE Trans. Microwave Theory Tech.* **41**, pp. 1574-1579, 1990.

[54] H.-M. Heiliger, M. Nagel, H. G. Roskos, H. Kurz, F. Schnieder, W. Heinrich, R. Hey, and K. Ploog, “Low-dispersion thin-film microstrip lines with cyclotene (benzocyclobutene) as dielectric medium,” *Appl. Phys. Lett.* **70**, pp. 2233-2235, 1997.

[55] E. S. Weibel, “High power rf pulse generator,” *Rev. Sci. Instrum.* **35**, pp. 173-175, 1964.

[56] J. M. Proud Jr. and S. L. Norman, “High-frequency generation using optoelectronic switching in silicon,” *IEEE Trans. Microwave Theory Tech.* **26**, pp. 137-140, 1978.

[57] C. H. Lee, “Picosecond optics and microwave technology,” *IEEE Trans. Microwave Theory Tech.* **38**, pp. 596-607, 1990.

[58] J. B. Thaxter and R. E. Bell, “Experimental 6-GHz frozen wave generator with fiber-optic feed,” *IEEE Trans. Microwave Theory Tech.* **43**, pp. 1798-1803, 1995.

[59] Y. Pastol, G. Arjavalingam, J. M. Halbout, and G. V. Kopcsay, “Characterization of an optoelectronically pulsed broadband microwave antenna,” *Electronic Lett.* **24**, pp. 1318-1319, 1988.

[60] M. L. Forcier, M. F. Rose, L. F. Rinehart, and R. J. Gripshover, “Frozen-wave Hertzian generators: Theory and applications,” 2nd *IEEE International Pulsed Power Conference Digest of Technical Papers* (Institute of Electrical and Electronics Engineers, New York, 1979), vol. 2, pp. 221-225.

[61] R. W. McGowan and D. Grischkowsky, “Experimental time-domain study of THz signals from impulse excitation of a horizontal surface dipole,” *Appl. Phys. Lett.* **74**, pp. 1764-1766, 1999.

[62] J. D. Kraus, *Antennas*, 2nd edition, (McGraw-Hill, New York, 1988), pp. 200-213.

[63] N. Engheta, C. H. Papas, and C. Elachi, “Radiation patterns of interfacial antennas,” *Radio Sci.* **17**, pp. 1557-1566, 1982.

[64] K. A. McIntosh, E. R. Brown, K. B. Nichols, O. B. McMahon, W. F. DiNatale, and T. M. Lyszczara, “Terahertz measurements of resonant planar antennas coupled to low-temperature-grown GaAs photomixers,” *Appl. Phys. Lett.* **69**, pp. 3632-3634, 1996.

CHAPTER 3.0

GENERATION AND DETECTION OF FREE-SPACE TERAHERTZ WAVEFORMS

3.1 Background

The concept of PC switching was introduced in Chapter 2.0 through the techniques of PC self-switching and PC frozen wave generation. It was shown that THz electrical waveforms could be generated on both microstrip and coplanar transmission lines with these techniques. It is interesting to note, however, that the generation process behind the formation of these ultrafast electrical waveforms will also result in the generation of free-space THz transients in the far-field regime of the PC device. Indeed, the acceleration of semiconductor charge carriers in the biased PC gap produces a time-varying photo-current, which, in turn, leads to a far-field THz waveform. The amplitude, shape, and duration of this THz transient is, therefore, intimately linked to the charge carrier dynamics in the semiconductor electron-hole plasma.

The idea of using PC switching [1] to generate free-space THz waveforms was first put to the test by Mourou et al. in 1981 [2]. By applying the ultrafast switching principles of PC excitation to the goal of X-band gigahertz signal transmission (with microwave dipole antenna transmitters and receivers) [3], the researchers were able to generate and detect the THz transients over distances much greater than the emission wavelength (the transients are, therefore, defined as far-field radiative THz emission). Since this pioneering work, efforts at PC free-space THz generation have continued, being motivated largely by a desire to produce electromagnetic transients with shorter pulse durations, broader bandwidths, and larger amplitudes. A major advancement in this drive was the successful integration of the PC generation process and the THz emission process into one device by Auston et al. in 1984 [4]. These researchers showed that THz electromagnetic pulses could be radiated directly from the PC medium, eliminating the need for microwave antenna transmission structures. Pulse broadening and signal attenuation effects that are associated with the transmission line structures and dipole radiators are, therefore, no longer present. Instead, the acceleration of electrons and holes in the semiconductor itself produces a time-varying photo-current whose ultrafast response leads to far-field THz radiation (the PC response of the semiconductor need not be on an ultrashort timescale, however, as the profile of the THz waveform in the far-field is prescribed by the *time derivative* of the photo-current). Using this direct technique, it was shown by Auston et al. [4], that freely propagating 1.6 ps electromagnetic waveforms could be generated and detected on opposite sides of a 1 mm thick alumina substrate. Since this time, investigations into direct PC THz emission have continued, driven by a desire to produce increasingly large THz powers. To date, researchers have been able to generate free-space THz beams with average powers up to 40 μW by simply increasing the size of the PC THz emitter, the bias voltage across the PC gap, and the intensity of the optical pump pulse [5].

It is important to note that, in addition to PC THz generation schemes, other THz emission techniques do exist. Of these alternative techniques, nonresonant free-space THz generation has become quite popular. Nonresonant free-space THz generation schemes, unlike PC THz generation, do not rely upon resonant absorption and free carrier generation in semiconductors. Instead, these techniques make use of the exceedingly high peak powers associated with ultrafast laser sources to initiate a nonlinear polarization response in crystalline media [6]. Optical rectification, for example, is a nonlinear mixing technique that makes use of a second-order EO medium [7]. Upon illumination, the second-order nonlinear polarization of the crystal responds with both a second-harmonic response (at twice the frequency of the optical pump beam) and a quasi-static (optical rectification) response [8]. The use of a pulsed laser source, in this case, truncates the duration of the quasi-static nonlinear response, however, forming a subpicosecond (THz) electromagnetic transient whose electric field closely follows the intensity envelope of the incident optical pulse. Ultra-broadband electromagnetic pulses with frequency components up to 41 THz have been generated using this technique [9].

Nonlinear THz generation schemes such as optical rectification are able to produce electromagnetic transients with ultrashort pulse durations and extremely broad THz bandwidths. These techniques are, however, limited in their ability to be scaled to large amplitudes. Unlike PC THz generation (where the spot size and intensity of the pump beam can be simply increased to amplify the THz power), optical rectification is fundamentally limited to pump powers below which free carrier absorption occurs. Under high enough optical fluences, large-bandgap nonlinear materials (such as ZnTe) will liberate electron-hole pairs through two-photon absorption. This will, in turn, screen the nonlinear THz polarization response of the medium. For this reason, nonlinear mixing techniques such as optical rectification are most commonly employed in THz applications requiring large THz bandwidths (such as charge carrier pump-probe dynamical studies) [10], while PC generation processes are most commonly employed in THz applications requiring large THz powers (such as THz-ray imaging [11] and time-domain material spectroscopy) [12].

The work that follows in this chapter will continue the development of PC THz emitters. After a brief introduction to the free-space THz generation and detection experimental system employed in this investigation (section 3.2), some of our recent work [13] related to the theoretical and experimental aspects of a ZnSe THz emitter will be introduced (in section 3.4) and compared to that of a conventional GaAs THz emitter (in section 3.3). It will be shown that the use of a ZnSe PC medium allows for the production of THz pulses with both a large amplitude (through scaling of the bias field) and a wide THz bandwidth (through the use of ultrafast two-photon absorption). Furthermore, it will be shown through some of our recent work [14], that both crystalline and polycrystalline ZnSe can be used for the efficient *detection* of free-space THz radiation (section 3.5). The large EO coefficient, small THz-probe group velocity mismatch, and ease of substrate fabrication make these ZnSe sensors particularly attractive for the detection of free-space THz transients.

3.2 The Generation and Detection System

Much like the THz electrical transients generated in Chapter 2.0, the free-space THz waveforms produced in this section are generated by optical excitation of a biased PC gap and detected by an EO crystal. Unlike the previous section, however, the photo-generated waveform does not propagate on a transmission line structure. Rather, it is made to radiate directly into free-space, where it is sampled in the far-field by a free-space EO detector. As with the THz electrical waveforms, time-domain images of these free-space THz waveforms are formed through the use of a time-resolved generation and detection process incorporating both an optical pump beam and an optical probe beam. By varying the relative delay between the THz excitation mechanism (initiated by the pump pulse) and the EO sampling process (initiated by the probe pulse) the time-resolved THz waveform is measured.

The complete layout for the time-resolved system is shown in figure 3.2.1. The relative time-delay between the pump and probe beams is set by the pump beam, whose arrival time is controlled by the pico- and femto-motor delay lines. The larger pico-motor translates forward in 12 μm steps, providing a coarse 80 fs resolution for the scan, while the femto-motor translates forward in 70 nm steps, providing a fine 0.463 fs resolution for the scan. The use of both a coarse delay line and a fine delay line, in this case, allows for a rapid determination of the zero-time with the pico-motor and a fine temporal resolution with the femto-motor.

The experimental setup for the generation and detection of free-space THz waveforms must be able to efficiently couple the emitted radiation from the THz source into the EO sensor. Moreover, the setup must allow the radiated THz beam to travel from

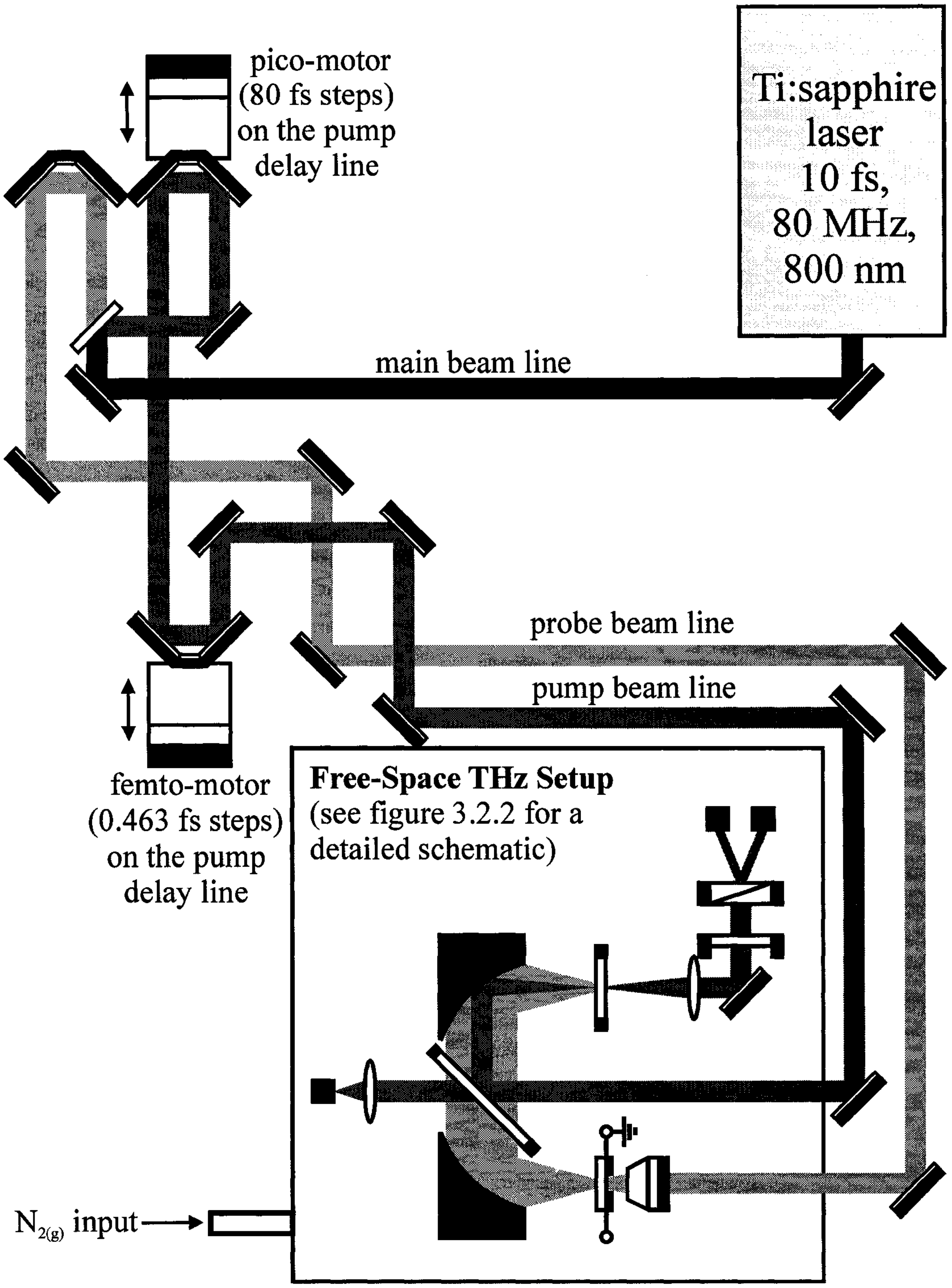

Figure 3.2.1 The complete time-resolved setup for the generation and detection of free-space THz radiation. The main beam from the laser is split into the pump and probe beams by the first beamsplitter. The optical delay for the time-resolved scans is provided by the pico- and femto-motor delay arms. A detailed schematic of the free-space THz setup is shown in figure 3.2.2.

the generator to the detector without passing through highly absorptive or highly dispersive optical elements. To accommodate these constraints, the experimental setup shown in figure 3.2.2 is implemented. Initiation of the free-space THz generation process is accomplished by focusing the optical pump pulse onto the PC THz emitter. The resulting photo-induced carriers are then accelerated by an externally applied bias field. To facilitate high-frequency lock-in detection, a square-wave bias voltage signal at a frequency of 54 kHz is used (rather than a DC voltage). In doing this, the large acoustic-frequency and laser noise levels associated with low-frequency laser measurements are avoided, and the signal-to-noise ratio of the system is increased. The resulting THz radiation that is emitted from the PC gap is collected and collimated next by a 5 cm focal length, 5 cm diameter (f/1.0) parabolic mirror. The THz beam is then overlapped with the near-infrared probe beam by way of a 1" diameter, 2 μm thick pellicle beamsplitter, and the two beams are focused by a second 5 cm focal length, 5 cm diameter (f/1.0) parabolic mirror onto the THz EO detector.

The THz detection process incorporated in the experimental setup is based upon the second-order EO nonlinearity in non-centrosymmetric materials. Indeed, by passing the co-propagating THz and probe beams through an electro-optically-active crystal, the magnitude of the THz electric field can be mapped onto the polarization state of the probe [15]. This THz-induced birefringence is measured subsequently, by directing the probe beam into a quarter waveplate and wallaston prism pair (identical to the polarization-sensitive detection system incorporated in section 2.2). Here, the slow axis and the fast axis of the quarter waveplate are aligned at a 45^0 angle off the incident probe polarization, and the two transmission axes of the wallaston prism are aligned parallel

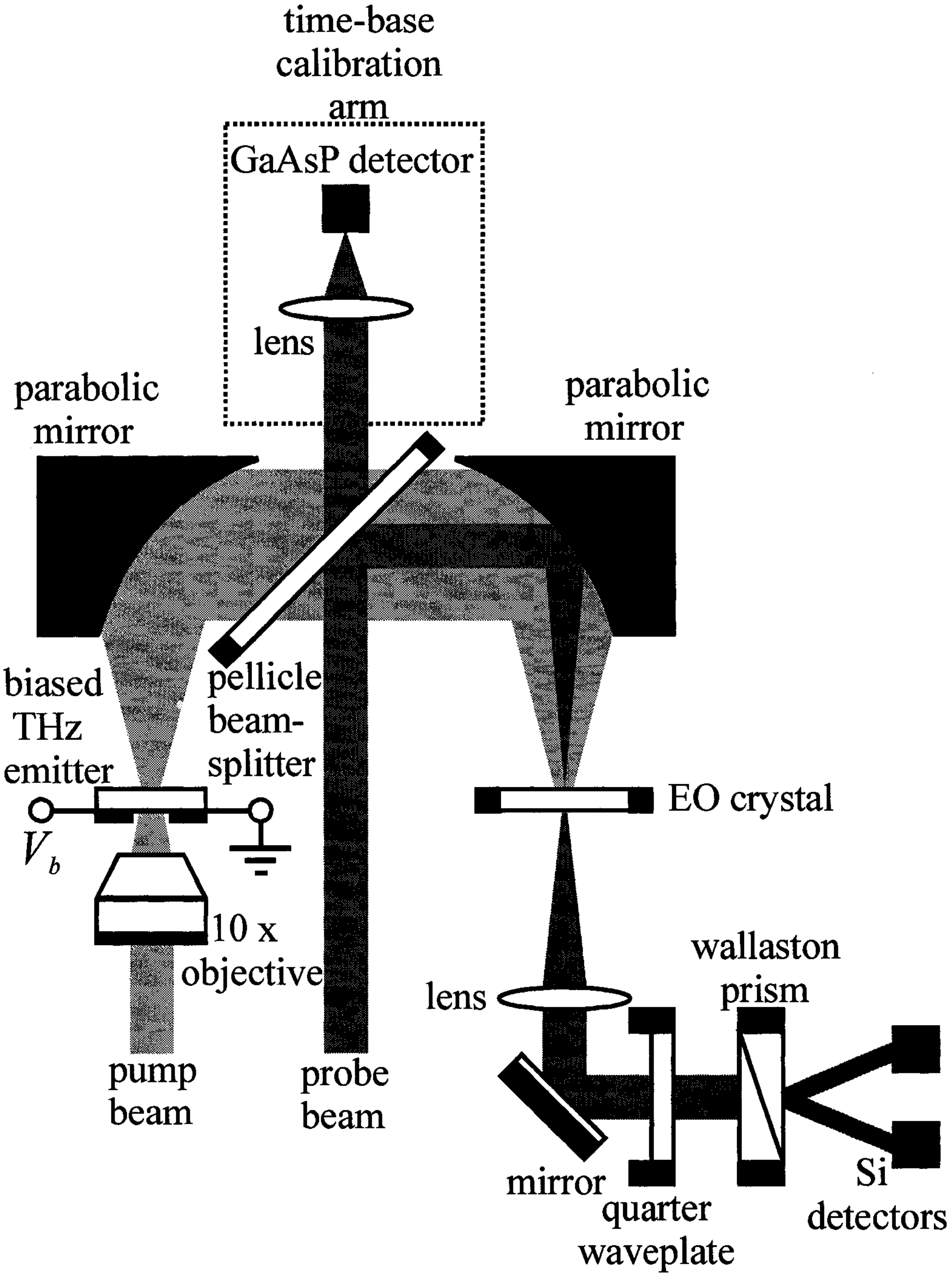

Figure 3.2.2 The setup for the generation and detection of free-space THz radiation. The pump beam excites the PC switch, generating THz radiation. A confocal arrangement of parabolic mirrors overlaps the THz beam with the probe beam and focuses them into the EO crystal.

and perpendicular to the incident probe polarization. With the measurement optics oriented in this way, the degree of polarization ellipticity of the probe (and therefore the probe power difference between the orthogonally-polarized beams exiting the wallaston prism) remains linearly proportional to the magnitude of the THz electric field [16]. Finally, the probe power difference between the beams exiting the wallaston prism is monitored by two Si photodetectors (Vishay Telefunken, Si PIN Photodiodes, BPW34). The resulting photo-currents are electronically differenced and then amplified (47000 V/A) by the transimpedance amplifier shown in Appendix G [5]. The resulting THz signal is then filtered by a Stanford Research Systems SR560 low-noise preamplifier and a Stanford Research Systems SR830 DSP lock-in amplifier and recorded by LabVIEW software on a personal computer.

To implement the THz generation and detection system described above, the far-infrared THz beam must be aligned precisely with the optical path of the near-infrared probe beam–a point which is further complicated by the fact that the far-infrared THz beam is not visible to the naked eye. To overcome these alignment issues, the biased THz emitter is temporarily removed from the system, and the microscope objective is positioned in a confocal arrangement with the first parabolic mirror (this allows the optical pump beam to pass through the system, tracing the path of the THz beam). Using this modified optical system, the first parabolic mirror and the pellicle beamsplitter are positioned to provide near perfect overlap between the collimated pump beam and the probe beam. Having achieved this, the two beams are focused onto a CCD array by the second parabolic mirror, and the alignment of this mirror is optimized while the image at its focal plane is monitored. The entire system is aligned when the CCD image shows that the pump and probe spots are both minimized and perfectly overlapped.

While the alignment procedure described above seeks to provide precise spatial overlap between the pump and probe beams, it is equally important to provide a temporal overlap between the pump and probe pulses (as the time-resolved process used to map the time-domain THz waveform is based upon the relative delay between the pump and probe pulses). To measure this zero-time for the system, the time-base calibration arm shown in figure 3.2.2 is employed. This calibration arm samples the pump and probe beams as they pass through the pellicle beamsplitter and focuses them onto a GaAsP photodiode. The bandgap of the GaAsP semiconductor used in the detector (E_g = 1.8 eV) is large enough that two 1.5 eV photons are required to complete the transition from the valence band to the conduction band. The two-photon photo-current generation process initiated by this nonlinear interaction (described in detail in Appendix H) produces a time-resolved optical correlation between the pump and probe pulses–the maximum value of which gives the zero-time for the system. To finalize the THz setup, the pump delay line is positioned at this zero-time, and the THz emitter and EO detector are returned to their respective positions in the setup.

3.3 GaAs Photoconductive Terahertz Emitters

3.3.1 Theoretical Framework

PC generation of free-space THz radiation is fundamentally based upon the acceleration of semiconductor charge carriers. When an ultrashort optical pulse strikes a biased PC gap, the photo-generated electrons and holes accelerate in the externally applied electric field, and the resulting time-varying current produces THz radiation. If the PC generation mechanism is fast enough–on a subpicosecond timescale for instance–the frequency content of the radiated field can span into the THz frequency-domain. To obtain a high THz bandwidth and a large signal level, THz radiation sources often employ a semi-insulating GaAs substrate for the PC medium [5]. The high carrier mobility (3000 $cm^2/V{\cdot}s$) and large dark resistivity (10^7 $\Omega{\cdot}cm$) of this semiconductor make it an attractive candidate for the generation and acceleration of the photo-induced charge carriers. Consequently, the experimental testing and optimization procedures carried out in this section study the operation of a conventional GaAs PC THz emitter.

To fully realize the potential of the GaAs PC THz source it is important to have a fundamental understanding of the physical processes behind the charge carrier motion in the substrate and the THz radiation in the far-field. As such, a model of the temporal and spatial charge carrier dynamics in the PC THz emitter is developed. The layout for the model is shown in figure 3.3.1.1. Here, photo-excitation of the biased PC gap is initiated by the optical pump pulse, whose intensity,

$$I(x,t) = \frac{E_p}{\tau_p}\exp\left[-4\ln 2\left(t-t_o\right)^2/\tau_p^2\right]\exp\left[-4\ln 2\left(x-x_o\right)^2/x_p^2\right], \qquad (3.3.1.1)$$

is a function of the pump energy fluence, E_p, the optical pulse duration, τ_p = 100 fs, the

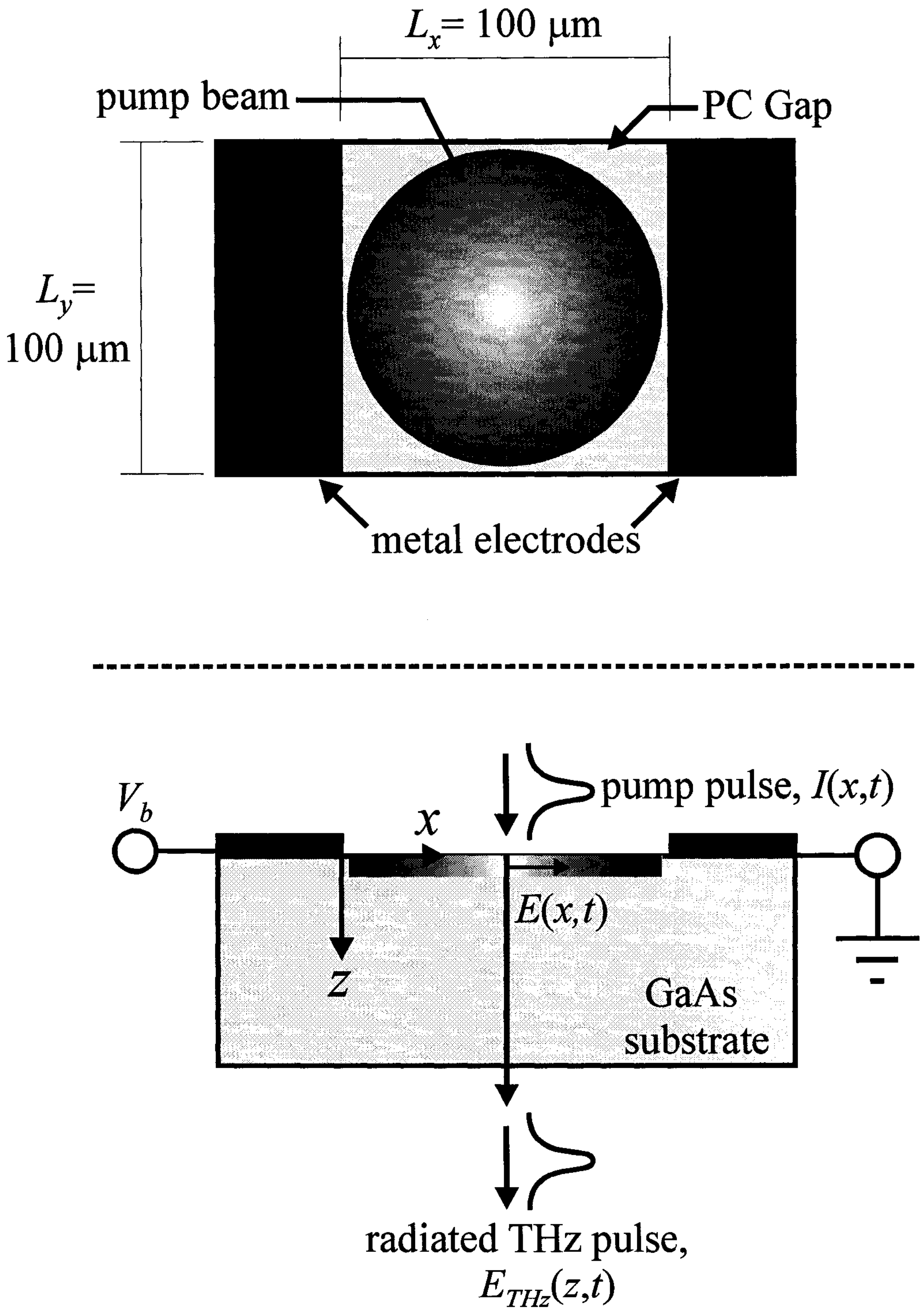

Figure 3.3.1.1 The schematic for the GaAs PC THz emitter. The optical pump pulse illuminates the entire PC gap, generating an electron-hole plasma. The subsequent acceleration of charge carriers produces the THz beam.

pump pulse arrival time, $t_o = 0$ ps, the pump spot diameter, $x_p = 100$ µm, and the pump beam centre, $x_o = 50$ µm. Excitation by the pump pulse generates a surface distribution of electrons, $n_s(x,t)$, and holes, $p_s(x,t)$, in the semiconductor. The generation and subsequent acceleration of the electrons and holes follows the relations

$$\frac{\partial n_s(x,t)}{\partial t} = \frac{(1-R)}{h\nu} I(x,t) + \frac{1}{e}\frac{\partial k_n(x,t)}{\partial x} \tag{3.3.1.2}$$

and

$$\frac{\partial p_s(x,t)}{\partial t} = \frac{(1-R)}{h\nu} I(x,t) - \frac{1}{e}\frac{\partial k_p(x,t)}{\partial x}, \tag{3.3.1.3}$$

respectively, where $R = 0.319$ is the reflectivity of the GaAs substrate, e is the electronic charge, h is Planck's constant, $\nu = 375$ THz is the central frequency of the optical photons, $k_n(x,t)$ is the electron surface current density, and $k_p(x,t)$ is the hole surface current density [17]. The units of $n_s(x,t)$ and $p_s(x,t)$ are cm^{-2}, while the units of $k_n(x,t)$ and $k_p(x,t)$ are C·s^{-1}·cm^{-1}·. Being that the hole mobility in GaAs (μ_p = 400 cm^2/V·s) is substantially lower than the electron mobility (μ_n = 3000 cm^2/V·s), the hole surface current density is assumed to be negligible for this investigation ($k_p(x,t) = 0$). As such, equation 3.3.1.3 is simplified and solved algebraically to give a surface hole distribution of

$$\begin{aligned} p_s(x,t) = {} & \sqrt{\frac{\pi}{16\ln 2}}\,\frac{(1-R)}{h\nu} E_p \left\{1 + erf\left[\frac{2\sqrt{\ln 2}\,(t-t_o)}{\tau_p}\right]\right\} \\ & \times \exp\left[\frac{-4\ln 2\,(x-x_o)^2}{x_p^2}\right]. \end{aligned} \tag{3.3.1.4}$$

Next, the electron surface current density, $k_n(x,t)$, is coupled to the electric field within the PC gap, $E(x,t)$, by matching the forward-traveling THz electric and magnetic fields in the GaAs substrate,

$$\vec{E}_1(x,z,t) = E_{01}(x,t)\exp[i(\omega\, t - k_1 z)]\hat{x} \tag{3.3.1.5}$$

and

$$\vec{B}_1(x,z,t) = \frac{E_{01}(x,t)\sqrt{\varepsilon_r}}{c}\exp[i(\omega\, t - k_1 z)]\hat{y}, \tag{3.3.1.6}$$

to the backward-traveling THz electric and magnetic fields in the air,

$$\vec{E}_2(x,z,t) = E_{02}(x,t)\exp[i(\omega\, t + k_2 z)]\hat{x} \tag{3.3.1.7}$$

and

$$\vec{B}_2(x,z,t) = \frac{-E_{02}(x,t)}{c}\exp[i(\omega\, t + k_2 z)]\hat{y}, \tag{3.3.1.8}$$

with the appropriate boundary conditions. Matching the tangential electric fields and the tangential magnetic fields at the $z = 0$ surface yields

$$E_{01}(x,t) = E_{02}(x,t) \tag{3.3.1.9}$$

and

$$\frac{\vec{B}_1(x,z=0,t)}{\mu_0} - \frac{\vec{B}_2(x,z=0,t)}{\mu_0} = k_n(x,t)\hat{x}\times\hat{z}, \tag{3.3.1.10}$$

respectively. Equations 3.3.1.5-3.3.1.10, together, can be expressed as

$$E_{01}(x,t)\left(1+\sqrt{\varepsilon_r}\right) = -\mu_0 c k_n(x,t) = -\mu_0 c \mu_n e n_s(x,t)\left[E_{01}(x,t) + E(x,t)\right]. \tag{3.3.1.11}$$

Here, c is the speed of light, ω is the frequency of the THz waves, k_1 is the forward traveling wavevector in the GaAs substrate, k_2 is the backward traveling wavevector in the air, μ_0 is the permeability of free-space, and $\varepsilon_r = 13.1$ is the dielectric constant of GaAs [15]. By solving for $E_{01}(x,t)$ and inserting it into the expression above for $k_n(x,t)$, the electron surface current density is found to be [17]

$$k_n(x,t) = \frac{\mu_n e n_s(x,t) E(x,t)}{1 + \left(1 + \sqrt{\varepsilon_r}\right)^{-1} \mu_n e c \mu_0 n_s(x,t)}. \tag{3.3.1.12}$$

Equation 3.3.1.12 demonstrates that large surface electron densities can saturate the current in the PC gap if the second term in the denominator becomes sufficiently large. This near-field THz screening mechanism arises from the fact that the direction of the THz electric field in the semiconductor, $\vec{E}_1(x,z,t)$, is in the opposite direction to the applied bias field; thus a large THz field can counteract the applied bias field. By exciting with increasingly large electron densities, this THz screening mechanism becomes more pronounced, and the magnitude of the THz radiation becomes saturated.

For the next step, the internal charge carrier dynamics of the semiconductor are tied to the time-varying field in the PC gap through the application of Poisson's equation,

$$\frac{\partial E(x,t)}{\partial x} = \frac{e}{\delta \varepsilon_r \varepsilon_o}\left[p_s(x,t) - n_s(x,t)\right]. \tag{3.3.1.13}$$

Here, $\delta = 0.74$ μm is the penetration depth of the 800 nm optical radiation [18], and ε_o is the permittivity of free-space. As with the near-field THz screening mechanism described above, Poisson's equation demonstrates that large electron-hole densities can also shield the external bias field. The acceleration of electrons and holes in opposite directions produces an internal field within the semiconductor in a direction opposite to that of the applied field. At high carrier densities this space-charge screening mechanism limits the overall photo-current in the gap and saturates the amplitude of the emitted THz radiation. For maximum efficiency, therefore, it is important to keep the THz emitter operating in a regime that is not limited by near-field THz screening or space-charge screening.

As a final step in the analysis of the PC THz emitter, the internal charge carrier dynamics in the semiconductor are related to the THz electric field strength in the far-field. This is done by summing the far-field radiation produced by the time- and space-varying electron surface currents within the PC gap. The resulting THz electric field can be expressed as [17]

$$E_{THz}(z,t) = \frac{L_y}{4\pi\varepsilon_o c^2 z} \frac{d}{dt} \int_0^{L_x} k_n(x,t)dx, \tag{3.3.1.14}$$

where $L_y = 100$ μm is the width of the gap in the y direction, $L_x = 100$ μm is the length of the gap in the x direction, and z is the propagation distance of the THz far-field pattern.

To implement the theoretical model, equations 3.3.1.1-3.3.1.4 and 3.3.1.12-3.3.1.14 are solved numerically for the far-field THz electric field, $E_{THz}(z,t)$, given a bias field strength of $E_b = 2$ kV/cm. The results are shown in figure 3.3.1.2, while the numerical method employed in solving these equations is described in detail in Appendix I. At the lowest pump energy fluence ($E_p = 0.016$ μJ/cm^2) a unipolar THz waveform is witnessed. The fact that the far-field THz pattern is related to the PC current through a temporal derivative suggests that, in this case, the electron surface current density, $k_n(x,t)$, follows a step-like response and is, therefore, proportional to the surface electron density, $n_s(x,t)$ (which is itself step-like in nature due to the long carrier lifetime in semi-insulating GaAs). Evidently, for a low photo-injection regime such as this (with a surface charge carrier density of only $n_s = 5 \times 10^{14}$ cm^{-2}), the strength of the induced space-charge field is minimal, and the carriers accelerate under a constant bias field–suggesting that little space-charge screening is introduced in the emitter.

To investigate the relationship between the pump energy fluence and the shape of the THz waveform, E_p is increased to 0.40, 0.80, 3.18, and 25.5 μJ/cm^2. The resulting free-space THz pulses calculated from the model are shown in figure 3.3.1.2. It is readily

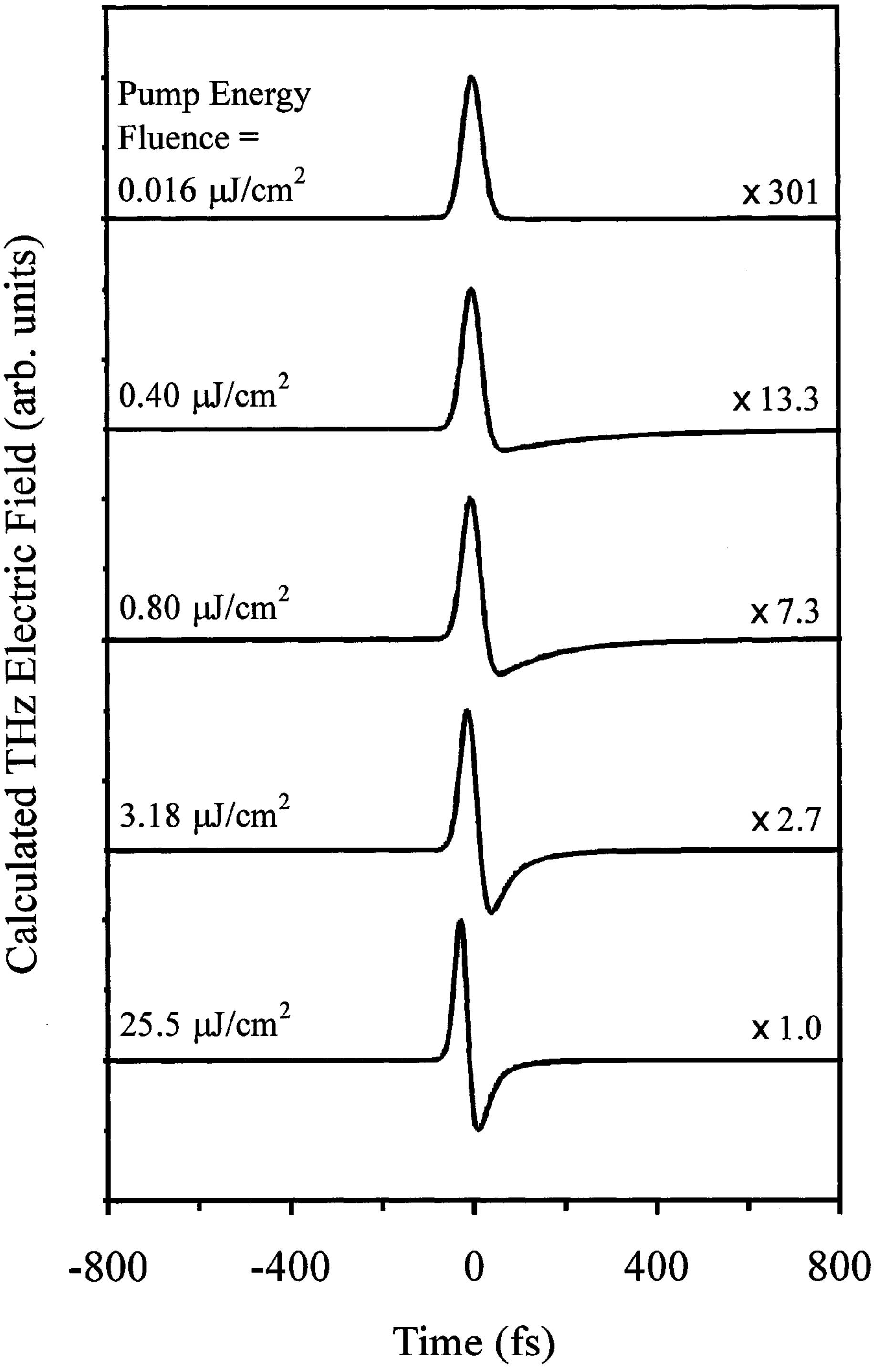

Figure 3.3.1.2 Normalized theoretical time-domain waveforms for the GaAs PC THz emitter, given pump energy fluences of 0.016, 0.40, 0.80, 3.18, and 25.5 μJ/cm². The PC gap and pump spot diameter are 100 μm wide, and the model includes both space-charge and near-field THz screening.

apparent from the figure that increasing the pump energy fluence significantly changes the shape of the waveform. In going from an energy fluence of 0.016 μJ/cm^2 to an energy fluence of 25.5 μJ/cm^2, the overall THz waveform evolves from its original unipolar profile to that of a bipolar profile. This evolution suggests that the current within the PC gap no longer takes the form of a simple step-like response. Instead, a process of acceleration and deceleration is incurred as the photo-injected carriers are accelerated by the bias field then decelerated by the induced space-charge field. In this way, the space-charge screening effect counteracts the applied bias field and decreases the current within the PC gap [19]. The resulting THz far-field pattern–which is related to the derivative of the current in the gap–shows a bipolar structure with both a positive lobe (due to the initial acceleration) and a negative lobe (due to the subsequent deceleration). At the highest energy fluence, E_p = 25.5 μJ/cm^2, this carrier screening process becomes pronounced, and the bipolar nature of the THz waveform becomes quite prominent.

The screening mechanisms induced at high carrier densities affect the amplitude of the resulting THz waveform as well as its overall shape. This point is illustrated by figure 3.3.1.3, which shows the peak-to-peak THz amplitudes as a function of the incident pump energy fluence. At pump fluences below 0.8 μJ/cm^2, the response to an increasing energy fluence is largely linear. The lack of space-charge screening and near-field THz screening in this regime maintains the overall linearity between the pump power, the carrier density, the surface current, and the emitted THz field strength. When the pump energy fluence is increased beyond 0.8 μJ/cm^2, however, the space-charge field and the THz field begin to screen the external bias field. The presence of these screening mechanisms manifests itself as both a transformation of the overall waveform profile and

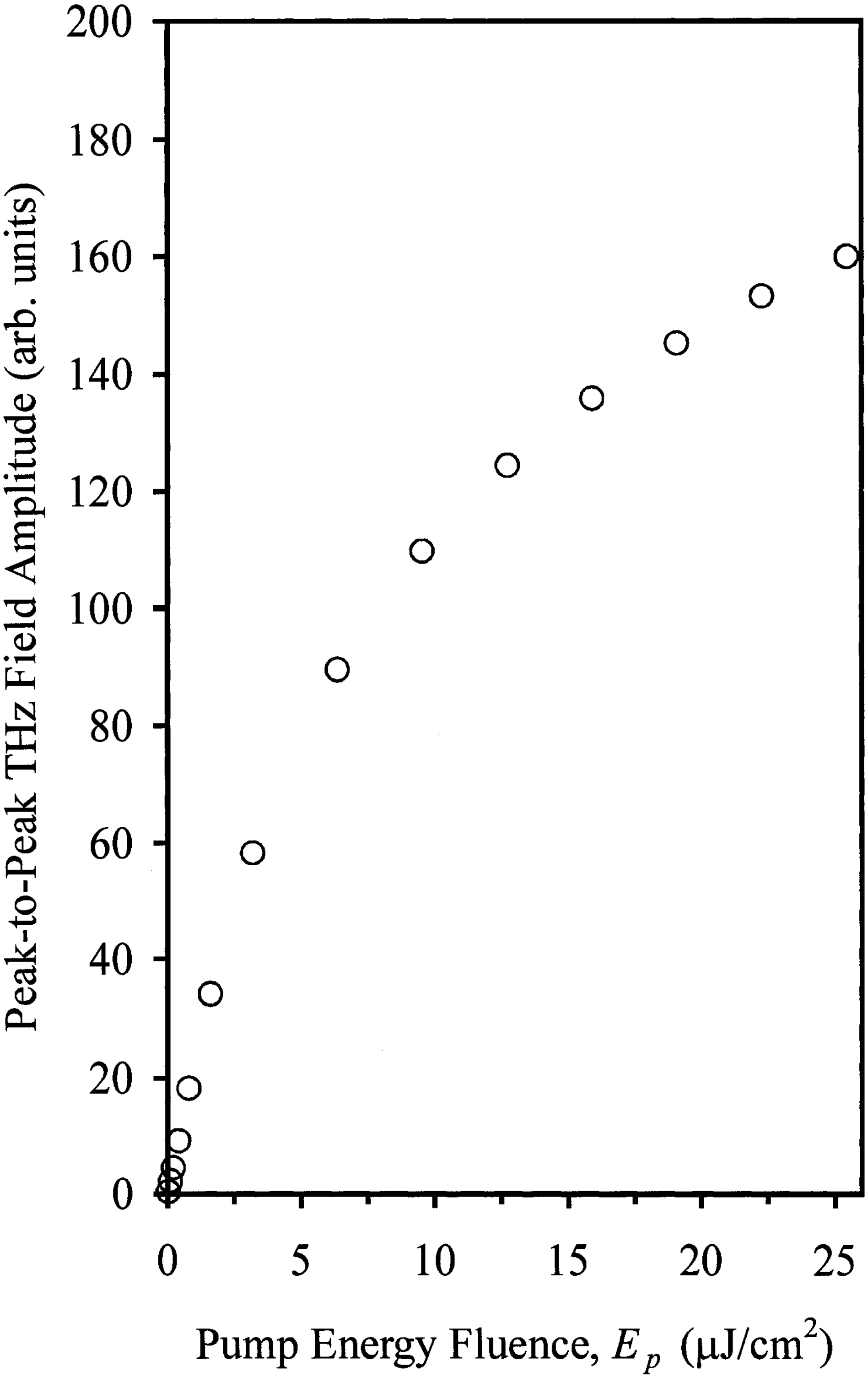

Figure 3.3.1.3 Calculated peak-to-peak THz amplitudes as a function of the pump energy fluence for the GaAs PC THz emitter. The PC gap and the pump spot diameter are 100 μm wide, the bias electric field is $E_b = 2$ kV/cm, and the model includes both space-charge and near-field THz screening.

a decrease in the THz amplitude. By increasing the pump energy fluence beyond 25.5 μJ/cm^2, the THz amplitude is found to be largely saturated. Clearly, if GaAs is to be used for the emission of high-power THz beams, techniques other than simply scaling up the injected pump energy must be employed.

3.3.2 Experimental Framework

To test the operational capabilities of GaAs THz sources, the GaAs THz emitter analyzed in the previous section is designed and built. The emitter is tested using the free-space THz detection system introduced in section 3.2. Illumination of the 100 μm wide GaAs PC emitter is carried out by a 160 mW pump beam (corresponding to a pump energy fluence of E_p = 25.5 μJ/cm^2), and a 500 μm thick <111> ZnSe crystal is placed in the focal plane of the second parabolic mirror to act as the EO sensor [20]. The 100 μm wide PC gap is biased by a 54 kHz, 40 $V_{p\text{-}p}$ AC signal (corresponding to a peak bias electric field strength of 2 kV/cm). A typical free-space THz waveform produced by this arrangement is shown in figure 3.3.2.1. Here, the vertical scale of the figure is presented in units of nanoamps (corresponding to the differential photo-current signal from the Si detectors), while the horizontal scale is presented in steps of 0.463 fs (corresponding to the time step of the femto-motor). The most striking feature of the figure is the bipolar nature of the electromagnetic pulse. This bipolar shape suggests that the 10^{18} cm^{-3} photo-induced carrier density induced by the pump pulse is large enough to drive the photo-current response into a space-charge screening regime–a point which is further supported by the theoretical calculations in section 3.3.1 for this energy fluence (E_p = 25.5 μJ/cm^2).

The electromagnetic pulse shown in figure 3.3.2.1 is characterized by a peak-to-

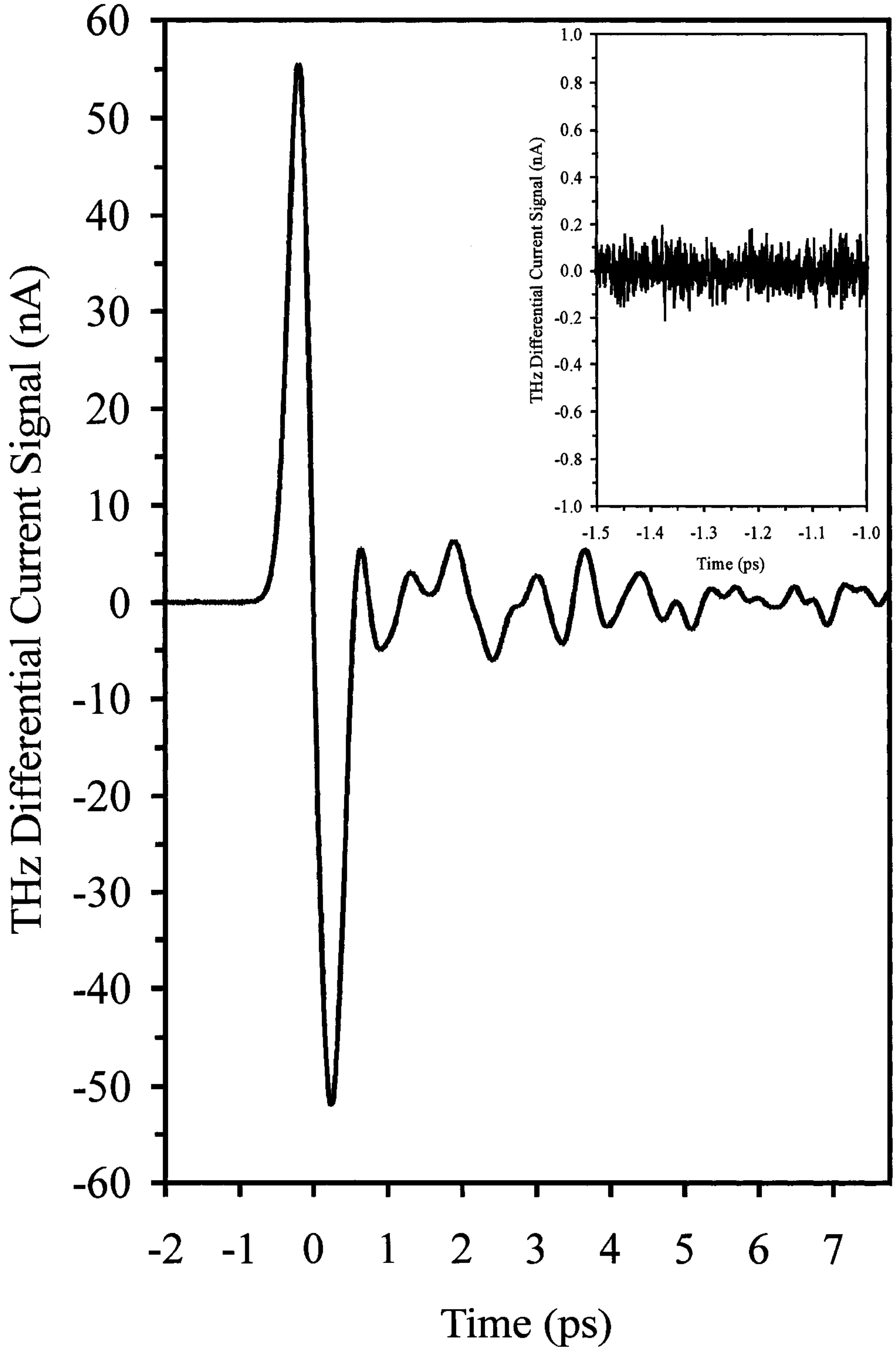

Figure 3.3.2.1 Free-space THz waveform generated by the 100 μm GaAs PC gap and detected by the 500 μm thick <111> ZnSe crystal. The gap is illuminated by a 160 mW pump beam (corresponding to a pump energy fluence of 25.5 μJ/cm^2). The inset shows a close-up of the noise level in the figure.

peak photo-current amplitude of 108 $nA_{p\text{-}p}$ and a signal-to-noise ratio of 720:1 (computed from the 0.15 $nA_{p\text{-}p}$ noise level shown in the inset). To transform this signal level to a differential probe power, the photo-current is divided by the 0.5 A/W responsivity of the BPW34 Si differential detectors to give a differential probe power of 216 nW for the beams exiting the wallaston prism. Using this differential probe power, along with a total probe power of P_{probe} = 6 mW, an EO coefficient of r_{41} = 2 pm/V, a refractive index of n_{ZnSe} = 2.5295 at 800 nm, and a crystal length of L = 500 μm, the peak-to-peak THz electric field is found to be E_{THz} = 3.47 $V_{p\text{-}p}$/cm. Finally, the instantaneous THz intensity,

$$I_{THz} = \frac{\sqrt{\varepsilon_{r,ZnSe}}}{2\eta_o}\left(\frac{E_{THz}}{2}\right)^2 = 12.1 \quad \text{mW/cm}^2, \tag{3.3.2.1}$$

is used to find the average power of the THz beam. For a 1 mm estimate of the THz spot size [21], a duty cycle of 10^{-4} (ratio of the 1 ps THz pulse duration over the 10 ns laser pulse-train period), and a dielectric constant of $\varepsilon_{r,ZnSe}$ = 9.2, the THz average power is found to be 10 nW. This value is comparable to that of similar GaAs PC THz systems.

An unusual attribute of the waveform presented in figure 3.3.2.1 is the oscillations found after the THz electromagnetic pulse. The fact that these oscillations are both reproducible and large in amplitude indicates that they cannot be attributed to random noise sources (unlike the small random noise fluctuations shown in the figure inset). The oscillatory nature of these features does, however, suggest that resonant THz absorption and subsequent re-radiation is occurring either in the EO crystal or in the air. To test this hypothesis, the free-space generation and detection setup is enclosed in a plexiglass housing, and dry nitrogen gas is pumped into the chamber. A photograph of the resulting THz system and its dry nitrogen chamber is shown in figure 3.3.2.2. Using this new

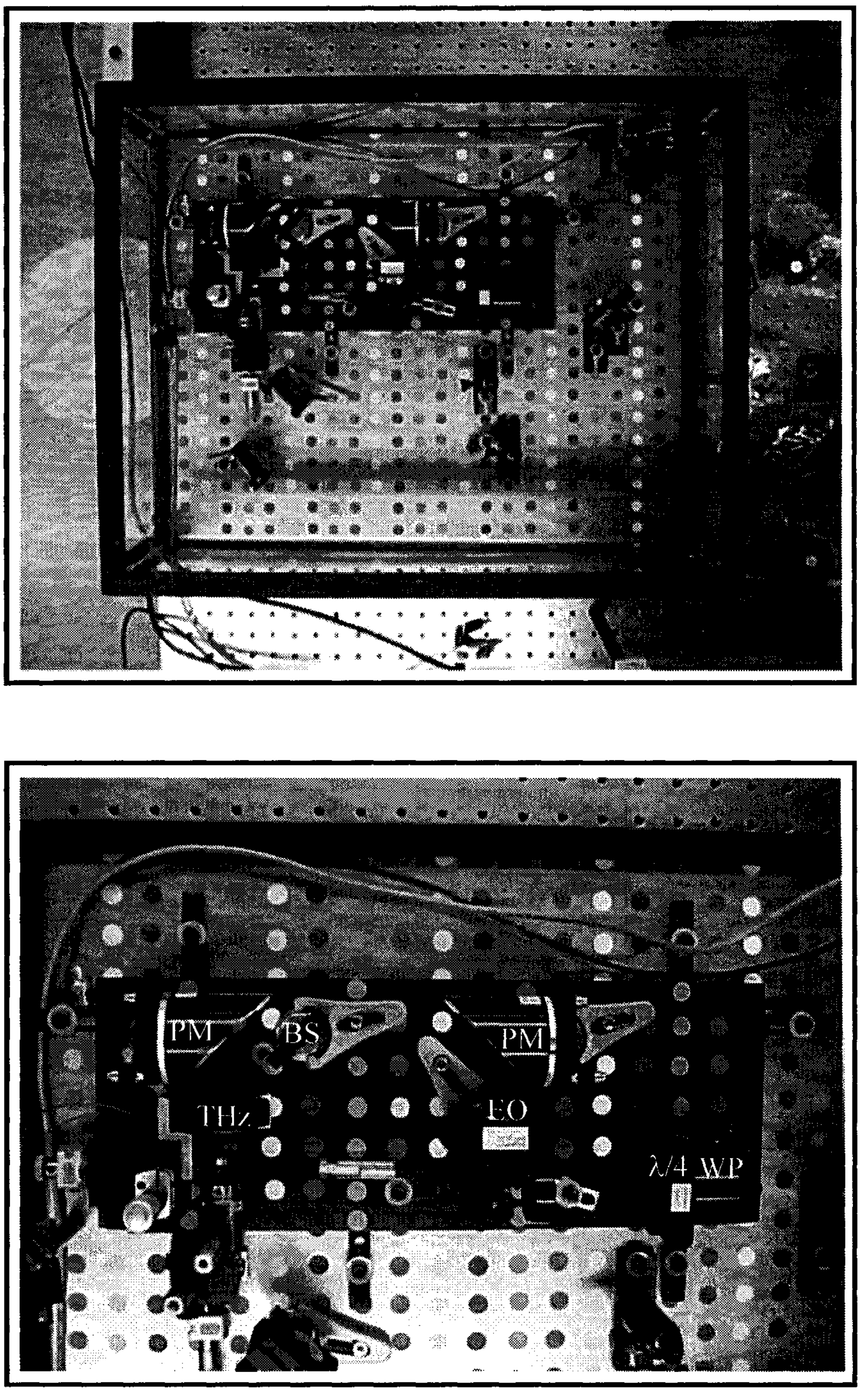

Figure 3.3.2.2 Photographs of the free-space THz generation and detection system. Here, PC is the PC THz emitter, PM is the parabolic mirror, BS is the pellicle beamsplitter, EO is the EO detector, $\lambda/4$ is the quarter waveplate, and WP is the wallaston prism.

enclosed system, the previous THz sampling experiment is repeated. Time-domain waveforms for both the atmospheric ambient (50% relative humidity) and the dry nitrogen ambient (1% relative humidity) are shown in figure 3.3.2.3, and the difference between these two waveforms is shown in the lower portion of the figure. It is readily apparent from these curves that the oscillations are significantly reduced by using the dry nitrogen ambient. This suggests that the oscillations are due to resonant absorption as the THz pulse propagates through the atmosphere (the small THz waveforms that occur at 9 ps are due to the reflection and subsequent re-sampling of the THz beam within the EO detector). To further understand the mechanisms behind this resonant absorption, the time-domain waveforms corresponding to the dry nitrogen ambient and the atmospheric ambient are Fourier transformed, and the absorption spectrum is computed (the absorption spectrum is, in this case, defined as the difference between the two Fourier spectra divided by the nitrogen ambient spectrum). The resulting absorption spectrum is displayed in figure 3.3.2.4, and the absorption peaks are listed in the figure inset along with the theoretical values for rotational water vapour absorption lines [22]. The experimental absorption peaks are in excellent agreement with the theoretical lines for water vapour, suggesting that the THz beam is modified largely by resonant water vapour absorption during its propagation through the air. To minimize this absorption process and maximize the THz signal, therefore, it is necessary to control the atmospheric conditions in which the THz beam propagates.

As shown indirectly above, the frequency content of the THz waveform can be used to evaluate the absorption spectra for various media. The fundamental bandwidth limitation for such investigations will be limited, however, by the frequency response of

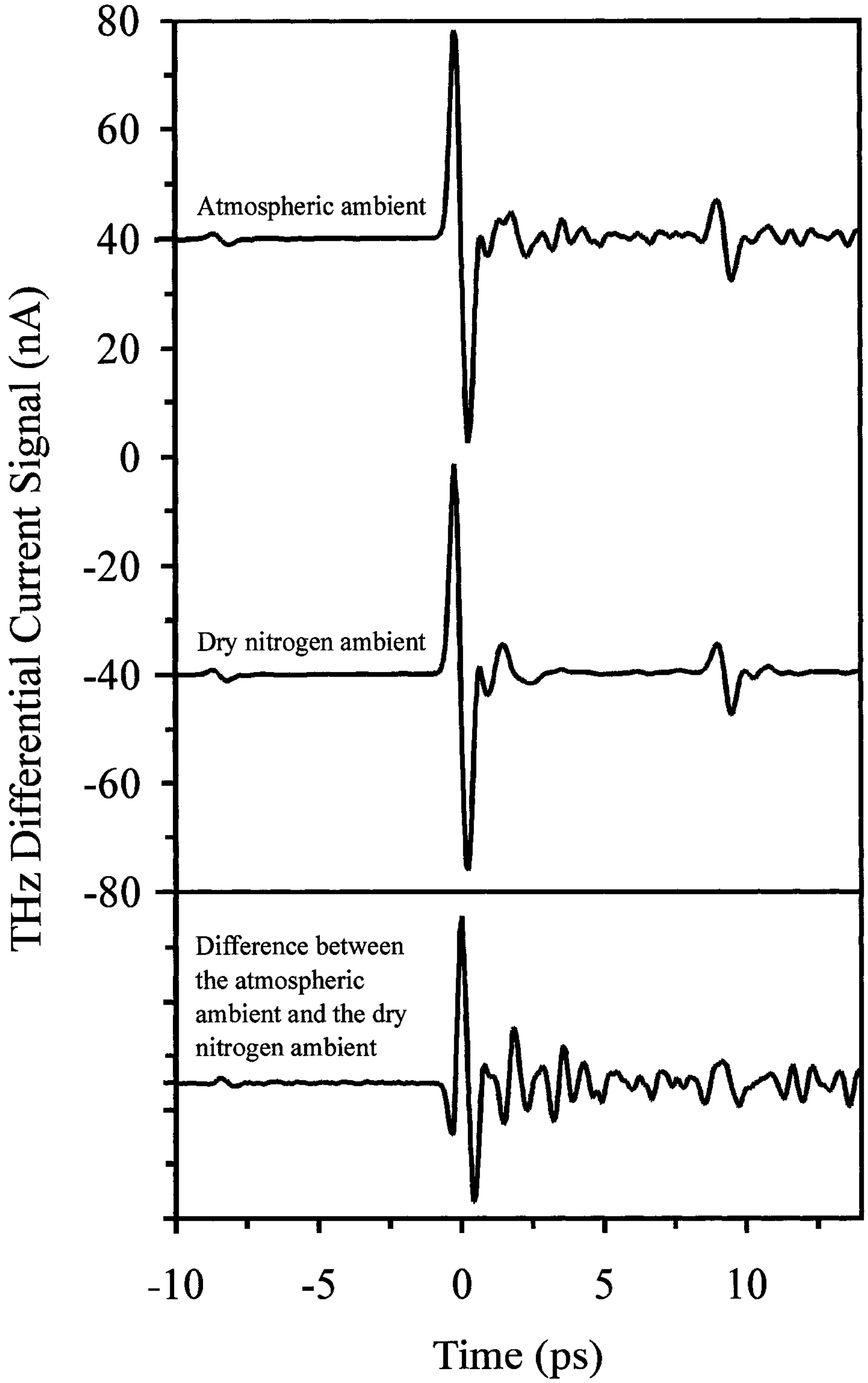

Figure 3.3.2.3 THz waveforms measured in atmospheric and dry nitrogen ambient conditions. The difference between these waveforms is shown at the bottom. The THz radiation is generated by a 100 μm PC gap on a GaAs substrate and detected by a 500 μm thick <111> ZnSe EO detector.

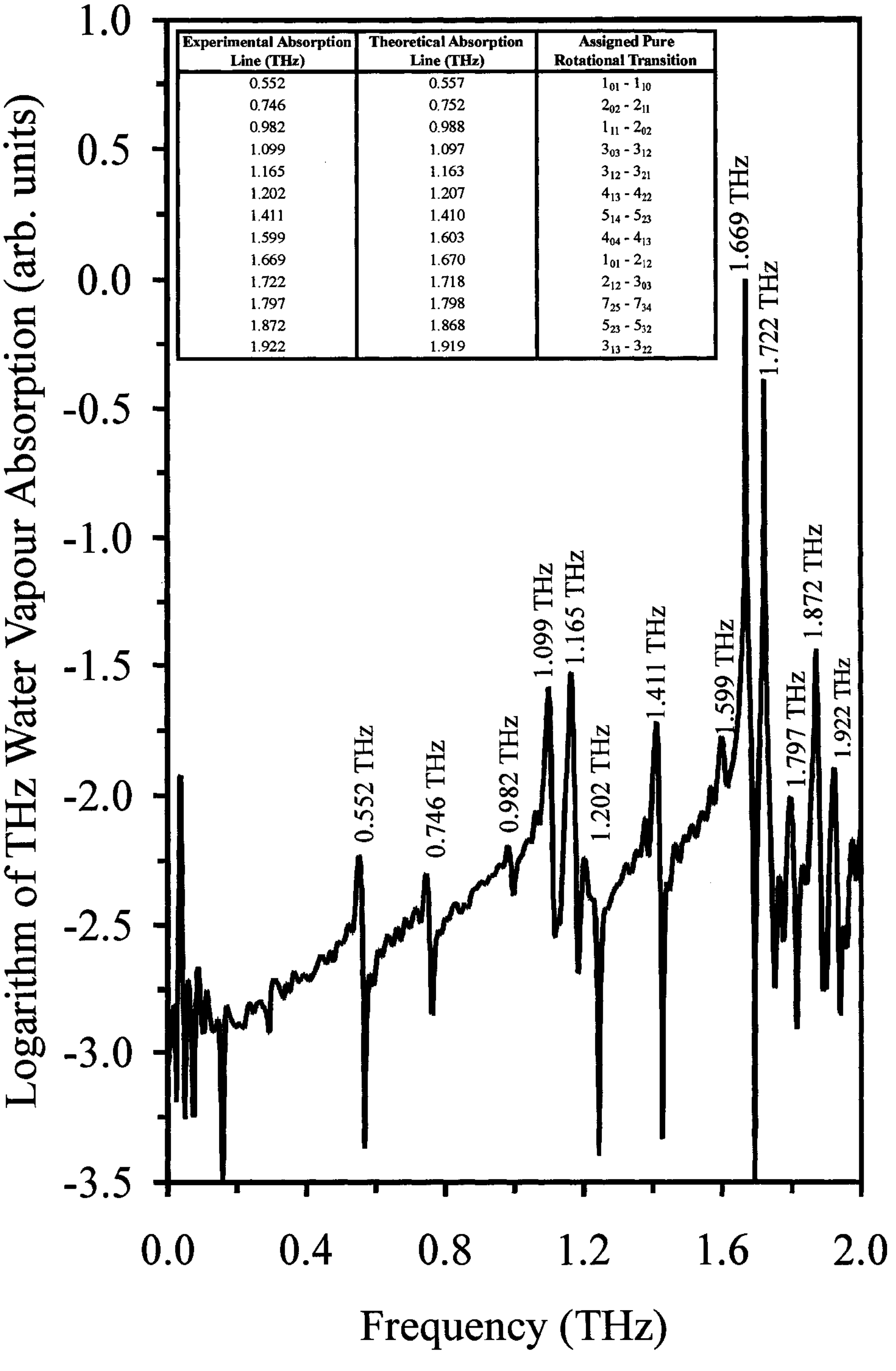

Experimental Absorption Line (THz)	Theoretical Absorption Line (THz)	Assigned Pure Rotational Transition
0.552	0.557	1_{01} - 1_{10}
0.746	0.752	2_{02} - 2_{11}
0.982	0.988	1_{11} - 2_{02}
1.099	1.097	3_{03} - 3_{12}
1.165	1.163	3_{12} - 3_{21}
1.202	1.207	4_{13} - 4_{22}
1.411	1.410	5_{14} - 5_{23}
1.599	1.603	4_{04} - 4_{13}
1.669	1.670	1_{01} - 2_{12}
1.722	1.718	2_{12} - 3_{03}
1.797	1.798	7_{25} - 7_{34}
1.872	1.868	5_{23} - 5_{32}
1.922	1.919	3_{13} - 3_{22}

Figure 3.3.2.4 Absorption spectrum of water vapour in the THz frequency-domain. The curve is formed by taking the Fourier transform of the difference between the time-domain signals measured with and without the dry nitrogen chamber. The THz radiation used for the scan is generated by a 100 μm PC gap on a GaAs substrate and detected by a 500 μm thick <111> ZnSe EO detector. The absorption lines are listed in the inset.

the THz generation and detection processes; knowing this maximum frequency is, therefore, a major issue in understanding the capabilities of the system. To determine the frequency response for the THz emission system described above the Fourier transform of the time-domain THz waveform in figure 3.3.2.1 is computed and plotted in figure 3.3.2.5. According to this figure, the system is capable of operating at frequencies up to 5 THz. As this 5 THz maximum frequency is below the transverse-optic (TO) phonon resonance (ν_{TO} = 6.15 THz) and longitudinal-optic (LO) phonon resonance (ν_{LO} = 7.50 THz) of the ZnSe detector [23], it is expected that limitations other than phonon resonance play a role in limiting the frequency response. For example, the ballistic acceleration and subsequent deceleration of the electron-hole plasma is fundamentally limited by the time it takes to form the dielectric space-charge field. It has been shown by Cummings et al. [24], that this field screening process can occur on a timescale of hundreds of femtoseconds (even for a charge carrier density as high as 6×10^{18} cm^{-3}). For the density regime of this investigation (1×10^{18} cm^{-3}), this finite response time will place an upper limit on the bandwidth of the THz pulse. In addition, mechanisms related to the detection of the THz pulse are expected to play a role in limiting the overall frequency response. Group velocity mismatch between the THz pulse and the probe pulse in the detector will, for example, broaden the measured time-domain waveform. Being that the velocity of the THz pulse in the ZnSe detector is 1.078×10^8 m/s and the velocity of the probe pulse in the ZnSe detector is 1.202×10^8 m/s, a phase mismatch of 1 ps/mm is expected between the probe pulse and the THz pulse [25]. For the 500 μm thick sensor used in this investigation, this dispersion will cause the measured waveform to be broadened by 500 fs, which will indeed limit the frequency response in figure 3.3.2.5.

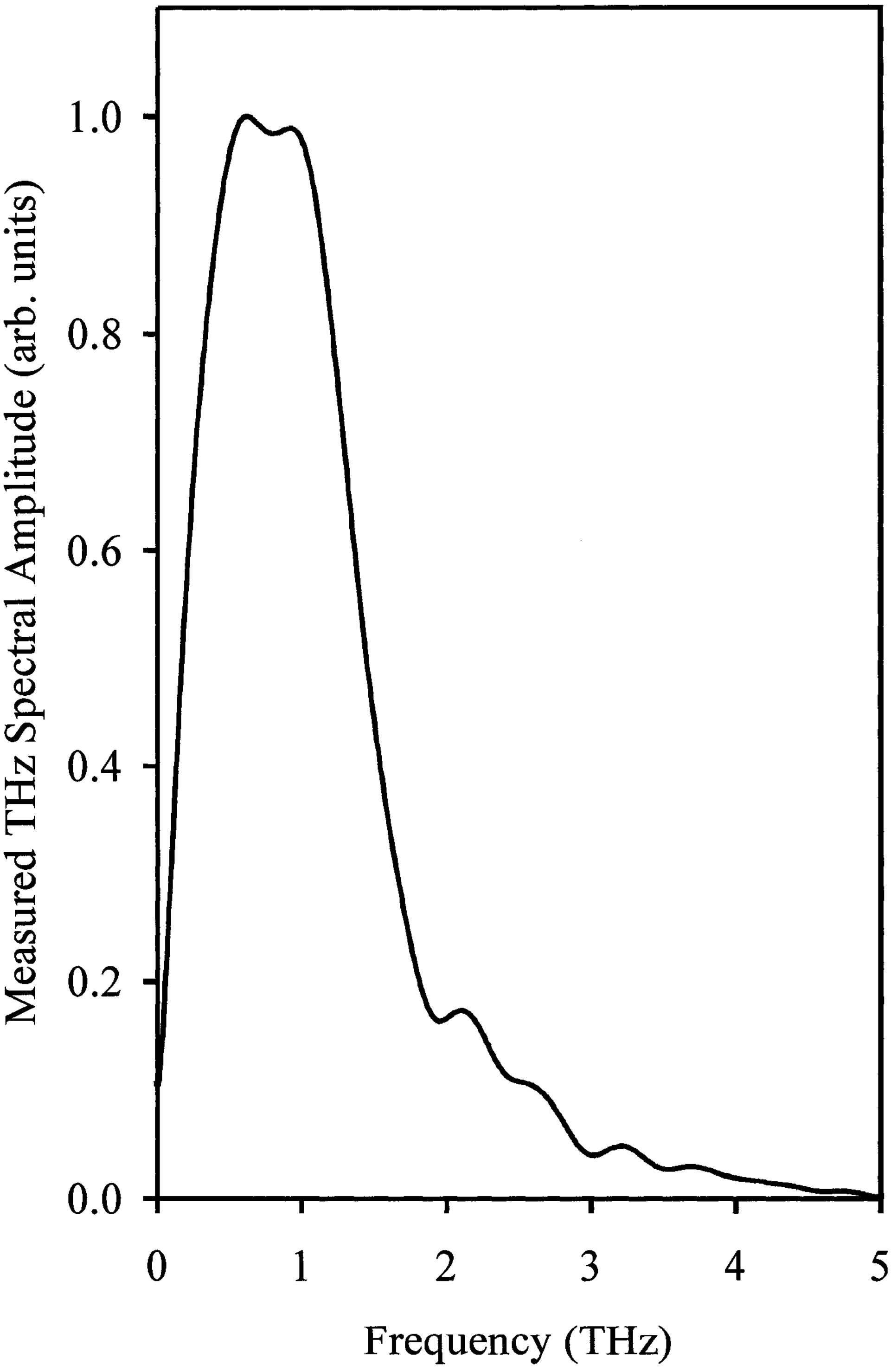

Figure 3.3.2.5 Spectrum of the free-space THz waveform generated by the 100 μm GaAs PC gap and detected by the 500 μm thick <111> ZnSe crystal. The gap is illuminated by a 160 mW pump beam (corresponding to a pump energy fluence of 25.5 μJ/cm²).

3.4 ZnSe Photoconductive Terahertz Emitters

3.4.1 Theoretical Framework

The THz power produced by PC sources is limited by a variety of mechanisms. Section 3.3 demonstrated that, at high optical fluences, saturation mechanisms such as space-charge screening and near-field THz screening decrease the emitted THz power by shielding the external bias field [17], [19]. While numerous attempts have been made to overcome these saturation mechanisms [26], the most promising attempts have made use of high bias voltages to scale the THz power to large amplitudes. By increasing the bias field within the gap, rather than the optical fluence, the effects of bias field screening are minimized as the overall injected carrier density is kept below the saturation level.

The ability to increase the THz amplitude by simply increasing the bias voltage is limited ultimately by the dielectric breakdown strength of the underlying substrate. For this reason, wide bandgap semiconductor materials–with high dielectric breakdown strengths–are particularly attractive. Unfortunately, semiconductor materials tend to exhibit decreasing carrier mobilities with increasing bandgap energies, limiting the overall photo-current in the THz source. There are, however, three noteworthy exceptions to this trend: GaAs, diamond, and ZnSe. Semi-insulating GaAs has received a great deal of attention as a PC THz source, as it exhibits both a large dark resistivity (10^7 Ω·cm) and a high carrier mobility (3000 $\mathrm{cm^2/V \cdot s}$) [17]. Unfortunately, GaAs is characterized by a relatively low dielectric breakdown field strength (at most 10 kV/cm), making it unsuitable for high bias voltage THz applications. In contrast to this, recent attention has been applied to PC THz generation using diamond substrates. Using a KrF pulsed laser source (248 nm, 10 mJ), Yoneda et al. have successfully generated high-power THz beams through PC excitation of a polycrystalline diamond film [27]. The use of a diamond PC medium, in this case, led to high-power THz pulses as the bias field could be scaled to exceptionally large values (10^6 V/cm). Unfortunately, the extremely wide bandgap of diamond (5.47 eV) necessitated the use of an ultraviolet laser source with picosecond pulse durations–leading to a relatively low THz bandwidth.

In this section, the PC generation of THz radiation using polycrystalline ZnSe is introduced. Like diamond, ZnSe exhibits a large breakdown field strength (100 kV/cm) [28], [29] and can be used to generate high-power THz pulses; unlike diamond, however, it offers a substantially higher mobility (600 $\text{cm}^2/\text{V}\cdot\text{s}$ versus 10 $\text{cm}^2/\text{V}\cdot\text{s}$ for diamond) [30] and a greater ease of fabrication (using conventional CVD growth) [31]. In addition, the 2.67 eV bandgap of ZnSe allows for two-photon photo-excitation with ultrafast Ti:sapphire laser sources–providing both a large THz amplitude (through scaling of the bias field) and a wide THz bandwidth (through the use of femtosecond pulsed laser sources).

Since two-photon photoconductivity is coupled to the incident optical intensity through a nonlinear relationship, a high optical fluence is needed to generate a large carrier density within the ZnSe material. This can be accomplished with either a large optical intensity, through the use of an amplified laser source, or a small focal spot size, through the use of a small excitation volume. To eliminate the requirement for an amplified optical excitation source, the investigation that follows employs the edge-illuminated PC geometry first introduced to THz generation by Katzenellenbogen and Grischkowsky [32]. The same THz generation process can, however, be scaled to large-aperture THz emitters with high-power amplified laser sources.

To fully understand the operation of the ZnSe PC THz emitter (shown in figure 3.4.1.1(a)) a model similar to the GaAs emitter in section 3.3.1 is introduced. The ZnSe PC THz emitter is, in this case, patterned onto a polycrystalline ZnSe substrate and is comprised of two 20 μm wide coplanar lines. The 70 μm wide spacing between these lines is spanned by an end-fed antenna with a small PC gap (with a length of $L_x = 9$ μm and a width of $L_y = 7$ μm). Photo-excitation of this gap is provided by the optical pump beam, whose intensity,

$$I(x,t) = \frac{E_p}{\tau_p}\exp\left[-4\ln 2(t-t_o)^2/\tau_p^2\right]\exp\left[-4\ln 2(x-x_o)^2/x_p^2\right], \tag{3.4.1.1}$$

is a function of the pump energy fluence, E_p, the pump pulse arrival time, $t_o = 0$, the temporal FWHM, $\tau_p = 50$ fs, the spatial beam centre, $x_o = 1.5$ μm, and the spatial FWHM, $x_p = 3$ μm. This asymmetric photo-excitation geometry (with the pump beam focused onto the high-field region next to the anode) provides the necessary conditions for edge-illuminated PC activation of the emitter [33]. The surface electron current, $k_n(x,t)$, and surface hole current, $k_p(x,t)$, transport equations in this case,

$$\frac{\partial n_s(x,t)}{\partial t} = \frac{(1-R)}{2h\nu} I(x,t) + \frac{1}{e}\frac{\partial k_n(x,t)}{\partial x} \tag{3.4.1.2}$$

and

$$\frac{\partial p_s(x,t)}{\partial t} = \frac{(1-R)}{2h\nu} I(x,t) - \frac{1}{e}\frac{\partial k_p(x,t)}{\partial x}, \tag{3.4.1.3}$$

are modified slightly from that of the GaAs emitter to accommodate the fact that two photons of energy $h\nu$ are required to make the transition from the valence band to the conduction band; here, e is the electronic charge, and $R = 0.3$ is the reflectivity including overlap onto the anode. Like the previous GaAs emitter, these transport equations differ

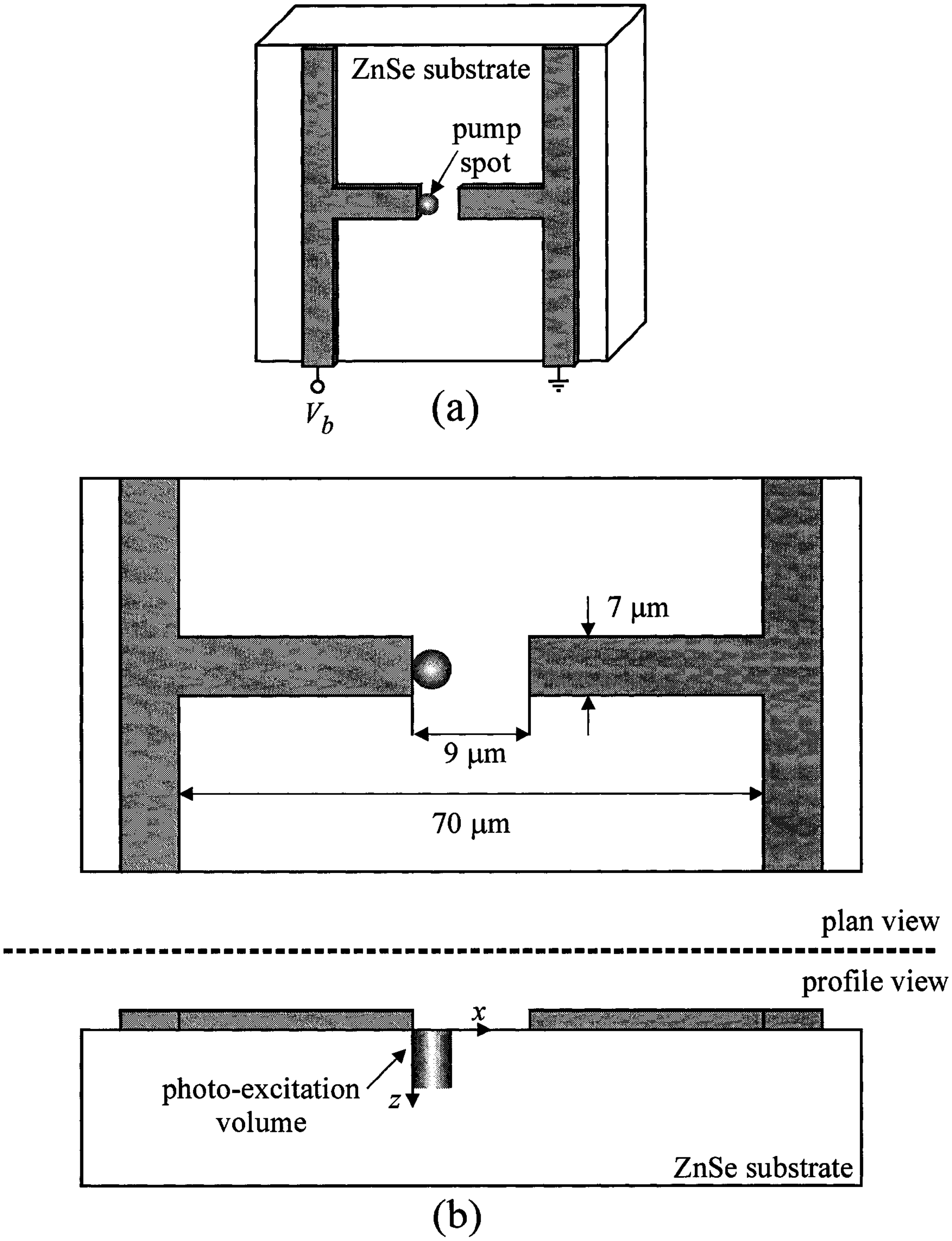

Figure 3.4.1.1 The (a) experimental layout and the (b) schematic for the ZnSe PC dipole THz emitter. The device is comprised of two Ti/Au coplanar lines that are separated by 70 µm. Between these lines is a 70 µm dipole antenna with a 9 µm PC gap. The pump spot is 3 µm in diameter.

from conventional volumetric transport equations in that they are expressed in terms of surface charge densities (cm^{-2}) and surface current densities (C·s^{-1}·m^{-1}). The expressions have been normalized over the intensity-dependent penetration depth, $\delta = 1/\beta I_p$, where $\beta = 3.5$ cm/GW is the two-photon absorption coefficient for ZnSe and $I_p = E_p/\tau_p$ is the peak pump intensity. This modification eliminates the standard squared intensity dependence for two-photon absorption materials in the first terms of equations 3.4.1.2 and 3.4.1.3. The resulting surface hole distribution, given a negligible surface hole current, $k_p(x,t) = 0$,

$$p_s(x,t) = \sqrt{\frac{\pi}{16\ln 2}}\,\frac{(1-R)}{2h\nu}E_p\left\{1+erf\left[\frac{2\sqrt{\ln 2}(t-t_o)}{\tau_p}\right]\right\}\times \exp\left[\frac{-4\ln 2(x-x_o)^2}{x_p^2}\right], \tag{3.4.1.4}$$

reflects this material absorption change as well.

The surface electron current for the ZnSe PC THz emitter, $k_n(x,t)$, is expected to differ greatly from that of the GaAs PC THz emitter. The application of a PC gap that is smaller than the THz wavelength precludes the use of a plane-wave matching boundary condition on the $z = 0$ surface. As shown by Rodriguez et al. [17], these small PC dipole emitters are dominated, instead, by space-charge screening effects rather than near-field THz screening, and the relationship between the surface electron current and the electron density,

$$k_n(x,t) = \mu_n e n_s(x,t) E_{eff}(x,t), \tag{3.4.1.5}$$

remains linear. Here, $\mu_n = 600$ cm^2/V·s is the mobility of the ZnSe substrate. As in section 3.3, the space-charge screening in the emitter is described by Poisson's equation,

$$\frac{\partial E_{eff}(x,t)}{\partial x} = \frac{e\beta I_p}{\varepsilon_r \varepsilon_o}\left[p_s(x,t) - n_s(x,t)\right], \tag{3.4.1.6}$$

where $\varepsilon_r = 9.2$ is the dielectric constant of ZnSe, and ε_o is the permittivity of free-space. The form of this equation is transformed from its original form in equation 3.3.1.13 to accommodate the intensity-dependent absorption depth within the ZnSe substrate and the effective electric field

$$E_{eff}(x = x_o, t = 0) = \frac{V_b \beta I_p}{\pi} \ln\left\{\left[\left(\frac{2}{\beta I_p L_x}\right)^2 + 1\right]^{1/2} + \left(\frac{2}{\beta I_p L_x}\right)\right\} \tag{3.4.1.7}$$

that exists within the bulk PC gap volume. An effective electric field is used in this case to allow incorporate the fact that the bias field diminishes within the substrate as [34]

$$E(x = x_o, t = 0, z) = \frac{V_b}{\pi}\left[\left(\frac{L_x}{2}\right)^2 + z^2\right]^{-1/2}. \tag{3.4.1.8}$$

By averaging the electric field in equation 3.4.1.8 over one optical penetration depth, the dependence between the effective bias field and the incident optical intensity is included within the dynamics of the model.

As a final step, the radiated THz field is computed from the electric field distribution in the PC gap. Unlike the large GaAs PC radiator, where the far-field THz radiation is produced directly from the photo-current within the gap, the emission of THz radiation from the small ZnSe PC emitter is mediated by the dipole antenna structure shown in detail in figure 3.4.1.1(b). In this case, the local electric field redistribution within the PC gap creates a displacement current on the antenna arms. This time-varying current produces the far-field THz radiation of interest. Specifically, it has been shown by Zhou [35], that the photo-current on the antenna arms is proportional to the time-derivative of local electric field at the anode ($x = 0$). As the far-field electric field is itself proportional to the time-rate-of-change of this photo-current, the THz time-domain waveform can be approximated by the second derivative of the local electric field at the anode. Thus,

$$E_{THz}(z,t) = a\frac{\partial^2 E_{eff}(x=0,t)}{\partial t^2}, \qquad (3.4.1.9)$$

where a is a proportionality constant. By solving the above system of equations for the time- and space- varying surface electron density, hole density, electron current, hole current, and effective electric field, the effective electric field at the anode, $E_{eff}(x = 0,t)$, can be determined. This time-varying function can then be used to calculate the free-space THz electric field, $E_{THz}(z,t)$, in the far-field regime of the ZnSe PC dipole THz emitter.

Equations 3.4.1.1-3.4.1.9 are first solved numerically for the far-field THz electric field, $E_{THz}(t)$, given a bias electric field strength of E_b = 128 kV/cm (above this field strength, we have found that our polycrystalline ZnSe samples undergo irreversible damage). The time-domain THz results are plotted for pump beam average powers of 40, 80, 120, and 160 mW and are displayed in figure 3.4.1.2. For the $x_p = 3$ μm spot size used in the model, these pump powers correspond to pump energy fluences of E_p = 7.1, 14.1, 21.2, and 28.3 mJ/cm^2, respectively. The numerical method employed in solving this system of equations is described in detail in Appendix J. For each of these pump energy fluences, the time-domain waveform is found to be bipolar in shape. This finding is due, in large part, to the fact that the charge carrier injection process occurs within a small PC volume. The large carrier density that results from this high injection regime

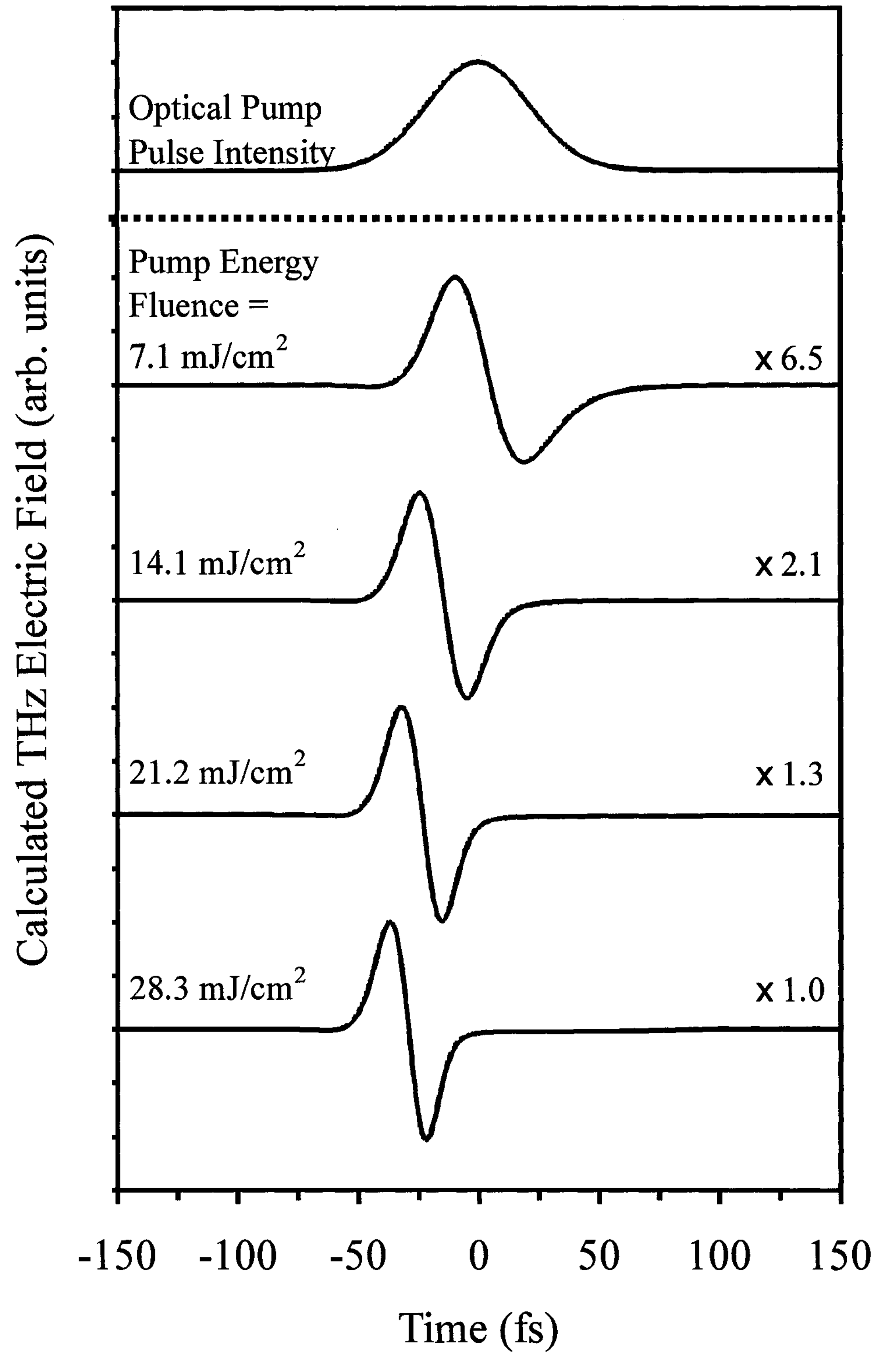

Figure 3.4.1.2 Normalized theoretical time-domain waveforms for the ZnSe PC dipole THz emitter, given pump energy fluences of E_d = 7.1, 14.1, 21.2, and 28.3 mJ/cm^2 and a bias electric field strength of E_b = 128 kV/cm. The optical pump pulse intensity is shown at the top of the figure.

introduces a significant degree of space-charge screening within the model (causing both the deceleration of carriers in the gap and the negative lobe in the figure). This point is further supported by the fact that, as the pump power is increased, the THz waveform arrives at earlier and earlier times. Indeed, at a pump energy fluence of $E_p = 7.1$ mJ/cm^2 the THz waveform is centred at the zero-time for the system (as defined by the pump pulse intensity centred at $t = 0$ at the top of the figure), while at a pump energy fluence of 28.3 mJ/cm^2, however, the waveform is seen to arrive approximately 30 fs earlier. This temporal shifting can be attributed to the fact that, as the energy fluence is increased, the intensity necessary to commence space-charge screening occurs at earlier points in time–initiating the formation of the negative lobe for the THz waveform. The fact that the THz waveforms occur well within the window of the optical pump pulse (as well as the fact that the peak-to-peak THz amplitudes are found to continually increase with the pump energy fluence) suggests, however, that the overall degree of saturation in the ZnSe dipole THz emitter is kept to relatively low levels for these injected carrier densities.

As a comparison for the ZnSe dipole THz emitter, the model above is applied to the simulation of an identical GaAs dipole emitter (the dimensions and excitation conditions are kept constant, here, though the bias electric field strength is decreased to $E_b = 10$ kV/cm to be below the damage threshold). Time-domain THz waveforms for the GaAs source are shown in figure 3.4.1.3. Like the ZnSe dipole emitter, the GaAs THz source produces bipolar time-domain waveforms. Unlike the ZnSe device, however, the resulting THz waveforms are seen to be largely saturated by the high-injection regime. The fact that the THz pulses occur at the leading edge of the optical pump pulse (shown at the top of the figure) suggests that space-charge screening saturates the THz emission

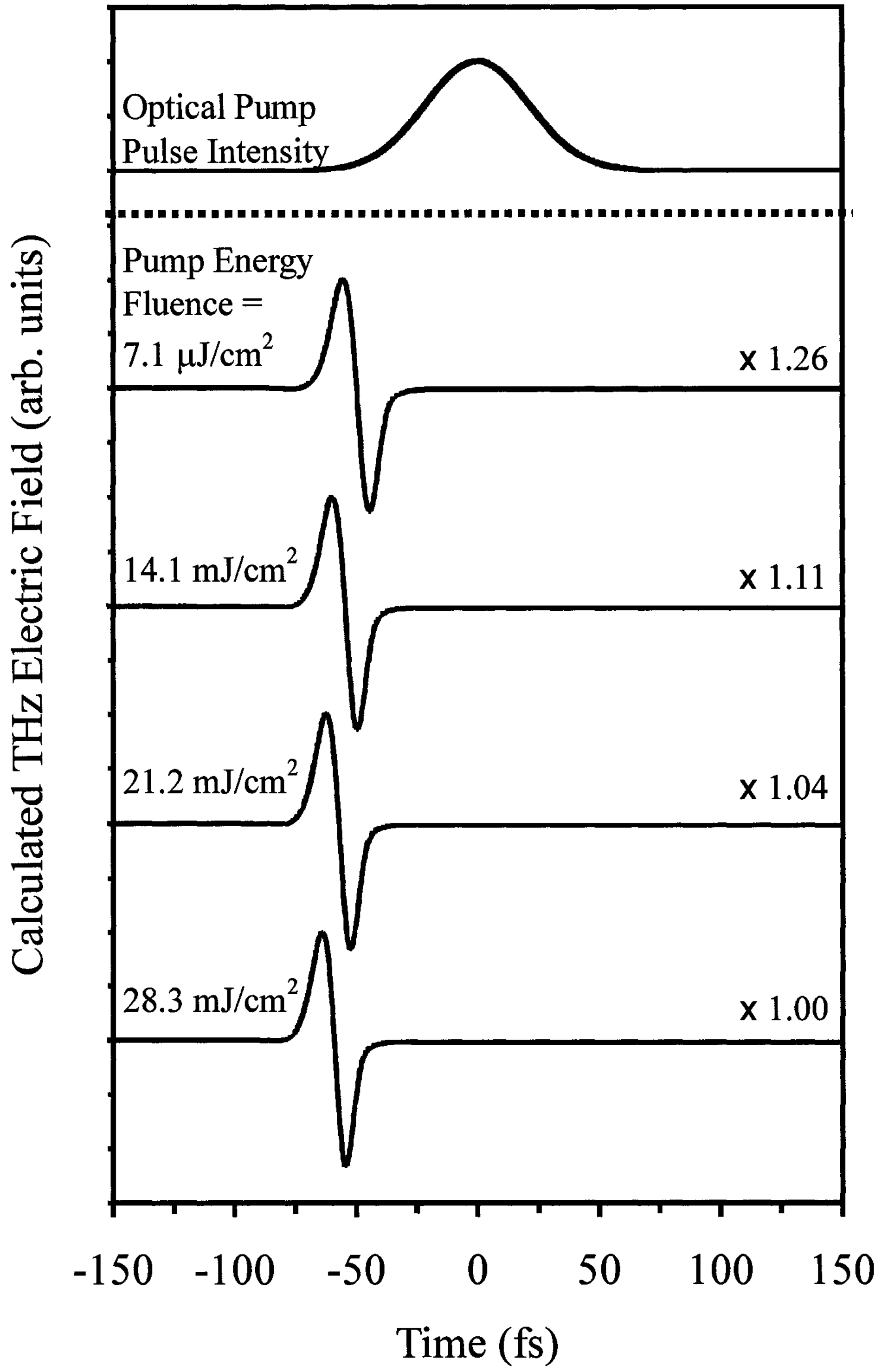

Figure 3.4.1.3 Normalized theoretical time-domain waveforms for the GaAs PC dipole THz emitter, given pump energy fluences of $E_d = 7.1, 14.1, 21.2$, and 28.3 mJ/cm² and a bias electric field strength of $E_b = 10$ kV/cm. The optical pump pulse intensity is shown at the top of the figure.

at an early stage of the photo-excitation process. Moreover, the amplitudes of the waveforms (as displayed by the magnification factors on the right side of the figure) are similar in magnitude, suggesting again that the THz emission is witnessing a considerable level of space-charge screening saturation for these levels of photo-excitation.

To fully understanding the saturation processes in the ZnSe and GaAs dipole THz emitters, the peak-to-peak amplitudes of these emitters are shown in figure 3.4.1.4 as a function of the incident pump energy fluence. It is readily apparent from this figure that the THz amplitudes for the ZnSe source scale linearly with the incident optical intensity, while the GaAs emitter becomes saturated at low levels of excitation. This suggests that the two-photon absorption process in the ZnSe emitter is able to minimize space-charge screening and allow the THz power to be scaled to increasingly large values.

The greatest advantage of the ZnSe dipole emitter is its ability to be operated under high bias fields. Given a PC gap length of L_x = 9 μm, it is expected that DC voltages up to 115 V can be applied to the gap (for a peak field strength of 128 kV/cm). Comparing this to the GaAs emitter (where the maximum field is less than 10 kV/cm), suggests that the ZnSe THz source can produce waveforms that are an order of magnitude larger in amplitude. To demonstrate this point through the PC emitter model, the peak-to-peak THz amplitudes are calculated as a function of the applied bias electric field strength, and the results are shown in figure 3.4.1.5. As both emitters are found to scale linearly with the applied field, the sole limitation on the amplitude to which these emitters can be scaled is the breakdown strength of the underlying substrate. Indeed, the fact that the ZnSe emitter can be biased by an order of magnitude larger field allows this emitter to produce THz pulses with significantly larger amplitudes.

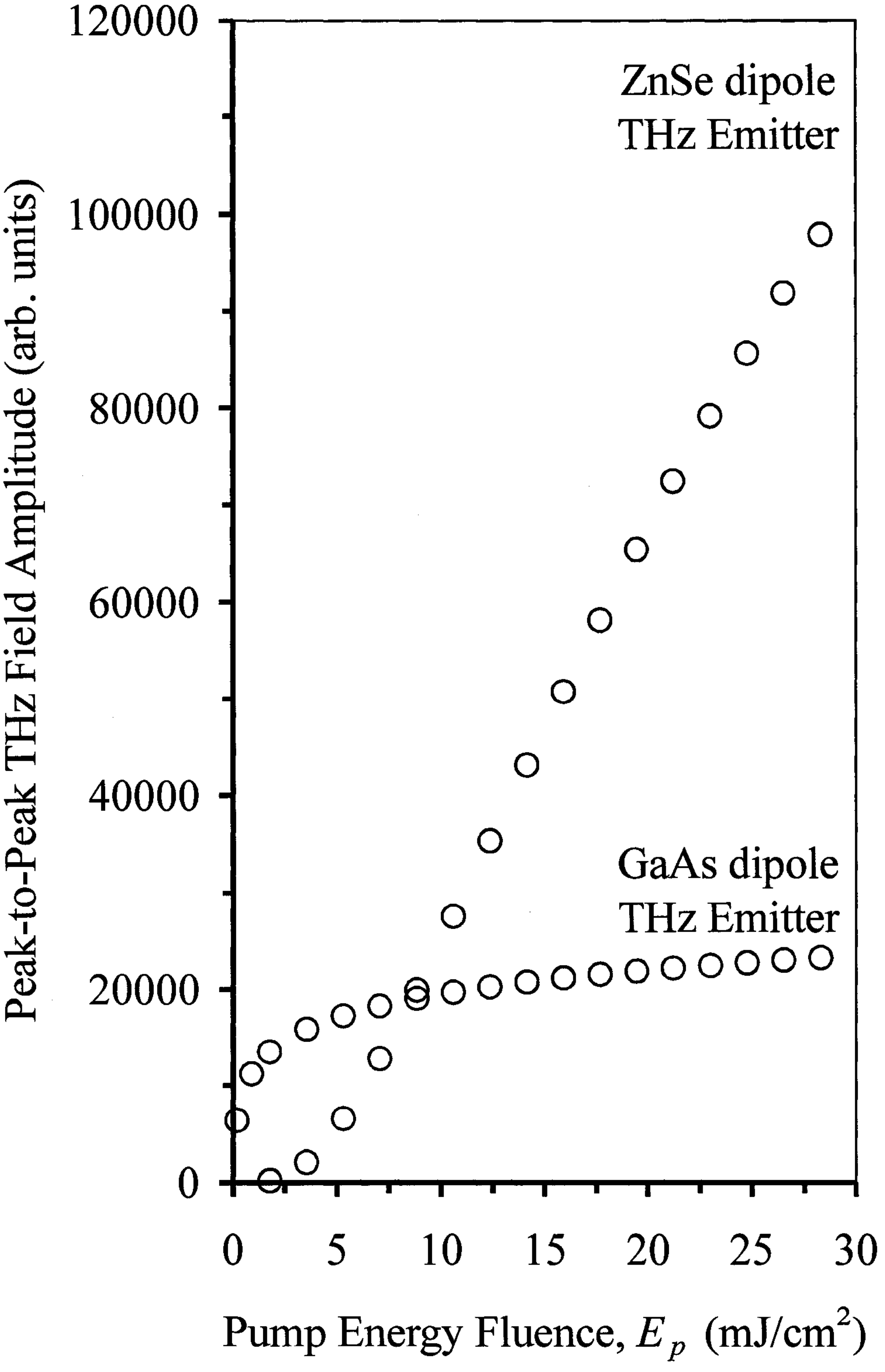

Figure 3.4.1.4 Calculated peak-to-peak THz amplitudes as a function of the pump energy fluence for the ZnSe and GaAs PC dipole THz emitters. Bias electric field strengths of E_b = 128 kV/cm and E_b = 10 kV/cm are used for the ZnSe and GaAs emitters, respectively. The spot size is x_p = 3 μm and the gap length is L_x = 9 μm.

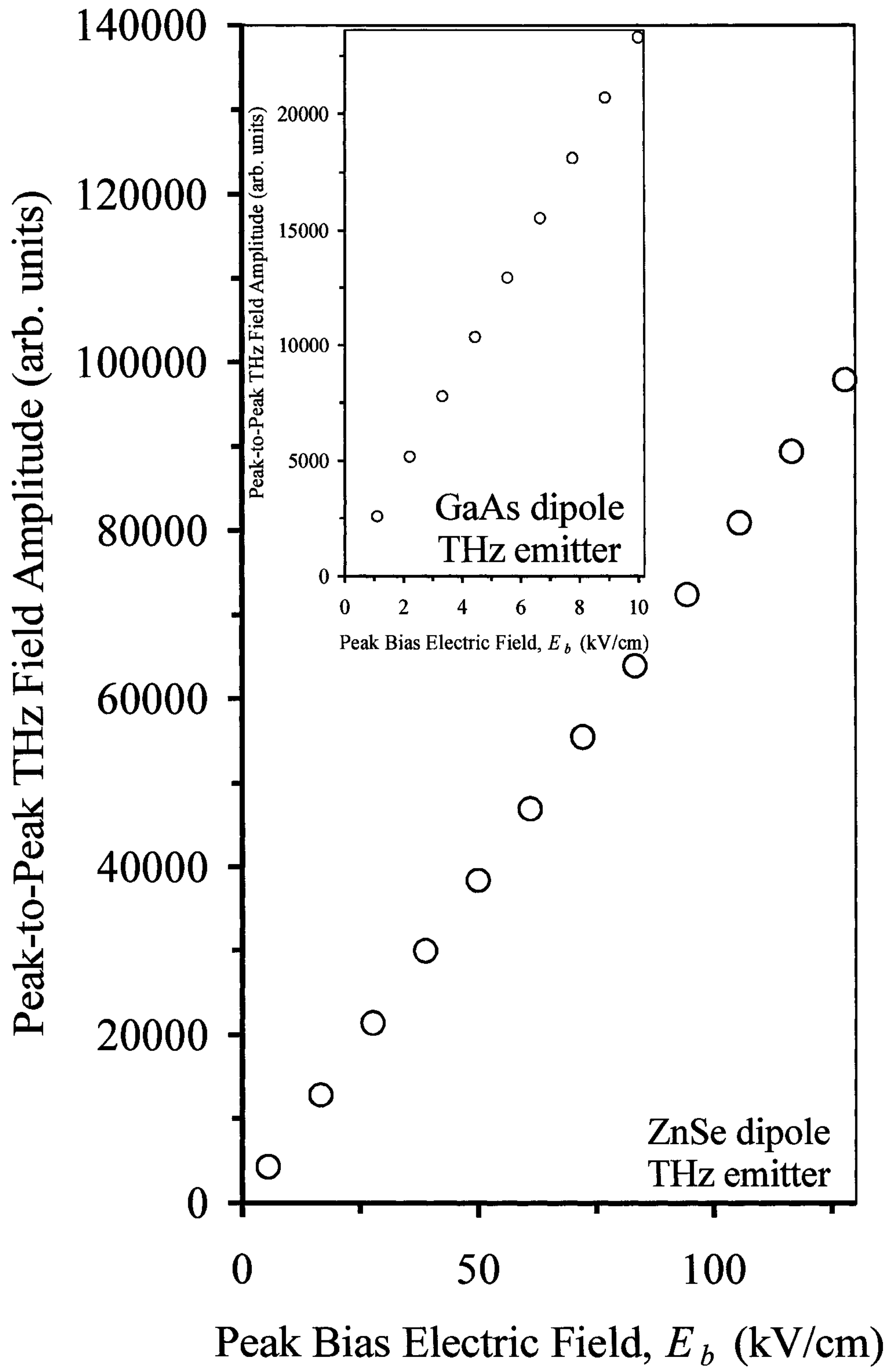

Figure 3.4.1.5 Calculated peak-to-peak THz amplitudes as a function of the applied bias electric field for the ZnSe dipole THz emitter. A pump energy fluence of 28.3 mJ/cm^2 is used in the model, along with a spot size of x_p = 3 μm and a gap length of L_x = 9 μm. Results for the corresponding GaAs dipole THz emitter are shown in the inset.

3.4.2 Experimental Framework

To test the experimental operation of the ZnSe PC THz emitter, the free-space THz generation and detection system described in section 3.2 is employed [13]. The ZnSe device (shown in figure 3.4.1.1) is comprised of two 20 μm wide Ti/Au coplanar transmission lines, between which lies a 70 μm long end-fed dipole antenna structure and a 9 μm PC gap. These Ti/Au metallization features are photolithographically patterned onto a 2.6 mm thick polycrystalline ZnSe substrate [36]; the photolithographic process employed is described in Appendix K. The coplanar line is biased by a 54 kHz AC voltage source (Wavetek Model 178 Programmable Waveform Synthesizer), and laser activation is provided by an 800 nm, 80 MHz, 10 fs Ti:sapphire oscillator (Femtolaser Femtosource Pro). The pump beam from the laser is focused onto the edge of the high-field anode region of the gap to initiate the edge-illuminated PC excitation process. The resulting THz radiation is collected and collimated by an f/1.0 parabolic mirror, and then focused–along with a co-propagating probe beam–by a second identical parabolic mirror. A 500 μm thick <111> ZnSe EO crystal [14], [20] is positioned at the focal plane of the beams to allow the probe to sample the THz electric field. The THz-induced polarization retardation of the probe is then extracted at the modulation frequency of the bias voltage.

The ZnSe dipole THz emitter is tested initially with a 160 mW pump beam and a focal spot size of 3 μm. The bias voltage is varied from V_b = 20 $V_{p\text{-}p}$ to V_b = 230 $V_{p\text{-}p}$ (corresponding to peak bias electric field amplitudes of E_b = 11 kV/cm to E_b = 128 kV/cm), and the time-domain THz waveforms are recorded. The resulting peak-to-peak THz amplitudes are shown in figure 3.4.2.1 as a function of the bias voltage, and a typical time-domain THz waveform, along with its spectrum, is shown in figure 3.4.2.2. It is

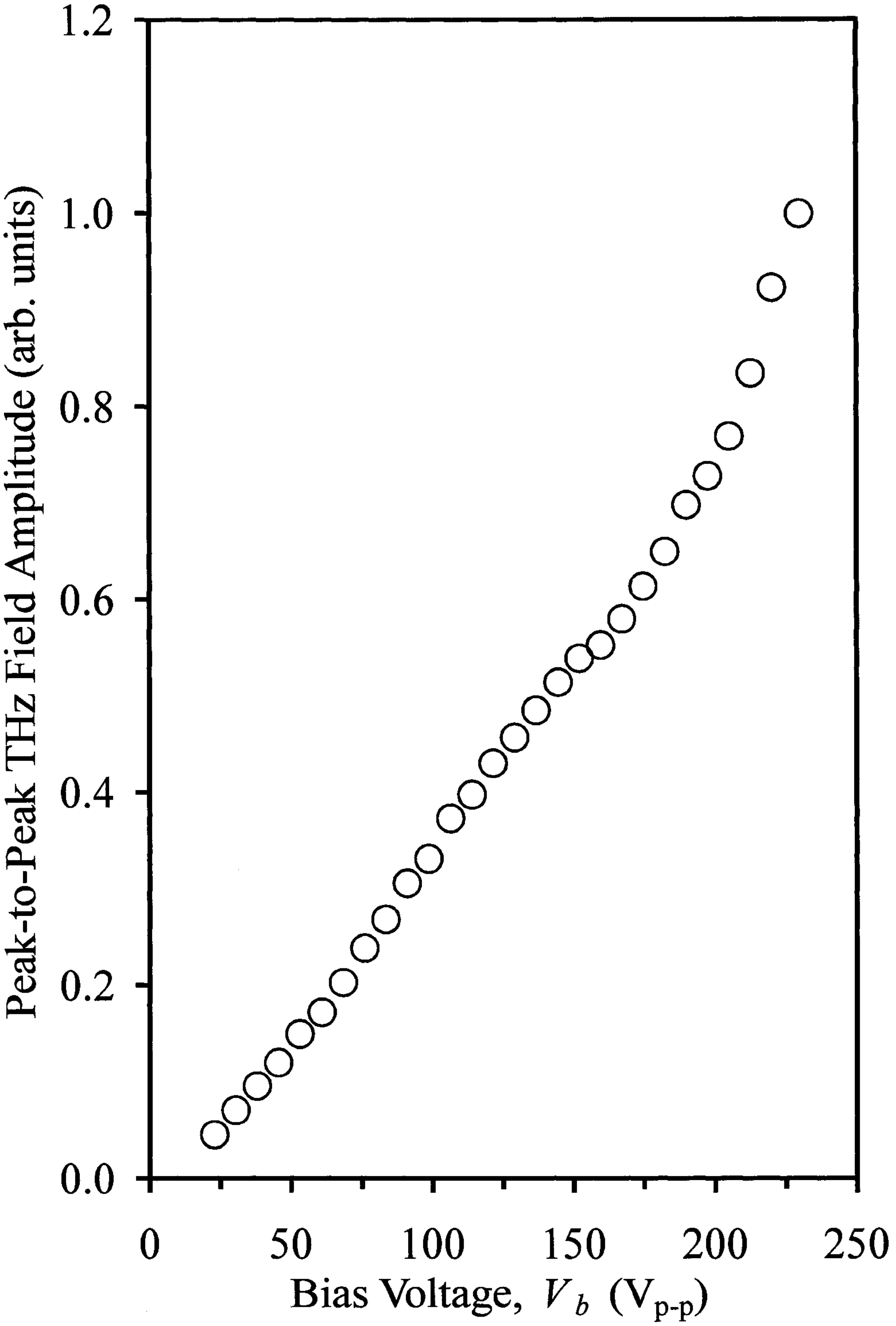

Figure 3.4.2.1 Measured peak-to-peak THz amplitudes as a function of the applied bias voltage, V_b, for the ZnSe dipole THz emitter. The PC gap is excited by a 160 mW pump beam that is focused to a spot size of $x_p = 3$ μm (corresponding to a pump energy fluence of $E_p = 28.3$ mJ/cm^2). These applied bias voltages correspond to peak electric field amplitudes of $E_b = 11$ kV/cm to $E_b = 128$ kV/cm).

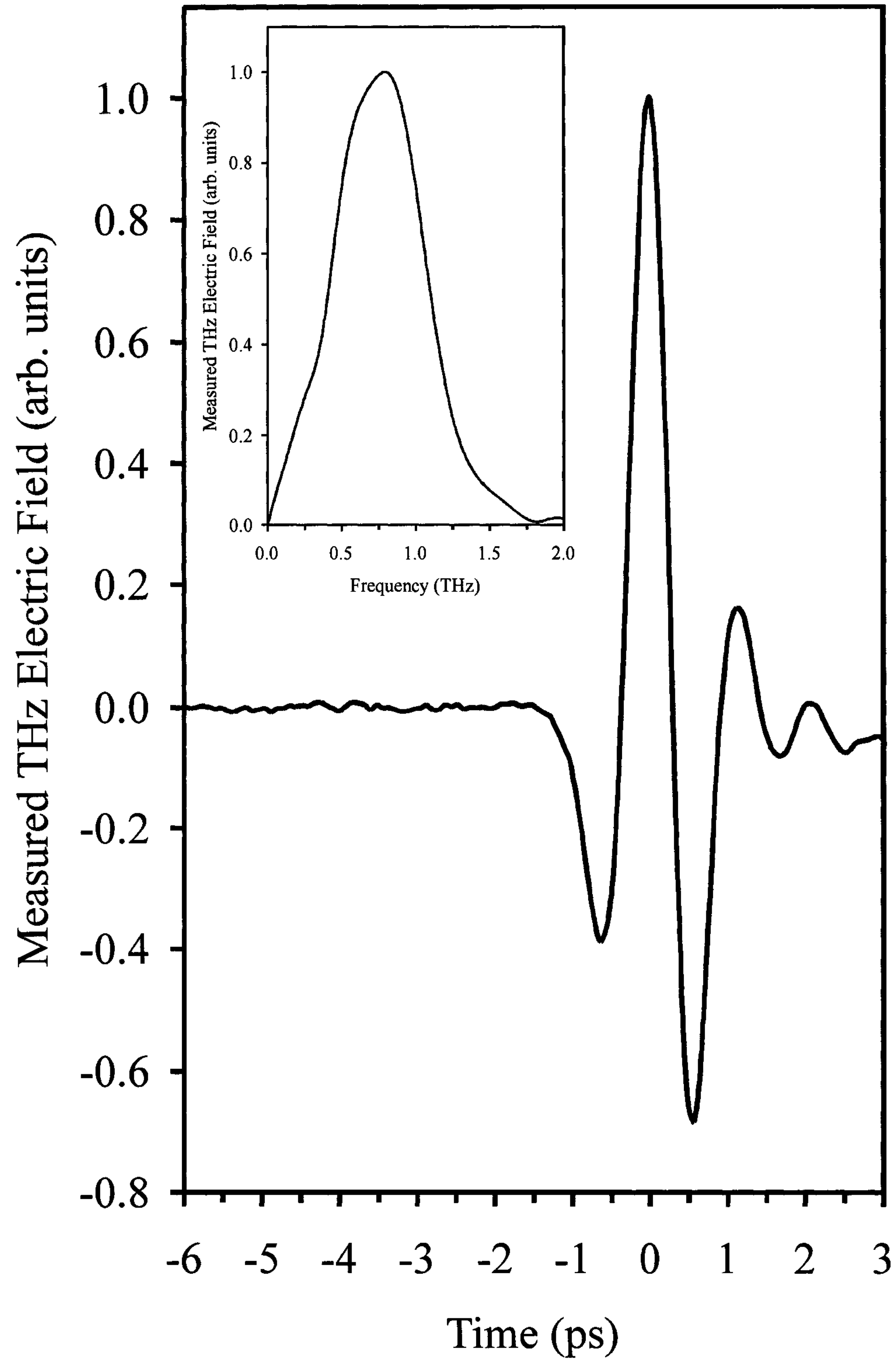

Figure 3.4.2.2 The THz time-domain waveform produced by the ZnSe dipole THz emitter. A bias voltage of $V_b = 230\ \mathrm{V_{p\text{-}p}}$ ($E_b = 128$ kV/cm) is used with a pump power of 160 mW ($E_p = 28.3$ mJ/cm^2) to activate the device. The corresponding spectrum is shown in the inset.

readily apparent from figure 3.4.2.1, that the THz amplitude increases as the bias voltage increases. For bias voltages from $V_b = 20$ V$_{\text{p-p}}$ to $V_b = 200$ V$_{\text{p-p}}$, this relationship is linear, in agreement with the theoretical results of section 3.4.1. Beyond $V_b = 200$ V$_{\text{p-p}}$, however, the relationship becomes super-linear, suggesting that a high-field photo-current avalanche processes has commenced in the substrate–a result of both the large optical pump fluence ($E_p = 28.3$ mJ/cm^2) and the high peak bias field ($E_b = 128$ kV/cm). The injection of a large number of highly energetic carriers, in this case, initiates photo-carrier avalanche multiplication in the electron-hole plasma and serves to increase both the current in the gap and the magnitude of the far-field THz radiation [28]. Beyond a voltage of $V_b = 230$ V$_{\text{p-p}}$ photo-carrier avalanche multiplication drives the carrier density above the damage threshold for the material, causing irreversible damage in the PC gap.

To determine the pump power saturation characteristics of the polycrystalline ZnSe THz emitter, the THz source is biased at a voltage of 230 V$_{\text{p-p}}$, and the average optical pump power is increased from 20 mW to 160 mW. Given a spot size of 3 μm, these pump powers correspond to energy fluences of $E_p = 3.5$ mJ/cm^2 to $E_p = 28.3$ mJ/cm^2. The resulting peak-to-peak THz field amplitudes are shown in figure 3.4.2.3 as a function of the incident energy fluence. It is readily apparent from this figure that the measured THz powers increase along with the pump power. Furthermore, the relationship between the THz field and the fluence shows no indication of saturation–even at an excitation level of 28 mJ/cm^2 (which is in agreement with the model presented in section 3.4.1). It is interesting to note that, according to this model and other studies on GaAs THz sources [37], GaAs dipole emitters saturate at or below a pump energy fluence of only $E_p = 0.5$ mJ/cm^2. In comparison, ZnSe THz emitters have a large dark resistivity

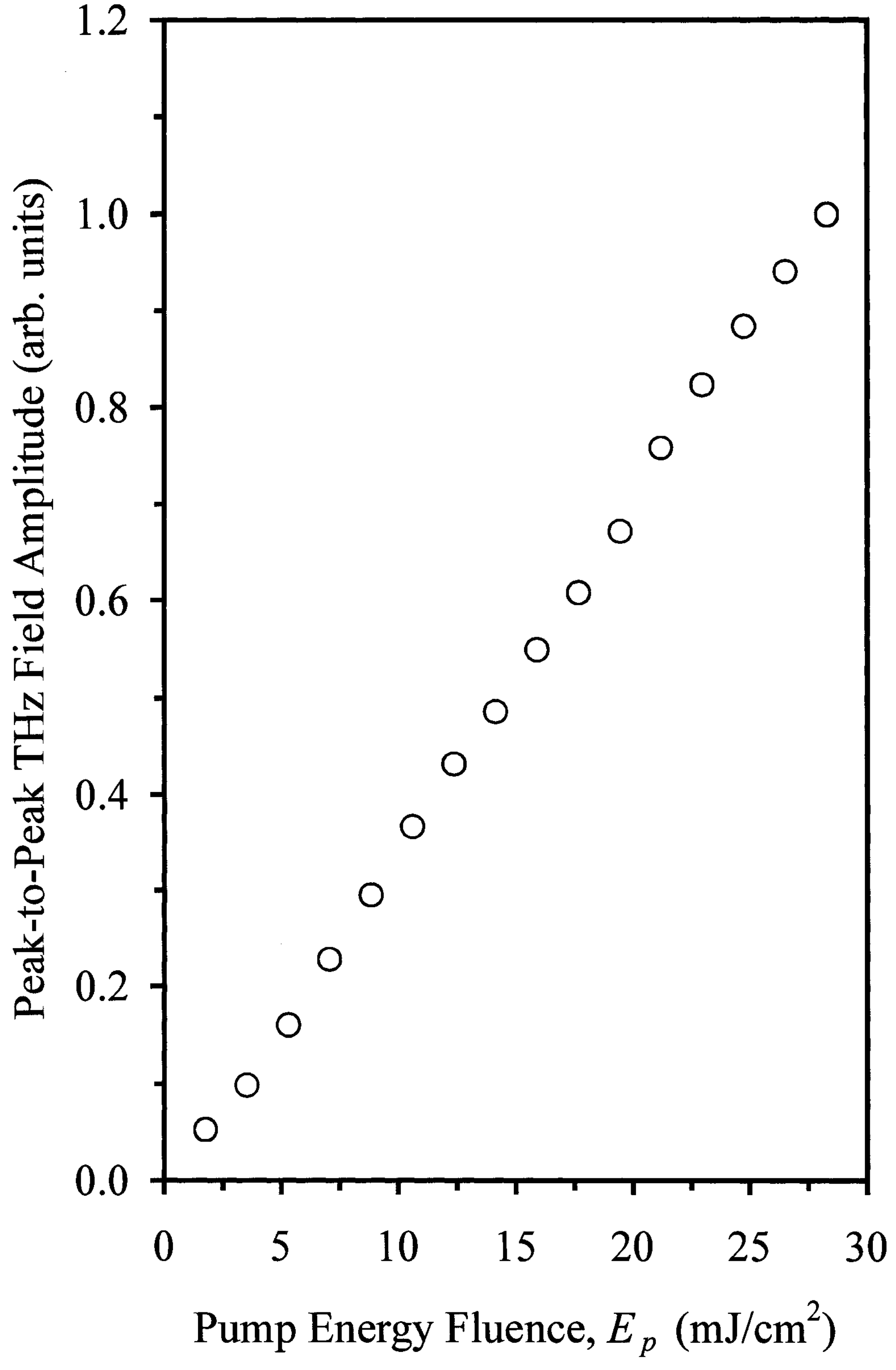

Figure 3.4.2.3 Measured peak-to-peak THz amplitudes as a function of the incident energy fluence, E_p, for the ZnSe dipole THz emitter. A bias voltage of V_b = 230 $V_{p\text{-}p}$ is applied to the L_x = 9 μm PC gap (yielding a bias electric field strength of E_b = 128 kV/cm).

(10^{12} Ω·cm) and a subsequent lack of thermally-excited electrons. This suspends the onset of thermal run-away and surface flashover, allowing for the application of peak bias fields up to 128 kV/cm and optical fluences up to 28.3 mJ/cm^2. It is expected, therefore, that ZnSe PC THz emitters can be made to produce extremely large THz powers by simply increasing both the optical fluence (with amplified optical pump sources) and the cross-sectional area of the THz emitter (with large-aperture THz emitters).

3.5 ZnSe Electro-Optic Terahertz Detectors

3.5.1 Theoretical Framework

Since its introduction, free-space EO sampling of ultrafast electromagnetic transients [38]-[41] has become a vital tool in the detection of coherent THz radiation. Compared to far-infrared detection techniques such as bolometric detection [42], free-space EO sampling provides high-sensitivity amplitude and phase information as well as an ultrawide detection bandwidth. The successful application of this technique does, however, require a nonlinear material with a large EO coefficient–for a high amplitude–and low group velocity mismatch between the probe beam and the THz beam–for a broad detection bandwidth.

Initial attempts at free-space EO sampling focused on the application of ionic nonlinear crystals, such as $LiTaO_3$, because of their large EO coefficients [38]. Unfortunately, the high static dielectric constants associated with ionic crystals do not allow for efficient phase-matching between the group velocity of the probe pulse and the phase velocity of the THz pulse. $LiTaO_3$, for example, has a probe group velocity of $(3\times10^8 m/s)/2.18 = 1.38\times10^8 m/s$ and a THz phase velocity of $(3\times10^8 m/s)/\sqrt{44} = 0.45\times10^8 m/s$, yielding an inter-pulse dispersion of 15 ps/mm. To overcome the deficiencies of ionic crystal detectors, therefore, contemporary THz sampling schemes often incorporate covalent zinc-blende crystals. Zinc-blende sensors offer reasonable nonlinear EO coefficients in addition to low static dielectric constants. EO sampling in ZnTe [40], for example, has a velocity mismatch of only 1 ps/mm (given a probe velocity of 1.05 x 10^8 m/s and a THz velocity of 0.94 x 10^8 m/s). For this reason, ZnTe has become the standard EO sensor used in free-space THz detection.

This section explores the possibility of utilizing ZnSe crystals rather than ZnTe crystals as THz EO sensors. ZnSe EO crystals offer EO coefficients and levels of group velocity mismatch that are comparable to that of ZnTe. On the other hand, the vibrational TO phonon resonance frequency (ν_{TO} = 6.15 THz) of ZnSe is higher than that of ZnTe (ν_{TO} = 5.31 THz), allowing for an increased potential bandwidth. Furthermore, the fabrication of ZnSe sensors is far more practical, as it can be accomplished with CVD growth processes, rather than physical vapour deposition (PVD) growth processes [43].

Given that the EO sampling mechanism for the THz signal is based upon an electric field induced birefringence, it is necessary to understand the relationship between the orientation of the EO crystal lattice and the resulting phase retardation. For a thorough analysis of ZnSe EO detectors, therefore, the following three sub-sections analyze the differential THz signals measured for <100>, <110>, and <111> ZnSe EO crystals. Specifically, the relationship between the crystal azimuthal angle and the emitted THz power is analyzed (given horizontally polarized THz and probe beams) to obtain a greater understanding of the optimal alignment required for detection with each of these sensors.

3.5.1.1 Electro-Optic Detection with <100> ZnSe Sensors

The most common commercially available zinc-blende lattice orientation is the <100> structure. For this reason, the EO response from the <100> ZnSe sensor is studied first. The sampling geometry for this crystal is shown in figure 3.5.1.1.1. To start with, the THz field-induced birefringence exhibited by the ZnSe sensor is linked to the THz electric field strength through the EO tensor

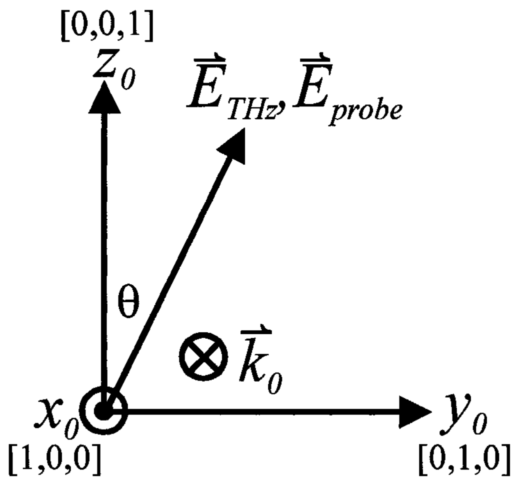

The laboratory coordinate system (x_0,y_0,z_0). The (x_0,y_0,z_0) directions are aligned with the basis vectors of the <100> unit cell. The THz beam and probe beam both enter the crystal at an angle θ with respect to the z_0 axis.

Figure 3.5.1.1.1 Coordinate system for the <100> ZnSe lattice.

$$r_{ij} = \begin{bmatrix} 0 & 0 & 0 \\ 0 & 0 & 0 \\ 0 & 0 & 0 \\ r_{41} & 0 & 0 \\ 0 & r_{41} & 0 \\ 0 & 0 & r_{41} \end{bmatrix}. \qquad (3.5.1.1.1)$$

Here, r_{41} = 2 pm/V is the only non-zero EO component for ZnSe [44]. In this representation, the probe beam and THz beam share the same beam path (the $-\vec{x}_0$ direction) and the same polarization (at an azimuthal rotation angle, θ, with respect to the z_0 basis vector of the <100> unit cell). Using the THz field-dependent impermeability tensor,

$$\eta_{ij}\left(\vec{E}_{THz}\right) = \eta_{ij}(0) + \sum_k r_{ijk} E_{THz\,k}\,, \qquad (3.5.1.1.2)$$

and the general expression for the THz electric field in the laboratory coordinate system (x_0,y_0,z_0),

$$\vec{E}_{THz} = E_{THz}\sin\theta\;\hat{y}_0 + E_{THz}\cos\theta\;\hat{z}_0\,, \qquad (3.5.1.1.3)$$

the modified index ellipsoid,

$$\sum_{ij} \eta_{ij}\left(\vec{E}_{THz}\right) x_i x_j = 1\,, \qquad (3.5.1.1.4)$$

may be expressed as

$$\frac{x_0^2}{n_{ZnSe}^2} + \frac{y_0^2}{n_{ZnSe}^2} + \frac{z_0^2}{n_{ZnSe}^2} + 2r_{41}E_{THz}\sin\theta\;x_0 z_0 + 2r_{41}E_{THz}\cos\theta\;x_0 y_0 = 1\,, \qquad (3.5.1.1.5)$$

where n_{ZnSe} is the static refractive index of the ZnSe crystal. By setting $x_0 = 0$ in the above expression, the normal modes for propagation through the (100) plane are determined. In this case, the index ellipsoid becomes

$$\frac{y_0^2}{n_{ZnSe}^2}+\frac{z_0^2}{n_{ZnSe}^2}=1, \tag{3.5.1.1.6}$$

suggesting that there is no THz-induced birefringence between the refractive indices of the principal axes

$$n_{y0}=n_{ZnSe} \tag{3.5.1.1.7}$$

and

$$n_{z0}=n_{ZnSe}\,. \tag{3.5.1.1.8}$$

Indeed, a <100> crystal cannot be used to map the THz electric field onto the polarization state of the probe beam for transverse EO sampling geometries, as the THz-induced phase retardation imparted onto the probe beam,

$$\Gamma_{<100>}=0, \tag{3.5.1.1.9}$$

is nonexistent. Similarly, there is no THz-induced differential power measured between the orthogonally-polarized beams exiting the wallaston prism, and the differential probe power is, therefore,

$$\Delta P_{<100>}=0, \tag{3.5.1.1.10}$$

for all values of θ. Qualitatively, the lack of an EO signal in <100> ZnSe can be attributed to the centrosymmetric nature of this crystal plane. The structure of the <100> plane, shown in figure 3.5.1.1.2, exhibits an inversion symmetry–thus the second-order nonlinear polarization responsible for the transverse EO effect is not present. The resulting theoretical curve (or lack thereof) for a <100> EO sensor is shown in figure 3.5.1.1.2 as a function of the azimuthal crystal rotation angle, θ.

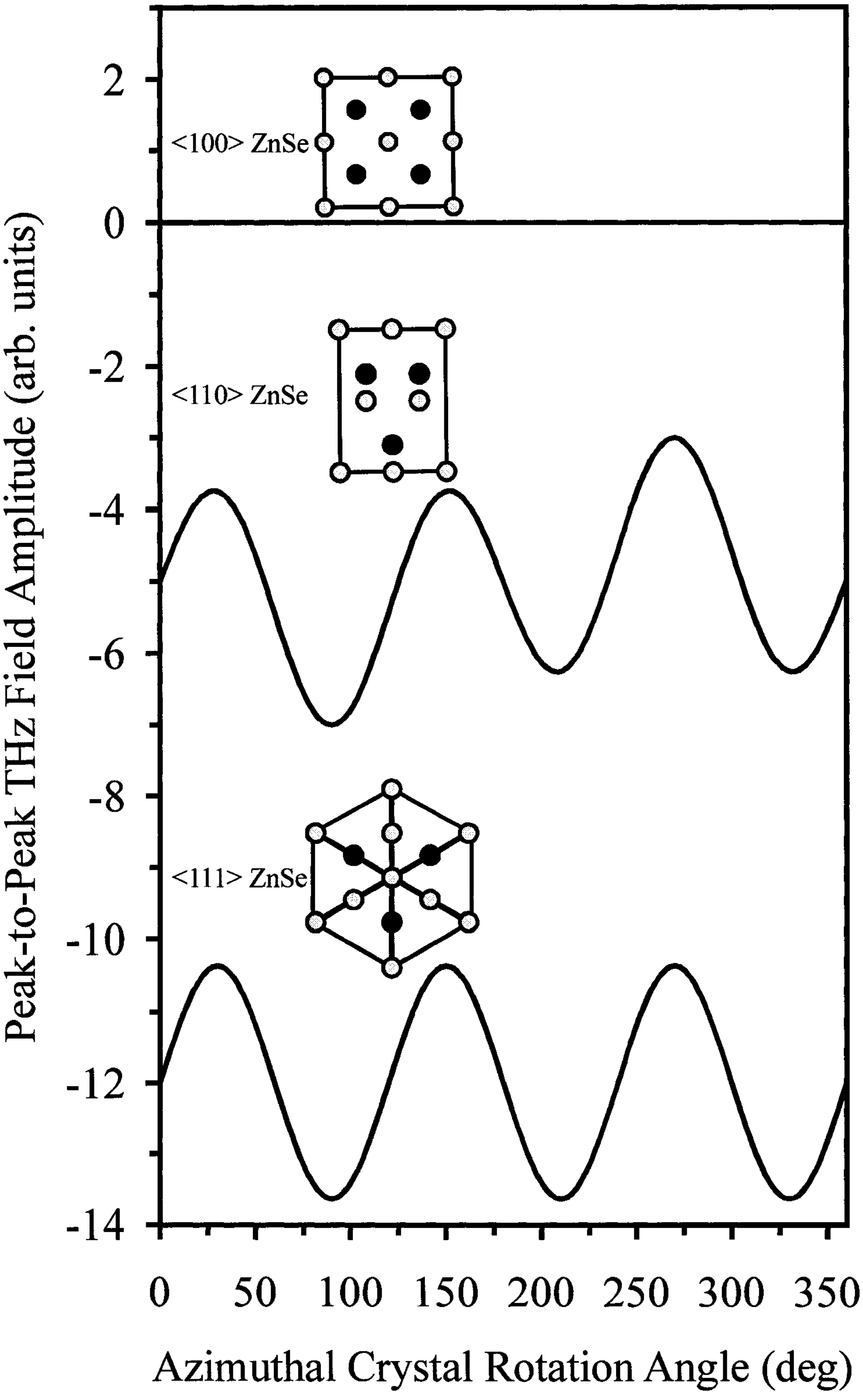

Figure 3.5.1.1.2 Theoretical EO response curves as a function of the azimuthal crystal rotation angle, θ, for <100>, <110>, and <111> ZnSe THz sensors. The planar crystal structures are shown within the figure.

3.5.1.2 Electro-Optic Detection with <110> ZnSe Sensors

The next ZnSe crystal orientation to be investigated for EO detection is the <110> crystal orientation [45]. The sampling scheme for this crystal is shown in figure 3.5.1.2.1(a). In this EO sampling geometry, the probe beam and THz beam enter the crystal along the [110] direction and are polarized at an angle, θ, from the z_0 basis vector of the laboratory coordinate system (x_0, y_0, z_0). As was the case for EO sampling in the <100> crystal, the incoming THz electric field,

$$\bar{E}_{THz} = E_{THz} \sin\theta \, \hat{y}_0 + E_{THz} \cos\theta \, \hat{z}_0 , \qquad (3.5.1.2.1)$$

is mapped onto the polarization state of the probe by way of the field-dependent impermeability tensor in equation 3.5.1.1.2. Using the expression for the THz electric field in the crystallographic coordinate system (x_1, y_1, z_1),

$$\bar{E}_{THz} = -\frac{E_{THz} \sin\theta}{\sqrt{2}} \hat{x}_1 + \frac{E_{THz} \sin\theta}{\sqrt{2}} \hat{y}_1 + E_{THz} \cos\theta \, \hat{z}_1 , \qquad (3.5.1.2.2)$$

the index ellipsoid,

$$\begin{aligned} &\frac{x_1^2}{n^2} + \frac{y_1^2}{n^2} + \frac{z_1^2}{n^2} - \sqrt{2} r_{41} E_{THz} \sin\theta \, y_1 z_1 + \sqrt{2} r_{41} E_{THz} \sin\theta \, x_1 z_1 \\ &+ 2 r_{41} E_{THz} \cos\theta \, x_1 y_1 = 1, \end{aligned} \qquad (3.5.1.2.3)$$

is determined. This expression can be rewritten for propagation of the probe beam through the (110) plane by transforming the axes to the laboratory coordinate system and setting $x_0 = 0$. The result is

$$y_0^2 \left(\frac{1}{n_{ZnSe}^2} - r_{41} E_{THz} \cos\theta \right) + z_0^2 \left(\frac{1}{n_{ZnSe}^2} \right) + y_0 z_0 \left(-2 r_{41} E_{THz} \sin\theta \right) = 1 . \qquad (3.5.1.2.4)$$

To eliminate the $y_0 z_0$ crossterm in the above equation and find the principal axes for propagation of the probe beam, the coordinate system is rotated about the x_0 axis by an

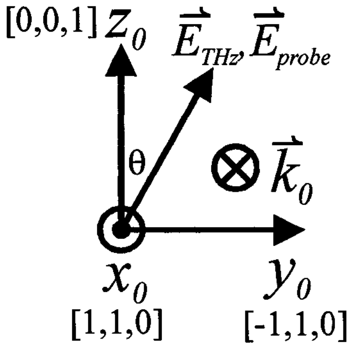

(a)
The laboratory coordinate system (x_0,y_0,z_0). The crystallographic coordinate system (x_1,y_1,z_1) is aligned with the basis vectors of the unit cell. The probe beam and THz beam propagate in the [110] direction and are polarized at an angle θ from the z_0 axis.

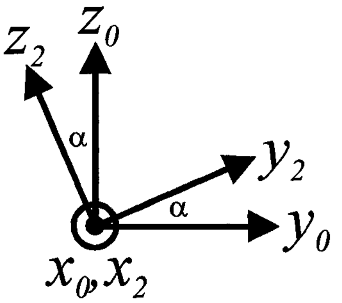

(b)
Coordinate rotation necessary to generate the principal coordinate system (x_2,y_2,z_2).

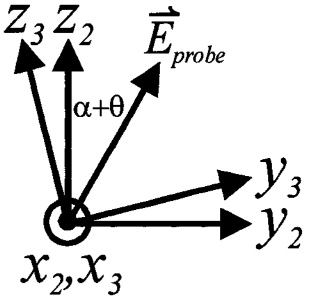

(c)
Probe beam and quarter waveplate axes (x_3,y_3,z_3) on the principal coordinate system.

Figure 3.5.1.2.1 Coordinate transformations for the <110> ZnSe lattice.

angle α (shown in figure 3.5.1.2.1(b)). The index ellipsoid becomes

$$\begin{aligned}&y_2^2\left(\frac{1}{n_{ZnSe}^2}-r_{41}E_{THz}\cos\theta\cos^2\alpha-r_{41}E_{THz}\sin\theta\sin2\alpha\right)+\\&z_2^2\left(\frac{1}{n_{ZnSe}^2}-r_{41}E_{THz}\cos\theta\sin^2\alpha+r_{41}E_{THz}\sin\theta\sin2\alpha\right)+\\&y_2z_2\left(r_{41}E_{THz}\cos\theta\sin2\alpha-2r_{41}E_{THz}\sin\theta\cos2\alpha\right)=1,\end{aligned}\tag{3.5.1.2.5}$$

which, for a coordinate rotation angle of $\alpha = \tan^{-1}(2\tan\theta)/2$, can be rewritten as

$$\begin{aligned}&y_2^2\left[\frac{1}{n_{ZnSe}^2}+r_{41}E_{THz}\left(-\frac{\cos\theta}{2}-\frac{\sqrt{1+3\sin^2\theta}}{2}\right)\right]+\\&z_2^2\left[\frac{1}{n_{ZnSe}^2}+r_{41}E_{THz}\left(-\frac{\cos\theta}{2}+\frac{\sqrt{1+3\sin^2\theta}}{2}\right)\right]=1.\end{aligned}\tag{3.5.1.2.6}$$

The corresponding principal refractive indices,

$$n_{y2}(\theta)\cong n_{ZnSe}+\frac{n_{ZnSe}^3r_{41}E_{THz}}{2}\left[\frac{\cos\theta}{2}+\frac{\sqrt{1+3\sin^2\theta}}{2}\right]\tag{3.5.1.2.7}$$

and

$$n_{z2}(\theta)\cong n_{ZnSe}+\frac{n_{ZnSe}^3r_{41}E_{THz}}{2}\left[\frac{\cos\theta}{2}-\frac{\sqrt{1+3\sin^2\theta}}{2}\right],\tag{3.5.1.2.8}$$

produce a THz-induced phase retardation of

$$\Gamma_{<110>}=\frac{\pi\nu n_{ZnSe}^3r_{41}E_{THz}L\sqrt{1+3\sin^2\theta}}{c},\tag{3.5.1.2.9}$$

between the y_2 and z_2 axes in the EO crystal. Here, ν is the frequency of the probe beam, c is the speed of light in free-space, and L is the length of the crystal.

The THz-induced birefringence produced by the dissimilar refractive indices in the crystal induces a change in the polarization state of the co-propagating probe beam. To measure this phase retardation, the probe beam is directed through a quarter waveplate and wallaston prism pair. The quarter waveplate is aligned such that its slow axis and fast axis (shown in figure 3.5.1.2.1(c) as the y_3 and z_3 directions) are 45° off the incident probe beam polarization. This orientation produces a static π/2 phase retardation between the probe beam electric field exiting the EO crystal,

$$\begin{aligned}\vec{E}_{probe}(t) = E_{probe}\sin(\alpha+\theta)\exp[i(2\pi\nu\, t - k_0 n_{y2}(\theta)L)]\hat{y}_2 \\ + E_{probe}\cos(\alpha+\theta)\exp[i(2\pi\nu\, t - k_0 n_{z2}(\theta)L)]\hat{z}_2\end{aligned}, \tag{3.5.1.2.10}$$

and the probe beam electric field exiting the quarter waveplate,

$$\begin{aligned}&\vec{E}_{probe}(t) = E_{probe}\times \\ &\{\sin(\alpha+\theta)\sin(\alpha+\theta+\pi/4)\exp[i(2\pi\nu\, t - k_0 n_{y2}(\theta)L+\pi/4)] \\ &+\cos(\alpha+\theta)\cos(\alpha+\theta+\pi/4)\exp[i(2\pi\nu\, t - k_0 n_{z2}(\theta)L+\pi/4)]\}\hat{y}_3 + \\ &E_{probe}\{-\sin(\alpha+\theta)\cos(\alpha+\theta+\pi/4)\exp[i(2\pi\nu\, t - k_0 n_{y2}(\theta)L-\pi/4)] \\ &+\cos(\alpha+\theta)\sin(\alpha+\theta+\pi/4)\exp[i(2\pi\nu\, t - k_0 n_{z2}(\theta)L-\pi/4)]\}\hat{z}_3,\end{aligned} \tag{3.5.1.2.11}$$

given a free-space probe wavevector of $k_0 = 2\pi\nu/c$.

After passing through the quarter waveplate, the probe beam is split into two orthogonal polarizations by the wallaston prism (whose two transmission axes are aligned both parallel and perpendicular to the incident probe beam polarization). The first of these polarizations is parallel to the incident probe beam polarization and can be written as

$$\begin{aligned}&E_{probe1}(t) = \frac{E_{probe}}{\sqrt{2}}\times\{ \\ &+\sin(\alpha+\theta)\sin(\alpha+\theta+\pi/4)\exp[i(2\pi\nu\, t - k_0 n_{y2}(\theta)L+\pi/4)] \\ &+\cos(\alpha+\theta)\cos(\alpha+\theta+\pi/4)\exp[i(2\pi\nu\, t - k_0 n_{z2}(\theta)L+\pi/4)] \\ &-\sin(\alpha+\theta)\cos(\alpha+\theta+\pi/4)\exp[i(2\pi\nu\, t - k_0 n_{y2}(\theta)L-\pi/4)] \\ &+\cos(\alpha+\theta)\sin(\alpha+\theta+\pi/4)\exp[i(2\pi\nu\, t - k_0 n_{z2}(\theta)L-\pi/4)]\ \}.\end{aligned} \tag{3.5.1.2.12}$$

The second of these polarization components is perpendicular to the incident probe beam polarization and can be written as

$$\begin{aligned} E_{probe2}(t) = \frac{E_{probe}}{\sqrt{2}} \times \{ & \\ & -\sin(\alpha+\theta)\sin(\alpha+\theta+\pi/4)\exp[i(2\pi\nu\, t - k_0 n_{y2}L + \pi/4)] \\ & -\cos(\alpha+\theta)\cos(\alpha+\theta+\pi/4)\exp[i(2\pi\nu\, t - k_0 n_{z2}L + \pi/4)] \\ & -\sin(\alpha+\theta)\cos(\alpha+\theta+\pi/4)\exp[i(2\pi\nu\, t - k_0 n_{y2}L - \pi/4)] \\ & +\cos(\alpha+\theta)\sin(\alpha+\theta+\pi/4)\exp[i(2\pi\nu\, t - k_0 n_{z2}L - \pi/4)] \ \}. \end{aligned} \tag{3.5.1.2.13}$$

The EO signal of interest is determined, finally, by taking the difference between the power of the first probe beam,

$$\begin{aligned} P_{probe1} &= \frac{A}{\eta_o}\left\langle E_{probe1}(t) \times E^*_{probe1}(t)\right\rangle \\ &= \frac{P_{probe}}{2} + \frac{P_{probe}}{2}\sin[2(\alpha+\theta)]\sin\left[\frac{2\pi\nu}{c}\left(n_{y2}(\theta) - n_{z2}(\theta)\right)L\right], \end{aligned} \tag{3.5.1.2.14}$$

and the power of the second beam,

$$\begin{aligned} P_{probe2} &= \frac{A}{\eta_o}\left\langle E_{probe2}(t) \times E^*_{probe2}(t)\right\rangle \\ &= \frac{P_{probe}}{2} - \frac{P_{probe}}{2}\sin[2(\alpha+\theta)]\sin\left[\frac{2\pi\nu}{c}\left(n_{y2}(\theta) - n_{z2}(\theta)\right)L\right]. \end{aligned} \tag{3.5.1.2.15}$$

The resulting differential EO signal is found to be

$$\begin{aligned} \Delta P_{<110>} &= P_{probe1} - P_{probe2} \\ &= P_{probe}\sin[2(\alpha+\theta)]\sin\left[\frac{2\pi\nu}{c}\left(n_{y2}(\theta) - n_{z2}(\theta)\right)L\right], \end{aligned} \tag{3.5.1.2.16}$$

for a total probe power of $P_{probe} = A/(2\eta_o)\, E_{probe}^2$ (the probe beam has an area of A, and the impedance of free-space is denoted by η_o). Given that the THz field-induced phase difference is small, the second sine term in equation 3.5.1.2.16 can be expanded, and the differential power can be rewritten as

$$\Delta P_{<110>} = P_{probe}\frac{\pi\nu n^3_{ZnSe} r_{41} E_{THz} L}{c}\left(\cos\theta\sin 2\theta + 2\cos 2\theta \sin\theta\right). \tag{3.5.1.2.17}$$

The resulting THz amplitude for the <110> EO sensor is shown in figure 3.5.1.1.2 as a function of the azimuthal crystal rotation angle, θ. The overall response is seen to be fairly complex in nature–a result of the complete lack of rotational symmetry in the <110> plane (also shown in figure 3.5.1.1.2).

3.5.1.3 Electro-Optic Detection with <111> ZnSe Sensors

The final ZnSe crystal orientation to be investigated for EO detection is the <111> crystal orientation [46]. The sampling scheme for this crystal is shown in figure 3.5.1.3.1(a). In this EO sampling geometry, the probe beam and THz beam enter the crystal along the [111] direction and are polarized at an angle θ from the z_0 basis vector of the laboratory coordinate system (x_0,y_0,z_0). The incoming THz electric field,

$$\vec{E}_{THz} = E_{THz}\sin\theta\ \hat{y}_0 + E_{THz}\cos\theta\ \hat{z}_0, \tag{3.5.1.3.1}$$

can, in this case, be expressed in terms of the crystallographic coordinate system (x_1,y_1,z_1), as

$$\begin{aligned}\vec{E}_{THz} &= E_{THz}\left(-\frac{\sin\theta}{\sqrt{2}}-\frac{\cos\theta}{\sqrt{6}}\right)\hat{x}_1 + E_{THz}\left(\frac{\sin\theta}{\sqrt{2}}-\frac{\cos\theta}{\sqrt{6}}\right)\hat{y}_1 \\ &+ E_{THz}\left(\sqrt{\frac{2}{3}}\cos\theta\right)\hat{z}_1,\end{aligned} \tag{3.5.1.3.2}$$

then inserted into the field-dependent impermeability tensor in equation 3.5.1.1.2, to produce the index ellipsoid,

$$\begin{aligned}&\frac{x_1^2}{n_{ZnSe}^2}+\frac{y_1^2}{n_{ZnSe}^2}+\frac{z_1^2}{n_{ZnSe}^2}+2r_{41}E_{THz}\left[-\frac{\sin\theta}{\sqrt{2}}-\frac{\cos\theta}{\sqrt{6}}\right]y_1z_1 \\ &+2r_{41}E_{THz}\left[\frac{\sin\theta}{\sqrt{2}}-\frac{\cos\theta}{\sqrt{6}}\right]x_1z_1+2r_{41}E_{THz}\left[\sqrt{\frac{2}{3}}\cos\theta\right]x_1y_1=1.\end{aligned} \tag{3.5.1.3.3}$$

By transforming this expression into the laboratory coordinate system (x_0,y_0,z_0) and

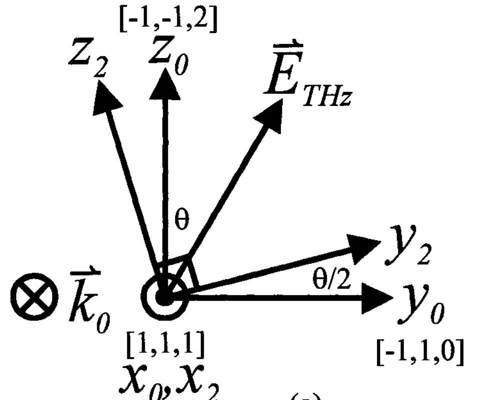

(a)

The THz electric field is shown in the laboratory coordinate system (x_0, y_0, z_0) and the rotated coordinate system (x_2, y_2, z_2). The laboratory coordinate system is aligned with the [-1,-1,2],[-1,1,0],[1,1,1] directions in the crystallographic coordinate system (x_l, y_l, z_l).

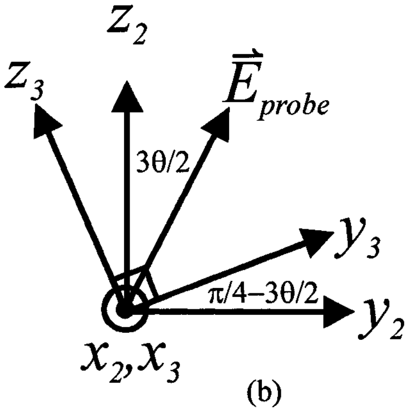

(b)

The probe electric field is shown in the principal coordinate system (x_2, y_2, z_2) and the quarter waveplate coordinate system (x_3, y_3, z_3).

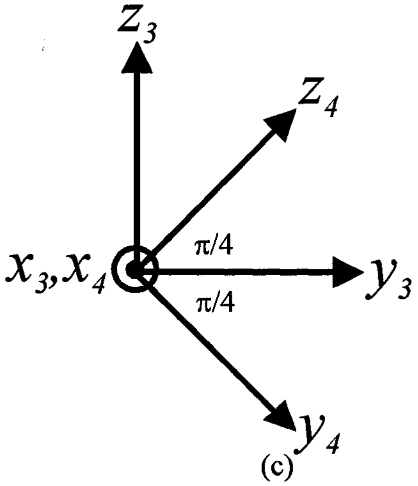

(c)

The coordinate systems for the quarter waveplate (x_3, y_3, z_3) and wallaston prism polarizers (x_4, y_4, z_4) are shown.

Figure 3.5.1.3.1 Coordinate transformations for the <111> ZnSe lattice.

setting $x_0 = 0$, the index ellipsoid in the (111) plane is found to be

$$\begin{aligned} &y_0^2\left(\frac{1}{n_{ZnSe}^2}-\sqrt{\frac{2}{3}}r_{41}E_{THz}\cos\theta\right)+z_0^2\left(\frac{1}{n_{ZnSe}^2}+\sqrt{\frac{2}{3}}r_{41}E_{THz}\cos\theta\right) \\ &+y_0z_0\left(-\sqrt{\frac{8}{3}}r_{41}\right)E_{THz}\sin\theta=1. \end{aligned} \tag{3.5.1.3.4}$$

A final coordinate transformation of $\hat{y}_0 = \hat{y}_2\cos\theta/2 - \hat{z}_2\sin\theta/2$ and $\hat{z}_0 = \hat{y}_2\sin\theta/2 + \hat{z}_2\cos\theta/2$, corresponding to a rotation of $\theta/2$ about the x_0 axis, eliminates the y_0z_0 crossterm and yields the index ellipsoid,

$$y_2^2\left(\frac{1}{n_{ZnSe}^2}-\sqrt{\frac{2}{3}}r_{41}E_{THz}\right)+z_2^2\left(\frac{1}{n_{ZnSe}^2}+\sqrt{\frac{2}{3}}r_{41}E_{THz}\right)=1, \tag{3.5.1.3.5}$$

with principal refractive indices of

$$n_{y2}(\theta)\cong n_{ZnSe}+\frac{1}{\sqrt{6}}n_{ZnSe}^3r_{41}E_{THz} \tag{3.5.1.3.6}$$

and

$$n_{z2}(\theta)\cong n_{ZnSe}-\frac{1}{\sqrt{6}}n_{ZnSe}^3r_{41}E_{THz}. \tag{3.5.1.3.7}$$

The principal refractive indices defined above represent the normal modes for propagation through the crystal. The probe beam electric field that exits the EO crystal,

$$\begin{aligned} \vec{E}_{probe}(t)= {}&E_{probe}\sin(3\theta/2)\exp[i(2\pi\nu\, t-k_0n_{y2}(\theta)L)]\hat{y}_2 \\ &+E_{probe}\cos(3\theta/2)\exp[i(2\pi\nu\, t-k_0n_{z2}(\theta)L)]\hat{z}_2, \end{aligned} \tag{3.5.1.3.8}$$

is modified by this THz-induced birefringence, and the resulting phase retardation,

$$\Gamma_{<111>}=\sqrt{\frac{8}{3}}\frac{\pi\nu n_{ZnSe}^3r_{41}E_{THz}L}{c}, \tag{3.5.1.3.9}$$

is measured through the quarter waveplate and wallaston prism pair. The slow axis and fast axis for the quarter waveplate are 45^0 off the incident probe beam polarization and are aligned with the y_3 and z_3 axes shown in figure 3.5.1.3.1(b). By applying the coordinate transformation $\hat{y}_2 = \cos(3\theta/2 - \pi/4)\ \hat{y}_3 + \sin(3\theta/2 - \pi/4)\ \hat{z}_3$ and $\hat{z}_2 = -\sin(3\theta/2 - \pi/4)\ \hat{y}_3 + \cos(3\theta/2 - \pi/4)\ \hat{z}_3$ to equation 3.5.1.3.8 and by introducing a $\pi/2$ phase shift, the electric field of the probe beam that exits the quarter waveplate is found to be

$$\begin{aligned}
&\vec{E}_{probe}(t) = \\
&+E_{probe}\{\sin(3\theta/2)\cos(3\theta/2-\pi/4)\exp[i(2\pi\nu\ t-k_0 n_{y2}(\theta)L+\pi/4)] \\
&-\cos(3\theta/2)\sin(3\theta/2-\pi/4)\exp[i(2\pi\nu\ t-k_0 n_{z2}(\theta)L+\pi/4)]\}\hat{y}_3 \\
&+E_{probe}\{\sin(3\theta/2)\sin(3\theta/2-\pi/4)\exp[i(2\pi\nu\ t-k_0 n_{y2}(\theta)L-\pi/4)] \\
&+\cos(3\theta/2)\cos(3\theta/2-\pi/4)\exp[i(2\pi\nu\ t-k_0 n_{z2}(\theta)L-\pi/4)]\}\hat{z}_3.
\end{aligned} \tag{3.5.1.3.10}$$

Finally, the wallaston prism splits the probe beam into two orthogonal polarizations: one that is parallel to the incident probe polarization (along the z_4 direction in figure 3.5.1.3.1(c)) and one that is perpendicular to the incident probe polarization (along the y_4 direction in figure 3.5.1.3.1(c)). The resulting electric field components become

$$\begin{aligned}
&E_{probe1}(t) = \frac{E_{probe}}{\sqrt{2}} \times \{ \\
&+\sin(3\theta/2)\cos(3\theta/2-\pi/4)\exp[i(2\pi\nu\ t-k_0 n_{y2}(\theta)L+\pi/4)] \\
&-\cos(3\theta/2)\sin(3\theta/2-\pi/4)\exp[i(2\pi\nu\ t-k_0 n_{z2}(\theta)L+\pi/4)] \\
&-\sin(3\theta/2)\sin(3\theta/2-\pi/4)\exp[i(2\pi\nu\ t-k_0 n_{y2}(\theta)L-\pi/4)] \\
&-\cos(3\theta/2)\cos(3\theta/2-\pi/4)\exp[i2\pi\nu\ t-k_0 n_{z2}(\theta)L-\pi/4]\ \}
\end{aligned} \tag{3.5.1.3.11}$$

and

$$\begin{aligned}
&E_{probe2}(t) = \frac{E_{probe}}{\sqrt{2}} \times \{ \\
&+\sin(3\theta/2)\cos(3\theta/2-\pi/4)\exp[i(2\pi\nu\ t-k_0 n_{y2}(\theta)L+\pi/4)] \\
&-\cos(3\theta/2)\sin(3\theta/2-\pi/4)\exp[i(2\pi\nu\ t-k_0 n_{z2}(\theta)L+\pi/4)] \\
&+\sin(3\theta/2)\sin(3\theta/2-\pi/4)\exp[i(2\pi\nu\ t-k_0 n_{y2}(\theta)L-\pi/4)] \\
&+\cos(3\theta/2)\cos(3\theta/2-\pi/4)\exp[i(2\pi\nu\ t-k_0 n_{z2}(\theta)L-\pi/4)]\ \}.
\end{aligned} \tag{3.5.1.3.12}$$

The power difference between the first output polarization,

$$\begin{aligned} P_{probe1} &= \frac{A}{2\eta_o}\left\langle E_{probe1}(t)\times E^*_{probe1}(t)\right\rangle \\ &= \frac{P_{probe}}{2}+\frac{P_{probe}}{2}\sin[3\theta]\sin\left[\frac{2\pi\nu}{c}\left(n_{y2}(\theta)-n_{z2}(\theta)\right)L\right], \end{aligned} \tag{3.5.1.3.13}$$

and the second output polarization,

$$\begin{aligned} P_{probe2} &= \frac{A}{2\eta_o}\left\langle E_{probe2}(t)\times E^*_{probe2}(t)\right\rangle \\ &= \frac{P_{probe}}{2}-\frac{P_{probe}}{2}\sin[3\theta]\sin\left[\frac{2\pi\nu}{c}\left(n_{y2}(\theta)-n_{z2}(\theta)\right)L\right], \end{aligned} \tag{3.5.1.3.14}$$

yields a differential EO signal of

$$\begin{aligned} \Delta P_{<111>} &= P_{probe1}-P_{probe2} = P_{probe}\sin\left[\frac{2\pi\nu}{c}\left(n_{y2}(\theta)-n_{z2}(\theta)\right)L\right]\sin 3\theta \\ &\cong P_{probe}\sqrt{\frac{8}{3}}\frac{2\pi\nu n^3 r_{41}E_{THz}L}{c}\sin 3\theta. \end{aligned} \tag{3.5.1.3.15}$$

The three-fold symmetry described by equation 3.5.1.3.15 is readily apparent from the structure of the <111> crystal plane shown in figure 3.5.1.1.2. The 120^0 rotational symmetry of this plane manifests itself as the three-fold symmetric EO response shown in figure 3.5.1.1.2 as a function of the azimuthal crystal rotation angle, θ.

3.5.2 Experimental Framework

To obtain the maximum possible THz signal strength it is important to understand the relationship between the orientation of the EO crystal lattice and the resulting THz-induced birefringence. Indeed, EO detection results, such as the theoretical results shown in the previous section, are highly dependent upon both the orientation of the zinc-blende lattice (whether it be <100>, <110>, or <111>) and the azimuthal rotation angle of this lattice with respect to the THz and probe polarizations. To gain further insight into this topic and test the validity of the theoretical investigation in section 3.5.1, this section investigates the measured THz field strength as a function of the azimuthal rotation angle of the <100>, <110>, and <111> ZnSe EO crystals. In addition, section 3.5.2.4 demonstrates, for the first time, the possibility of using polycrystalline ZnSe EO sensors.

3.5.2.1 Electro-Optic Detection with <100> ZnSe Sensors

In section 3.5.1.1, it was determined that transverse EO sampling in <100> ZnSe crystals does not produce a THz electric field-induced polarization signal. To test this theoretical assertion, a 500 μm thick <100> ZnSe crystal is inserted in the free-space THz generation and detection system for analysis. As was the case for section 3.3, photo-excitation of the 100 μm wide GaAs THz emitter is provided by a 160 mW pump beam, and EO detection is carried out using horizontally polarized THz and probe beams. The peak-to-peak THz electric field strength is measured as the EO sensor is rotated. A typical THz waveform corresponding to the maximum achievable amplitude is shown at the top of figure 3.5.2.1.1, and the peak-to-peak THz amplitudes for the <100> sensor are shown in figure 3.5.2.1.2 as a function of the azimuthal rotation angle, θ.

As described in section 3.5.1.1, the EO detection of THz fields in <100> zinc-blende structures is theoretically characterized by a total lack of measured signals. Even though the results in figures 3.5.2.1.1 and 3.5.2.1.2 show a small differential current signal level (between –7 nA and +7 nA), the fact that the signal even exists is a contradiction to this theoretical assertion. In addition to this, the azimuthal symmetry exhibited by the rotated sensor is two-fold in nature, which is theoretically impossible for a transverse EO modulator (as the EO effect is fundamentally based upon the presence of

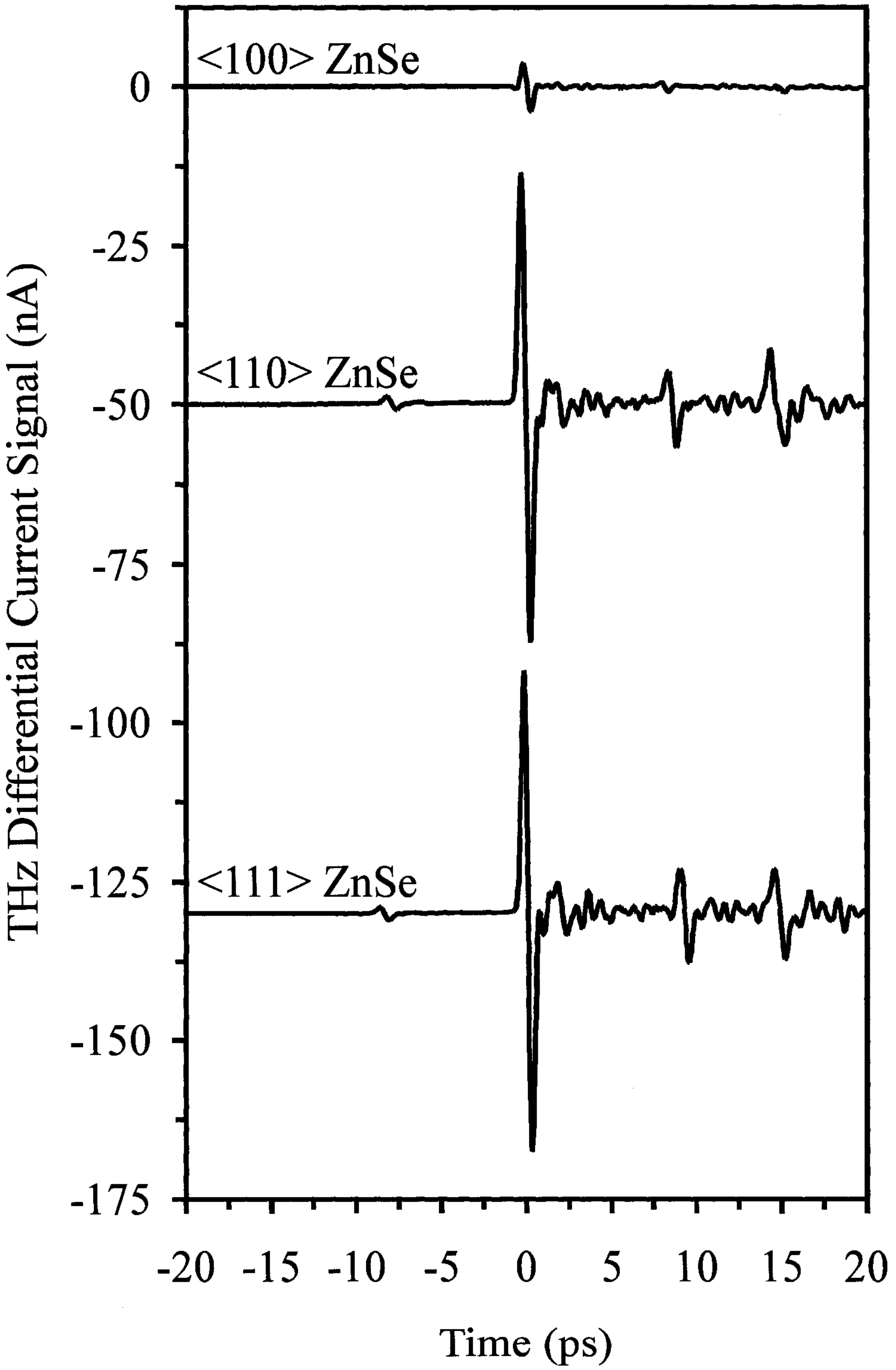

Figure 3.5.2.1.1 Free-space THz waveforms measured using 500 μm thick <100>, <110>, and <111> ZnSe sensors. The time-domain waveforms shown are measured using the optimal EO crystal rotation angle. The 100 μm wide GaAs PC THz emitter is illuminated by a 160 mW pump beam. The artifacts at 8 and 15 ps are due to successive reflections of the THz beam in the EO crystal.

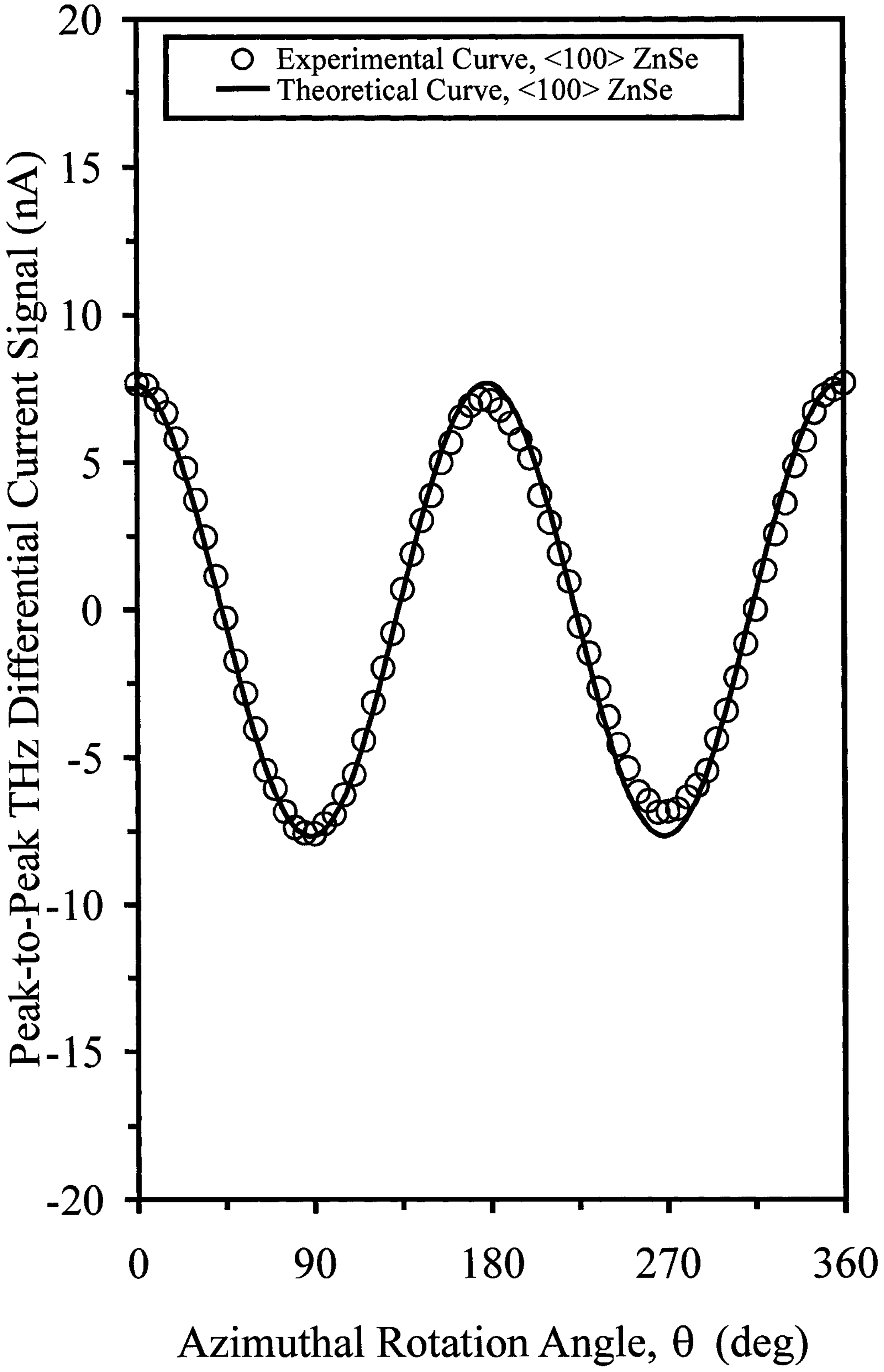

Figure 3.5.2.1.2 Peak-to-peak THz electric field amplitudes as a function of the azimuthal crystal rotation angle, θ, for a 500 μm thick <100> ZnSe sensor.

an inversion symmetry in the crystal lattice). The fact that the EO symmetry shown in figure 3.5.2.1.2 requires an identical crystal structure after a rotation of 180°, means that a transverse the EO effect cannot be at work. It is apparent, therefore, that the THz waveform is being mapped onto the polarization state of the probe through a technique other than the transverse EO effect.

It is likely that the existence of the finite THz signal in figures 3.5.2.1.1 and 3.5.2.1.2 is due to the existence of a non-transverse THz electric field component in the ZnSe crystal. A longitudinal electric field component could, for example, be introduced into the EO sampling process and create the small but finite THz signal. To test this assertion, the EO analysis carried out in section 3.5.1.1, can be repeated with a longitudinal THz electric field component, $E_{THz,long}$, in the direction of propagation of the probe. Here, the general expression for this longitudinal component,

$$\bar{E}_{THz,long} = -E_{THz,long}\hat{x}_0 , \tag{3.5.2.1.1}$$

is inserted into the field-dependent impermeability tensor to give the modified index ellipsoid,

$$\frac{x_0^2}{n_{ZnSe}^2} + \frac{y_0^2}{n_{ZnSe}^2} + \frac{z_0^2}{n_{ZnSe}^2} - 2r_{41}E_{THz,long}\,y_0 z_0 = 1 . \tag{3.5.2.1.2}$$

This expression can be rewritten in the principal axes coordinate system for the (100) plane using a 45^0 coordinate rotation about the x_0 axis. With the corresponding transformation, $x_0 = 0$, $y_0 = (y_1 + z_1)/\sqrt{2}$, and $z_0 = (-y_1 + z_1)/\sqrt{2}$, the modified index ellipsoid becomes

$$y_1^2\left(\frac{1}{n_{ZnSe}^2} + r_{41}E_{THz,long}\right) + z_1^2\left(\frac{1}{n_{ZnSe}^2} - r_{41}E_{THz,long}\right) = 1 , \tag{3.5.2.1.3}$$

with corresponding principal refractive indices of

$$n_{y1} = n_{ZnSe} - \frac{1}{2} n_{ZnSe}^3 r_{41} E_{THz,long} \tag{3.5.2.1.4}$$

and

$$n_{z1} = n_{ZnSe} + \frac{1}{2} n_{ZnSe}^3 r_{41} E_{THz,long} . \tag{3.5.2.1.5}$$

For a probe beam polarized at an angle θ from the z_0 axis, the THz-induced phase retardation between the y_1 and z_1 axes is

$$\Gamma_{<100>,long} = \frac{2\pi \nu n_{ZnSe}^3 r_{41} E_{THz} L}{c} . \tag{3.5.2.1.6}$$

To detect this retardation, the probe beam is directed through a quarter waveplate and wallaston prism pair (where, again, the quarter waveplate is aligned such that its slow axis and fast axis are 45^0 off the incident probe beam polarization). The electric field of the probe beam that exits the EO crystal,

$$\begin{aligned} \vec{E}_{probe}(t) = & -E_{probe} \sin(\pi/4 - \theta) \exp[i(2\pi\nu\, t - k_0 n_{y1} L)] \hat{y}_1 \\ & + E_{probe} \cos(\pi/4 - \theta) \exp[i(2\pi\nu\, t - k_0 n_{z1} L)] \hat{z}_1 \end{aligned} , \tag{3.5.2.1.7}$$

is biased by this π/2 phase shift to become,

$$\begin{aligned} \vec{E}_{probe}(t) = & \\ & + E_{probe} \{ -\sin\theta \sin(\pi/4 - \theta) \exp[i(2\pi\nu\, t - k_0 n_{y1} L + \pi/4)] \\ & \qquad + \cos\theta \cos(\pi/4 - \theta) \exp[i(2\pi\nu\, t - k_0 n_{z1} L + \pi/4)] \} \hat{y}_2 \\ & + E_{probe} \{ \cos\theta \sin(\pi/4 - \theta) \exp[i(2\pi\nu\, t - k_0 n_{y1} L - \pi/4)] \\ & \qquad + \sin\theta \cos(\pi/4 - \theta) \exp[i(2\pi\nu\, t - k_0 n_{z1} L - \pi/4)] \} \hat{z}_2 . \end{aligned} \tag{3.5.2.1.8}$$

Next, the probe beam is split into two orthogonal polarizations by the wallaston prism: the first polarization, which is perpendicular to the incident probe polarization, has an electric field component of

$$\begin{aligned} E_{probe1}(t) = \frac{E_{probe}}{\sqrt{2}} \times \{ & \\ & -\sin\theta \sin(\pi/4 - \theta) \exp[i(2\pi\nu\, t - k_0 n_{y1} L + \pi/4)] \\ & +\cos\theta \cos(\pi/4 - \theta) \exp[i(2\pi\nu\, t - k_0 n_{z1} L + \pi/4)] \\ & -\cos\theta \sin(\pi/4 - \theta) \exp[i(2\pi\nu\, t - k_0 n_{y1} L - \pi/4)] \\ & -\sin\theta \cos(\pi/4 - \theta) \exp[i(2\pi\nu\, t - k_0 n_{z1} L - \pi/4)] \ \} \end{aligned} \tag{3.5.2.1.9}$$

associated with it, while the second polarization, which is parallel to the incident probe polarization, has an electric field component of

$$\begin{aligned} E_{probe2}(t) = \frac{E_{probe}}{\sqrt{2}} \times \{ & \\ & -\sin\theta \sin(\pi/4 - \theta) \exp[i(2\pi\nu\, t - k_0 n_{y1} L + \pi/4)] \\ & +\cos\theta \cos(\pi/4 - \theta) \exp[i(2\pi\nu\, t - k_0 n_{z1} L + \pi/4)] \\ & +\cos\theta \sin(\pi/4 - \theta) \exp[i(2\pi\nu\, t - k_0 n_{y1} L - \pi/4)] \\ & +\sin\theta \cos(\pi/4 - \theta) \exp[i(2\pi\nu\, t - k_0 n_{z1} L - \pi/4)] \ \} \end{aligned} \tag{3.5.2.1.10}$$

associated with it. By extracting the probe power difference between the power of the second beam,

$$\begin{aligned} P_{probe2} &= \frac{A}{\eta_o} \left\langle E_{probe2}(t) \times E^*_{probe2}(t) \right\rangle \\ &= \frac{P_{probe}}{2} + \frac{P_{probe}}{2} \cos 2\theta \sin\left[\frac{2\pi\nu}{c} (n_{z1} - n_{y1}) L \right], \end{aligned} \tag{3.5.2.1.11}$$

and the power of the first beam,

$$\begin{aligned} P_{probe1} &= \frac{A}{\eta_o} \left\langle E_{probe1}(t) \times E^*_{probe1}(t) \right\rangle \\ &= \frac{P_{probe}}{2} - \frac{P_{probe}}{2} \cos 2\theta \sin\left[\frac{2\pi\nu}{c} (n_{z1} - n_{y1}) L \right], \end{aligned} \tag{3.5.2.1.12}$$

the differential EO signal is found to be

$$\Delta P_{<100>,long} = P_{probe2} - P_{probe1} = P_{probe}\cos 2\theta \sin\left[\frac{2\pi\nu}{c}\left(n_{z1} - n_{y1}\right)L\right]$$
$$\cong P_{probe}\frac{2\pi\nu n_{ZnSe}^{3} r_{41} E_{THz} L}{c}\cos 2\theta. \qquad (3.5.2.1.13)$$

This theoretical EO response is plotted in figure 3.5.2.1.2. The two-fold symmetric nature of the theoretical curve (sold line) is readily apparent and is found to agree well with the experimental curve (open circles). Clearly, the existence of a longitudinal component of the THz electric field can, therefore, explain the finite EO signal and its corresponding two-fold inversion symmetry. The physical source of this longitudinal field component can be understood through a variance between the focal plane of the second parabolic mirror and the location of the EO crystal. By refocusing the probe beam as it reflects off the parabolic mirror and by positioning the EO crystal within the new beam waist, this longitudinal component of the THz electric field can be minimized, and the EO signal detected by the <100> ZnSe sensor can be eliminated.

3.5.2.2 Electro-Optic Detection with <110> ZnSe Sensors

Detection of free-space THz radiation is investigated next with a 500 μm thick <110> ZnSe detector. Again, the average pump power is set at 160 mW, and the THz waveform is monitored as the azimuthal crystal orientation angle, *θ*, is rotated. The free-space THz waveform, corresponding to the maximum achievable signal strength, is shown in figure 3.5.2.1.1, while the resulting peak-to-peak THz signal amplitudes, that vary between +76 nA and –76 nA, are shown as the open circles in figure 3.5.2.2.1. The theoretical azimuthal response, derived in section 3.5.1.2 for <110> zinc-blende structures, is shown in the figure (solid curve) and is in excellent agreement with the experimental response.

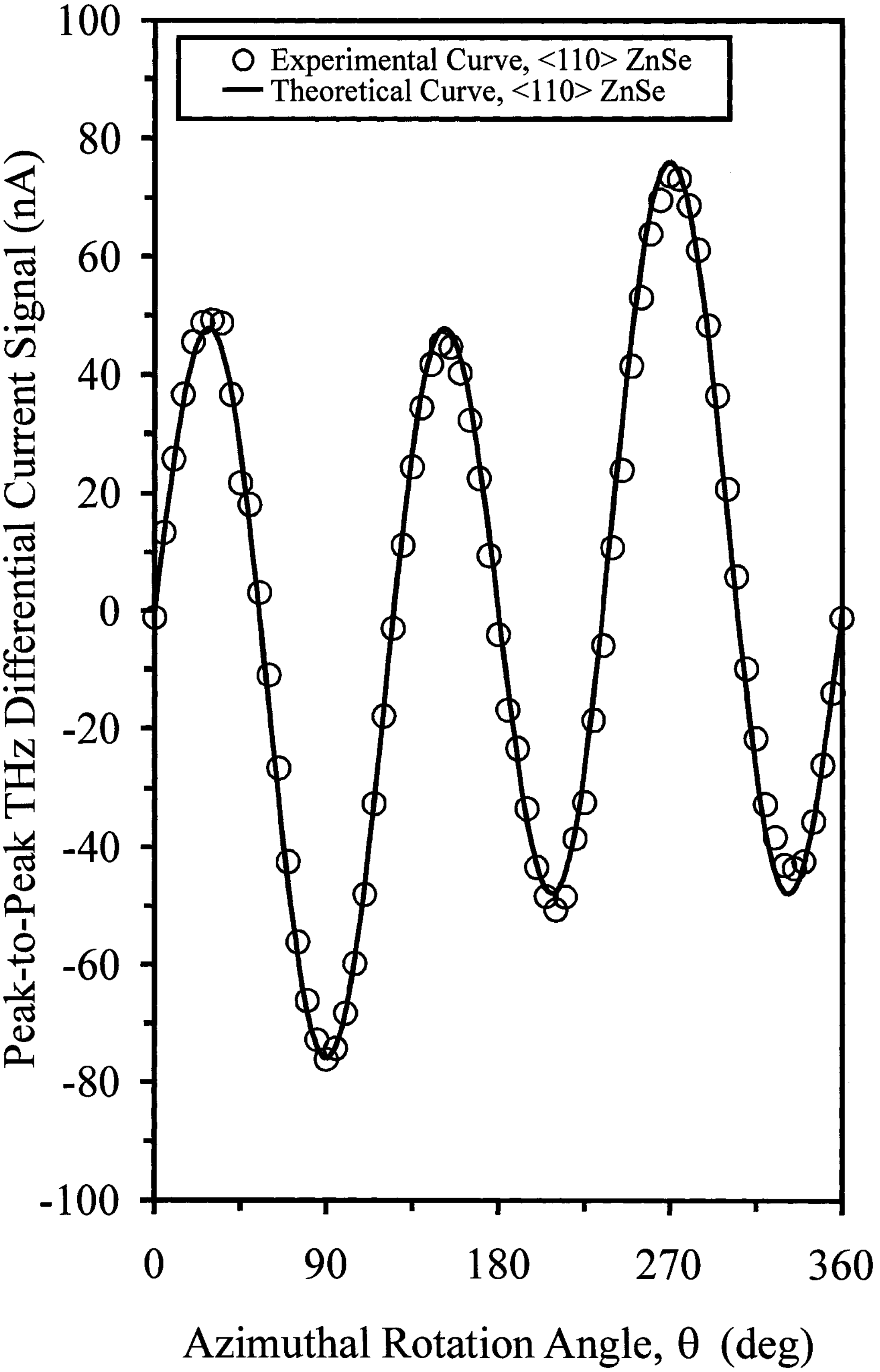

Figure 3.5.2.2.1 Peak-to-peak THz electric field amplitudes as a function of the azimuthal crystal rotation angle, θ, for a 500 μm thick <110> ZnSe sensor.

3.5.2.3 Electro-Optic Detection with <111> ZnSe Sensors

The next ZnSe detector to be investigated for EO detection of free-space THz transients is the <111> ZnSe sensor. A 160 mW pump beam is used to photo-excite the GaAs THz emitter, and detection is carried out by a 500 μm thick <111> ZnSe crystal. Again, the THz waveforms are monitored while the azimuthal crystal orientation, θ, is rotated. The resulting peak-to-peak THz amplitudes are presented in figure 3.5.2.3.1 as open circles, while the corresponding theoretical curve is shown in the same figure as a solid line. A THz time-domain waveform, corresponding to one of the peak-signal crystal orientations, is presented in figure 3.5.2.1.1. It is readily apparent from figure 3.5.2.3.1 that the theoretical and experimental results for the azimuthal dependence of the EO sensor are in excellent agreement. The curve shows a clear 120° rotational period in the response–a result of the three-fold symmetry associated with the <111> plane in the crystal lattice–and a differential current signal level that oscillates between +64 nA and –64 nA.

3.5.2.4 Electro-Optic Detection with Polycrystalline ZnSe Sensors

The previous three sections explored the application of <100>, <110>, and <111> single-crystal samples of ZnSe for the detection of THz transients. It was found that ZnSe EO crystals are excellent candidates for free-space THz sensing (given the proper crystal orientation). In this section, some of our recent experimental results pertaining to polycrystalline ZnSe THz sensors are presented [14]. Polycrystalline semiconductors offer some practical advantages when compared to their single-crystal counterparts, including a greater ease of fabrication (a 500 μm thick sample requires only 8 hours [31] for CVD growth but up to 130 hours [47], [48] for PVD growth) and the possibility of

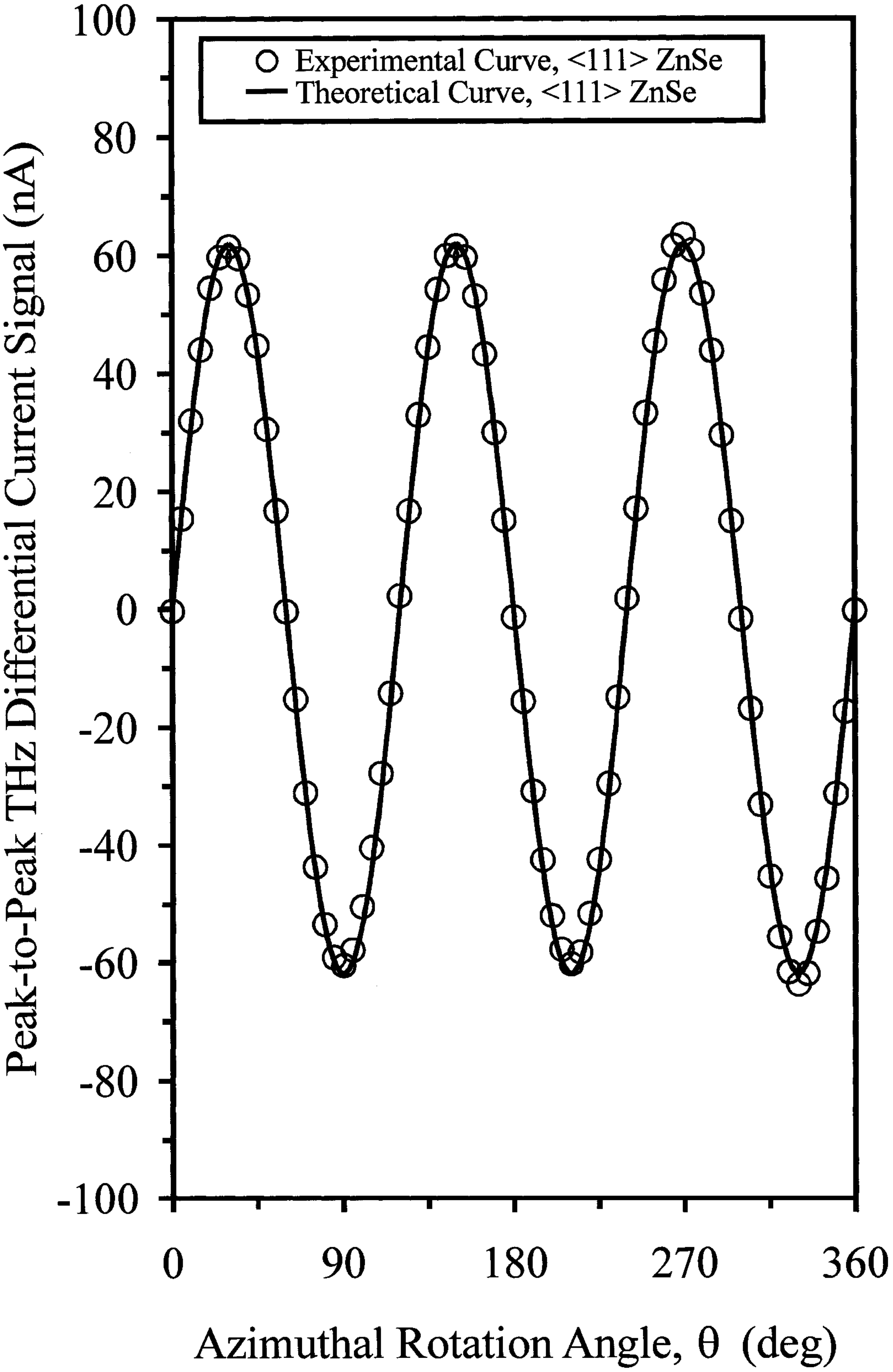

Figure 3.5.2.3.1 Peak-to-peak THz electric field amplitudes as a function of the azimuthal crystal rotation angle, θ, for a 500 μm thick <111> ZnSe sensor.

fabricating non-lattice-matched thin film integrated free-space EO sensors, such as multi-layered and quasi-phase matched detectors and generators.

Polycrystalline ZnSe bulk material, prepared via CVD on randomly orientated substrates, is shown in this section to exhibit preferred grain orientations. By measuring the free-space EO signal from a polycrystalline ZnSe sample as a function of azimuthal axis angle, θ, this preferred grain orientation is illustrated. Furthermore, it is found that the signal sensitivity and detection bandwidth of the polycrystalline ZnSe EO sensors are strong functions of the thickness of the material. Given a polycrystalline sample whose thickness is on the same order as the polycrystalline grain size, the amplitude and phase characteristics of a single-crystal sensor are matched.

Like the previous three sections, the free-space THz generation mechanism used in this investigation is resonant free-carrier photo-excitation from a 100 μm PC gap on a semi-insulating GaAs substrate. The PC gap is biased at 40 $V_{p\text{-}p}$ and a 160 mW pump beam is used to generate charge carriers within this gap. To provide a comparison for the results from the polycrystalline samples, THz detection is first carried out with a 500 μm thick single-crystal <111> ZnSe sensor. The time-domain EO sampling results are shown in figure 3.5.2.4.1(a), the corresponding spectrum is shown in figure 3.5.2.4.2(a), and the peak-to-peak THz amplitude is shown in figure 3.5.2.4.3(a) as a function of the azimuthal rotation angle, θ.

To demonstrate the potential of polycrystalline EO THz sensors, THz detection is explored first using a 1.0 mm thick polycrystalline ZnSe sample. The time-domain THz waveform for this sample is shown in figure 3.5.2.4.1(b), while its corresponding spectral amplitude is presented in figure 3.5.2.4.2(b). It is evident from the time-domain signal

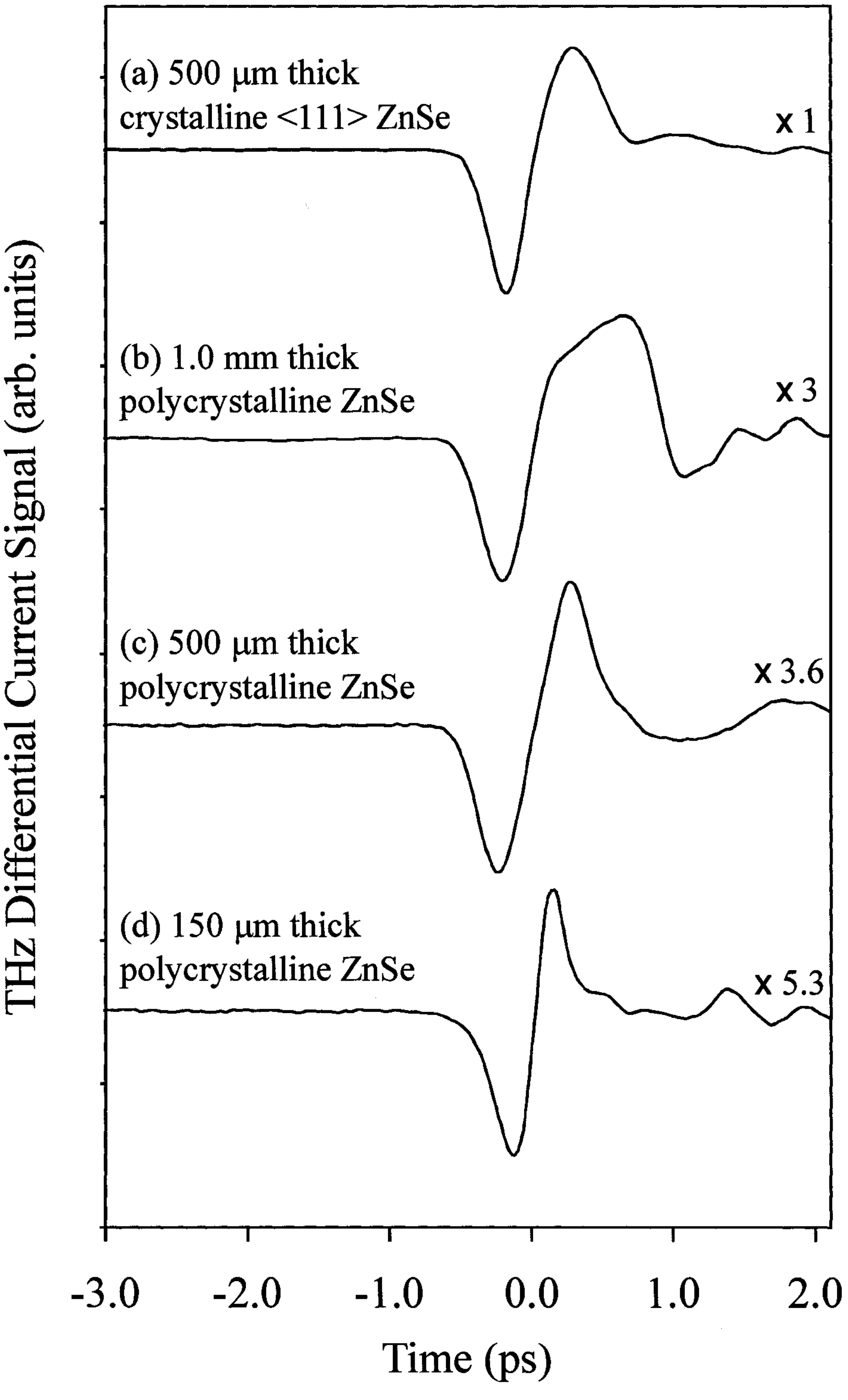

Figure 3.5.2.4.1 Free-space THz waveforms detected with a (a) 500 μm thick <111> ZnSe EO sensor, a (b) 1.0 mm thick polycrystalline ZnSe sensor, a (c) 500 μm thick polycrystalline ZnSe EO sensor, and a (d) 150 μm thick polycrystalline ZnSe EO sensor.

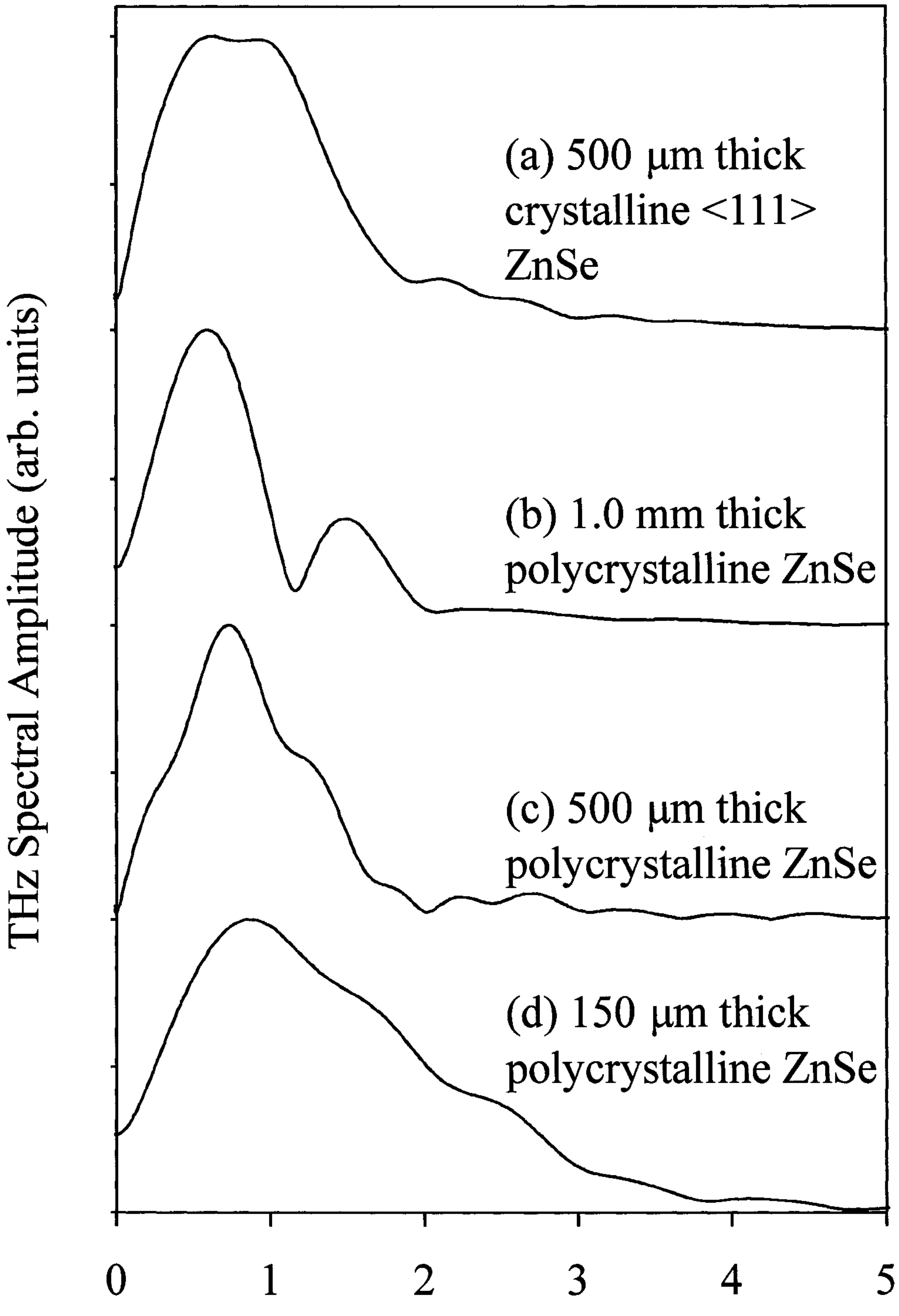

Figure 3.5.2.4.2 Free-space THz spectra detected with a (a) 500 μm thick <111> ZnSe EO sensor, a (b) 1.0 mm thick polycrystalline ZnSe sensor, a (c) 500 μm thick polycrystalline ZnSe EO sensor, and a (d) 150 μm thick polycrystalline ZnSe EO sensor.

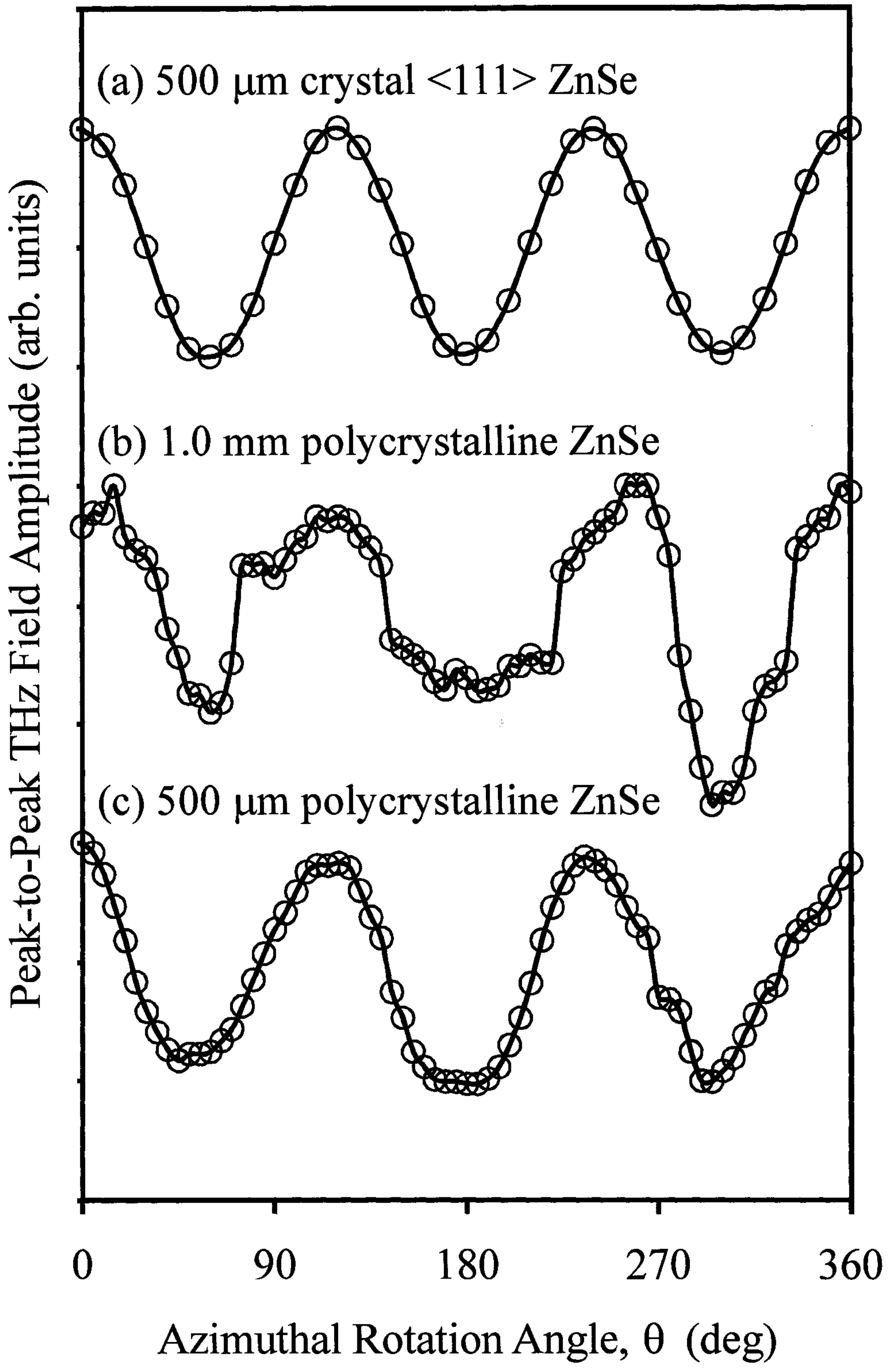

Figure 3.5.2.4.3 Peak-to-peak THz amplitudes as a function of the EO crystal azimuthal angle for a (a) 500 μm thick <111> ZnSe EO sensor, a (b) 1.0 mm thick polycrystalline ZnSe sensor, and a (c) 500 μm thick polycrystalline ZnSe EO sensor.

that the measured THz waveform is not the expected single-cycle bipolar response predicted for a PC THz emitter in a high-injection regime. Clearly, the use of a thick polycrystalline EO sensor, rather than the <111> crystalline sensor, introduces a phase distortion over the period of the THz pulse. This distortion is due to the interplay of the velocity mismatch between the co-propagating far-infrared THz beam and near-infrared probe beam, and the numerous grain orientations that vary along the interaction length. For the simple case where the EO sensor is comprised of only a single grain (analogous to a conventional single-crystal EO sensor), only pulse broadening of the THz waveform is witnessed–a result of the velocity mismatch which exists between the probe pulse and the THz pulse [25]. For the case of a polycrystalline EO sensor, however, the THz waveform is further distorted by the aforementioned fact that the various grains within the interaction region have a random crystal orientation and, therefore, an incoherent phase response to the applied THz electric field. In essence, the measured THz waveform is a composition of the EO response of several grains through the sample, with each response shifted slightly in time. The resulting phase distortion due to this effect limits both the overall amplitude and the effective THz bandwidth, as shown in figure 3.5.2.4.2(b). Attempts to minimize the distortion by rotating the sensor proved unsuccessful, suggesting that the distortion is mainly due to the grain structure along the interaction length. The peak-to-peak amplitude of the THz signal as a function of the sensor azimuthal axis angle, θ, is shown in figure 3.5.2.4.3(b) and displays some overall three-fold symmetry, suggesting that a preferential grain orientation exists within the ZnSe structure [49]. To confirm this finding, X-ray diffraction studies were carried out on the polycrystalline ZnSe sample, and the results are shown in figure 3.5.2.4.4. The

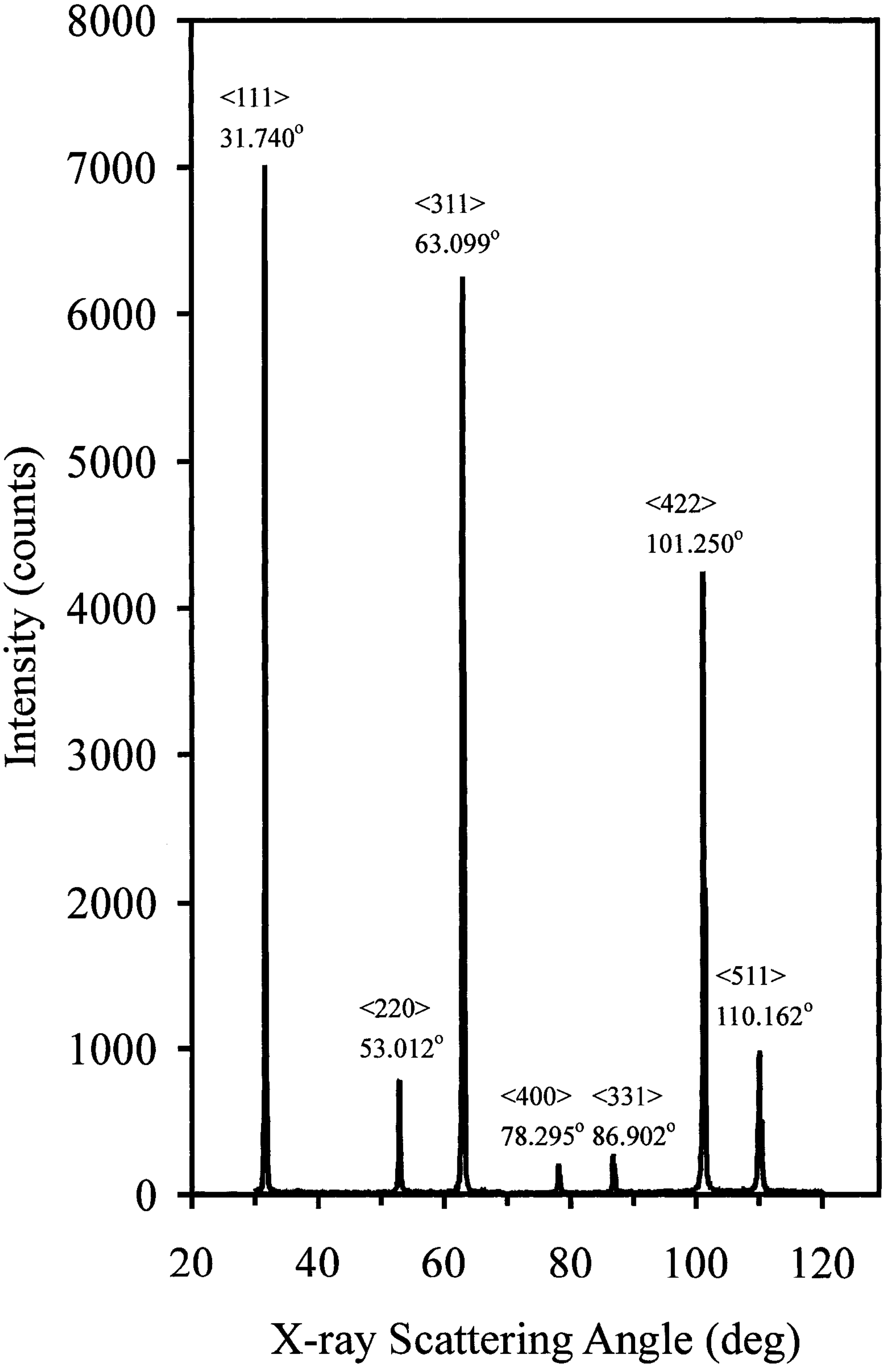

Figure 3.5.2.4.4 X-ray diffraction study on the polycrystalline ZnSe sample. The peaks for stilleite ZnSe are labeled on the curve.

crystallographic orientations for stilleite-ZnSe are indicated on the figure, and are found to match the X-ray diffraction peaks of our polycrystalline sample. The three strongest diffraction peaks, at 31.721^0, 53.002^0, and 63.106^0, correspond to the <111>, <220>, and <311> crystallographic planes, respectively.

To gain a better understanding of the relationship between the grain size within the polycrystalline ZnSe sensor and the distortion of the detected THz pulse, the sample is thinned to a thickness of 500 μm. The resulting THz time-domain waveform is shown in figure 3.5.2.4.1(c), while the associated spectral amplitude is presented in figure 3.5.2.4.2(c). It is readily apparent from the single-cycle bipolar response shown in the figure that the 500 μm thick sample exhibits diminished distortion over the duration of the waveform. By thinning the polycrystalline sensor, therefore, the effective anisotropy of the sample along the interaction length is increased, enhancing the EO response. The increased THz bandwidth and diminished phase distortion are readily apparent from the amplitude spectrum in figure 3.5.2.4.2(c). As with the 1.0 mm thick sample, the sensor is rotated and the peak-to-peak THz amplitude is measured as function of azimuthal axis angle. The results, shown in figure 3.5.2.4.3(c), exhibit a significantly enhanced three-fold symmetric sinusoidal profile, suggesting that the 500 μm thick polycrystalline sensor has a crystal symmetry similar to that of the <111> orientation. In the limit where the sample thickness matches the grain size of the sample, the response would match that of the single-crystal sensor shown in figure 3.5.2.4.3(a).

To further reduce the effects due to phase distortion on the THz signal and improve the THz sampling bandwidth, the polycrystalline ZnSe sensor thickness is reduced to 150 μm. The EO sampling results for this sensor are shown in figure

3.5.2.4.1(d), with the corresponding spectrum shown in figure 3.5.2.4.2(d). It is evident from the time-domain figure that little phase distortion exists, and the duration of the THz pulse is greatly reduced–a result of the fact that significantly less pulse spreading occurs for the thinner sample. The spectrum confirms this, as the THz bandwidth now extends beyond 4 THz. Clearly, polycrystalline sensors offer a wide THz bandwidth and little phase distortion when the sample thickness is made sufficiently small.

Chapter 3.0 References:

[1] D. H. Auston, "Picosecond optoelectronic switching and gating in silicon," *Appl. Phys. Lett.* **26**, pp. 101-103, 1975.

[2] G. Mourou, C. V. Stancampiano, A. Antonetti, and A. Orszag, "Picosecond microwave pulses generated with a subpicosecond laser-driven semiconductor switch," *Appl. Phys. Lett.* **39**, pp. 295-296, 1981.

[3] G. Mourou, C. V. Stancampiano, and D. Blumenthal, "Picosecond microwave pulse generation," *Appl. Phys. Lett.* **38**, pp. 470-472, 1981.

[4] D. H. Auston, K. P. Cheung, and P. R. Smith, "Picosecond photoconducting Hertzian dipoles," *Appl. Phys. Lett.* **45**, pp. 284-286, 1984.

[5] G. Zhao, R. N. Schouten, N. van der Valk, W. Th. Wenckebach, and P. C. M. Planken, "Design and performance of a THz emission and detection setup based on a semi-insulating GaAs emitter," *Rev. Sci Instrum.* **73**, pp. 1715-1719, 2002.

[6] It is also possible to generate THz beams through third-order nonlinear polarization processes in random and centrosymmetric media.

[7] D. H. Auston, K. P. Cheung, J. A. Valdmanis, and D. A. Kleinman, "Cherenkov radiation from femtosecond optical pulses in electro-optic media," *Phys. Rev. Lett.* **53**, pp. 1555-1558, 1984.

[8] A. Rice, Y. Jin, X. F. Ma, X.-C. Zhang, D. Bliss, J. Larkin, and M. Alexander, "Terahertz optical rectification from 110 zinc-blende crystals," *Appl. Phys. Lett.* **64**, pp. 1324-1326, 1994.

[9] R. Huber, A. Brodschelm, F. Tauser, A. Leitenstorfer, “Generation and field-resolved detection of femtosecond electromagnetic pulses tunable up to 41 THz,” *Appl. Phys. Lett.* **76**, pp. 3191-3193, 2000.

[10] M. Schall and P. Uhd Jepsen, “Photoexcited GaAs surfaces studied by transient terahertz time-domain spectroscopy,” *Opt. Lett.* **25**, pp. 13-15, 2000.

[11] D. M. Mittleman, R. H. Jacobsen, and M. C. Nuss, “T-ray imaging,” *IEEE J. Select. Topics Quantum Electron.* **2**, pp. 679-692, 1996.

[12] P. Y. Han, M. Tani, M. Usami, S. Kono, R. Kersting, and X.-C. Zhang, “A direct comparison between terahertz time-domain spectroscopy and far-infrared Fourier transform spectroscopy,” *J. Appl. Phys.* **89**, pp. 2357-2359, 2001.

[13] J. F. Holzman and A. Y. Elezzabi, “Two-photon photoconductive terahertz generation in ZnSe,” *Appl. Phys. Lett.*, to be published, 2003.

[14] J. F. Holzman, F. E. Vermeulen, S. E. Irvine, and A. Y. Elezzabi, "Free-space detection of terahertz radiation using crystalline and polycrystalline ZnSe electro-optic sensors," *Appl. Phys. Lett.* **81**, pp. 2294-2296, 2002.

[15] Q. Wu and X.-C. Zhang, “Design and characterization of traveling-wave electrooptic terahertz sensors,” *IEEE J. Select. Topics Quantum Electron.* **2**, pp. 693-700, 1996.

[16] For a detailed analysis on the polarization response from the quarter waveplate and wallaston prism, and its relationship to the measured differential current signal, see section 3.5.

[17] G. Rodriguez and A. J. Taylor, “Screening of the bias field in terahertz generation from photoconductors,” *Opt. Lett.* **21**, pp. 1046-1048, 1996.

[18] D. E. Aspnes and A. A. Studna, “Dielectric functions and optical parameters of Si,

Ge, GaP, GaAs, GaSb, InP, InAs, and InSb from 1.5 to 6.0 eV," *Phys. Rev. B* **27**, pp. 985-1009, 1983.

[19] A. J. Taylor, G. Rodriguez, and D. Some, "Ultrafast field dynamics in large-aperture photoconductors," *Opt. Lett.* **22**, pp. 715-717, 1997.

[20] For a detailed analysis on the EO detection process for <111> ZnSe, see section 3.4.

[21] Y. Cai, I. Brener, J. Lopata, J. Wynn, L. Pfeiffer, and J. Federici, "Design and performance of singular electric field terahertz photoconducting antennas," *Appl. Phys. Lett.* **71**, pp. 2076-2078, 1997.

[22] R. T. Hall, D. Vrabec, and J. M. Dowling, "A high-resolution, far infrared double-beam lamellar grating interferometer," *Appl. Opt.* **5**, pp. 1147-1158, 1966.

[23] B. K. Rai, R. S. Katiyar, K.-T. Chen, and A. Burger, "Raman and photoluminescence studies on intrinsic and Cr-doped ZnSe single crystals," *J. Appl. Phys.* **83**, pp. 6011-6017, 1998.

[24] M. D. Cummings, J. F. Holzman, and A. Y. Elezzabi, "Femtosecond carrier dynamics in an asymmetrically excited GaAs photoconductive switch," *Appl. Phys. Lett.* **78**, pp. 3535-3537, 2001.

[25] The velocity of the THz and probe beams in the EO crystal were measured by comparing the time it takes the THz and probe pulses to be reflected off the back-side of the crystal. Given a 500 μm thickness for the ZnSe sensor, the reflected probe beam sampled the THz pulse 8.32 ps before the system zero-time, and the reflected THz pulse was sampled 9.28 ps after the system zero-time.

[26] C. W. Siders, J. L. W. Siders, A. J. Taylor, S.-G. Park, M. R. Melloch, and A. M. Weiner, "Generation and characterization of terahertz pulse trains from biased, large-aperture photoconductors," *Opt. Lett.* **24**, pp. 241-243, 1999.

[27] H. Yoneda, K. Tokuyama, K. Ueda, H. Yamamoto, and K. Baba, "High-power terahertz radiation emitter with a diamond photoconductive switch array," *Appl. Opt.* **40**, pp. 6733-6736, 2001.

[28] A. Y. Elezzabi, H. Houtman, and J. Meyer, "Time-Resolved Impact Ionization in ZnSe High-Voltage Switches," *IEEE Trans. on Plasma Science* **22**, pp. 1043-1048, 1994.

[29] P. S. Cho, P.-T. Ho, J. Goldhar, and C. H. Lee, "Photoconductivity in ZnSe under high electric fields," *IEEE J. Quantum Electron.* **23**, pp. 1489-1497, 1994.

[30] H. Yoneda, K. Ueda, Y. Aikawa, K. Baba, and N. Shohata, "Photoconductive properties of chemical vapor deposited diamond switch under high electric field strength," *Appl. Phys. Lett.* **66**, pp. 460-462, 1995.

[31] J. S. Goela and R. L. Taylor, "Monolithoc material fabrication by chemical vapour deposition," *J. Mater. Sci.* **23**, pp. 4331-4339, 1988.

[32] N. Katzenellenbogen and D. R. Grischkowsky, "Efficient generation of 380 fs pulses of THz radiation by ultrafast laser pulse excitation of a biased metal-semiconductor interface," *Appl. Phys. Lett.* **58**, pp. 222-224, 1991.

[33] U. D. Keil and D. R. Dykaar, "Ultrafast pulse generation in photoconductive switches," *IEEE J. Quantum Electron.* **32**, pp. 1664-1671, 1996.

[34] S. S. Gevorgian, "Design considerations for an optically-excited semiconductor microstrip gap at microwave frequencies," *Proc. IEE J, Optoelectron.* **139**, pp. 153-157, 1992.

[35] X. Zhou, "On the physics of femto-second electrical pulse generation in transmission-line gaps," *Optoelectron.-Devices* **10**, pp. 491-504, 1995.

[36] The polycrystalline ZnSe substrate was supplied by II-VI Inc.

[37] M. Tani, S. Matsuura, K. Sakai, and S. Nakashima, "Emission characteristics of photoconductive antennas based on low-temperature-grown GaAs and semi-insulating GaAs," *Appl. Opt.* **36**, pp. 7853-7859, 1997.

[38] Q. Wu and X.-C. Zhang, "Free-space electro-optic sampling of terahertz beams," *Appl. Phys. Lett.* **67**, 3523-3525, 1995.

[39] Q. Wu and X.-C. Zhang, "Ultrafast electro-optic field sensors," *Appl. Phys. Lett.* **68**, 1604-1606, 1996.

[40] Q. Wu, M. Litz, and X.-C. Zhang, "Broadband detection capability of ZnTe electro-optic field detectors," *Appl. Phys. Lett.* **68**, 2924-2926, 1996.

[41] Q. Wu and X.-C. Zhang, "Free-space electro-optics sampling of mid-infrared pusles," *Appl. Phys. Lett.* **71**, pp. 1285-1286, 1997.

[42] S. E. Ralph and D. Grischkowsky, "THz spectroscopy and source characterization by optoelectronic interferometry," *Appl. Phys. Lett.* **60**, pp. 1070-1072, 1992.

[43] The use of CVD-grown polycrystalline ZnSe sensors is demonstrated in section 3.5.2.4.

[44] B. E. A. Saleh and M. C. Teich, *Fundamentals of Photonics*, (John Wiley & Sons, New York, 1991), pp. 696-736.

[45] P. C. M. Planken, H.-K. Nienhuys, H. J. Bakker, and W. Th. Wenckebach, "Measurement and calculation of the orientation dependence of THz pulse detection in ZnTe," *J. Opt. Soc. Am.* B **18**, pp. 313-317, 2001.

[46] Q. Chen, M. Tani, Z. Jiang, and X.-C. Zhang, "Electro-optic transceivers for terahertz-wave applications," *J. Opt. Soc. Am.* B **18**, pp. 823-831, 2001.

[47] F. Kadotsuji, H. Ohnishi, N. Kawabata, M. Kimura, A. Tanaka, and T. Sukegawa, "ZnSe thick layers grown on GaAs by physical vapour deposition," *J. Crystal Growth* **155**, pp. 23-26, 1995.

[48] T. Sukegawa, F. Kadotsuji, T. Tsujimoto, M. Kaji, M. Kimura, and A. Tanaka, "Preparation of ZnSe substrates by PVD and selective etching," *J. Crystal Growth* **174**, pp. 289-292, 1997.

[49] S. Rummel, II-VI Inc., Personal communication.

CHAPTER 4.0

CONCLUSIONS

4.0 Conclusions

The work within chapter 2.0 presented the theoretical and experimental frameworks necessary to generate transmission line-coupled THz electrical waveforms. The concepts of PC self-switching and PC frozen wave generation were introduced within the chapter as viable sources for these THz electrical transients. To begin with, Section 2.3 successfully demonstrated the operation of self-switching with the ultrathin Si PC switch. Here, it was found that electrical pulses as short as 1.2 ps could be generated on a microstrip transmission line using a 10 μm thick float-zone Si substrate. This result demonstrates a 17000-fold increase in the PC switching speed of conventional Si devices (which are currently limited by a 20 ns carrier lifetime). The same self-switching principle was applied next to PC switching on a GaAs substrate in section 2.4. The small penetration depth of GaAs (0.74 μm) meant, in this case, that the operation of the self-switching process must be decoupled from the substrate thickness. For this reason, the coplanar self-switching layout was introduced. With this novel device, it was found that 2 ps electrical pulses could be routinely formed using a GaAs substrate whose carrier lifetime is 250 ps. Again, the carrier lifetime-independent operation of the switch allowed for a 125-fold increase in the PC switching speed of conventional GaAs PC devices. As a final effort in the generation of ultrafast electrical transients, the concept of PC frozen wave generation was introduced in section 2.5. The technique of frozen wave generation utilizes a DC to RF conversion process that maps the spatial extent of the bias electrode structure onto the temporal shape of the electrical transient. By employing sufficiently short electrode spacings, it was found that the operation of the device could be extended into the THz frequency-domain.

The work within chapter 3.0 presented the theoretical and experimental frameworks necessary to generate and detect free-space THz waveforms. To begin with, section 3.3 introduced a 100 μm wide GaAs PC THz emitter. The theoretical and experimental attributes of the device were analyzed, and it was determined that the operation of the GaAs emitter is limited by both space-charge and near-field THz screening under high optical pump fluences. To scale the THz power to higher levels, therefore, the ZnSe PC THz emitter was designed and tested in section 3.4. The large bandgap of ZnSe allowed this emitter to be operated under high bias field strengths (rather than high pump power fluences). The fact that the operation of the emitter output remained linear with the pump power and the bias voltage for optical fluences up to 28.3 mJ/cm^2 and peak bias fields up to 128 kV/cm, means that the device can be successfully scaled to large-area, high-power THz applications where bias field screening effects dominate the saturation characteristics. Finally, crystalline and polycrystalline ZnSe samples were tested toward the potential application of THz radiation detection in section 3.5. It was found that both the crystalline and polycrystalline samples could be used for THz sensing applications. Theoretical and experimental work showed that the operation of the crystalline ZnSe sensors was highly dependent upon the azimuthal symmetries within the crystal lattice. In comparison, the successful operation of the polycrystalline ZnSe sensor was highly dependent upon the detector thickness–as the random nature of the crystallographic grain orientations within the sample introduced an interaction length-dependent phase distortion on the THz waveform.

It is important to note that the work described above is far from concluded. A major step in the continuing development of THz-bandwidth electronic devices will be the successful application of the THz electrical sources in Chapter 2.0 to the fields of high-speed communication and signal transmission. The integrated dipole antenna structures introduced in section 2.5.2, for example, merely scratch the surface of this vast research topic. It is expected that these integrated THz transmission structures could be applied in the future to *intra-chip* signal transmission applications, where radiative losses currently dominate the transmission line propagation characteristics. Similarly, the research efforts on the generation and detection of free-space THz waveforms in Chapter 3.0 offer the possibility for continued study. While the ZnSe dipole antenna introduced in section 3.4 was successful in applying two-photon PC absorption to THz emission, the true test for this device would be the integration of this technique into a large aperture THz emitter with an amplified optical laser source. This would dramatically increase the THz amplitude as the emitted THz field scales linearly with the PC area. Finally, the investigation into ZnSe THz detection introduced in section 3.5, offers some intriguing possibilities into alternative THz sampling schemes. In particular, ZnSe is known to have an extremely high Verdet coefficient ($V = 40$ rad m^{-1} T^{-1}) and can, therefore, be applied to THz magneto-optic sampling techniques, where the THz *magnetic* field, rather than the THz *electric* field, is mapped onto the polarization state of the probe beam. This would open the door to numerous time-resolved THz magnetic field mapping investigations, and it would allow for picosecond analysis of magnetization dynamics. Indeed, the extremely short pulse durations and exceptionally wide bandwidths associated with the THz waveforms described above make them ideal for a wide array of emerging technologies.

APPENDICES

Appendix A

RESPONSE OF THE $LiTaO_3$ ELECTRO-OPTIC PROBE

The THz electrical transient detection system operates by way of a THz electric field-dependent phase retardation between the extraordinary and ordinary axes of the $LiTaO_3$ EO crystal. This phase retardation maps itself onto the polarization state of the probe beam through the EO tensor

$$r_{ij} = \begin{bmatrix} 0 & -r_{22} & r_{13} \\ 0 & r_{22} & r_{13} \\ 0 & 0 & r_{33} \\ 0 & r_{51} & 0 \\ -r_{51} & 0 & 0 \\ -r_{22} & 0 & 0 \end{bmatrix}, \tag{A.1}$$

which provides the directional dependence for the field-dependent refractive index changes in the $LiTaO_3$ lattice. The sampling scheme can be simplified, however, by aligning the fringing electric field in the direction of the optical axis of the $LiTaO_3$ crystal. In this way, only the third column of equation A.1 is involved in the EO process. The remaining EO coefficients, $r_{13} = 8.4$ pm/V and $r_{33} = 30.5$ pm/V, are then coupled to the externally applied electric field, $\vec{E}_{THz} = E_{THz}\hat{z}_0$, through the modified index ellipsoid,

$$\sum_{ij} \eta_{ij}\left(\vec{E}_{THz}\right)x_i x_j = 1, \tag{A.2}$$

where $\eta_{ij}(\vec{E}_{THz})$ is the field-dependent impermeability tensor defined by

$$\eta_{ij}\left(\vec{E}_{THz}\right)=\eta_{ij}(0)+\sum_{k} r_{ijk}E_{THz\,k}\,, \tag{A.3}$$

and $\eta_{ij}(0)$ is the static impermeability tensor. Expansion of this tensor in the laboratory coordinate system (x_0,y_0,z_0) gives the relation

$$\frac{x_0^2}{n_{o,LiTaO3}^2}+\frac{y_0^2}{n_{o,LiTaO3}^2}+\frac{z_0^2}{n_{e,LiTaO3}^2}+r_{13}E_{THz}x_0^2+r_{13}E_{THz}y_0^2+r_{33}E_{THz}z_0^2=1\,, \tag{A.4}$$

which can be rewritten in the principal axes coordinate system as

$$\left(\frac{1}{n_{o,LiTaO3}^2}+r_{13}E_{THz}\right)x_0^2+\left(\frac{1}{n_{o,LiTaO3}^2}+r_{13}E_{THz}\right)y_0^2+\left(\frac{1}{n_{e,LiTaO3}^2}+r_{33}E_{THz}\right)z_0^2=1\,. \tag{A.5}$$

Here, $n_{o,LiTaO3}$ and $n_{e,LiTaO3}$ are the respective refractive indices of the ordinary and extraordinary directions in the EO crystal. The resulting principal refractive indices are

$$n_{x0}=\left(\frac{1}{n_{o,LiTaO3}^2}+r_{13}E_{THz}\right)^{-1/2}\cong n_{o,LiTaO3}-\frac{1}{2}r_{13}E_{THz}n_{o,LiTaO3}^3\,, \tag{A.6}$$

$$n_{y0}=\left(\frac{1}{n_{o,LiTaO3}^2}+r_{13}E_{THz}\right)^{-1/2}\cong n_{o,LiTaO3}-\frac{1}{2}r_{13}E_{THz}n_{o,LiTaO3}^3\,, \tag{A.7}$$

and

$$n_{z0}=\left(\frac{1}{n_{o,LiTaO3}^2}+r_{13}E_{THz}\right)^{-1/2}\cong n_{e,LiTaO3}-\frac{1}{2}r_{33}E_{THz}n_{e,LiTaO3}^3\,. \tag{A.8}$$

The difference in refractive indices for each of these directions produces a field-dependent birefringence within the crystal that can be measured as a change in the polarization state of the incident probe beam. For a probe beam propagating in the x_0 direction, with a polarization set at 45^0 between the y_0 and z_0 axes, the phase difference between the y_0 and z_0 directions is found to be

$$\Delta\Gamma_{LiTaO3} = \frac{2\pi}{\lambda_o}\left[n_{e,LiTaO3} - n_{o,LiTaO3} - \frac{1}{2}E_{THz}\left(r_{33}n^3_{e,LiTaO3} - r_{13}n^3_{o,LiTaO3}\right)\right]L, \tag{A.9}$$

given an interaction length of L in the crystal and a probe central wavelength of λ_o. To measure the induced phase retardation, the probe beam is passed through a quarter waveplate and wallaston prism pair. The quarter waveplate is aligned such that its slow axis and fast axis are parallel to the y_0 and z_0 axes, respectively. This orientation produces a static $\pi/2$ phase retardation between the probe beam electric field that exits the EO crystal,

$$\begin{aligned}\vec{E}_{probe}(t) &= \frac{E_{probe}}{\sqrt{2}}\exp[i(2\pi\nu\, t - k_0 n_{y0} L)]\hat{y}_0 \\ &+ \frac{E_{probe}}{\sqrt{2}}\exp[i(2\pi\nu\, t - k_0 n_{z0} L)]\hat{z}_0\end{aligned}, \tag{A.10}$$

and the probe beam electric field that exits the quarter waveplate,

$$\begin{aligned}\vec{E}_{probe}(t) &= \frac{E_{probe}}{\sqrt{2}}\exp[i(2\pi\nu\, t - k_0 n_{y0} L + \pi/4)]\hat{y}_0 \\ &+ \frac{E_{probe}}{\sqrt{2}}\exp[i(2\pi\nu\, t - k_0 n_{z0} L - \pi/4)]\hat{z}_0\end{aligned}, \tag{A.11}$$

given the optical probe frequency, ν, speed of light, c, and a free-space wavevector of $k_0 = 2\pi\nu/c$. Next, the beam is passed through the wallaston prism, whose transmission axes are aligned both parallel and perpendicular to the incident probe beam polarization. The resulting parallel and perpendicular transmitted field components are

$$\begin{aligned}E_{probe1}(t) = \frac{E_{probe}}{2} \times \{ &\exp[i(2\pi\nu\, t - k_0 n_{y0} L + \pi/4)] \\ &- \exp[i(2\pi\nu\, t - k_0 n_{z0} L - \pi/4)] \}\end{aligned} \tag{A.12}$$

and

$$E_{probe2}(t) = \frac{E_{probe}}{2} \times \{ \exp[i(2\pi\nu\, t - k_0 n_{y0} L + \pi/4)] + \exp[i(2\pi\nu\, t - k_0 n_{z0} L - \pi/4)] \}, \qquad (A.13)$$

respectively. The EO signal of interest is determined, finally, by taking the difference between the power of each of the beams exiting the wallaston prism. The power of the first probe beam is

$$P_{probe1} = \frac{A}{\eta_o}\left\langle E_{probe1}(t) \times E^{*}_{probe1}(t)\right\rangle = \frac{P_{probe}}{2} + \frac{P_{probe}}{2}\sin\left[k_o\left(n_{z0} - n_{y0}\right)L\right], \qquad (A.14)$$

and the power of the second beam is

$$P_{probe2} = \frac{A}{\eta_o}\left\langle E_{probe2}(t) \times E^{*}_{probe2}(t)\right\rangle = \frac{P_{probe}}{2} - \frac{P_{probe}}{2}\sin\left[k_o\left(n_{z0} - n_{y0}\right)L\right], \qquad (A.15)$$

giving a differential EO signal of

$$\Delta P_{LiTaO3} = P_{probe1} - P_{probe2} = P_{probe}\sin\left[k_o\left(n_{z0} - n_{y0}\right)L\right], \qquad (A.16)$$

for a total probe power of $P_{probe} = A/(2\eta_o)\, E_{probe}^{2}$ and a probe spot size of area A. Here, η_o is the impedance of free-space. Given that the induced phase difference is small, the sine term in equation A.16 can be expanded, and the differential power can be rewritten as

$$\Delta P_{LiTaO3} = P_{probe}\frac{2\pi\nu}{c}\left[\left(n_{e,LiTaO3} - n_{o,LiTaO3}\right) - \frac{E_{THz}\left(n^{3}_{e,LiTaO3}r_{33} - n^{3}_{o,LiTaO3}r_{13}\right)}{2}\right]L. \qquad (A.17)$$

The first term in equation A.17 will create a small but finite offset on the measured differential power. The small static birefringence of $LiTaO_3$ will keep this DC value to a minimal level, however. The second term in equation A.17 is the term of interest to the EO sampling experiment. Being linear to the strength of the fringing field on the transmission line (E_{THz}), this signal can be used to form a time-resolved image of the ultrafast voltage waveform.

Appendix B

ULTRAFAST OPTICAL BEAM CHOPPER

The development of ultrafast pulsed laser systems has led to a wide variety of contemporary applications. The ultrashort optical pulses made available by these sources have been applied to a variety of fields, including charge carrier dynamical studies [1], free-space THz generation [2], far-infrared material spectroscopy [3], and ultrawide-bandwidth semiconductor switching [4]. These time-resolved pump-probe experiments make use of optical beam chopping and lock-in signal detection to overcome the elevated noise levels associated with DC and low-frequency laser measurements. In doing so, random signal fluctuations due to internal laser noise and environmental noise sources are minimized, and the overall stability of the sampling process is significantly improved.

Optical beam chopping using mechanical fan-blades is often employed in ultrafast laser applications to reduce the level of noise. Indeed, by operating these beam choppers at increasingly high frequencies, it is found that the noise level can be greatly reduced. Unfortunately, the use of conventional mechanical choppers is restricted to frequencies below a few kilohertz as the number of transmission slots which can be incorporated into the rotating blade is physically limited–a result of the fact that the transmission slots must be larger than the laser beam diameter to avoid aliasing between the adjacent slots. To overcome these physical limitations and raise the beam modulation frequencies to an increasingly noise-free domain, alternative modulation techniques such as EO [5] and acousto-optic [6] modulation are often employed. These high-speed switching techniques significantly reduce the noise level of an experiment by operating at frequencies in the megahertz regime. Unfortunately, EO and acousto-optic modulators cannot be applied to ultrafast laser applications requiring femtosecond temporal resolution as material dispersive effects in the crystals severely broaden the ultrashort optical pulses.

To overcome the limited frequency range associated with conventional mechanical beam choppers and the pulse dispersion effects of EO and acousto-optic modulators, a compact dispersion-free high-speed mechanical beam chopper is designed and tested [7]. This mechanical chopper is able to operate at exceptionally high frequencies, as it employs a ring of fine transmission slots on the outer circumference of the rotating blade. By focusing the ultrafast laser pulse train of interest through these transmission slots and operating the precision-balanced drive motor at very high speeds, it is found that beam modulation rates beyond 100 kHz can be achieved. Furthermore, by incorporating all-reflective optics into the high-speed chopper design, material dispersive effects are eliminated, and the femtosecond laser pulse duration is preserved.

The output from a 30 fs, 800 nm Ti:sapphire laser is directed into the ultrafast chopper unit shown figure B.1(a). The beam is focused by a 25 mm diameter, 50 mm focal length Au-coated parabolic mirror, then collimated at the output by a second identical parabolic mirror. The rotating chopper blade is positioned on the focal plane of these confocal parabolic mirrors, such that the beam waist passes directly through the transmission slots. With this configuration, the output beam intensity is modulated as the chopper blade is rotated. To monitor the modulation frequency of the beam chopper, a tracking laser beam is focused through the blade and onto a high-speed detector (Vishay

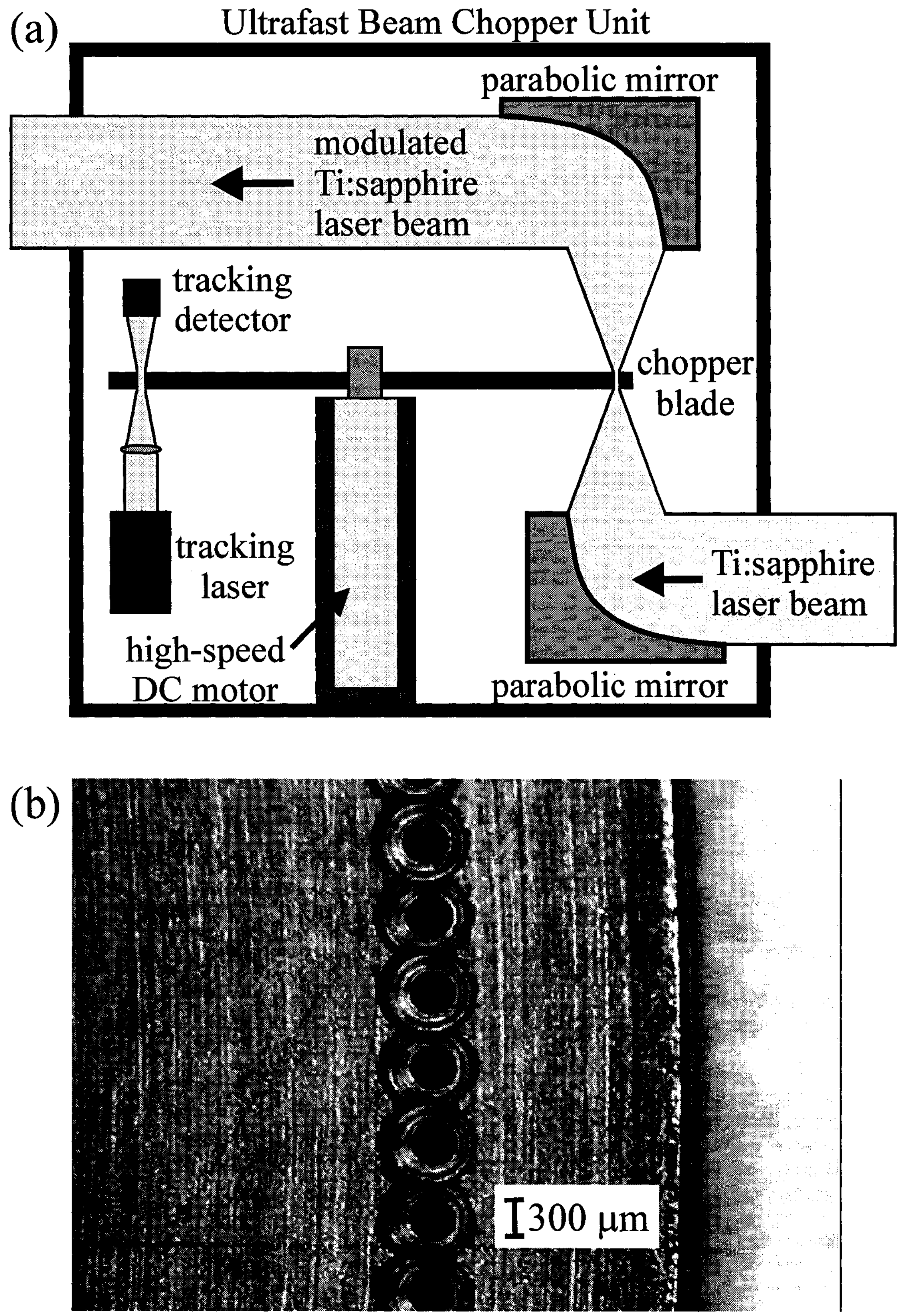

Figure B.1 A (a) schematic diagram of the high-speed optical beam chopper system and a (b) photograph of the beveled holes in the chopper blade.

PIN Photodiode, Model BPW34). The signal from this tracking detector is amplified to 0.5 V by a transimpedance amplifier (Burr-Brown, Model OPA655) and then sent to the reference input of the lock-in amplifier (Stanford Research Systems, Model SR830).

To achieve rapid beam chopping, it is necessary for the chopper blade to have both a large number of transmission slots and a high rate of rotation. To realize this, a series of 360 holes are milled into a 1 mm thick, 74 mm diameter brass disc (35 mm from the centre) to form the chopper blade. The 300 μm diameter holes, which are beveled to accommodate the finite depth-of-focus of the Gaussian beam waist, are machined with a 600 μm centre-to-centre pitch to ensure that the duty-cycle of the output laser beam is 50%. A photograph of the chopper blade is shown in figure B.1(b). To provide for rapid modulation of the optical beam, the blade is mounted to a precision-balanced high-speed DC electric motor (Maxon Precision Motors, Brushless DC Motor, Model EC22) that is capable of running at speeds in excess of 17000 rpm. The chopper blade and electric motor are mounted in a rigid vertical mount to minimize vibrations and torsional imbalances on the motor drive shaft at high rates of speed. With these high rates of rotation and the large number of the holes on the circumference of the blade it will be possible to obtain dispersion-free optical chopping at frequencies beyond 100 kHz.

To test the operation of the ultrafast chopper, the modulated Ti:sapphire laser beam is directed into the interferometric autocorrelator shown in figure B.2(a). The interferometric autocorrelator produces a time-resolved image of the femtosecond laser pulses by splitting the incoming laser pulse train into two optical delay arms and recombining them on a nonlinear GaAsP photodiode (Hamamatsu, Model G1126-02) [8]. The photodiode response is monitored as a function of the relative phase

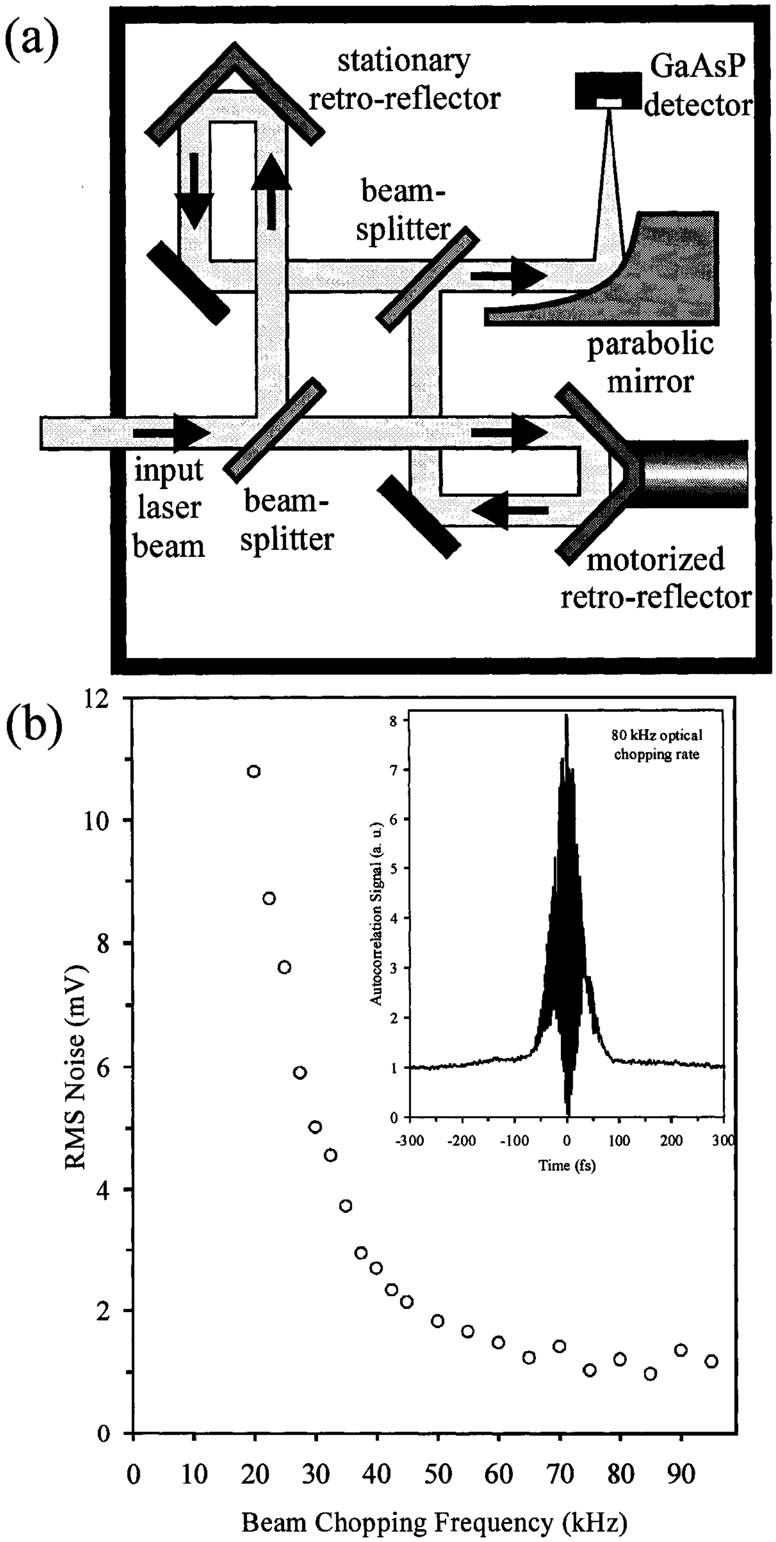

Figure B.2 A (a) schematic diagram of the autocorrelator and the (b) resulting RMS noise levels measured as a function of the beam chopping frequency. A typical autocorrelation function (for 80 kHz) is shown in the inset of (b).

delay between the arms, and an interferometric scan of the ultrashort laser pulses is resolved. The relative phase delay for the setup shown in the figure is provided by the motorized retro-reflector, whose 70 nm step size offers a 0.5 fs temporal resolution.

To test the relationship between the beam chopping frequencies and the experimental noise levels, the chopper blade's high-speed DC electric motor is operated at rotational speeds from 3333 rpm to 16666 rpm (corresponding to beam chopping rates from 20 kHz to 100 kHz), and the autocorrelation signal is monitored. To facilitate lock-in detection, the reference signal from the tracking detector is sent to the reference input of the lock-in amplifier, and the photocurrent from the autocorrelator's GaAsP photodiode is monitored by the signal input of the lock-in amplifier. Figure B.2(b) shows the resulting root-mean-square (RMS) noise levels measured for each of the chopping frequencies, while the inset of this figure shows a typical autocorrelation trace for an 80 kHz chopping rate. It is readily apparent from this figure that the RMS noise levels on the autocorrelation function drop drastically as the chopping frequency is increased. Beyond a chopping frequency of 60 kHz, the RMS noise level is seen to level off at a noise floor of 1.5 mV which, for a measured signal strength of 180 mV, corresponds to a signal-to-noise ratio of 120. This dramatic decrease in noise can be attributed to both a reduction in laser noise and a decrease in the environmental acoustic noise. Moreover, the 60 fs FWHM of the autocorrelation function suggests that the Ti:sapphire laser pulse duration remains at 30 fs–a direct result of the use of all-reflective optics. Clearly, the operation of this high-speed beam chopper in ultrafast pulsed laser applications allows for a significant reduction in experimental noise levels without inducing optical pulse broadening.

Appendix B References:

[1] M. D. Cummings, J. F. Holzman, and A. Y. Elezzabi, "Femtosecond carrier dynamics in an asymmetrically excited GaAs photoconductive switch," *Appl. Phys. Lett.* **78**, pp. 3535-3537, 2001.

[2] J. F. Holzman, F. E. Vermeulen, S. E. Irvine, and A. Y. Elezzabi, "Free-space detection of terahertz radiation using crystalline and polycrystalline ZnSe electro-optic sensors," *Appl. Phys. Lett.* **81**, pp. 2294-2296, 2002.

[3] D. Grischkowsky, S. R. Keiding, M. van Exter, and Ch. Fatinger, "Far-infrared time-domain spectroscopy with terahertz beams of dielectrics and semiconductors," *J. Opt. Soc. B* 7, pp. 2006-2015, 1990.

[4] J. F. Holzman, F. E. Vermeulen, and A. Y. Elezzabi, "Generation of 1.2 ps electrical pulses through parallel gating in ultrathin silicon photoconductive switches," *Appl. Phys. Lett.* **79**, pp. 4249-4251, 2001.

[5] Q. Chen Q and X.-C. Zhang, "Polarization modulation in optoelectronic generation and detection of terahertz beams," *Appl. Phys. Lett.* **74**, pp. 3435-3437, 1999.

[6] C. Manzanares, N. Mina-Camilde, A. Brock, J. Peng, and V. M. Blunt, "Piezoelectric detection of vibrational overtones at cryogenic temperatures," *Rev. Sci. Instrum.* **66**, pp. 2644-2651, 1995.

[7] J. F. Holzman and A. Y. Elezzabi, "Dispersion-free high-speed beam chopper for ultrafast pulsed laser applications," *Meas. Sci. Technol.* **14**, pp. N41-N44, 2003.

[8] Y. Takagi, T. Kobayashi, K. Yoshihara, and S. Imamura, "Multiple- and single-shot autocorrelator based on two-photon conductivity in semiconductors," *Opt. Lett.* **17**, pp. 658-660, 1992.

Appendix C

TERAHERTZ ELECTRICAL MIXER UNIT:

TERAMETRICS MODEL 100

TWO-CHANNEL RF MIXER SYSTEM

To minimize the noise within the measurement system it is important to stay well above the low frequency noise levels associated with laser and acoustic noise sources. To accomplish this, the Terametrics Model 100 Two-Channel RF Mixer System shown in figure C.1 is incorporated into the setup. To start, two RF waveform generators are employed in the setup: the first is a Wavetek Model 178 Programmable Waveform Synthesizer that is operated at a frequency of f_1 = 3.050 MHz (channel 1), and the second is a HP Model 33120A Waveform Generator that is operated at a frequency of f_2 = 3.000 MHz (channel 2). The reference frequency output on the back panel of the channel 1 source is connected to the reference frequency input on the back panel of the channel 2 source to ensure that the sources are frequency-synchronized at a constant difference of $f_1 - f_2$ = 50 kHz. Next, the voltage output of the channel 1 source is set at the desired bias voltage amplitude, V_b, and connected to the bias line in the experiment. The 1.4 V_p (TTL) signal from the sync out of the channel 1 source and the 8.0 $V_{p\text{-}p}$ output from the channel 2 source are then fed into the channel 1 and channel 2 inputs of the Reference Mixer

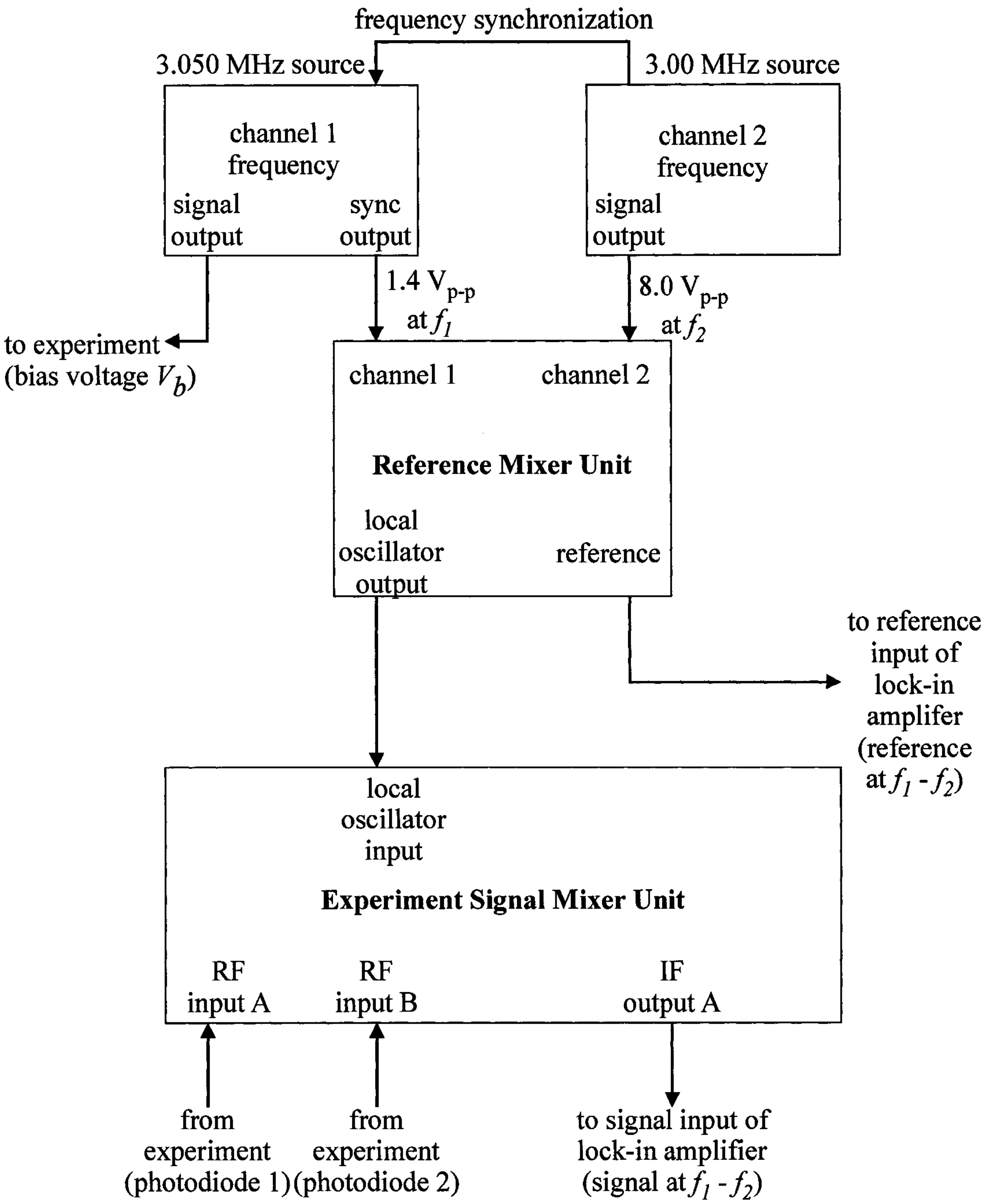

Figure C.1 The Terametrics Model 100 Two-Channel RF Mixer System.

Unit, respectively. To couple the local oscillator connections between the reference and experimental mixers, the local oscillator output from the Reference Mixer Unit is connected to the local oscillator input of the Experimental Signal Mixer Unit. The 1.5 V_{p-p} reference signal necessary for phase-sensitive detection in the experiment (at a frequency of $f_1 - f_2$) is then connected from the reference output of the Experimental Signal Mixer Unit to the reference input of the lock-in amplifier (Stanford Research Systems Model SR830 DSP lock-in amplifier). Finally, the signals from the differential photodiodes in the experiment are fed into the Experimental Signal Mixer Unit through the RF inputs A and B, while the output of this unit (carrying the experimental signal at the frequency $f_1 - f_2$) is sent, via the IF output A, to the signal input of the lock-in amplifier. By incorporating this nonlinear electronic mixing scheme into the system, the low-noise attributes of high-frequency (3 MHz) phase-sensitive detection are exploited using only low-frequency (50 kHz) lock-in detection equipment.

Appendix D

NUMERICAL ANALYSIS OF THE ULTRATHIN Si PHOTOCONDUCTIVE SWITCH

The model for the ultrathin Si PC switch (equations 2.3.1.1-2.3.1.13) is solved using a fifth-order Runge-Kutta method. Initially, the electron density, $n(z,t)$, is found as a function of space (depth) and time. This function is then used to compute the time-varying conductance terms for the gap and shunt conductance elements, $G_g(t)$ and $G_s(t)$, respectively, through the use of Simpson's 1/3 rule of integration. Finally, these time-varying conductance functions are used in a fifth-order Runge-Kutta method to solve for the transmitted voltage waveform, $v_t(t)$. The program shown is in its most general form, with the respective gap capacitance and gap conductance terms described by C_1 and $G_1(t)$, and the shunt capacitance and shunt conductance terms described by C_2 and $G_2(t)$ at the output and C_3 and $G_3(t)$ at the input.

```
/////////////////////////////////////////////////////////////////////////////////////////
// Model3.cpp: Computes the transmitted voltage for the ultrathin silicon switch   //
// Date: March 25, 2003                                                             //
/////////////////////////////////////////////////////////////////////////////////////////
#include <math.h>
#include <stdio.h>
#define Vi 5.0                // input waveform, vi(t), half the bias voltage in V
#define Vip 0.0               // derivative of the input waveform in V/s
#define Zo 120.0              // impedance of the transmission line in Ω
#define C1 10.0               // gap capacitance between the input and output in fF
```

```
#define C2 200.0              // shunt capacitance between the output and ground in fF
#define C3 200.0              // shunt capacitance between the input and ground in fF
#define to 1000.0             // excitation and probing zero-time in fs
#define tp 10.0               // FWHM of the optical pulse in fs
#define R 0.300               // surface reflectivity of Si
#define ueff 0.178            // mobility of Si in m^2/V/s
#define alpha 1E5             // attenuation coefficient of Si in m^-1
#define hnu 2.4848175E-19     // photon energy in joules
#define Ed 2.78521150411      // pump energy density (70 mW beam,20 um spot) in J/m^2
#define wid 20E-6             // PC gap width in m
#define len 20E-6             // PC gap length in m
#define dep 10E-6             // substrate thickness in m
#define no 3.42               // refractive index of Si
#define c 3E8                 // speed of light in m/s
#define e 1.60219E-19         // electronic charge in C
#define ts 0.00433333333333// step in time in fs
#define zs 0.1E-6             // step in space in m
#define pi 3.14159265358979// pi
#define imax 1153847          // number of data points used for the time interval
#define jmax 101              // number of data points used for the space interval
double xp(double xd,double yd,double td,double G1d,double G1pd,double G2d,double
G2pd,double G3d,double G3pd);
double yp(double xd,double yd,double td,double G1d,double G1pd,double G2d,double
G2pd,double G3d,double G3pd);
double A(double td,double G1d,double G1pd,double G2d,double G2pd,double
G3d,double G3pd);
double B(double td,double G1d,double G1pd,double G2d,double G2pd,double
G3d,double G3pd);
double C(double td,double G1d,double G1pd,double G2d,double G2pd,double
G3d,double G3pd);
double D(double td,double G1d,double G1pd,double G2d,double G2pd,double
G3d,double G3pd);
double E(double td,double G1d,double G1pd,double G2d,double G2pd,double
G3d,double G3pd);
double f(double td,double G1d,double G1pd,double G2d,double G2pd,double
G3d,double G3pd);
double g(double td,double G1d,double G1pd,double G2d,double G2pd,double
G3d,double G3pd);
double h(double td,double G1d,double G1pd,double G2d,double G2pd,double
G3d,double G3pd);
double derf(double x);

/////////////////////////////////////////////////////////////////////////////////////////////////////////////////
// Main program                                                                                              //
/////////////////////////////////////////////////////////////////////////////////////////////////////////////////
int main(int argc, char* argv[])
```

```
{
 double k1,l1,k2,l2,k3,l3,k4,l4,k5,l5,k6,l6;
 double t[imax],x[imax],y[imax],n[imax][jmax],Gg[imax],Gs[imax];
 double Ggp[imax],Gsp[imax],Intg[imax],Ints[imax],Vt[imax],z[jmax];
 int i,j,k;
 FILE* fp;
 ////////////////////////////////////////////////////////////////////////////////////////////////////////////
 // Solve for the electron density as a function of space and time                                       //
 ////////////////////////////////////////////////////////////////////////////////////////////////////////////
 t[0]=0.0;
 for(i=1;i<imax;i++)
 {
  t[i]=t[i-1]+ts;
 }
 z[0]=0.0;
 for(j=1;j<jmax;j++)
 {
  z[j]=z[j-1]+zs;
 }
 for(i=0;i<imax;i++)
 {
  for(j=0;j<jmax;j++)
    {
    n[i][j]=(1-R)*alpha*Ed*sqrt(pi)/4.0/hnu/sqrt(log(2.0))*
   (1.0+derf(2.0*sqrt(log(2.0))/tp*(t[i]-to-z[j]*no/c*1E15)))*exp(-alpha*z[j]);
    }
 }
 ////////////////////////////////////////////////////////////////////////////////////////////////////////////
 // Solve for the gap and shunt capacitances and their derivatives                                        //
 ////////////////////////////////////////////////////////////////////////////////////////////////////////////
 for(i=0;i<imax;i++)
 {
 Intg[i]=0.0;Ints[i]=0.0;
 for(j=2;j<(jmax-1);j=j+2)
 {
  Intg[i]=Intg[i]+zs/3.0*(n[i][j-2]+4.0*n[i][j-1]+n[i][j]);
  Ints[i]=Ints[i]+zs/3.0*(1.0/n[i][j-2]+4.0/n[i][j-1]+1.0/n[i][j]);
 }
 Gg[i]=wid*ueff*e/len*Intg[i];
 Gs[i]=wid*len*ueff*e/Ints[i];
 }
 Ggp[0]=0.0;Ggp[1]=0.0;Ggp[imax-1]=0.0;Ggp[imax-2]=0.0;
 Gsp[0]=0.0;Gsp[1]=0.0;Gsp[imax-1]=0.0;Gsp[imax-2]=0.0;
 for(i=2;i<(imax-2);i++)
 {
  Ggp[i]=(-Gg[i+2]+8.0*Gg[i+1]-8.0*Gg[i-1]+Gg[i-2])/12.0/ts;
```

```
  Gsp[i]=(-Gs[i+2]+8.0*Gs[i+1]-8.0*Gs[i-1]+Gs[i-2])/12.0/ts;
 }
/////////////////////////////////////////////////////////////////////////////////////////////
// Solve for the transmitted waveform using the Fifth-Order Runge-Kutta Meth.  //
/////////////////////////////////////////////////////////////////////////////////////////////
t[0]=0.0;x[0]=0.0;y[0]=0.0;Vt[0]=0.0;
for(i=4;i<imax;i=i+4)
{
  k1=4.0*ts*xp(x[i-4],y[i-4],t[i-4],Gg[i-4],Ggp[i-4],Gs[i-4],Gsp[i-4],Gs[i-4],Gsp[i-4]);
  l1=4.0*ts*yp(x[i-4],y[i-4],t[i-4],Gg[i-4],Ggp[i-4],Gs[i-4],Gsp[i-4],Gs[i-4],Gsp[i-4]);
  k2=4.0*ts*xp(x[i-4]+k1/4.0,y[i-4]+l1/4.0,t[i-4]+ts,Gg[i-3],Ggp[i-3],Gs[i-3],
       Gsp[i-3],Gs[i-3],Gsp[i-3]);
  l2=4.0*ts*yp(x[i-4]+k1/4.0,y[i-4]+l1/4.0,t[i-4]+ts,Gg[i-3],Ggp[i-3],Gs[i-3],
       Gsp[i-3],Gs[i-3],Gsp[i-3]);
  k3=4.0*ts*xp(x[i-4]+k1/8.0+k2/8.0,y[i-4]+l1/8.0+l2/8.0,t[i-4]+ts,Gg[i-3],
       Ggp[i-3],Gs[i-3],Gsp[i-3],Gs[i-3],Gsp[i-3]);
  l3=4.0*ts*yp(x[i-4]+k1/8.0+k2/8.0,y[i-4]+l1/8.0+l2/8.0,t[i-4]+ts,Gg[i-3],
       Ggp[i-3],Gs[i-3],Gsp[i-3],Gs[i-3],Gsp[i-3]);
  k4=4.0*ts*xp(x[i-4]-k2/2.0+k3,y[i-4]-l2/2.0+l3,t[i-4]+2.0*ts,Gg[i-2],
       Ggp[i-2],Gs[i-2],Gsp[i-2],Gs[i-2],Gsp[i-2]);
  l4=4.0*ts*yp(x[i-4]-k2/2.0+k3,y[i-4]-l2/2.0+l3,t[i-4]+2.0*ts,Gg[i-2],
       Ggp[i-2],Gs[i-2],Gsp[i-2],Gs[i-2],Gsp[i-2]);
  k5=4.0*ts*xp(x[i-4]+3.0/16.0*k1+9.0/16.0*k4,y[i-4]+3.0/16.0*l1+
       9.0/16.0*l4,t[i-4]+3.0*ts,Gg[i-1],Ggp[i-1],Gs[i-1],Gsp[i-1],Gs[i-1],Gsp[i-1]);
  l5=4.0*ts*yp(x[i-4]+3.0/16.0*k1+9.0/16.0*k4,y[i-4]+3.0/16.0*l1+
       9.0/16.0*l4,t[i-4]+3.0*ts,Gg[i-1],Ggp[i-1],Gs[i-1],Gsp[i-1],Gs[i-1],Gsp[i-1]);
  k6=4.0*ts*xp(x[i-4]-3.0/7.0*k1+3.0/7.0*k2+12.0/7.0*k3-12.0/7.0*k4+
       8.0/7.0*k5,y[i-4]-3.0/7.0*l1+2.0/7.0*l2+12.0/7.0*l3-12.0/7.0*l4+
       8.0/7.0*l5,t[i-4]+4.0*ts,Gg[i],Ggp[i],Gs[i],Gsp[i],Gs[i],Gsp[i]);
  l6=4.0*ts*yp(x[i-4]-3.0/7.0*k1+3.0/7.0*k2+12.0/7.0*k3-12.0/7.0*k4+
       8.0/7.0*k5,y[i-4]-3.0/7.0*l1+2.0/7.0*l2+12.0/7.0*l3-12.0/7.0*l4+
       8.0/7.0*l5,t[i-4]+4.0*ts,Gg[i],Ggp[i],Gs[i],Gsp[i],Gs[i],Gsp[i]);
  x[i]=x[i-4]+1.0/90.0*(7.0*k1+32.0*k3+12.0*k4+32.0*k5+7.0*k6);
  y[i]=y[i-4]+1.0/90.0*(7.0*l1+32.0*l3+12.0*l4+32.0*l5+7.0*l6);
  Vt[i]=x[i]/C2;
  printf("20 mW %1.6f        \n",t[i]/(imax-1)/ts*100);
}
fp=fopen("output ","w");
for(i=0;i<imax;i=i+1000)
{
  fprintf(fp,"%1.6f    %1.6f  %1.6f  %1.6f\n",t[i]/1000,Gg[i],Gs[i],Vt[i]);
}
fclose(fp);
return 0;
}
```

```
//////////////////////////////////////////////////////////////////////////////////////////////////
// Functions in double precision                                                              //
//////////////////////////////////////////////////////////////////////////////////////////////////
double xp(double xd,double yd,double td,double G1d,double G1pd,double G2d,
        double G2pd,double G3d,double G3pd)
{
 return yd;
}
double yp(double xd,double yd,double td,double G1d,double G1pd,double G2d,
        double G2pd,double G3d,double G3pd)
{
 return -D(td,G1d,G1pd,G2d,G2pd,G3d,G3pd)/
 A(td,G1d,G1pd,G2d,G2pd,G3d,G3pd)*Vip-
 E(td,G1d,G1pd,G2d,G2pd,G3d,G3pd)/
 A(td,G1d,G1pd,G2d,G2pd,G3d,G3pd)*Vi-
 B(td,G1d,G1pd,G2d,G2pd,G3d,G3pd)/
 A(td,G1d,G1pd,G2d,G2pd,G3d,G3pd)*yd-
 C(td,G1d,G1pd,G2d,G2pd,G3d,G3pd)/
 A(td,G1d,G1pd,G2d,G2pd,G3d,G3pd)*xd;
}
double A(double td,double G1d,double G1pd,double G2d,double G2pd,
        double G3d,double G3pd)
{
 return 2.0*C1*C2*f(td,G1d,G1pd,G2d,G2pd,G3d,G3pd)*
 h(td,G1d,G1pd,G2d,G2pd,G3d,G3pd)*Zo+C2*C3*
 f(td,G1d,G1pd,G2d,G2pd,G3d,G3pd)*
 h(td,G1d,G1pd,G2d,G2pd,G3d,G3pd)*Zo;
}
double B(double td,double G1d,double G1pd,double G2d,double G2pd,
        double G3d,double G3pd)
{
 return 2.0*C1*C2*g(td,G1d,G1pd,G2d,G2pd,G3d,G3pd)*
 h(td,G1d,G1pd,G2d,G2pd,G3d,G3pd)*Zo+C2*C3*
 g(td,G1d,G1pd,G2d,G2pd,G3d,G3pd)*
 h(td,G1d,G1pd,G2d,G2pd,G3d,G3pd)*
 Zo-2.0*C2*f(td,G1d,G1pd,G2d,G2pd,G3d,G3pd)*
 G3pd*Zo*Zo+2.0*C2*C3/C1*f(td,G1d,G1pd,G2d,G2pd,G3d,G3pd)*
 G1pd*Zo*Zo-C2*C3/C1*f(td,G1d,G1pd,G2d,G2pd,G3d,G3pd)*G3pd*
 Zo*Zo+C2*C3*C3/C1/C1*f(td,G1d,G1pd,G2d,G2pd,G3d,G3pd)*
 G1pd*Zo*Zo-C1*C3*h(td,G1d,G1pd,G2d,G2pd,G3d,G3pd)*
 h(td,G1d,G1pd,G2d,G2pd,G3d,G3pd)*Zo+
 C1*C2*h(td,G1d,G1pd,G2d,G2pd,G3d,G3pd)*
 h(td,G1d,G1pd,G2d,G2pd,G3d,G3pd)*Zo+C2*h(td,G1d,G1pd,G2d,G2pd,G3d,G3pd)*
 f(td,G1d,G1pd,G2d,G2pd,G3d,G3pd)+2.0*C2*
 h(td,G1d,G1pd,G2d,G2pd,G3d,G3pd)*
 f(td,G1d,G1pd,G2d,G2pd,G3d,G3pd)*G1d*Zo+
```

```
 C2*h(td,G1d,G1pd,G2d,G2pd,G3d,G3pd)*
 f(td,G1d,G1pd,G2d,G2pd,G3d,G3pd)*G3d*Zo;
}
double C(double td,double G1d,double G1pd,double G2d,double G2pd,double
                    G3d,double G3pd)
{
 return 2.0*C1*h(td,G1d,G1pd,G2d,G2pd,G3d,G3pd)*G2pd*Zo*Zo+2.0*C3*
 h(td,G1d,G1pd,G2d,G2pd,G3d,G3pd)*G2pd*Zo*Zo+2.0*C1*
 h(td,G1d,G1pd,G2d,G2pd,G3d,G3pd)*G3pd*Zo*Zo+C3*
 h(td,G1d,G1pd,G2d,G2pd,G3d,G3pd)*G2pd*Zo*Zo+C3*C3/C1*
 h(td,G1d,G1pd,G2d,G2pd,G3d,G3pd)*G2pd*Zo*Zo+C3*
 h(td,G1d,G1pd,G2d,G2pd,G3d,G3pd)*G3pd*Zo*Zo-2.0*C2*
 g(td,G1d,G1pd,G2d,G2pd,G3d,G3pd)*G3pd*Zo*Zo+2.0*C2*C3/C1*
 g(td,G1d,G1pd,G2d,G2pd,G3d,G3pd)*G1pd*Zo*Zo-C2*C3/C1*
 g(td,G1d,G1pd,G2d,G2pd,G3d,G3pd)*G3pd*Zo*Zo+C2*C3*C3/C1/C1*
 g(td,G1d,G1pd,G2d,G2pd,G3d,G3pd)*G1pd*Zo*Zo+C2*
 h(td,G1d,G1pd,G2d,G2pd,G3d,G3pd)*g(td,G1d,G1pd,G2d,G2pd,G3d,G3pd)+
 2.0*C2*h(td,G1d,G1pd,G2d,G2pd,G3d,G3pd)*
 g(td,G1d,G1pd,G2d,G2pd,G3d,G3pd)*G1d*Zo+C2*
 h(td,G1d,G1pd,G2d,G2pd,G3d,G3pd)*g(td,G1d,G1pd,G2d,G2pd,G3d,G3pd)*
 G3d*Zo-C1*h(td,G1d,G1pd,G2d,G2pd,G3d,G3pd)*
 h(td,G1d,G1pd,G2d,G2pd,G3d,G3pd)*G3d*Zo+C1*
 h(td,G1d,G1pd,G2d,G2pd,G3d,G3pd)*h(td,G1d,G1pd,G2d,G2pd,G3d,G3pd)*
 G2d*Zo;
}
double D(double td,double G1d,double G1pd,double G2d,double G2pd,
        double G3d,double G3pd)
{
 return -4.0*C1*C2*h(td,G1d,G1pd,G2d,G2pd,G3d,G3pd)*Zo-2.0*C2*C3*
 h(td,G1d,G1pd,G2d,G2pd,G3d,G3pd)*Zo;
}
double E(double td,double G1d,double G1pd,double G2d,double G2pd,
        double G3d,double G3pd)
{
 return 4.0*C2*G3pd*Zo*Zo-4.0*C2*C3/C1*G1pd*Zo*Zo+
 2.0*C2*C3/C1*G3pd*Zo*Zo-2.0*C2*C3*C3/C1/C1*G1pd*Zo*Zo-2.0*C2*
 h(td,G1d,G1pd,G2d,G2pd,G3d,G3pd)-4.0*C2*
 h(td,G1d,G1pd,G2d,G2pd,G3d,G3pd)*G1d*Zo-2.0*C2*
 h(td,G1d,G1pd,G2d,G2pd,G3d,G3pd)*G3d*Zo+2.0*C1*C2*
 h(td,G1d,G1pd,G2d,G2pd,G3d,G3pd)*h(td,G1d,G1pd,G2d,G2pd,G3d,G3pd);
}
double f(double td,double G1d,double G1pd,double G2d,double G2pd,
        double G3d,double G3pd)
{
 return Zo+Zo*C3/C1+Zo*C3/C2;
}
```

```
double g(double td,double G1d,double G1pd,double G2d,double G2pd,
        double G3d,double G3pd)
{
 return Zo*G2d/C2+Zo*C3*G2d/C1/C2+2.0/C2+C3/C1/C2+Zo*G3d/C2;
}
double h(double td,double G1d,double G1pd,double G2d,double G2pd,
        double G3d,double G3pd)
{
 return 1.0/C1+Zo*G3d/C1-Zo*C3*G1d/C1/C1;
}
///////////////////////////////////////////////////////////////////////////////////////////////////////////////
// Error function in double precision                                                   //
///////////////////////////////////////////////////////////////////////////////////////////////////////////////
double derf(double x)
{
   int k;
   double w, t, y;
   static double a[65] = {
      5.958930743e-11, -1.13739022964e-9,
      1.466005199839e-8, -1.635035446196e-7,
      1.6461004480962e-6, -1.492559551950604e-5,
      1.2055331122299265e-4, -8.548326981129666e-4,
      0.00522397762482322257, -0.0268661706450773342,
      0.11283791670954881569, -0.37612638903183748117,
      1.12837916709551257377,
      2.372510631e-11, -4.5493253732e-10,
      5.90362766598e-9, -6.642090827576e-8,
      6.7595634268133e-7, -6.21188515924e-6,
      5.10388300970969e-5, -3.7015410692956173e-4,
      0.00233307631218880978, -0.0125498847718219221,
      0.05657061146827041994, -0.2137966477645600658,
      0.84270079294971486929,
      9.49905026e-12, -1.8310229805e-10,
      2.39463074e-9, -2.721444369609e-8,
      2.8045522331686e-7, -2.61830022482897e-6,
      2.195455056768781e-5, -1.6358986921372656e-4,
      0.00107052153564110318, -0.00608284718113590151,
      0.02986978465246258244, -0.13055593046562267625,
      0.67493323603965504676,
      3.82722073e-12, -7.421598602e-11,
      9.793057408e-10, -1.126008898854e-8,
      1.1775134830784e-7, -1.1199275838265e-6,
      9.62023443095201e-6, -7.404402135070773e-5,
      5.0689993654144881e-4, -0.00307553051439272889,
      0.01668977892553165586, -0.08548534594781312114,
```

```
    0.56909076642393639985,
    1.55296588e-12, -3.032205868e-11,
    4.0424830707e-10, -4.71135111493e-9,
    5.011915876293e-8, -4.8722516178974e-7,
    4.30683284629395e-6, -3.445026145385764e-5,
    2.4879276133931664e-4, -0.00162940941748079288,
    0.00988786373932350462, -0.05962426839442303805,
    0.49766113250947636708
  };
  static double b[65] = {
    -2.9734388465e-10, 2.69776334046e-9,
    -6.40788827665e-9, -1.6678201321e-8,
    -2.1854388148686e-7, 2.66246030457984e-6,
    1.612722157047886e-5, -2.5616361025506629e-4,
    1.5380842432375365e-4, 0.00815533022524927908,
    -0.01402283663896319337, -0.19746892495383021487,
    0.71511720328842845913,
    -1.951073787e-11, -3.2302692214e-10,
    5.22461866919e-9, 3.42940918551e-9,
    -3.5772874310272e-7, 1.9999935792654e-7,
    2.687044575042908e-5, -1.1843240273775776e-4,
    -8.0991728956032271e-4, 0.00661062970502241174,
    0.00909530922354827295, -0.20160072778491013140,
    0.51169696718727644908,
    3.147682272e-11, -4.8465972408e-10,
    6.3675740242e-10, 3.377623323271e-8,
    -1.5451139637086e-7, -2.03340624738438e-6,
    1.947204525295057e-5, 2.854147231653228e-5,
    -0.00101565063152200272, 0.00271187003520095655,
    0.02328095035422810727, -0.16725021123116877197,
    0.32490054966649436974,
    2.31936337e-11, -6.303206648e-11,
    -2.64888267434e-9, 2.050708040581e-8,
    1.1371857327578e-7, -2.11211337219663e-6,
    3.68797328322935e-6, 9.823686253424796e-5,
    -6.5860243990455368e-4, -7.5285814895230877e-4,
    0.02585434424202960464, -0.11637092784486193258,
    0.18267336775296612024,
    -3.677789363e-12, 2.0876046746e-10,
    -1.93319027226e-9, -4.35953392472e-9,
    1.8006992266137e-7, -7.8441223763969e-7,
    -6.75407647949153e-6, 8.428418334440096e-5,
    -1.7604388937031815e-4, -0.00239729611435071610,
    0.02064129023876022970, -0.06905562880005864105,
    0.09084526782065478489
  };
```

```
    w = x < 0 ? -x : x;
    if (w < 2.2) {
       t = w * w;
       k = (int) t;
       t -= k;
       k *= 13;
       y = ((((((((((((a[k] * t + a[k + 1]) * t +
          a[k + 2]) * t + a[k + 3]) * t + a[k + 4]) * t +
          a[k + 5]) * t + a[k + 6]) * t + a[k + 7]) * t +
          a[k + 8]) * t + a[k + 9]) * t + a[k + 10]) * t +
          a[k + 11]) * t + a[k + 12]) * w;
    } else if (w < 6.9) {
       k = (int) w;
       t = w - k;
       k = 13 * (k - 2);
       y = (((((((((((b[k] * t + b[k + 1]) * t +
          b[k + 2]) * t + b[k + 3]) * t + b[k + 4]) * t +
          b[k + 5]) * t + b[k + 6]) * t + b[k + 7]) * t +
          b[k + 8]) * t + b[k + 9]) * t + b[k + 10]) * t +
          b[k + 11]) * t + b[k + 12];
       y *= y;
       y *= y;
       y *= y;
       y = 1 - y * y;
    } else {
       y = 1;
    }
    return x < 0 ? -y : y;
}
```

Appendix E

NUMERICAL ANALYSIS OF THE COPLANAR PHOTOCONDUCTIVE SWITCH

The model for the coplanar PC switch is solved using a second-order differencing scheme. Initially, the electron density, $n(z,t)$, is found as a function of space (depth) and time. This function is then used to compute the time-varying gap conductance terms across the bias-to-signal gap, $G_{g1}(t)$, and the signal-to-ground gap, $G_{g2}(t)$. Finally, these time-varying conductance functions are inserted into the second-order differential equation describing the transmitted waveforms, $v_t(t)$, and the transmitted waveforms are calculated numerically using a second-order differential scheme. The difference equation for the second-order differential equation becomes

$$A_{i-1}\frac{v_{t,i}-2v_{t,i-1}+v_{t,i-2}}{\Delta t^2}+B_{i-1}\frac{v_{t,i}-v_{t,i-2}}{2\Delta t}+C_{i-1}v_{t,i-1}-D_{i-1}=0, \tag{D.1}$$

where

$$A_{i-1}=C_{g1}C_{g2}Z_{01}, \tag{D.2}$$

$$B_{i-1}=C_{g1}+C_{g2}+\frac{2C_{g1}Z_{01}}{Z_{02}}+C_{g2}Z_{01}G_{g1,i-1}+C_{g1}Z_{01}G_{g2,i-1}, \tag{D.3}$$

$$C_{i-1}=\frac{2}{Z_{02}}+G_{g1,i-1}+G_{g2,i-1}+\frac{2Z_{01}}{Z_{02}}G_{g1,i-1}+Z_{01}G_{g1,i-1}G_{g2,i-1}+C_{g1}Z_{01}G_{g2,i-1}, \tag{D.4}$$

and

$$D_{i-1} = G_{g1,i-1}V_b. \tag{D.5}$$

Using these relations the transmitted voltage at the current time step is found to be

$$v_{t,i} = \left(\frac{A_{i-1}}{\Delta t^2} + \frac{B_{i-1}}{2\Delta t}\right)^{-1}\left[\left(\frac{2A_{i-1}}{\Delta t^2} - C_{i-1}\right)v_{t,i-1} + \left(\frac{-A_{i-1}}{\Delta t^2} + \frac{B_{i-1}}{2\Delta t}\right)v_{t,i-2} + D_{i-1}\right]. \tag{D.6}$$

This numerical process is implemented through the C-program shown below.

```
//////////////////////////////////////////////////////////////////////////////////////////////////////
// CoplanarPCSwitchModel2.cpp: Computes the vt(t) for a coplanar PC switch          //
// The conductance terms model the charge carrier dynamics.                          //
// The voltage on the bias electrode varies with time (vi(t) and vr(t)).             //
//////////////////////////////////////////////////////////////////////////////////////////////////////
#include <math.h>
#include <stdio.h>
#define Ppump 135.0            // pump power in mW
#define spot 100.0             // spot size in um
#define Asymm 1.0              // asymmetry factor in the illumination
#define Vb 22.5                // bias voltage for the switch in V
#define Zo1 270.0              // impedance of the bias electrode in Ohms from AppCAD
#define Zo2 100.0              // impedance of the signal line in Ohms from Hoffmann
#define C1 0.5                 // capacitance of the bias-to-signal gap in fF
#define C2 1.0                 // capacitance of the signal-to-ground gap in fF
#define to 1000.0              // excitation and probing zero-time in fs
#define tp 100.0               // FWHM of the optical pulse in fs
#define R 0.31947              // surface reflectivity
#define tdelay 333.0           // delay time through the SiO2 layer in fs
#define ueff 0.3               // mobility in m^2/V/s
#define alpha 1.351351E6       // attenuation coefficient in m^-1
#define hnu 2.4848175E-19      // photon energy in joules
#define len1 40E-6             // first PC gap length in m
#define len2 20E-6             // second PC gap length in m
#define no 3.68                // refractive index of the GaAs substrate
#define c 299792458            // speed of light in m/s
#define e 1.60219E-19          // electronic charge in C
#define ts 0.0043333333333     // step in time in fs
#define zs 0.05E-6             // step in space in m
#define pi 3.14159265358979// pi
#define imax 700000            // maximum number of data points used for time
#define jmax 21                // maximum number of data points used for space
double derf(double x);

int main(int argc, char* argv[])
 {
```

```
double k1,k2,k3,k4;
double t[imax],n[imax][jmax],Gg1[imax],Gg2[imax],Gg2p[imax];
double Int[imax],vt[imax],z[jmax],Ed,A,B,C,D;
int i,j,k;
FILE* fp;
////////////////////////////////////////////////////////////////////////////////////////////////////////
// Solve for the electron density as a function of space and time                                   //
////////////////////////////////////////////////////////////////////////////////////////////////////////
Ed=Ppump/1000.0/80E6/3.14159265358979/spot/spot*4.0*1E12;
t[0]=0.0;
for(i=1;i<imax;i++)
{
 t[i]=t[i-1]+ts;
}
z[0]=0.0;
for(j=1;j<jmax;j++)
{
 z[j]=z[j-1]+zs;
}
for(i=0;i<imax;i++)
{
 for(j=0;j<jmax;j++)
 {
  n[i][j]=(1-R)*alpha*Ed*sqrt(pi)/4.0/hnu/sqrt(log(2.0))
  *(1.0+derf(2.0*sqrt(log(2.0))/tp*(t[i]-to-z[j]*no/c*1E15)))*exp(-alpha*z[j]);
 }
}
////////////////////////////////////////////////////////////////////////////////////////////////////////
// Solve for gap capacitance functions as a function of space and time                              //
////////////////////////////////////////////////////////////////////////////////////////////////////////
for(i=0;i<imax;i++)
{
 Int[i]=0.0;
 for(j=2;j<(jmax-1);j=j+2)
 {
  Int[i]=Int[i]+zs/3.0*(n[i][j-2]+4.0*n[i][j-1]+n[i][j]);
 }
 Gg1[i]=spot*1E-6*ueff*e/len1*Int[i]/sqrt(Asymm);
}
for(i=int(tdelay/ts);i<imax;i++)
{
 Gg2[i]=Gg1[i-int(tdelay/ts)]*len1/len2*Asymm;
}
Gg2p[0]=0.0;Gg2p[imax-1]=0.0;
for(i=1;i<(imax-1);i++)
{
```

```
  Gg2p[i]=(Gg2[i+1]-Gg2[i-1])/2.0/ts;
 }
 ////////////////////////////////////////////////////////////////////////////////////////////////////////////////////
 // Solve for the transmitted waveform using the second-order difference equation    //
 ////////////////////////////////////////////////////////////////////////////////////////////////////////////////////
 t[0]=0.0;vt[0]=0.0;
 for(i=2;i<imax;i++)
 {
  A=C1*C2*Zo1;
  B=2.0*C1*Zo1/Zo2+C1*Zo1*Gg2[i-1]+C1+C2+C2*Zo1*Gg1[i-1];
  C=C1*Zo1*Gg2p[i-1]+2.0*Zo1/Zo2*Gg1[i-1]+Zo1*Gg1[i-1]*Gg2[i-1]
  +Gg1[i-1]+Gg2[i-1]+2.0/Zo2;
  D=Gg1[i-1]*Vb;
  vt[i]=((2.0*A/ts/ts-C)*vt[i-1]+(-A/ts/ts+B/2.0/ts)*vt[i-2]+D)/(A/ts/ts+B/2.0/ts);
  printf("%1.6f        \n",t[i]/(imax-1)/ts*100);
 }
 fp=fopen("output.txt","w");
 for(i=0;i<imax;i=i+1000)
 {
  fprintf(fp,"%1.6f    %1.6f  %1.6f  %1.6f\n",t[i]/1000,Gg1[i],Gg2[i],vt[i]);
 }
 fclose(fp);
 return 0;
}
////////////////////////////////////////////////////////////////////////////////////////////////////////////////////
// Error function in double precision                                                //
////////////////////////////////////////////////////////////////////////////////////////////////////////////////////
double derf(double x)
{
  int k;
  double w, t, y;
  static double a[65] = {
    5.958930743e-11, -1.13739022964e-9,
    1.466005199839e-8, -1.635035446196e-7,
    1.6461004480962e-6, -1.492559551950604e-5,
    1.2055331122299265e-4, -8.548326981129666e-4,
    0.00522397762482322257, -0.0268661706450773342,
    0.11283791670954881569, -0.37612638903183748117,
    1.12837916709551257377,
    2.372510631e-11, -4.5493253732e-10,
    5.90362766598e-9, -6.642090827576e-8,
    6.7595634268133e-7, -6.21188515924e-6,
    5.10388300970969e-5, -3.7015410692956173e-4,
    0.00233307631218880978, -0.0125498847718219221,
    0.05657061146827041994, -0.2137966477645600658,
    0.84270079294971486929,
```

```
    9.49905026e-12, -1.8310229805e-10,
    2.39463074e-9, -2.721444369609e-8,
    2.8045522331686e-7, -2.61830022482897e-6,
    2.195455056768781e-5, -1.6358986921372656e-4,
    0.00107052153564110318, -0.00608284718113590151,
    0.02986978465246258244, -0.13055593046562267625,
    0.67493323603965504676,
    3.82722073e-12, -7.421598602e-11,
    9.793057408e-10, -1.126008898854e-8,
    1.1775134830784e-7, -1.1199275838265e-6,
    9.62023443095201e-6, -7.404402135070773e-5,
    5.0689993654144881e-4, -0.00307553051439272889,
    0.01668977892553165586, -0.08548534594781312114,
    0.56909076642393639985,
    1.55296588e-12, -3.032205868e-11,
    4.0424830707e-10, -4.71135111493e-9,
    5.011915876293e-8, -4.8722516178974e-7,
    4.30683284629395e-6, -3.445026145385764e-5,
    2.4879276133931664e-4, -0.00162940941748079288,
    0.00988786373932350462, -0.05962426839442303805,
    0.49766113250947636708
  };
  static double b[65] = {
    -2.9734388465e-10, 2.69776334046e-9,
    -6.40788827665e-9, -1.6678201321e-8,
    -2.1854388148686e-7, 2.66246030457984e-6,
    1.612722157047886e-5, -2.5616361025506629e-4,
    1.5380842432375365e-4, 0.00815533022524927908,
    -0.01402283663896319337, -0.19746892495383021487,
    0.71511720328842845913,
    -1.951073787e-11, -3.2302692214e-10,
    5.22461866919e-9, 3.42940918551e-9,
    -3.5772874310272e-7, 1.9999935792654e-7,
    2.687044575042908e-5, -1.1843240273775776e-4,
    -8.0991728956032271e-4, 0.00661062970502241174,
    0.00909530922354827295, -0.2016007277849101314,
    0.51169696718727644908,
    3.147682272e-11, -4.8465972408e-10,
    6.3675740242e-10, 3.377623323271e-8,
    -1.5451139637086e-7, -2.03340624738438e-6,
    1.947204525295057e-5, 2.854147231653228e-5,
    -0.00101565063152200272, 0.00271187003520095655,
    0.02328095035422810727, -0.16725021123116877197,
    0.32490054966649436974,
    2.31936337e-11, -6.303206648e-11,
    -2.64888267434e-9, 2.050708040581e-8,
```

```
        1.13718573275 78e-7, -2.11211337219663e-6,
        3.68797328322935e-6, 9.823686253424796e-5,
        -6.5860243990455368e-4, -7.5285814895230877e-4,
        0.02585434424202960464, -0.11637092784486193258,
        0.18267336775296612024,
        -3.677789363e-12, 2.0876046746e-10,
        -1.93319027226e-9, -4.35953392472e-9,
        1.8006992266137e-7, -7.8441223763969e-7,
        -6.75407647949153e-6, 8.428418334440096e-5,
        -1.7604388937031815e-4, -0.00239729611435071 61,
        0.02064129023876022 97, -0.06905562880005864105,
        0.09084526782065478489
    };

    w = x < 0 ? -x : x;
    if (w < 2.2) {
        t = w * w;
        k = (int) t;
        t -= k;
        k *= 13;
        y = ((((((((((((a[k] * t + a[k + 1]) * t +
            a[k + 2]) * t + a[k + 3]) * t + a[k + 4]) * t +
            a[k + 5]) * t + a[k + 6]) * t + a[k + 7]) * t +
            a[k + 8]) * t + a[k + 9]) * t + a[k + 10]) * t +
            a[k + 11]) * t + a[k + 12]) * w;
    } else if (w < 6.9) {
        k = (int) w;
        t = w - k;
        k = 13 * (k - 2);
        y = (((((((((((b[k] * t + b[k + 1]) * t +
            b[k + 2]) * t + b[k + 3]) * t + b[k + 4]) * t +
            b[k + 5]) * t + b[k + 6]) * t + b[k + 7]) * t +
            b[k + 8]) * t + b[k + 9]) * t + b[k + 10]) * t +
            b[k + 11]) * t + b[k + 12];
        y *= y;
        y *= y;
        y *= y;
        y = 1 - y * y;
    } else {
        y = 1;
    }
    return x < 0 ? -y : y;
}
```

Appendix F

NUMERICAL ANALYSIS OF THE PHOTOCONDUCTIVE FROZEN WAVE GENERATOR

To obtain the solution for the traveling waves formed on the coplanar transmission line by the FWG, equations 2.5.1.10-2.5.1.12 are solved simultaneously as a function of space and time. The results are then summed in series for the overall electrical response (as described by equation 2.5.1.13), and the waveforms are plotted as a function of space at various points in time. The MATLAB program used for this procedure is shown below.

```
%%%%%%%%%%%%%%%%%%%%%%%%%%%%%%%%%%%%%%%%%%%%%%%%%%
% This is a traveling wave simulation program for a four-electrode frozen wave      %
% generator. The electrodes are biased at as + - + - . Last edited: April 30, 2003.  %
%%%%%%%%%%%%%%%%%%%%%%%%%%%%%%%%%%%%%%%%%%%%%%%%%%
% The forward and reverse traveling waves are determined from the analysis of a     %
% series PC gaps. Given a normal PC gap that is positive on the left and grounded on %
% the right, the forward wave will be the transmitted function, vfor(t) = vt(t), while the %
% reverse wave will be vrev(t) = -Vb/2+vr(t). Using these definitions, summed with  %
% the stationary waveform that is +Vb on the left and zero on the right, gives the   %
% correct boundary conditions and traveling waves. The value and sign of the waves   %
% for each PC gap is taken to be the initial potential to the right of the gap       %
% subtracted from the initial potential to the left of the gap.                      %
%%%%%%%%%%%%%%%%%%%%%%%%%%%%%%%%%%%%%%%%%%%%%%%%%%

%%%%%%%%%%%%%%%%%%%%%%%%%%%%%%%%%%%%%%%%%%%%%%%%%%
% This physical constants for the device are as follows:                             %
%%%%%%%%%%%%%%%%%%%%%%%%%%%%%%%%%%%%%%%%%%%%%%%%%%
a=50.0;                 % length of one of the FWG bias electrodes in microns
Zo=100.0;               % impedance of the transmission line in Ohms
Gg=10.0;                % conductance across the photoconductive gap in Ohm^-1
Cg=1.0;                 % capacitance across the photoconductive gap in pF
c=300.0;                % speed of light in microns per picosecond
neff=3.0;               % effective refractive index for the transmission line
Vb=5.0;                 % peak bias voltage
```

```
xstep=1.0;                    % step size used in the array of x
tau=1.0/(1.0/2.0/Zo/Cg+Gg/Cg); % time constant for the PC gap in ps
x=-10*a:xstep:10*a;           % this is the spatial dimension across the device
t=x.'*neff/c;                 % interval for the simulation in ps

%%%%%%%%%%%%%%%%%%%%%%%%%%%%%%%%%%%%%%%%%%%%%%%
% Solve for the initial standing waveform on the transmission line          %
%%%%%%%%%%%%%%%%%%%%%%%%%%%%%%%%%%%%%%%%%%%%%%%
vstand=zeros(size(t,1),size(x,2));
for it=1:size(t,1)
vstand(it,:)=Vb.*(x>(-2.0*a)).*(x<-a)-Vb.*(x>-a).*(x<0)+Vb.*(x>0).*(x<a)-
Vb.*(x>a).*(x<(2.0*a))+Vb.*(x==(-2.0*a))+Vb/2.0.*(x==(-2.0*a-xstep))-Vb.*(x==-a)-
Vb.*(x==(-a-xstep))+Vb.*(x==0)+Vb.*(x==-xstep)-Vb.*(x==a)-Vb.*(x==(a-
1))+Vb/2.0.*(x==(2.0*a-1));
end

%%%%%%%%%%%%%%%%%%%%%%%%%%%%%%%%%%%%%%%%%%%%%%%
% Solve for the reverse and forward traveling waves from the first PC gap       %
%%%%%%%%%%%%%%%%%%%%%%%%%%%%%%%%%%%%%%%%%%%%%%%
vrev1=zeros(size(t,1),size(x,2));
for ix=1:round((size(x,2)-1)/2-2.0*a/xstep)
vrev1(:,ix)=-Vb/2.0*(-1.0+1.0/(1.0+2.0*Zo*Gg).*(1.0+2.0*Zo*Gg.*exp(-
(t+(x(ix)+2.0*a)*neff/c)/tau))).*((t+(x(ix)+2.0*a)*neff/c)>0.0);
end
vfor1=zeros(size(t,1),size(x,2));
for ix=round((size(x,2)-1)/2-2.0*a/xstep):size(x,2)
vfor1(:,ix)=-Vb/2.0*(2.0*Zo*Gg)/(1.0+2.0*Zo*Gg)*(1.0-exp(-(t-
(x(ix)+2.0*a)*neff/c)/tau)).*((t-(x(ix)+2.0*a)*neff/c)>0.0);
end

%%%%%%%%%%%%%%%%%%%%%%%%%%%%%%%%%%%%%%%%%%%%%%%
% Solve for the reverse and forward traveling waves from the second PC gap     %
%%%%%%%%%%%%%%%%%%%%%%%%%%%%%%%%%%%%%%%%%%%%%%%
vrev2=zeros(size(t,1),size(x,2));
for ix=1:round((size(x,2)-1)/2-a/xstep)
vrev2(:,ix)=+Vb*(-1.0+1.0/(1.0+2.0*Zo*Gg).*(1.0+2.0*Zo*Gg.*exp(-
(t+(x(ix)+a)*neff/c)/tau))).*((t+(x(ix)+a)*neff/c)>0.0);
end
vfor2=zeros(size(t,1),size(x,2));
for ix=round((size(x,2)-1)/2-a/xstep):size(x,2)
vfor2(:,ix)=+Vb*(2.0*Zo*Gg)/(1.0+2.0*Zo*Gg)*(1.0-exp(-(t-
(x(ix)+a)*neff/c)/tau)).*((t-(x(ix)+a)*neff/c)>0.0);
end

%%%%%%%%%%%%%%%%%%%%%%%%%%%%%%%%%%%%%%%%%%%%%%%
% Solve for the reverse and forward traveling waves from the third PC gap        %
```

```
%%%%%%%%%%%%%%%%%%%%%%%%%%%%%%%%%%%%%%%%%%
vrev3=zeros(size(t,1),size(x,2));
for ix=1:round((size(x,2)-1)/2)
 vrev3(:,ix)=-Vb*(-1.0+1.0/(1.0+2.0*Zo*Gg).*(1.0+2.0*Zo*Gg.*exp(-
(t+x(ix)*neff/c)/tau))).*((t+x(ix)*neff/c)>0.0);
end
vfor3=zeros(size(t,1),size(x,2));
for ix=round((size(x,2)-1)/2):size(x,2)
 vfor3(:,ix)=-Vb*(2.0*Zo*Gg)/(1.0+2.0*Zo*Gg)*(1.0-exp(-(t-x(ix)*neff/c)/tau)).*((t-
x(ix)*neff/c)>0.0);
end

%%%%%%%%%%%%%%%%%%%%%%%%%%%%%%%%%%%%%%%%%%
% Solve for the reverse and forward traveling waves from the fourth PC gap          %
%%%%%%%%%%%%%%%%%%%%%%%%%%%%%%%%%%%%%%%%%%
vrev4=zeros(size(t,1),size(x,2));
for ix=1:round((size(x,2)-1)/2+a/xstep)
vrev4(:,ix)=+Vb*(-1.0+1.0/(1.0+2.0*Zo*Gg).*(1.0+2.0*Zo*Gg.*exp(-(t+(x(ix)-
a)*neff/c)/tau))).*((t+(x(ix)-a)*neff/c)>0.0);
end
vfor4=zeros(size(t,1),size(x,2));
for ix=round((size(x,2)-1)/2+a/xstep):size(x,2)
vfor4(:,ix)=+Vb*(2.0*Zo*Gg)/(1.0+2.0*Zo*Gg)*(1.0-exp(-(t-(x(ix)-a)*neff/c)/tau)).*((t-
(x(ix)-a)*neff/c)>0.0);
end

%%%%%%%%%%%%%%%%%%%%%%%%%%%%%%%%%%%%%%%%%%
% Solve for the reverse and forward traveling waves from the fifth PC gap           %
%%%%%%%%%%%%%%%%%%%%%%%%%%%%%%%%%%%%%%%%%%
vrev5=zeros(size(t,1),size(x,2));
for ix=1:round((size(x,2)-1)/2+2.0*a/xstep)
vrev5(:,ix)=-Vb/2.0*(-1.0+1.0/(1.0+2.0*Zo*Gg).*(1.0+2.0*Zo*Gg.*exp(-(t+(x(ix)-
2.0*a)*neff/c)/tau))).*((t+(x(ix)-2.0*a)*neff/c)>0.0);
end
vfor5=zeros(size(t,1),size(x,2));
for ix=round((size(x,2)-1)/2+2.0*a/xstep):size(x,2)
vfor5(:,ix)=-Vb/2.0*(2.0*Zo*Gg)/(1.0+2.0*Zo*Gg)*(1.0-exp(-(t-(x(ix)-
2.0*a)*neff/c)/tau)).*((t-(x(ix)-2.0*a)*neff/c)>0.0);
end

%%%%%%%%%%%%%%%%%%%%%%%%%%%%%%%%%%%%%%%%%%
% Compute the total voltage on the transmission line as a function of time and space  %
%%%%%%%%%%%%%%%%%%%%%%%%%%%%%%%%%%%%%%%%%%
 v=vstand+(vrev1+vfor1)+(vrev2+vfor2)+(vrev3+vfor3)+(vrev4+vfor4)+(vrev5+vfor5);
```

Appendix G

TRANSIMPEDANCE AMPLIFIER AND DIFFERENCING CIRCUIT

The circuit shown in figure G.1 takes the difference between the probe beam powers that exit the wallaston prism. The difference between the resulting photo-currents is amplified by the 47000 V/A transimpedance gain of the Burr-Brown PPA655 amplifier.

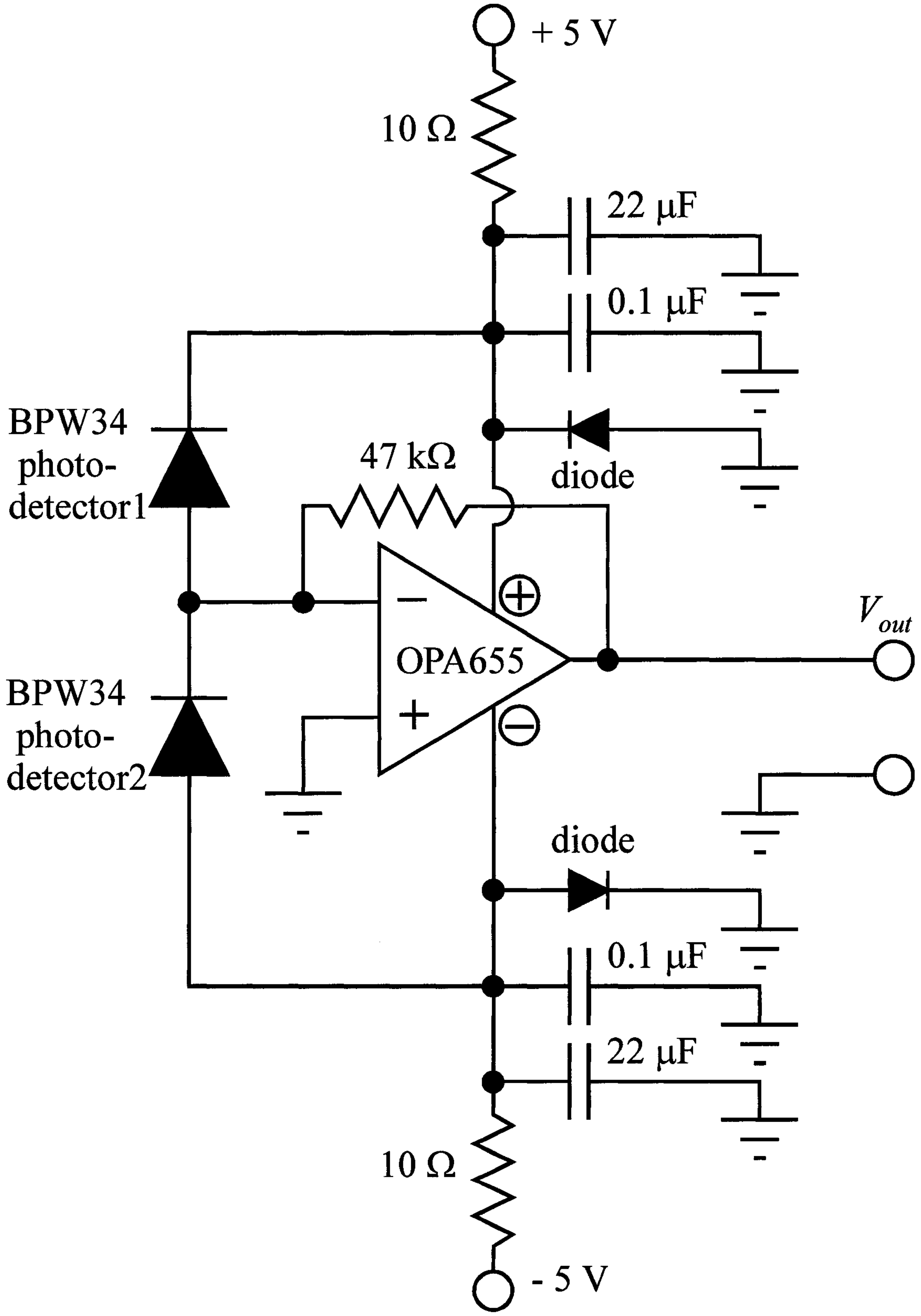

Figure G.1 The transimpedance amplifier and differencing circuit.

Appendix H

TWO-PHOTON ZERO-TIME MEASUREMENTS

A key element in the implementation of any time-resolved experiment is the determination of the zero-time. The zero-time is the time-delay for which the pump pulse and the probe pulse simultaneously reach the location of interaction. To optimize the signal for the free-space THz setup, therefore, the delay along both the pump beam path and probe beam path must first be made equal.

The resolution achieved by physically measuring the pump beam and probe beam path lengths is relatively inaccurate. To obtain a more accurate value for the zero-time, therefore, a two-photon correlation technique is implemented within the free-space THz setup. To do this, the THz emitter is removed from the free-space THz setup, and the pump and probe beams are overlapped in the time-base calibration arm. Both the pump beam and the probe beam are then focused onto the GaAsP two-photon detector (with a bandgap of E_g = 1.8 eV). The intensities of the two beams are made to be equal, and the current from the detector is monitored as a function of the pump delay line position.

The response of the two-photon detector differs from that of a conventional single-photon detector in that two photons are required to make a transition from the valence band to the conduction band. The current induced within the detector is, therefore, proportional to the square of the incident intensity, and can be written as

$$i(\tau)=\int_{-\infty}^{\infty}\left\{\left[E(t-\tau)+E(t)\right]^2\right\}^2 dt\,, \tag{G.1}$$

where

$$E(t)=\Re e\left\{\varepsilon(t)e^{i\omega_o t}\right\} \tag{G.2}$$

is the electric field of both the pump and probe beams, τ is the time-delay between the pulses, ω_o is the central frequency of the near-infrared pulses, and $\varepsilon(t)$ is the envelope of the near-infrared pulses. With this, the current becomes

$$i(\tau)=\Re e\left\{\int_{-\infty}^{\infty}\left[\varepsilon^2(t)+\varepsilon^2(t-\tau)+\varepsilon(t)\varepsilon(t-\tau)e^{i\omega_o\tau}+\varepsilon(t)\varepsilon(t-\tau)e^{-i\omega_o\tau}\right]^2 dt\right\}, \tag{G.3}$$

which can be rewritten as

$$\begin{aligned}
i(\tau)=&\int_{-\infty}^{\infty}\left[\varepsilon^4(t)+\varepsilon^4(t-\tau)+4\varepsilon^2(t)\varepsilon^2(t-\tau)\right]dt\\
&+2\Re e\left\{\int_{-\infty}^{\infty}\left[\varepsilon^3(t-\tau)\varepsilon(t)e^{i\omega_o\tau}+\varepsilon^3(t-\tau)\varepsilon(t)e^{-i\omega_o\tau}\right]dt\right\}\\
&+2\Re e\left\{\int_{-\infty}^{\infty}\left[\varepsilon(t-\tau)\varepsilon^3(t)e^{i\omega_o\tau}+\varepsilon(t-\tau)\varepsilon^3(t)e^{-i\omega_o\tau}\right]dt\right\}\\
&+\Re e\left\{\int_{-\infty}^{\infty}\left[\varepsilon^2(t-\tau)\varepsilon^2(t)e^{i2\omega_o\tau}+\varepsilon^2(t-\tau)\varepsilon^2(t)e^{-i2\omega_o\tau}\right]dt\right\}.
\end{aligned} \tag{G.4}$$

Experimentally, the noise level in the system is lowered by using both a long time constant for the data acquisition system and a running average across the waveform. This slow response time for the system (as a function of τ) washes out the interference effects from the last three terms, leaving the intensity autocorrelation function,

$$i(\tau)=\int_{-\infty}^{\infty}\left[\varepsilon^4(t)+\varepsilon^4(t-\tau)+4\varepsilon^2(t)\varepsilon^2(t-\tau)\right]dt\,, \tag{G.5}$$

with a 3:1 ratio between the signal peak and the signal background. The maximum value of this function provides the zero-time for the THz generation and detection system.

Using the free-space THz setup, the current from the GaAsP two-photon detector is monitored while the pump delay line is scanned. The result is the signal shown in figure H.1. The measured current shows an intensity autocorrelation envelope with some fringes visible at the centre of the function–suggesting that the pump scanning mechanism and the beam alignments are capable of resolving some features on the scale of the optical wavelength. Using the peak value from this scan as the zero-time for the experiment, the position of the pump delay line is recorded, and the setup is returned to its free-space generation and detection form.

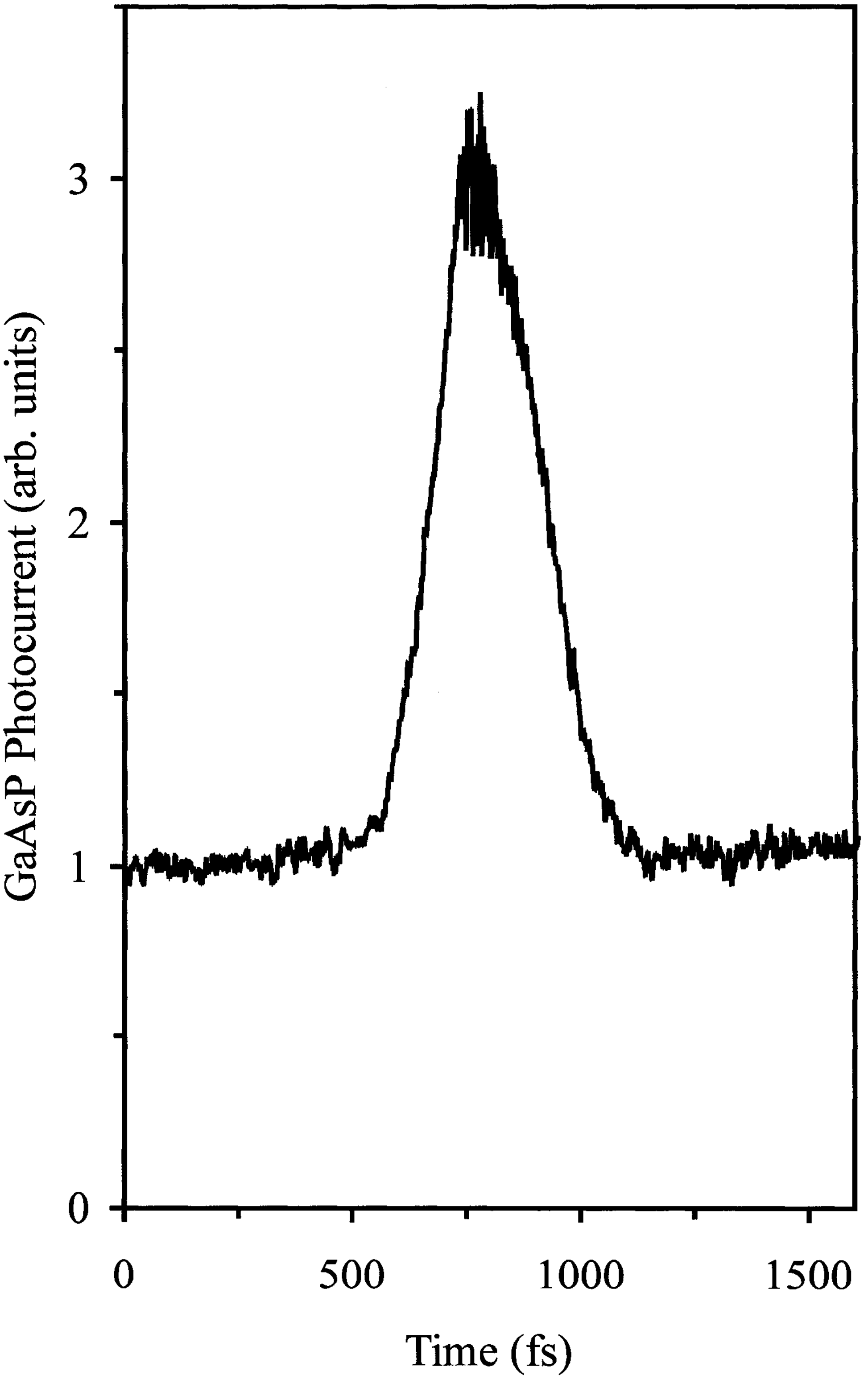

Figure H.1 Intensity autocorrelation function measured by the two-photon GaAsP photodiode in the zero-time calibration arm of the free-space THz generation and detection system.

Appendix I

NUMERICAL ANALYSIS OF THE LARGE GaAs TERAHERTZ EMITTER

To solve for the far-field THz radiation pattern, equations 3.3.1.1-3.3.1.14 are solved simultaneously for the surface electron density, $n_s(x,t)$, the surface hole density, $p_s(x,t)$, the electric field with the PC gap, $E(x,t)$, the surface electron current within the PC gap, $k_n(x,t)$, and the far-field THz radiation pattern, $E_{THz}(z,t)$. To start, equations 3.3.1.1, 3.3.1.12, and 3.3.1.13 are substituted into equation 3.3.1.2, and a finite differencing scheme is applied to solve for $n_s(x,t)$. A forward differencing scheme is applied for the time derivatives at the current spatial step (j), using a second-order predictor-corrector method, and a second-order central derivative is applied for the spatial derivatives at the current time step (i). Using this method, the surface electron density for the predictor becomes

$$n_{ij} = n_{i-1j} + \Delta t\left[\frac{(1-R)I_{i-1j}}{h\nu} - \frac{\mu_n E_{i-1j}}{g_{i-1j}^2}\frac{(n_{i-1j+1} - n_{i-1j-1})}{2\Delta x} + \frac{e\mu_n n_{i-1j}(p_{i-1j} - n_{i-1j})}{l\varepsilon_r\varepsilon_o g_{i-1j}}\right], \tag{H.1}$$

where

$$g_{i-1j} = \left[1 + \left(1 + \sqrt{\varepsilon_r}\right)^{-1}\mu_n e\mu_o c n_{i-1j}\right]. \tag{H.2}$$

This predictor value for n_{ij} is then used to find the electric field. Equation 3.3.1.13 becomes

$$E_{ij} = E_{ij-2} + \frac{e\Delta x}{3l\varepsilon_r\varepsilon_o}\left[\left(p_{ij-2} - n_{ij-2}\right) + 4\left(p_{ij-1} - n_{ij-1}\right) + \left(p_{ij} - n_{ij}\right)\right]. \tag{H.3}$$

The field across the gap is then renormalized to give a constant voltage across it, and $n_s(x,t)$ is found for the corrector step to be

$$\begin{aligned} n_{ij} &= n_{i-1j} \\ &+ \frac{\Delta t}{2}\left[\frac{(1-R)I_{i-1j}}{h\nu} - \frac{\mu_n E_{i-1j}}{g_{i-1j}^2}\frac{\left(n_{i-1j+1} - n_{i-1j-1}\right)}{2\Delta x} + \frac{e\mu_n n_{i-1j}\left(p_{i-1j} - n_{i-1j}\right)}{l\varepsilon_r\varepsilon_o g_{i-1j}}\right] \\ &+ \frac{\Delta t}{2}\left[\frac{(1-R)I_{ij}}{h\nu} - \frac{\mu_n E_{ij}}{g_{ij}^2}\frac{\left(n_{ij+1} - n_{ij-1}\right)}{2\Delta x} + \frac{e\mu_n n_{ij}\left(p_{ij} - n_{ij}\right)}{l\varepsilon_r\varepsilon_o g_{ij}}\right]. \end{aligned} \tag{H.4}$$

$E(x,t)$ is then found for the corrector step to be

$$E_{ij} = E_{ij-2} + \frac{e\Delta x}{3l\varepsilon_r\varepsilon_o}\left[\left(p_{ij-2} - n_{ij-2}\right) + 4\left(p_{ij-1} - n_{ij-1}\right) + \left(p_{ij} - n_{ij}\right)\right]. \tag{H.5}$$

The field is renormalized again to give a constant voltage across it, and the electron surface current density is determined using equation 3.3.1.12. Finally, the far-field THz electric field, $E_{THz}(z,t)$, is determined by numerically integrating equation 3.3.1.14.

The program used to carry out the above analysis is written in Visual C++. The program code is as follows:

```
///////////////////////////////////////////////////////////////////////////////////////////////////
// Model of the far-field radiation from a biased PC gap:                                      //
// Jonathan Holzman                                                                             //
// Ultrafast Photonics and Nano-Optics Laboratory                                               //
// Department of Electrical and Computer Engineering                                            //
// University of Alberta                                                                        //
// July 2, 2003                                                                                 //
//                                                                                              //
// Model7.cpp:                                                                                  //
// This program models the charge carrier dynamics and far-field radiation from a //
// biased GaAs PC gap. The model is for a large PC gap and, therefore, includes   //
// both space charge screening and near-field THz screening. The electric field is //
```

```
// integrated across the entire numerical evaluation range (0 to 2xo) to give Vinit,  //
// and the program holds the integral across the range at this value. This integral   //
// boundary condition essentially holds the current at the edges of the evaluation    //
// range at 0. The gap runs from (xo-Lx/2) to (xo+Lx/2), and the program runs          //
// from 0 to 2xo. The differencing routine uses a forward derivative in time at j,     //
// with a second-order predictor-corrector method, and a second-order central          //
// derivative in space at i.                                                           //
////////////////////////////////////////////////////////////////////////////////////////
// Include the header files and list the functions.                                    //
////////////////////////////////////////////////////////////////////////////////////////
#include <math.h>
#include <stdio.h>
double derf(double x);

////////////////////////////////////////////////////////////////////////////////////////
// Define the physical parameters for the setup.                                       //
////////////////////////////////////////////////////////////////////////////////////////
#define P 0.16                // incident average power in W
#define Eb 2E5                // external biasing field in V/m
#define z 0.25                // distance at which the far-field is measured in m
#define tFWHM 50E-15          // duration of optical pulse in sec
#define xFWHM 100E-6          // spot size FWHM in um
#define xo 500E-6             // centre of beam for numerical interval from 0 to 2xo in m
#define to 1E-12              // delay time for the optical pulse in sec
#define u 0.3                 // mobility in m^2/V/s
#define R 0.31947             // reflectivity of the semiconductor
#define l 0.74E-6             // optical penetration depth in m
#define ni 0.0                // intrinsic surface carrier concentration in m^-2
#define er 12.8               // dielectric constant of the substrate for THz
#define eo 8.85419E-12        // permittivity of free space
#define pi 3.14159265359      // pi
#define c 3E8                 // speed of light in vacuum in m/s
#define e 1.60219E-19         // electronic charge in C
#define h 6.62618E-34         // Planck's constant
#define nu 375E12             // optical frequency
#define no 376.69473          // impedance of free-space in Ohms
```

```
#define Ly 100E-6            // transverse dimension of the PC gap in m
#define Lx 100E-6            // length of the PC gap in m
#define dt 0.02E-15          // step size for time in sec
#define dx 0.05E-6           // step size for x in m
#define imax 100001          // number of steps in time
#define jmax 20001           // number of steps in space

////////////////////////////////////////////////////////////////////////////////////////////////////
// Main program                                                                                   //
////////////////////////////////////////////////////////////////////////////////////////////////////
int main(int argc, char* argv[])
{
 ///////////////////////////////////////////////////////////////////////////////////////////////////
 // Declare the variables.                                                                        //
 ///////////////////////////////////////////////////////////////////////////////////////////////////
 double t[imax],x[jmax],I0[jmax],I1[jmax],p0[jmax],p1[jmax],n0[jmax],n1[jmax];
 double E0[jmax],E1[jmax],j0[jmax],Er[imax],jintegral[imax],Vinit,V;
 int i,j;
 FILE* fp;
 ///////////////////////////////////////////////////////////////////////////////////////////////////
 // Create the arrays for space (x) and time (s).                                                 //
 ///////////////////////////////////////////////////////////////////////////////////////////////////
 x[0]=0.0;t[0]=0.0;
 for(j=1;j<jmax;j++)
 {
  x[j]=x[j-1]+dx;
 }
 for(i=1;i<imax;i++)
 {
  t[i]=t[i-1]+dt;
 }
 ///////////////////////////////////////////////////////////////////////////////////////////////////
 // Initial conditions at t=0 for the intensity (I), hole density (p), electron density          //
 // (n), E-field (E), and current (j).                                                            //
 ///////////////////////////////////////////////////////////////////////////////////////////////////
 for(j=0;j<jmax;j++)
```

```
{
 I1[j]=P*(1-R)/80E6/tFWHM*4.0/pi/xFWHM/xFWHM*
 exp(-4.0*log(2.0)*(0.0- to)*(0.0-to)/tFWHM/tFWHM)*
 exp(-4.0*log(2.0)*(x[j]-xo)*(x[j]-xo)/xFWHM/xFWHM);I0[j]=I1[j];
 p1[j]=sqrt(pi)/4.0/sqrt(log(2.0))*P*(1-R)/80E6*4.0/pi/xFWHM/xFWHM*
 (1+derf(2.0*sqrt(log(2.0))/tFWHM*(0.0-to)))/h/nu*exp(-4.0*log(2.0)*(x[j]-xo)*
 (x[j]-xo)/xFWHM/xFWHM);p0[j]=p1[j];
 n1[j]=p1[j];n0[j]=n1[j];
 E1[j]=Eb;E0[j]=E1[j];
 j0[j]=0.0;
 jintegral[0]=0.0;
}
/////////////////////////////////////////////////////////////////////////////////////////////////////////
// Calculate the initial voltage across the PC gap from (xo-Lx/2) to (xo+Lx/2)   //
// to renormalize later.                                                          //
/////////////////////////////////////////////////////////////////////////////////////////////////////////
for(j=2;j<(jmax-1);j=j+2)
{
 Vinit=Vinit+dx/3.0*(E0[j-2]+4.0*E0[j-1]+E0[j]);
}
/////////////////////////////////////////////////////////////////////////////////////////////////////////
// Solve for I, p, n, E, and j as a function of space and time. Variables ending   //
// in 0 are at the current time step (i), while variables ending in 1 are at the   //
// previous time step (i-1).                                                        //
/////////////////////////////////////////////////////////////////////////////////////////////////////////
for(i=1;i<imax;i++)
{
 ////////////////////////////////////////////////////////////////////////////////////////////////////////
 // Calculate p on the edges of the PC gap.                                        //
 ////////////////////////////////////////////////////////////////////////////////////////////////////////
 p0[0]=sqrt(pi)/4.0/sqrt(log(2.0))*P*(1-R)/80E6*4.0/pi/xFWHM/xFWHM*
 (1+derf(2.0*sqrt(log(2.0))/tFWHM*(t[i]-to)))/h/nu*
 exp(-4.0*log(2.0)*(0.0-xo)*(0.0-xo)/xFWHM/xFWHM);n0[0]=p0[0];
 p0[1]=sqrt(pi)/4.0/sqrt(log(2.0))*P*(1-R)/80E6*4.0/pi/xFWHM/xFWHM*
 (1+derf(2.0*sqrt(log(2.0))/tFWHM*(t[i]-to)))/h/nu*
 exp(-4.0*log(2.0)*(dx-xo)*(dx-xo)/xFWHM/xFWHM);n0[1]=p0[1];
```

```
p0[jmax-1]=sqrt(pi)/4.0/sqrt(log(2.0))*P*(1-R)/80E6*4.0/pi/xFWHM/xFWHM*
(1+derf(2.0*sqrt(log(2.0))/tFWHM*(t[i]-to)))/h/nu*
exp(-4.0*log(2.0)*(xo)*(xo)/xFWHM/xFWHM);n0[jmax-1]=p0[jmax-1];
p1[0]=sqrt(pi)/4.0/sqrt(log(2.0))*P*(1-R)/80E6*4.0/pi/xFWHM/xFWHM*
(1+derf(2.0*sqrt(log(2.0))/tFWHM*(t[i-1]-to)))/h/nu*
exp(-4.0*log(2.0)*(0.0-xo)*(0.0-xo)/xFWHM/xFWHM);n1[0]=p1[0];
p1[1]=sqrt(pi)/4.0/sqrt(log(2.0))*P*(1-R)/80E6*4.0/pi/xFWHM/xFWHM*
(1+derf(2.0*sqrt(log(2.0))/tFWHM*(t[i-1]-to)))/h/nu*
exp(-4.0*log(2.0)*(dx-xo)*(dx-xo)/xFWHM/xFWHM);n1[1]=p1[1];
p1[jmax-1]=sqrt(pi)/4.0/sqrt(log(2.0))*P*(1-R)/80E6*4.0/pi/xFWHM/xFWHM*
(1+derf(2.0*sqrt(log(2.0))/tFWHM*(t[i-1]-to)))/h/nu*
exp(-4.0*log(2.0)*(xo)*(xo)/xFWHM/xFWHM);n1[jmax-1]=p1[jmax-1];
//////////////////////////////////////////////////////////////////////////////////////////
// Calculate n and E at the current time step as the predictor.                         //
//////////////////////////////////////////////////////////////////////////////////////////
for(j=2;j<(jmax-1);j++)
{
 I0[j]=P*(1-R)/80E6/tFWHM*4.0/pi/xFWHM/xFWHM*
 exp(-4.0*log(2.0)*(t[i]-to)*(t[i]-to)/tFWHM/tFWHM)*
 exp(-4.0*log(2.0)*(x[j]-xo)*(x[j]-xo)/xFWHM/xFWHM);
 p0[j]=sqrt(pi)/4.0/sqrt(log(2.0))*P*(1-R)/80E6*4.0/pi/xFWHM/xFWHM*
 (1+derf(2.0*sqrt(log(2.0))/tFWHM*(t[i]-to)))/h/nu*
 exp(-4.0*log(2.0)*(x[j]-xo)*(x[j]-xo)/xFWHM/xFWHM);
 n0[j]=n1[j]+dt*(I1[j]/h/nu+u*E1[j]/(1+e*u*no/(1+sqrt(er))*n1[j])/
 (1+e*u*no/(1+sqrt(er))*n1[j])*(n1[j+1]-n1[j-1])/2.0/dx+
 e*u*n1[j]*(p1[j]-n1[j])/l/er/eo/(1+e*u*no/(1+sqrt(er))*n1[j]));
 E0[j]=E0[j-2]+dx/3.0*e/l/er/eo*((p0[j-2]-n0[j-2])+4.0*
 (p0[j-1]-n0[j-1])+(p0[j]-n0[j]));
}
//////////////////////////////////////////////////////////////////////////////////////////
// Renormalize E to give a constant integral of Vinit across the numerical              //
// evaluation range.                                                                    //
//////////////////////////////////////////////////////////////////////////////////////////
V=0.0;
for(j=2;j<(jmax-1);j=j+2)
{
```

```
 V=V+dx/3.0*(E0[j-2]+4.0*E0[j-1]+E0[j]);
}
for(j=0;j<jmax;j++)
{
 E0[j]=E0[j]+(Vinit-V)/2.0/xo;
}
////////////////////////////////////////////////////////////////////////////////////////////////////
// Calculate n and E at the current time step as the corrector.                                   //
////////////////////////////////////////////////////////////////////////////////////////////////////
for(j=2;j<(jmax-1);j++)
{
 n0[j]=n1[j]+dt/2.0*((I1[j]/h/nu+u*E1[j]/(1+e*u*no/(1+sqrt(er))*n1[j])/
 (1+e*u*no/(1+sqrt(er))*n1[j])*(n1[j+1]-n1[j-1])/2.0/dx+
 e*u*n1[j]*(p1[j]-n1[j])/l/er/eo/(1+e*u*no/(1+sqrt(er))*n1[j]))
 +(I0[j]/h/nu+u*E0[j]/(1+e*u*no/(1+sqrt(er))*n0[j])/
 (1+e*u*no/(1+sqrt(er))*n0[j])*(n0[j+1]-n0[j-1])/2.0/dx+
 e*u*n0[j]*(p0[j]-n0[j])/l/er/eo/(1+e*u*no/(1+sqrt(er))*n0[j])));
 E0[j]=E0[j-2]+dx/3.0*e/l/er/eo*((p0[j-2]-n0[j-2])+
 4.0*(p0[j-1]-n0[j-1])+(p0[j]-n0[j]));
}
////////////////////////////////////////////////////////////////////////////////////////////////////
// Renormalize E to give a constant integral of Vinit across the numerical                        //
// evaluation range.                                                                              //
////////////////////////////////////////////////////////////////////////////////////////////////////
V=0.0;
for(j=2;j<(jmax-1);j=j+2)
{
 V=V+dx/3.0*(E0[j-2]+4.0*E0[j-1]+E0[j]);
}
for(j=0;j<jmax;j++)
{
 E0[j]=E0[j]+(Vinit-V)/2.0/xo;
}
////////////////////////////////////////////////////////////////////////////////////////////////////
// Calculate j at the current time step.                                                          //
////////////////////////////////////////////////////////////////////////////////////////////////////
```

```
  for(j=0;j<jmax;j++)
  {
   j0[j]=e*u*E0[j]*n0[j]/(1+e*u*no/(1+sqrt(er))*n0[j]);
  }
  ///////////////////////////////////////////////////////////////////////////////////////////////////////
  // Integrate j across the gap.                                                                        //
  ///////////////////////////////////////////////////////////////////////////////////////////////////////
  jintegral[i]=0.0;
  for(j=2;j<(jmax-1);j=j+2)
  {
   jintegral[i]=jintegral[i]+dx/3.0*(j0[j-2]+4.0*j0[j-1]+j0[j]);
  }
  ///////////////////////////////////////////////////////////////////////////////////////////////////////
  // Finally, shift the previous values (I1,p1,n1,E1) to the current values                             //
  // (I0,p0,n0,E0) and begin   the next loop in time.                                                   //
  ///////////////////////////////////////////////////////////////////////////////////////////////////////
  for(j=0;j<jmax;j++)
  {
   I1[j]=I0[j];
   p1[j]=p0[j];
   n1[j]=n0[j];
   E1[j]=E0[j];
  }
  printf("%1.6f\n",t[i]*1E12);
 }
 /////////////////////////////////////////////////////////////////////////////////////////////////////////
 // Find the radiated field in the far-field at z in V/m.                                                 //
 /////////////////////////////////////////////////////////////////////////////////////////////////////////
 Er[0]=0.0;Er[1]=0.0;
 for(i=2;i<imax;i++)
 {
  Er[i]=Ly/4.0/pi/eo/c/c/z*(3.0*jintegral[i]-4.0*jintegral[i-1]+jintegral[i-2])/2.0/dt;
 }
 /////////////////////////////////////////////////////////////////////////////////////////////////////////
 // Write the output to a file.                                                                           //
 /////////////////////////////////////////////////////////////////////////////////////////////////////////
```

```
 fp=fopen("output_500mW.txt","w");
 for(i=0;i<imax;i=i+10)
 {
  fprintf(fp,"%1.6f    %1.6f\n",t[i]*1E12,Er[i]);
 }
 fclose(fp);
 return 0;
}
//////////////////////////////////////////////////////////////////////////////////////////////////////////////
// Error function in double precision                                                        //
//////////////////////////////////////////////////////////////////////////////////////////////////////////////
double derf(double x)
{
  int k;
  double w, t, y;
  static double a[65] = {
    5.958930743e-11, -1.13739022964e-9,
    1.466005199839e-8, -1.635035446196e-7,
    1.6461004480962e-6, -1.492559551950604e-5,
    1.2055331122299265e-4, -8.548326981129666e-4,
    0.00522397762482322257, -0.0268661706450773342,
    0.11283791670954881569, -0.37612638903183748117,
    1.12837916709551257377,
    2.372510631e-11, -4.5493253732e-10,
    5.90362766598e-9, -6.642090827576e-8,
    6.7595634268133e-7, -6.21188515924e-6,
    5.103883009709969e-5, -3.7015410692956173e-4,
    0.00233307631218880978, -0.0125498847718219221,
    0.05657061146827041994, -0.2137966477645600658,
    0.84270079294971486929,
    9.49905026e-12, -1.8310229805e-10,
    2.39463074e-9, -2.721444369609e-8,
    2.8045522331686e-7, -2.61830022482897e-6,
    2.195455056768781e-5, -1.6358986921372656e-4,
    0.00107052153564110318, -0.00608284718113590151,
    0.02986978465246258244, -0.13055593046562267625,
```

```
    0.67493323603965504676,
    3.82722073e-12, -7.421598602e-11,
    9.793057408e-10, -1.126008898854e-8,
    1.1775134830784e-7, -1.1199275838265e-6,
    9.62023443095201e-6, -7.404402135070773e-5,
    5.0689993654144881e-4, -0.00307553051439272889,
    0.01668977892553165586, -0.08548534594781312114,
    0.56909076642393639985,
    1.55296588e-12, -3.032205868e-11,
    4.0424830707e-10, -4.71135111493e-9,
    5.011915876293e-8, -4.8722516178974e-7,
    4.30683284629395e-6, -3.445026145385764e-5,
    2.4879276133931664e-4, -0.00162940941748079288,
    0.00988786373932350462, -0.05962426839442303805,
    0.49766113250947636708
};
static double b[65] = {
    -2.9734388465e-10, 2.69776334046e-9,
    -6.40788827665e-9, -1.6678201321e-8,
    -2.1854388148686e-7, 2.66246030457984e-6,
    1.612722157047886e-5, -2.5616361025506629e-4,
    1.5380842432375365e-4, 0.00815533022524927908,
    -0.01402283663896319337, -0.19746892495383021487,
    0.71511720328842845913,
    -1.951073787e-11, -3.2302692214e-10,
    5.22461866919e-9, 3.42940918551e-9,
    -3.5772874310272e-7, 1.9999935792654e-7,
    2.687044575042908e-5, -1.1843240273775776e-4,
    -8.0991728956032271e-4, 0.00661062970502241174,
    0.00909530922354827295, -0.20160072778491013140,
    0.51169696718727644908,
    3.147682272e-11, -4.8465972408e-10,
    6.3675740242e-10, 3.377623323271e-8,
    -1.5451139637086e-7, -2.03340624738438e-6,
    1.947204525295057e-5, 2.854147231653228e-5,
    -0.00101565063152200272, 0.00271187003520095655,
```

```
    0.02328095035422810727, -0.16725021123116877197,
    0.32490054966649436974,
    2.31936337e-11, -6.303206648e-11,
    -2.64888267434e-9, 2.050708040581e-8,
    1.1371857327578e-7, -2.11211337219663e-6,
    3.68797328322935e-6, 9.823686253424796e-5,
    -6.5860243990455368e-4, -7.5285814895230877e-4,
    0.02585434424202960464, -0.11637092784486193258,
    0.18267336775296612024,
    -3.677789363e-12, 2.0876046746e-10,
    -1.933190272226e-9, -4.35953392472e-9,
    1.8006992266137e-7, -7.8441223763969e-7,
    -6.75407647949153e-6, 8.428418334440096e-5,
    -1.7604388937031815e-4, -0.00239729611435071610,
    0.02064129023876022970, -0.06905562880005864105,
    0.09084526782065478489
};

w = x < 0 ? -x : x;
if (w < 2.2) {
    t = w * w;
    k = (int) t;
    t -= k;
    k *= 13;
    y = ((((((((((((a[k] * t + a[k + 1]) * t +
        a[k + 2]) * t + a[k + 3]) * t + a[k + 4]) * t +
        a[k + 5]) * t + a[k + 6]) * t + a[k + 7]) * t +
        a[k + 8]) * t + a[k + 9]) * t + a[k + 10]) * t +
        a[k + 11]) * t + a[k + 12]) * w;
} else if (w < 6.9) {
    k = (int) w;
    t = w - k;
    k = 13 * (k - 2);
    y = ((((((((((((b[k] * t + b[k + 1]) * t +
        b[k + 2]) * t + b[k + 3]) * t + b[k + 4]) * t +
        b[k + 5]) * t + b[k + 6]) * t + b[k + 7]) * t +
```

```
            b[k + 8]) * t + b[k + 9]) * t + b[k + 10]) * t +
            b[k + 11]) * t + b[k + 12];
        y *= y;
        y *= y;
        y *= y;
        y = 1 - y * y;
    } else {
        y = 1;
    }
    return x < 0 ? -y : y;
}
```

Appendix J

NUMERICAL ANALYSIS OF THE ZnSe DIPOLE TERAHERTZ EMITTER

To solve for the far-field THz radiation pattern produced by the ZnSe PC THz emitter, equations 3.4.1.1-3.4.1.9 are solved simultaneously for the surface electron density, $n_s(x,t)$, the surface hole density, $p_s(x,t)$, the electric field with the PC gap, $E_{eff}(x,t)$, the surface electron current within the PC gap, $k_n(x,t)$, and the far-field THz radiation pattern, $E_{THz}(z,t)$. To start, equations 3.4.1.1, 3.4.1.5, and 3.4.1.6 are substituted into 3.4.1.2, and a finite differencing scheme is applied to solve for $n_s(x,t)$. A forward differencing scheme is applied for the time-derivatives at the current spatial step (j), using a second-order predictor-corrector method, and a second-order central derivative is applied for the spatial derivatives at the current time step (i). Using this method, the surface electron density for the predictor becomes

$$\begin{aligned} n_{ij} &= n_{i-1j} \\ &+ \Delta t\left[\frac{(1-R)I_{i-1j}}{2h\nu} - \frac{\mu_n E_{i-1j}\left(n_{i-1j+1} - n_{i-1j-1}\right)}{2\Delta x} + \frac{e\mu_n n_{i-1j}\beta I_p\left(p_{i-1j} - n_{i-1j}\right)}{\varepsilon_r \varepsilon_o}\right]. \end{aligned} \tag{I.1}$$

This predictor value for n_{ij} is then used to find the electric field,

$$E_{ij} = E_{ij-2} + \frac{e\Delta x \beta I_p}{3\varepsilon_r\varepsilon_o}\left[\left(p_{ij-2} - n_{ij-2}\right) + 4\left(p_{ij-1} - n_{ij-1}\right) + \left(p_{ij} - n_{ij}\right)\right]. \tag{I.2}$$

The field is then renormalized across the gap to give a constant voltage. Next, $n_s(x,t)$ is calculated for the corrector step through the relation

$$\begin{aligned} n_{ij} &= n_{i-1j} \\ &+\frac{\Delta t}{2}\left[\frac{(1-R)I_{i-1j}}{2h\nu}-\mu_n E_{i-1j}\frac{\left(n_{i-1j+1}-n_{i-1j-1}\right)}{2\Delta x}+\frac{e\mu_n n_{i-1j}\beta I_p\left(p_{i-1j}-n_{i-1j}\right)}{\varepsilon_r\varepsilon_o}\right], \\ &+\frac{\Delta t}{2}\left[\frac{(1-R)I_{ij}}{2h\nu}-\mu_n E_{ij}\frac{\left(n_{ij+1}-n_{ij-1}\right)}{2\Delta x}+\frac{e\mu_n n_{ij}\beta I_p\left(p_{ij}-n_{ij}\right)}{\varepsilon_r\varepsilon_o}\right]. \end{aligned} \tag{I.3}$$

and $E_{eff}(x,t)$ is calculated for the corrector step though the relation

$$E_{ij} = E_{ij-2} + \frac{e\Delta x\beta I_p}{3\varepsilon_r\varepsilon_o}\left[\left(p_{ij-2}-n_{ij-2}\right)+4\left(p_{ij-1}-n_{ij-1}\right)+\left(p_{ij}-n_{ij}\right)\right]. \tag{I.4}$$

The field is renormalized again to give a constant voltage across it. Finally, the electric field at the anode ($x = 0$) is recorded, and it's second derivative is computed numerically in Microsoft Excel. The second derivative is proportional to the far-field THz electric field, $E_{THz}(z,t)$. The program used to carry out the above analysis is written in Visual C++. The program code is as follows:

```
///////////////////////////////////////////////////////////////////////////////////////////////////
// Model of the far-field radiation from a small ZnSe PC THz emitter:            //
// Jonathan Holzman                                                              //
// Ultrafast Photonics and Nano-Optics Laboratory                                //
// Department of Electrical and Computer Engineering                             //
// University of Alberta                                                         //
// June 27, 2003                                                                 //
//                                                                               //
// Model5.cpp:                                                                   //
// This program models the charge carrier dynamics and far-field radiation from a //
// biased ZnSe PC gap. The model is for a small radiative dipole and, therefore, //
// includes only space charge screening. The electric field is integrated across the //
// PC gap (from (jmax*dx/2-Lx/2) to (jmax*dx/2+Lx/2) and held at a voltage of   //
// Vb; the field is initially constant across the gap. An effective bias voltage is //
// used for the field, and it is averaged over one penetration depth. The program //
// runs over the interval from 0 to jmax*dx, and the beam (of width xFWHM) is    //
```

```
// centred at xo. The electric field at the anode is recorded, and it's time derivative //
// is calculated (as it is proportional to the displacement current. The derivative of //
// the displacement current is used next to calculate the far-field radiation. The     //
// differencing routine uses a forward derivative in time at j with a second-order     //
// predictor-corrector method, and a second-order central derivative in space at i.    //
////////////////////////////////////////////////////////////////////////////////////////

////////////////////////////////////////////////////////////////////////////////////////
// Include the header files and list the functions.                                   //
////////////////////////////////////////////////////////////////////////////////////////
#include <math.h>
#include <stdio.h>
double derf(double x);

////////////////////////////////////////////////////////////////////////////////////////
// Define the physical parameters for the setup.                                      //
////////////////////////////////////////////////////////////////////////////////////////
#define P 0.16                  // average pump power in W
#define z 0.25                  // distance at which the far-field is measured in m
#define tFWHM 50E-15            // duration of optical pulse in sec
#define xFWHM 3E-6              // spot size FWHM in um
#define to 200E-15              // delay time for the optical pulse in sec
#define xo 5E-6                 // dist. from electrode at x = 0 (anode) to beam centre in m
#define u 0.06                  // mobility in m^2/V/s
#define R 0.300                 // reflectivity of the semiconductor
#define beta 3.5E-11            // ZnSe two-photon absorption coefficient in m/W
#define ni 0.0                  // intrinsic surface carrier concentration in m^-2
#define er 9.2                  // dielectric constant of the substrate for THz
#define eo 8.85419E-12          // permittivity of free space
#define pi 3.14159265359        // pi
#define c 3E8                   // speed of light in vacuum in m/s
#define e 1.60219E-19           // electronic charge in C
#define h 6.62618E-34           // Planck's constant
#define nu 375E12               // optical frequency
#define no 376.69473            // impedance of free-space in Ohms
#define Ly 7E-6                 // transverse dimension of the PC gap in m
```

```
#define Lx 9E-6              // length of the PC gap in m
#define dt 0.5E-18           // step size for time in sec
#define dx 1E-9              // step size for x in m
#define imax 600001          // number of steps in time
#define jmax 15001           // number of steps in space

//////////////////////////////////////////////////////////////////////////////////////////////////
// Main program                                                                                //
//////////////////////////////////////////////////////////////////////////////////////////////////
int main(int argc, char* argv[])
{
 ////////////////////////////////////////////////////////////////////////////////////////////////
 // Declare the variables.                                                                    //
 ////////////////////////////////////////////////////////////////////////////////////////////////
 double t[imax],x[jmax],I0[jmax],I1[jmax],p0[jmax],p1[jmax],n0[jmax],n1[jmax];
 double E0[jmax],E1[jmax],j0[jmax],Vinit,V,Ip,Vb;
 double Eanode[imax],Ecathode[imax];
 int i,j,loop;
 FILE* fp;
 char filename[256];
 ////////////////////////////////////////////////////////////////////////////////////////////////
 // Create the arrays for space (x) and time (s).                                             //
 ////////////////////////////////////////////////////////////////////////////////////////////////
 x[0]=0.0;t[0]=0.0;
 for(j=1;j<jmax;j++)
 {
  x[j]=x[j-1]+dx;
 }
 for(i=1;i<imax;i++)
 {
  t[i]=t[i-1]+dt;
 }
 ////////////////////////////////////////////////////////////////////////////////////////////////
 // Create the loop for solving each bias voltage                                             //
 ////////////////////////////////////////////////////////////////////////////////////////////////
 Vb=115.0;
```

```
for(loop=1;loop<=12;loop++)
{
 ////////////////////////////////////////////////////////////////////////////////////////////////////////////////////
 // Initial conditions at t=0 for the intensity (I), hole density (p), electron density //
 // (n), E-field (E), and current (j).                                                   //
 ////////////////////////////////////////////////////////////////////////////////////////////////////////////////////
 Ip=P*(1-R)/80E6/tFWHM*4.0/pi/xFWHM/xFWHM;
 jintegral[0]=0.0;Eanode[0]=Vb/Lx;Ecathode[0]=Vb/Lx;
 for(j=0;j<jmax;j++)
 {
  I1[j]=P*(1-R)/80E6/tFWHM*4.0/pi/xFWHM/xFWHM*
  exp(-4.0*log(2.0)*(0.0-to)*(0.0-to)/tFWHM/tFWHM)*
  exp(-4.0*log(2.0)*(x[j]-xo)*(x[j]-xo)/xFWHM/xFWHM);I0[j]=I1[j];
  p1[j]=sqrt(pi)/4.0/sqrt(log(2.0))*P*(1-R)/80E6*4.0/pi/xFWHM/xFWHM*
  (1+derf(2.0*sqrt(log(2.0))/tFWHM*(0.0-to)))/2.0/h/nu*
  exp(-4.0*log(2.0)*(x[j]-xo)*(x[j]-xo)/xFWHM/xFWHM);p0[j]=p1[j];
  n1[j]=p1[j];n0[j]=n1[j];
  E1[j]=Vb/pi*beta*Ip*log(sqrt(1.0+(2.0/beta/Ip/Lx)*(2.0/beta/Ip/Lx))+
  (2.0/beta/Ip/Lx));E0[j]=E1[j];
  j0[j]=0.0;
 }
 ////////////////////////////////////////////////////////////////////////////////////////////////////////////////////
 // Calculate the initial effective bias voltage across the PC gap for                  //
 // renormalization later.                                                               //
 ////////////////////////////////////////////////////////////////////////////////////////////////////////////////////
 Vinit=0.0;
 for(j=int(jmax/2.0-Lx/2.0/dx);j<int(jmax/2.0+Lx/2.0/dx);j=j+2)
 {
  Vinit=Vinit+dx/3.0*(E0[j-2]+4.0*E0[j-1]+E0[j]);
 }
 ////////////////////////////////////////////////////////////////////////////////////////////////////////////////////
 // Solve for I, p, n, E, and j as a function of space and time. Variables ending       //
 // in 0 are at the current time step (i), while variables ending in 1 are at the       //
 // previous time step (i-1).                                                            //
 ////////////////////////////////////////////////////////////////////////////////////////////////////////////////////
 for(i=1;i<imax;i++)
```

```
{
//////////////////////////////////////////////////////////////////////////////////////////////////////////
// Calculate p on the edges of the PC gap.                                                              //
//////////////////////////////////////////////////////////////////////////////////////////////////////////
p0[0]=sqrt(pi)/4.0/sqrt(log(2.0))*P*(1-R)/80E6*4.0/pi/xFWHM/xFWHM*
(1+derf(2.0*sqrt(log(2.0))/tFWHM*(t[i]-to)))/2.0/h/nu*
exp(-4.0*log(2.0)*(0.0-xo)*(0.0-xo)/xFWHM/xFWHM);n0[0]=p0[0];
p0[1]=sqrt(pi)/4.0/sqrt(log(2.0))*P*(1-R)/80E6*4.0/pi/xFWHM/xFWHM*
(1+derf(2.0*sqrt(log(2.0))/tFWHM*(t[i]-to)))/2.0/h/nu*
exp(-4.0*log(2.0)*(dx-xo)*(dx-xo)/xFWHM/xFWHM);n0[1]=p0[1];
p0[jmax-1]=sqrt(pi)/4.0/sqrt(log(2.0))*P*(1-R)/80E6*4.0/pi/xFWHM/xFWHM*
(1+derf(2.0*sqrt(log(2.0))/tFWHM*(t[i]-to)))/2.0/h/nu*
exp(-4.0*log(2.0)*(Lx-xo)*(Lx-xo)/xFWHM/xFWHM);n0[jmax-1]=p0[jmax-1];
p1[0]=sqrt(pi)/4.0/sqrt(log(2.0))*P*(1-R)/80E6*4.0/pi/xFWHM/xFWHM*
(1+derf(2.0*sqrt(log(2.0))/tFWHM*(t[i-1]-to)))/2.0/h/nu*
exp(-4.0*log(2.0)*(0.0-xo)*(0.0-xo)/xFWHM/xFWHM);n1[0]=p1[0];
p1[1]=sqrt(pi)/4.0/sqrt(log(2.0))*P*(1-R)/80E6*4.0/pi/xFWHM/xFWHM*
(1+derf(2.0*sqrt(log(2.0))/tFWHM*(t[i-1]-to)))/2.0/h/nu*
exp(-4.0*log(2.0)*(dx-xo)*(dx-xo)/xFWHM/xFWHM);n1[1]=p1[1];
p1[jmax-1]=sqrt(pi)/4.0/sqrt(log(2.0))*P*(1-R)/80E6*4.0/pi/xFWHM/xFWHM*
(1+derf(2.0*sqrt(log(2.0))/tFWHM*(t[i-1]-to)))/2.0/h/nu*
exp(-4.0*log(2.0)*(Lx-xo)*(Lx-xo)/xFWHM/xFWHM);n1[jmax-1]=p1[jmax-1];
//////////////////////////////////////////////////////////////////////////////////////////////////////////
// Calculate n and E at the current time step as the predictor.                                        //
//////////////////////////////////////////////////////////////////////////////////////////////////////////
for(j=2;j<(jmax-1);j++)
{
 I0[j]=P*(1-R)/80E6/tFWHM*4.0/pi/xFWHM/xFWHM*
 exp(-4.0*log(2.0)*(t[i]-to)*(t[i]-to)/tFWHM/tFWHM)*
 exp(-4.0*log(2.0)*(x[j]-xo)*(x[j]-xo)/xFWHM/xFWHM);
 p0[j]=sqrt(pi)/4.0/sqrt(log(2.0))*P*(1-R)/80E6*4.0/pi/xFWHM/xFWHM*
 (1+derf(2.0*sqrt(log(2.0))/tFWHM*(t[i]-to)))/2.0/h/nu*
 exp(-4.0*log(2.0)*(x[j]-xo)*(x[j]-xo)/xFWHM/xFWHM);
 n0[j]=n1[j]+dt*(I1[j]/2.0/h/nu+u*E1[j]*(n1[j+1]-n1[j-1])/2.0/dx+
 e*u*n1[j]*(p1[j]-n1[j])*beta*Ip/er/eo);
 E0[j]=E0[j-2]+dx/3.0*e*beta*Ip/er/eo*((p0[j-2]-n0[j-2])+
```

```
 4.0*(p0[j-1]-n0[j-1])+(p0[j]-n0[j]));
}
//////////////////////////////////////////////////////////////////////////////////////////////////////////
// Renormalize E to give a constant integral of Vinit across the PC gap.          //
//////////////////////////////////////////////////////////////////////////////////////////////////////////
V=0.0;
for(j=int(jmax/2.0-Lx/2.0/dx);j<int(jmax/2.0+Lx/2.0/dx);j=j+2)
{
 V=V+dx/3.0*(E0[j-2]+4.0*E0[j-1]+E0[j]);
}
for(j=0;j<jmax;j++)
{
 E0[j]=E0[j]+(Vinit-V)/Lx;
}
//////////////////////////////////////////////////////////////////////////////////////////////////////////
// Calculate n and E at the current time step as the corrector.                    //
//////////////////////////////////////////////////////////////////////////////////////////////////////////
for(j=2;j<(jmax-1);j++)
{
 n0[j]=n1[j]+dt/2.0*((I1[j]/2.0/h/nu+u*E1[j]*(n1[j+1]-n1[j-1])/2.0/dx+
 e*u*n1[j]*(p1[j]-n1[j])*beta*Ip/er/eo)+(I0[j]/2.0/h/nu+u*E0[j]*
 (n0[j+1]-n0[j-1])/2.0/dx+e*u*n0[j]*(p0[j]-n0[j])*beta*Ip/er/eo));
 E0[j]=E0[j-2]+dx/3.0*e*beta*Ip/er/eo*
 ((p0[j-2]-n0[j-2])+4.0*(p0[j-1]-n0[j-1])+(p0[j]-n0[j]));
}
//////////////////////////////////////////////////////////////////////////////////////////////////////////
// Renormalize E to give a constant integral of Vinit across the PC gap.          //
//////////////////////////////////////////////////////////////////////////////////////////////////////////
V=0.0;
for(j=int(jmax/2.0-Lx/2.0/dx);j<int(jmax/2.0+Lx/2.0/dx);j=j+2)
{
 V=V+dx/3.0*(E0[j-2]+4.0*E0[j-1]+E0[j]);
}
for(j=0;j<jmax;j++)
{
 E0[j]=E0[j]+(Vinit-V)/Lx;
```

```
 }
 ////////////////////////////////////////////////////////////////////////////////////////////////////////////
 // Calculate j at the current time step.                                                        //
 ////////////////////////////////////////////////////////////////////////////////////////////////////////////
 for(j=0;j<jmax;j++)
 {
  j0[j]=e*u*n0[j]*E0[j];
 }
 ////////////////////////////////////////////////////////////////////////////////////////////////////////////
 // Find the E-field at the anode.                                                                   //
 ////////////////////////////////////////////////////////////////////////////////////////////////////////////
 Eanode[i]=E0[int(jmax/2.0-Lx/2.0/dx)];
 Ecathode[i]=E0[int(jmax/2.0+Lx/2.0/dx)];
 ////////////////////////////////////////////////////////////////////////////////////////////////////////////
 // Finally, shift the previous values (I1,p1,n1,E1) to the current values          //
 // (I0,p0,n0,E0) and begin the next loop in time.                                       //
 ////////////////////////////////////////////////////////////////////////////////////////////////////////////
 for(j=0;j<jmax;j++)
 {
  I1[j]=I0[j];
  p1[j]=p0[j];
  n1[j]=n0[j];
  E1[j]=E0[j];
 }
 printf("Simulation: ZnSe Emitter for %d mW and %d V: %1.6f
 percent \n",(int)(P*1000),(int)(Vb),t[i]/(imax*dt)*100);
}
////////////////////////////////////////////////////////////////////////////////////////////////////////////
// Write the output to a file.                                                                          //
////////////////////////////////////////////////////////////////////////////////////////////////////////////
sprintf(filename,"ZnSe_Eanode_Ecathode_%dmW_%dV.txt",(int)(P*1000),(int)(Vb));
fp=fopen(filename,"w");
for(i=0;i<imax;i=i+100)
{
 fprintf(fp,"%1.6f  %1.15f%1.15 \n",t[i]*1E15,Eanode[i],Ecathode[i]);
}
```

```
  fclose(fp);
  sprintf(filename,"ZnSe_E_n_%dmW_%dV.txt",(int)(P*1000),(int)(Vb));
  fp=fopen(filename,"w");
  for(j=0;j<jmax;j=j+10)
  {
   fprintf(fp,"%1.6f  %1.15f%1.15f \n",x[j]*1E6,E0[j],n0[j]);
  }
  fclose(fp);
  Vb=Vb-20.0;
  }
 return 0;
}
//////////////////////////////////////////////////////////////////////////////////////////////////////////////
// Error function in double precision                                                                      //
//////////////////////////////////////////////////////////////////////////////////////////////////////////////
double derf(double x)
{
 int k;
 double w, t, y;
 static double a[65] = {
  5.958930743e-11, -1.13739022964e-9,
  1.466005199839e-8, -1.635035446196e-7,
  1.6461004480962e-6, -1.492559551950604e-5,
  1.2055331122299265e-4, -8.548326981129666e-4,
  0.00522397762482322257, -0.0268661706450773342,
  0.11283791670954881569, -0.37612638903183748117,
  1.12837916709551257377,
  2.372510631e-11, -4.5493253732e-10,
  5.90362766598e-9, -6.642090827576e-8,
  6.7595634268133e-7, -6.21188515924e-6,
  5.10388300970969e-5, -3.7015410692956173e-4,
  0.00233307631218880978, -0.0125498847718219221,
  0.05657061146827041994, -0.2137966477645600658,
  0.84270079294971486929,
  9.49905026e-12, -1.8310229805e-10,
  2.39463074e-9, -2.721444369609e-8,
```

```
  2.8045522331686e-7, -2.61830022482897e-6,
  2.19545505676878le-5, -1.6358986921372656e-4,
  0.0010705215356411031 8, -0.0060828471811359015 1,
  0.0298697846524625824 4, -0.1305559304656226762 5,
  0.6749332360396550467 6,
  3.82722073e-12, -7.421598602e-11,
  9.793057408e-10, -1.126008898854e-8,
  1.17751348307 84e-7, -1.1199275838265e-6,
  9.62023443095201e-6, -7.404402135070773e-5,
  5.068999365414488 1e-4, -0.00307553051439272889,
  0.01668977892553165586, -0.08548534594781312114,
  0.56909076642393639985,
  1.55296588e-12, -3.032205868e-11,
  4.0424830707e-10, -4.71135111493e-9,
  5.011915876293e-8, -4.8722516178974e-7,
  4.30683284629395e-6, -3.445026145385764e-5,
  2.4879276133931664e-4, -0.00162940941748079288,
  0.00988786373932350462, -0.05962426839442303805,
  0.49766113250947636708
};
static double b[65] = {
  -2.97343 88465e-10, 2.69776334046e-9,
  -6.40788827665e-9, -1.6678201321e-8,
  -2.18543881486 86e-7, 2.66246030457984e-6,
  1.612722157047886e-5, -2.5616361025506629e-4,
  1.5380842432375365e-4, 0.00815533022524927908,
  -0.01402283663896319337, -0.19746892495383021487,
  0.71511720328842845913,
  -1.951073787e-11, -3.2302692214e-10,
  5.22461866919e-9, 3.42940918551e-9,
  -3.5772874310272e-7, 1.9999935792654e-7,
  2.687044575042908e-5, -1.1843240273775776e-4,
  -8.0991728956032271e-4, 0.00661062970502241174,
  0.00909530922354827295, -0.20160072778491013 14,
  0.51169696718727644908,
  3.147682272e-11, -4.8465972408e-10,
```

```
  6.3675740242e-10, 3.377623323271e-8,
  -1.5451139637086e-7, -2.033406247384 38e-6,
  1.947204525295057e-5, 2.854147231653228e-5,
  -0.001015650631522 00272, 0.0027118700352009 5655,
  0.0232809503542281 0727, -0.1672502112311 6877197,
  0.3249005496664943 6974,
  2.31936337e-11, -6.303206648e-11,
  -2.64888267434e-9, 2.050708040581e-8,
  1.1371857327578e-7, -2.11211337219663e-6,
  3.68797328322935e-6, 9.823686253424796e-5,
  -6.5860243990455368e-4, -7.5285814895230877e-4,
  0.0258543442420296 0464, -0.1163709278448619 3258,
  0.1826733677529661 2024,
  -3.67789363e-12, 2.0876046746e-10,
  -1.93319027226e-9, -4.35953392472e-9,
  1.8006992266137e-7, -7.8441223763969e-7,
  -6.75407647949153e-6, 8.428418334440096e-5,
  -1.7604388937031815e-4, -0.0023972961143507161,
  0.0206412902387602297, -0.0690556288000586 4105,
  0.090845267820654 78489
};
w = x < 0 ? -x : x;
if (w < 2.2) {
  t = w * w;
  k = (int) t;
  t -= k;
  k *= 13;
  y = ((((((((((((a[k] * t + a[k + 1]) * t +
    a[k + 2]) * t + a[k + 3]) * t + a[k + 4]) * t +
    a[k + 5]) * t + a[k + 6]) * t + a[k + 7]) * t +
    a[k + 8]) * t + a[k + 9]) * t + a[k + 10]) * t +
    a[k + 11]) * t + a[k + 12]) * w;
  } else if (w < 6.9) {
    k = (int) w;
    t = w - k;
    k = 13 * (k - 2);
```

```
    y = ((((((((((b[k] * t + b[k + 1]) * t +
      b[k + 2]) * t + b[k + 3]) * t + b[k + 4]) * t +
      b[k + 5]) * t + b[k + 6]) * t + b[k + 7]) * t +
      b[k + 8]) * t + b[k + 9]) * t + b[k + 10]) * t +
      b[k + 11]) * t + b[k + 12];
    y *= y;
    y *= y;
    y *= y;
    y = 1 - y * y;
  } else {
    y = 1;
  }
 return x < 0 ? -y : y;
}
```

Appendix K

DEVICE MICROFABRICATION PROCESSES

The micron-scaled devices described within this thesis were patterned using metal sputtering and ultraviolet photolithography. The processes I employed are described below.

Metallization Process:

Metal: Ti
Sputter System: Kurt J. Lesker Magnetron Sputter System
Process Gas: Argon
Process Gas Pressure: 7 mtorr
Base Pressure: 10^{-8} torr (typical)
Ar Mass Flow Rate: 9.6 sccm
Sputter Gun Power: 300 W
Sputter Gun Position: Low
Deposition Time: 40 minutes, 5 minute burn-in (approximately 50 nm thickness)

Metal: Au
Sputter System: Kurt J. Lesker Magnetron Sputter System
Process Gas: Argon
Process Gas Pressure: 7 mtorr
Base Pressure: 10^{-8} torr (typical)
Ar Mass Flow Rate: 9.6 sccm
Sputter Gun Power: 75 W
Sputter Gun Position: High
Deposition Time: 20 minutes, 1 minute burn-in (approximately 150 nm thickness)
40 minutes, 1 minute burn-in (approximately 300 nm thickness)

Photolithographic Process:

Metal:	50/150 nm Ti/Au
Photoresist:	HPR504
Spinning:	Spread at 500 rpm for 10 seconds (Solitec Spinner) Spin at 4000 rpm for 40 seconds (Solitec Spinner)
Soft Bake:	Bake at 110^0C for 30 minutes
Expose:	4.0 seconds (ABM Mask Aligner)
Develop:	Developer 354 for approximately 10 seconds (resist dissolves)
Hard Bake:	Bake at 120^0C for 30 minutes
Etch:	Dip in Au etch for approximately 30 seconds (Au) Dip in 5% HF solution for approximately 2 seconds (Ti)

Curriculum Vitae

Jonathan F. Holzman

Ultrafast Photonics and Nano-Optics Laboratory
Department of Electrical and Computer Engineering
University of Alberta, ECERF W310
Edmonton, AB, Canada
T6G 2V4
Phone: (780) 492-0756
Fax: (780) 492-1811
E-mail: holzman@ee.ualberta.ca

Academics:

B.Sc. in Engineering Physics, University of Alberta, 1998.
Ph.D. in Electrical Engineering, University of Alberta, current.

Research Interests:

Metal/semiconductor guided-wave structures for optical-optical modulation
Ultrafast semiconductor plasma dynamics
Ultrashort electrical pulse generation and photoconductive switching processes
Free-space THz generation and detection

Academic Achievements and Awards:

Izaak Walton Killam Memorial Scholarship, 2000-2001
Julie Payette-NSERC Scholarship, PGS B, 2000-2003
Ralph Steinhauer Award of Distinction, 2000-2001 and 2001-2002
Natural Sciences and Engineering Research Council Scholarship, PGS A, 1999-2001
Walter H. Johns Graduate Fellowship, 1999-2002
Governor General's Silver Medal for excellence at the University of Alberta, 1999
Henry Birks and Sons Silver Medal for excellence in engineering, 1999
APEGGA medal for excellence in Engineering Physics, 1999
Canadian Gas Processors Silver Anniversary Scholarship, 1997-98

Schlumberger Scholarship, 1994-98
Louise Mckinney Scholarship, 1994-98
Hewlett-Packard Computer Award, 1994
TransAlta Utilities Memorial Scholarship, 1994
Canada Scholarship, 1993-95
Governor General's Bronze Medal, 1993
H. S. Perkins Scholarship, 1993
University of Alberta Academic Excellence Scholarship, 1993

Selected Journal Publications:

J. F. Holzman and A. Y. Elezzabi, "Two-photon photoconductive terahertz generation in ZnSe," *Applied Physics Letters,* to be published, 2003.

J. F. Holzman and A. Y. Elezzabi, "Dispersion-free high-speed beam chopper for ultrafast pulsed laser applications," *Measurement Science and Technology* **14**, pp. N41-N44, 2003.

A. Y. Elezzabi and J. F. Holzman, "Photoconductive generation and detection of guided-wave and free-space terahertz waveforms," *IEICE Transactions on Electronics* **E86C**, pp. 1218-1225, 2003. **(Invited)**

J. F. Holzman, F. E. Vermeulen, S. E. Irvine, and A. Y. Elezzabi, "Free-space detection of terahertz radiation using crystalline and polycrystalline ZnSe electro-optic sensors," *Applied Physics Letters* **81**, pp. 2294-2296, 2002.

M. D. Cummings, J. F. Holzman, and A. Y. Elezzabi, "Ultrafast high-field transport in a GaAs photoconductive switch," *Journal of Vacuum Science and Technology* **20**, pp. 1057-1060, 2002.

J. F. Holzman, F. E. Vermeulen, and A. Y. Elezzabi, "Generation of 1.2 ps electrical pulses through parallel-gating in ultra-thin silicon photoconductive switches," *Applied Physics Letters* **79**, pp. 4249-4251, 2001.

M. D. Cummings, J. F. Holzman, and A. Y. Elezzabi, "Femtosecond carrier dynamics in an asymmetrically excited GaAs photoconductive switch," *Applied Physics Letters* **78**, pp. 3535-3537, 2001.

J. F. Holzman, F. E. Vermeulen, B. W. Arnold, and A. Y. Elezzabi, "Photoconductive gating of picosecond electrical pulses on thinned-silicon substrates," *Electronics Letters* **36**, pp. 1225-1226, 2000.

J. F. Holzman, F. E. Vermeulen, and A. Y. Elezzabi, "Frozen wave generation of bandwidth tunable two-cycle THz radiation," *Journal of the Optical Society of America B* **17**, pp. 1457-1463, 2000.

J. F. Holzman, A. Y. Elezzabi, and F. E. Vermeulen, "Ultrafast photoconductive self-switching of subpicosecond electrical pulses," *IEEE Journal of Quantum Electronics* **36**, pp. 130-136, 2000.

J. F. Holzman, F. E. Vermeulen, and A. Y. Elezzabi, "Recombination-independent photogeneration of ultrashort electrical pulses," *Applied Physics Letters* **76**, pp. 134-136, 2000.

J. F. Holzman, F. E. Vermeulen, and A. Y. Elezzabi, "Ultrafast all-optical modulation of infrared radiation via metal-semiconductor waveguide structures," *IEEE Journal of Quantum Electronics* **35**, pp. 583-589, 1999.

A. Y. Elezzabi, J. C. Sit, J. F. Holzman, K. Robbie, and M. Brett, "Thin film vertical diffraction gratings fabricated using glancing angle deposition," *Electronics Letters* **35**, pp. 491-493, 1999.

Refereed Conference Proceedings:

J. F. Holzman, M. D. Cummings, and A. Y. Elezzabi, "Terahertz photonics: Ultrafast physics and applications," *Proceedings of SPIE* **4833**, *Applications of Photonic Technology* 5, pp. 85-96, 2003. **(Invited)**

J. F. Holzman, F. E. Vermeulen, and A. Y. Elezzabi, "Photoconductive generation of 2 ps electrical pulses with semi-insulating GaAs," *Proceedings of SPIE* **4111**, pp. 108-115, 2000.

J. F. Holzman, F. E. Vermeulen, and A. Y. Elezzabi, "Frozen wave sources for multi-cycle THz generation," *Proceedings of SPIE* **4111**, pp. 100-107, 2000.

J. F. Holzman, F. E. Vermeulen, and A. Y. Elezzabi, "Guided-wave metal-semiconductor switch for modulation of 10.6 μm radiation," *Proceedings of SPIE* **3795**, pp. 137-144, 1999.

J. F. Holzman, A. Y. Elezzabi, F. E. Vermeulen, and C. E. Capjack, "Slow wave guiding structures for phase matching in high harmonic generation processes," *Proceedings of SPIE* **3771**, pp. 22-29, 1999.

J. F. Holzman, A. Y. Elezzabi, and F. E. Vermeulen, "Metal-semiconductor waveguides for application to optical-optical switching," *Proceedings of the IEEE Canadian Conference on Electrical and Computer Engineering* **2**, pp. 606-610, 1999.